TEHNIČKI GLASNIK

TEHNIČKI GLASNIK / TECHNICAL JOURNAL – GODIŠTE / VOLUME 13 – BROJ / NUMBER 3

RUJAN 2019 / SEPTEMBER 2019 – STRANICA / PAGES 165-259

/

SVEUČILIŠTE SJEVER / UNIVERSITY NORTH – CROATIA – EUROPE

ISSN 1846-6168 (PRINT) / ISSN 1848-5588 (ONLINE)

TECHNICAL JOURNAL

ISSN 1846-6168 (Print) ISSN 1848-5588 (Online)

TEHNIČKI GLASNIK - TECHNICAL JOURNAL

Scientific-professional journal of University North

Volume 13 Number 3
Varaždin, September 2019 Pages 165–259

Editorial Office:
Sveučilište Sjever – Tehnički glasnik
Sveučilišni centar Varaždin
104. brigade 3, 42000 Varaždin, Hrvatska
Tel. ++385 42 493 328, Fax.++385 42 493 333
E-mail: tehnickiglasnik@unin.hr
https://tehnickiglasnik.unin.hr
https://www.unin.hr/djelatnost/izdavastvo/tehnicki-glasnik/
https://hrcak.srce.hr/tehnickiglasnik

Founder and Publisher:
Sveučilište Sjever / University North

Print:
Centar za digitalno nakladništvo, Sveučilište Sjever

All manuscripts published in journal have been reviewed.
Manuscripts are not returned.

The journal is free of charge and four issues per year are published.
Circulation: 100 copies

Journal is indexed and abstracted in:
Web of Science Core Collection (Emerging Sources Citation Index - ESCI), EBSCOhost Academic Search Complete, EBSCOhost – One Belt, One Road Reference Source Product, ERIH PLUS, CITEFACTOR – Academic Scientific Journals, Hrčak - Portal znanstvenih časopisa RH

Registration of journal:
The journal "Tehnički glasnik" is listed in the HGK Register on the issuance and distribution of printed editions on the 18th October 2007 under number 825.

Preparation ended:
September 2019

Legend:
(1) University North, (2) Mechanical Engineering Faculty in Slavonski Brod, (3) Faculty of Graphic Arts Zagreb, (4) Faculty of Civil Engineering Osijek, (5) Faculty of Engineering Rijeka, (6) Faculty of Mechanical Engineering and Naval Architecture Zagreb, (7) Faculty of Metallurgy Sisak, (8) Tomas Bata University in Zlín, (9) Department of Physics of the University of Josip Juraj Strossmayer in Osijek, (10) Faculty of Humanities and Social Sciences Osijek, (11) Karlovac University of Applied Sciences, (12) University of Applied Sciences Velika Gorica, (13) Department of Polytechnics - Faculty of Humanities and Social Sciences Rijeka, (14) Faculty of Electrical Engineering and Computer Science - University of Maribor, (15) Faculty of Civil Engineering - University of Maribor, (16) University College of Teacher Education of Christian Churches Vienna/Krems, (17) Mechanical Engineering Faculty Tuzla, (18) Mechanical Engineering Faculty Sarajevo, (19) University of Travnik - Faculty of Technical Studies, (20) Higher Education Technical School of Professional Studies in Novi Sad, (21) University of Novi Sad - Faculty of Technical Sciences, (22) Faculty of Mechanical Engineering - University of Montenegro, (23) Brno University of Technology, (24) Odessa State Academy of Civil Engineering and Architecture, (25) Faculty of Civil Engineering - University of Mostar, (26) Faculty of Manufacturing Technologies with the seat in Prešov - Technical University in Košice

Note from the Editor-in-Chief *

Dragi čitatelji,

Dana 11. srpnja 2019. u Velikoj predavaonici Prehrambeno-biotehnološkog fakulteta u Zagrebu, a na inicijativu prof. dr. sc. Vladimira Mrše, glavnog urednika časopisa Food Technology and Biotechnology (izdavač je Prehrambeno-biotehnološki fakultet u Zagrebu), održan je inicijalni sastanak za pokretanje Udruge urednika i ostalih osoba uključenih u izdavanje hrvatskih znanstvenih i znanstveno-stručnih časopisa te onih za popularizaciju znanosti. Sastanku je nazočilo preko 100 zainteresiranih. Jedan od razloga za ovakvu inicijativu je i Javni poziv za financijsku potporu znanstvenim časopisima i časopisima za popularizaciju znanosti u 2019. godini, objavljen na stranicama Ministarstva znanosti i obrazovanja 12. lipnja 2019. (https://mzo.gov.hr/istaknute-teme/natjecaji-196/javni-poziv-za-financijsku-potporu-znanstvenim-casopisima-i-casopisima-za-popularizaciju-znanosti-u-2019-godini/1910). U tom Javnom pozivu pod II. Korisnici financijske potpore je navedeno da "Pravo prijave imaju i znanstvene organizacije iz sustava znanstvene djelatnosti, odnosno ustanove upisane u Upisnik znanstvenih organizacija *osim javnih znanstvenih instituta i javnih visokih učilišta jer su im troškovi izdavanja znanstvenih i znanstveno-stručnih časopisa te časopisa za popularizaciju znanosti prihvatljivi u sklopu programskog financiranja*." Dakle, Sveučilište Sjever (izdavač časopisa TEHNIČKI GLASNIK) nema pravo prijave što mi je e-poštom iz MZO i potvrđeno. Jedna od primjedaba na sastanku bila je da je neprihvatljivo da MZO usred godine donosi odluku o promjeni načina financiranja, radi koje je budućnost mnogih časopisa upitna. Ti isti časopisi osiguravaju znanstvenicima vrednovanje njihovoga rada, a temelje se na volonterskom radu, bez sustavne potpore, pri čemu se ovakvim odlukama omalovažava rad urednika i suradnika. Također je izražena i sumnja da se financiranje u 2019. godini može ostvariti putem programskih potpora jer (navodno) ne postoje podaci o kojim se iznosima radi, već se navodi izdavačka djelatnost kao jedna od stavki. Koje bi aktivnosti Udruge s početka ovog uvodnika trebale biti? Istaknuto je prije svega sljedeće:

- Sudjelovanje u održavanju sustava znanstvenog izdavaštva – prije svega komunikacija između časopisa i MZO te Povjerenstva za izdavačku djelatnost, koja je trenutačno manjkava.
- Osiguravanje stabilnog sustava financiranja – časopisi su suočeni s neizvjesnošću jer MZO često mijenja kriterije, nisu unaprijed poznati iznosi potpore i hoće li je uopće biti, a časopisi kao periodičke publikacije moraju imati stabilnost prihoda.
- Razmjena mišljenja i iskustava, te pružanja potpore časopisima u svim aspektima njihova rada.
- Istupanje prema MZO, tijelima javne uprave, NSK, HR DOI uredu, bazama, vanjskim institucijama i dr.
- Promocija otvorenog pristupa znanosti u skladu s preporukama Europske komisije objavljenima u "Planu S", prema kojima bi od 1. siječnja 2020. godine svi znanstveni rezultati proizašli iz istraživanja financiranih javnim sredstvima trebali biti objavljeni u časopisima u otvorenom pristupu – Hrvatska već ima, zahvaljujući dosadašnjem sustavu financiranja putem MZO, većinu časopisa u otvorenom pristupu, pa je cilj Udruge održati takav trend.

Radi pripreme dokumenata potrebnih za registraciju Udruge je nakon kraće rasprave i nominacije kandidata iz raznih područja znanosti predložena Radna grupa. Radnu grupu radi lakše operativnosti (čestih sastanaka) čine članovi iz Zagreba, a svrha je radne grupe da pripremi nacrt statuta koji će poslati putem mailing lista svim urednicima na razmatranje i dopunu.

Tijekom kolovoza je pripremljen nacrt statuta udruge koja bi se trebala zvati "Hrvatsko udruženje za znanstvenu komunikaciju" (skraćeno ZNAK, no to je samo prijedlog i još nije konačno odlučeno da li skraćeni naziv ostaje).

Mišljenja sam da TEHNIČKI GLASNIK svakako treba podržati osnivanje Udruge i biti aktivan u njoj, jer dugoročno može imati samo koristi od ovog članstva.

Srdačan pozdrav,

Milan Kljajin, glavni urednik

* There is no English version of foreword because it is of local importance

ISSN 1846-6168 (Print), ISSN 1848-5588 (Online)
https://doi.org/10.31803/tg-20190312191013

Original scientific paper

TENSILE PROPERTIES OF POLYPROPYLENE/LINEAR LOW-DENSITY POLYETHYLENE/NANO-TITANIUM DIOXIDE NANOCOMPOSITES USING A TWO-LEVEL FACTORIAL EXPERIMENT

Sajjad DANESHPAYEH, Faramarz ASHENAI GHASEMI, Ismail GHASEMI

Abstract: In this paper, a 2^3 factorial design analysis was used to study the parameters affecting the mechanical characteristics of polypropylene/linear low-density polyethylene/nano-titanium dioxide (PP/LLDPE/TiO_2) nanocomposites, and to optimize these factors in order to predict the maximum ultimate tensile strength (UTS), elastic modulus (EM), and yield strength (YS) simultaneously. To do this, two levels of nano-titanium dioxide (TiO_2), linear low-density polyethylene (LLDPE) and styrene-ethylene-butylene-styrene (SEBS) as the coupling agent were selected and eight experiments were conducted for every response. The most effective factors influencing the UTS, EM, and YS were found, and acceptable prediction regression models were taken. One noted that nanoparticles increased the elastic modulus. The attendance of high levels of LLDPE and SEBS resulted in a decrease in YS and UTS. Moreover, the optimum values of variables were determined by using the contour plot.

Keywords: elastic modulus; factorial design; nanocomposite; polypropylene; tensile strength

1 INTRODUCTION

Nowadays, polymeric products, especially polyethylene (PE) and polypropylene (PP), are developed for their low expense, good mechanical features, small weight, and other desirable characteristics [1]. Different kinds of polyethylene, containing high-density polyethylene (HDPE), low-density polyethylene (LDPE), and linear low-density polyethylene (LLDPE) are used to improve the mechanical and physical characteristics of PP [2]. Additionally, LLDPE has numerous applications, and the importance of LLDPE has increased due to its special characteristics [3].

To refine the particular characteristics of these polymers, several additives are mixed with them. Adding some micro- or nanoscale fillers may improve the disadvantages of neat polymers. Nanocomposites are polymers that are embedded with nanoscale fillers [4]. Polymer nanocomposites can modify the mechanical strength, heat resistance, elastic modulus, thermal degradation and viscoelasticity more than other traditional polymer composites [5]. By adding small values of nanoparticles, melt processing, polymer crystallization, and electric and thermal conductivity can be improved [6, 7].

Polymer nanocomposites have recently gained the attention of many material researchers. They usually study the effects of embedding various nanoparticles on the characteristics of polymer materials. Organic and inorganic nanoparticles can be utilized as reinforcement. Some of the most used inorganic nanoparticles are SiO_2, TiO_2, Al_2O_3, and ZrO_2 [3]. TiO_2 is a very special material due to special characteristics such as light density and thermal degradation [8]. The main problem in manufacturing the TiO_2 nanocomposite is its conflict with the polymer matrix, because TiO_2 is hydrophilic and the polymer matrix is hydrophobic. TiO_2 nanoparticles also have a large surface area ratio which makes them aggregate easily. To avoid this, styrene ethylene-butylene-styrene (SEBS) can be applied as a coupling agent to improve the TiO_2 surface [9-11].

Many scientists have investigated the mechanical properties of polymers and polymer composites. Garcia et al. [12], for instance, added SiO_2 nanoparticles to the PP matrix and observed that the impact strength and elastic modulus were improved. Selvin et al. [13] found that TiO_2 nanoparticles significantly increased the elastic modulus of the polystyrene matrix. Moreover, Sirirat et al. [14] added small values of TiO_2 to the PP matrix and reported an improvement in some mechanical properties of the based material. Moreover, Altan [15] showed that, by embedding TiO_2 nanoparticles in the PP matrix, the elastic modulus of the structure increased, but its impact strength was reduced.

Ternary nanocomposites, including a system of the polymer matrix, elastomer, and filler, have newly been incorporated in different applications [16, 17]. Liu et al. [18] showed that, by adding TiO_2 nanoparticles to PP/LLDPE, some mechanical properties of the compounds were enhanced. Furthermore, Abu Ghalia et al. [17] reported that, by embedding calcium carbonate ($CaCO_3$) in PP/LLDPE compounds, some of their mechanical characteristics were improved. Altan and Yildirim [19] showed that structures including TiO_2 and SEBS present better mechanical characteristics compared to ones without SEBS.

Guo and Li [20] found that SEBS/titania nanocomposites showed good mechanical attributes. They also reported that the uniform dispersion of titania nanoparticles in the SEBS matrix increased the thermal stability of samples. Additionally, Nguyen et al. [9] concluded that some mechanical characteristics of LDPE/modified TiO_2 nanocomposites increased compared to the based LDPE/unmodified structures. Xue et al. [21] verified that the coexistence of organo-montmorillonite (OMMT) and nano-Cu in Cu/OMMT/LLDPE nanocomposites may improve the anticorrosion properties of samples.

Here, a 2^3 factorial design was used to supply a relation for the YS, UTS, and EM of PP/LLDPE/TiO_2 nanocomposites as a mathematical function of parameters (SEBS, TiO_2, and LLDPE). Moreover, the effect of every agent on mechanical characteristics was studied and the optimal range of each parameter was found in order to achieve the best tensile properties.

2 THE EXPERIMENTS

2.1 Materials

Polypropylene (PP-Z30S, MFR-25, 230 °C, 2.16 kg) and linear low-density polyethylene (LLDPE-0209, MFR-0.9, 190 °C, 2.16 kg, and density of 0.920 gr ml^{-1}) were procured from the Arak Petrochemical Company, Iran. The nano-TiO_2 rutile structure with the mean size of 30 nm and density of 4.23 g/cm was obtained from the Iranian Nanomaterials Pioneers (INP), Iran. Moreover, the KRATON polymer type G, namely styrene-ethylene/butylene-styrene (SEBS), was used as a coupling agent. The compound was prepared by using a co-rotating screw extruder (ZSK 25 P8.2E WLE) with a 170 to 190 °C temperature range. Next, they were made as granules. Granules were injected with the help of an injection molding machine (IMAN MACHINE 125g) with the temperature profiles of 190-200-210 °C, and the samples were hence prepared.

2.2 Mechanical Testing

The elastic modulus, yield, and ultimate tensile strength were specified by a Zwick/Roell–Z100 machine (Germany) due to the ASTM D638 standard with the strain rate of 50 mm/min at room temperature. Fig. 1 shows a sample before and after the tensile tests.

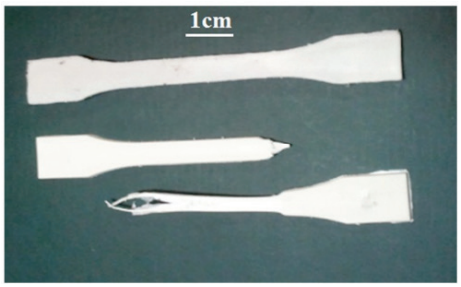

Figure 1 A sample before and after the tensile tests

2.3 Experiment Design

The factorial design of experiments (DOE) is a good and well-known procedure of testing in which all parameters are changed together in the experimental runs [22]. In this work, DOE was applied to study the effect of significant factors on the EM, YS, and UTS of PP/LLDPE/TiO_2 nanocomposites. The main aspect in DOE is the choice of control factors [23]. Here, the studied factors were LLDPE, TiO_2 nanoparticles, and SEBS. After the choice of factors, the 2^3 factorial design method was offered the levels which were coded within the −1 and +1 range in such a way that the researcher could choose an experimental design from a list of designs.

The 2^k factorial design is one of the most widely applied designs to investigate the effects of various parameters on a particular response, where k is the number of parameters and the base 2 shows the level of treatment for each discussed parameter [22]. The performed design is shown in Tab. 1 which briefly discusses the parameters and the change of their levels. Furthermore, different modes of combining materials via the software were determined. As presented in Tab. 2, eight tests had to be prepared for each response having three replicates.

Table 1 Level of factors applied to study the effect of LLDPE, TiO_2 and SEBS

Factors		LLDPE	TiO_2	SEBS
Level	−1 (low)	40	0	0
	+1(high)	60	2	3

Table 2 Results of running the software

Full Factorial Design								
Sample No.	1	2	3	4	5	6	7	8
PP (Wt. %)	80	60	78	58	77	57	75	55
LLDPE (Wt. %)	20	40	20	40	20	40	20	40
TiO_2 (Wt. %)	0	0	2	2	0	0	2	2
SEBS (Wt. %)	0	0	0	0	3	3	3	3
Random order of samples	3	2	8	1	6	4	7	5

As three parameters at two levels were assumed, the experimental design was named a 2^3 full factorial design that needed eight test runs for every response. The average of results is presented in Tab. 3.

Table 3 The experimental results for YS, UTS and EM

Sample No.	1	2	3	4	5	6	7	8
YS (MPa)	19.63	12.9	15.33	11.56	21.86	13.33	16.16	11.9
UTS (MPa)	23.63	19.5	21.86	18.3	23.93	18.03	20.33	19
EM (MPa)	223	189	226.6	207.3	212	184.6	222.6	199.3

3 RESULTS AND DISCUSSION

3.1 Analysis of Variance (ANOVA) for Tensile Strength

The p-value is described as the minimum level of importance leading to the rejection of the null hypothesis and interaction is a kind of action that occur as two or more objects have an effect upon one another [22]. F value is the measure of variation in the data about the mean. Due to the p-value described as the minimum level of importance leading to the rejection of the null hypothesis, it seems that the effect of every parameter was statistically important at the p-value of less than 0.05.

The ANOVA results for YS are presented in Tab. 4. One sees that LLDPE (P = 0.000), TiO_2 (P = 0.000), SEBS (P = 0.001), LLDPE×TiO_2 (P = 0.000), and LLDPE×SEBS (P = 0.021) with the p-values below or equal to 0.05 for a 95% assurance level should be statistically important for YS. In addition to that, Fisher's variance ratio (F-value) is the amount of variability from the mean. Applying the F-value, the respective significance of each parameter and its interaction would be:

LLDPE>TiO_2>LLDPE×TiO_2> SEBS>LLDPE×SEBS.

Table 4 ANOVA results for YS

Source	*F*	*P*
Main Effects	249.31	0.000
LLDPE	555.84	0.000
TiO_2	175.14	0.000
SEBS	16.95	0.001
2-Way Interactions	21.94	0.000
LLDPE×TiO_2	57.56	0.000
LLDPE×SEBS	6.51	0.021
TiO_2×SEBS	1.76	0.203

The effects of the LLDPE×TiO_2 interaction on YS are greater than the importance effect of a single-factor (i.e. factor SEBS). The important interaction of LLDPE and TiO_2 shows that these parameters are related, i.e. if the level of one parameter varies, the effect of the other one varies, too.

The ANOVA results of UTS are presented in Tab. 5. It is clear that LLDPE (P = 0.000), TiO_2 (P = 0.000), SEBS (P = 0.003), and LLDPE×TiO_2 (P = 0.000) whose p-values were below or equal to 0.05 for UTS should be statistically important. Moreover, from the F-values in Tab. 5, the relative importance of each factor and its interactions would be:

LLDPE>TiO_2> LLDPE×TiO_2> SEBS.

Table 5 ANOVA results for UTS

Source	*F*	*P*
Main Effects	261.86	0.000
LLDPE	678.05	0.000
TiO_2	95.35	0.000
SEBS	12.16	0.003
2-Way Interactions	27.04	0.000
LLDPE×TiO_2	80.12	0.000
LLDPE×SEBS	0.66	0.428
TiO_2×SEBS	0.34	0.569

Table 6 ANOVA results for EM

Source	*F*	*P*
Main Effects	235.29	0.000
LLDPE	553.29	0.000
TiO_2	114.57	0.000
SEBS	38.20	0.000
2-Way Interactions	6.25	0.005
LLDPE×TiO_2	17.82	0.001
LLDPE×SEBS	0.36	0.555
TiO_2×SEBS	0.57	0.462

The EM ANOVA results are presented in Tab. 6. It is observed that LLDPE (P = 0.000), TiO_2 (P = 0.000), SEBS (P = 0.000), and LLDPE×TiO_2 (P = 0.001), whose p-values were below or equal to 0.05 for EM would be statistically important. Moreover, from the F-values in Tab. 6, the relative importance of each factor and its interactions would be:

LLDPE>TiO_2> SEBS> LLDPE×TiO_2.

The multiple regression analysis was performed on the experimentally collected data for the YS, UTS, and EM of the PP/LLDPE/TiO_2 nanocomposites. Here, the analysis was done by the Minitab® 16 software which applies the ordinary least squares technique to find the regression function. Relying on ANOVA for YS, UTS, and EM, a fitted regression model with statistical importance was found as follows:

$$\text{Yield Strength} = 15313 - 2.888\text{LLDPE} - 1.621TiO_2 + 0.504\text{SEBS} + 0.929\text{LLDPE} \times TiO_2 - 0.312\text{LLDPE} \times \text{SEBS} \quad (1)$$

R-sq: 98.07%, R-sq(Pred): 95.67%, R-sq(Adj): 97.23%

$$\text{Ultimate Tensile Strength} = 20.575 - 1.867\text{LLDPE} - 0.7TiO_2 - 0.25\text{SEBS} + 0.642\text{LLDPE} \times TiO_2 \quad (2)$$

R-sq: 98.28% R-sq(Pred): 96.13%, R-sq(Adj): 97.53%

$$\text{Elastic Modulus} = 208.08 - 13\text{LLDPE} + 5.92TiO_2 - 3.42\text{SEBS} + 2.33\text{LLDPE} \times TiO_2 \quad (3)$$

R-sq: 97.86%, R-sq(Pred): 95.18%, R-sq(Adj): 96.92%

From Eq. (2), one sees that all factors had a negative main effect on UTS. Thus, a lower factor setting (−1) would result in a higher response. In the situation of Eq. (1), an increase in LLDPE×TiO_2 and SEBS from small to high levels resulted in 2.77% and 6.76% increases in YS, whereas an increase in LLDPE and TiO_2 resulted in a decrease in YS by 31.7% and 19.14%. Thus, LLDPE had a maximum effect on YS with a 31.7% contribution. In the case of Eq. (2), by adding of LLDPE, TiO_2, and SEBS decreased UTS by 16.63%, 6.58%, and 2.40%, respectively. Therefore, LLDPE had a maximum effect on UTS with a 16.63% contribution. In Eq. (3), an increase in TiO_2 and LLDPE × TiO_2 from low to high levels resulted in 2.57% and 5.85% increases in EM, whereas an increase in LLDPE and SEBS decreased EM by 11.76% and 3.2%, respectively. Hence, LLDPE had a maximum effect on EM with a 11.76% contribution.

A verified model must predict the response with good accuracy with respect to the experimental data. Model adequacy is checked by R-Sq, R-Sq (adj), and R-Sq (pred). A R-Sq value near 100% means a reliable fit to the experimental data [22]. Based on the ANOVA results, the R-squared of the regression equations was 98.07 % for YS, 98.28% for UTS, and 97.86% for EM, which means that the model is verified. The adjusted R-square was 97.23% for YS, 97.53% for UTS, and 96.92% for EM, which accounts for the amount of predictors in the model. The prediction R-squared statistic was calculated to be 95.67% for YS, 96.13% for UTS, and 95.18% for EM. Because the predicted R-square values were near the R-square and the adjusted R-square values for every response, none of the models appeared to be overfitting and none had an adequate predictive ability [22].

3.2 Main Effects and Interaction Plot for Yield Strength

The main effects plot in Fig. 2 indicates that YS decreases as LLDPE and TiO_2 contents increase. Therefore, the maximum YS of PP/LLDPE/TiO_2 nanocomposites could be found at a lower LLDPE and TiO_2. Moreover, Fig. 2 shows that by increasing the amount of the SEBS factor increases the yield strength. The relative strength of the effect of different parameters can also be seen. The main effects

plot for YS (Fig. 2) showed that LLDPE was the most important factor.

Fig. 3 shows the interaction plot between the three discussed factors, namely LLDPE, TiO_2, and SEBS for YS, respectively. The plots, known as interaction plots, are employed to explain important interactions between process parameters. The interaction plot summarizes the interaction between the maximum and minimum amounts of each factor. From these plots, one sees that the initial interaction happened between LLDPE and TiO_2 for YS, demonstrated by non-parallel lines.

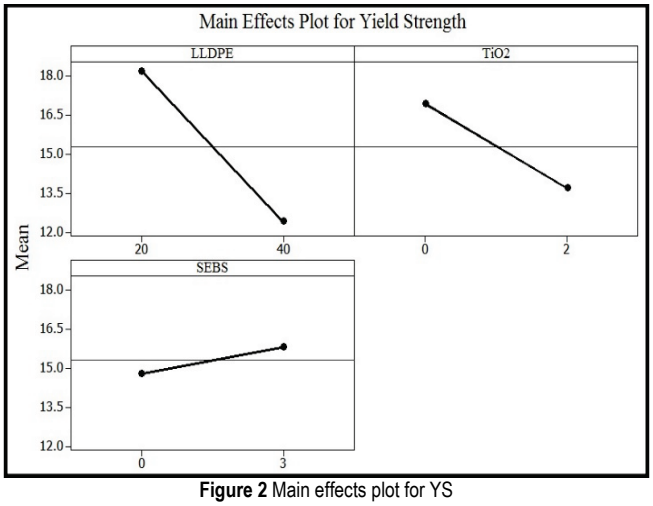

Figure 2 Main effects plot for YS

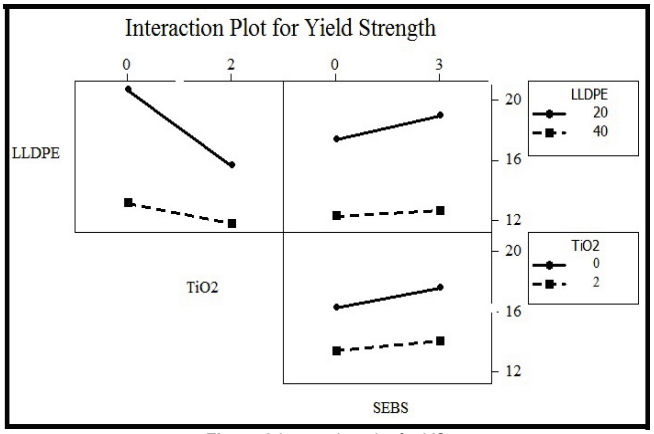

Figure 3 Interaction plot for YS

According to Fig. 3, at a low level of LLDPE (20 wt. %) and TiO_2 (0 wt. %), the interaction was very important, but adding both parameters produced a low interaction. However, the important interaction of LLDPE versus TiO_2 for YS showed that a lower TiO_2 (0 wt. %) would result in an improvement in the YS of PP/LLDPE/TiO_2 nanocomposites when factor LLDPE was under the low level (20 wt. %), while the influence of TiO_2 was reduced at the high level of LLDPE (40 wt. %). These data for YS suggested that the ideal TiO_2 of PP/LLDPE/TiO_2 nanocomposites differs from the LLDPE. The models with low TiO_2 show a large YS when LLDPE is low, and the models with great TiO_2 indicate a low YS when LLDPE is high.

3.3 Main Effects and Interaction Plot for Ultimate Tensile Strength

The main effects plot in Fig. 4 indicates that increasing the amount of all three major factors, especially polyethylene, the ultimate tensile strength is reduced. LLDPE decreased UTS for LLDPE, which was much smoother than PP. Therefore, the maximum UTS of PP/LLDPE/TiO_2 nanocomposites would be reached at a less amount of LLDPE, TiO_2, and SEBS. The relative strength of the effect of different parameters could also be seen. The main effects plot for UTS (Fig. 4) showed that LLDPE was the most important factor.

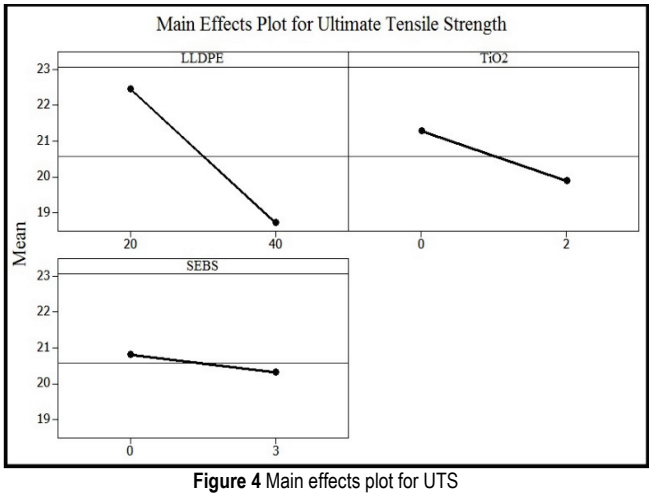

Figure 4 Main effects plot for UTS

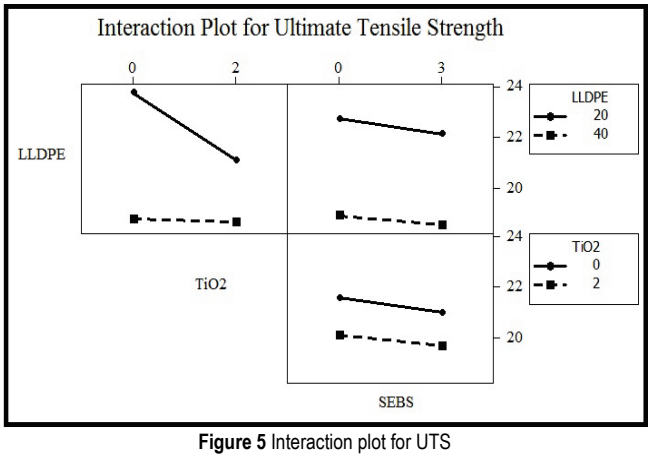

Figure 5 Interaction plot for UTS

Fig. 5 demonstrates the interaction plot between the three discussed factors, namely LLDPE, TiO_2, and SEBS, for UTS, respectively. From the plot, one sees that the initial interaction happened between LLDPE and TiO_2 for UTS, showed by non-parallel lines.

Fig. 5 shows that, at the low levels of LLDPE (20 wt. %) and TiO_2 (0 wt. %), the interaction was very important, but by adding both parameters, it produced a low interaction. However, the important interaction of LLDPE in respect to TiO_2 for UTS showed that lower TiO_2 (0 wt. %) would result in an increase in the UTS of PP/LLDPE/TiO_2 nanocomposites when LLDPE was under the low level (20

wt. %), while the effect of TiO_2 was reduced at the high level of LLDPE (40 wt. %). These data for UTS suggested that the ideal TiO_2 of PP/LLDPE/TiO_2 nanocomposites differs with LLDPE. The models with low TiO_2 show large UTS when LLDPE is low, and the models with high TiO_2 demonstrate small UTS when LLDPE is high.

3.4 Main Effects and Interaction Plot for Elastic Modulus

The main effects plot in Fig. 6 indicates that the elastic modulus decreased as LLDPE and SEBS varied from a low to a high level. Consequently, the maximum elastic modulus of PP/LLDPE/TiO_2 nanocomposites could be obtained at lower LLDPE and SEBS.

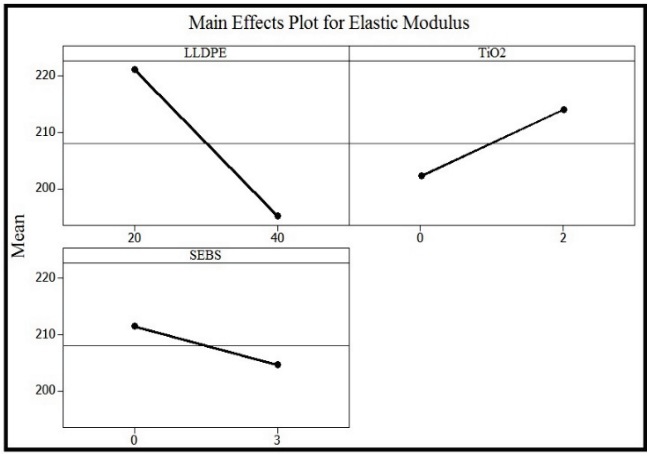

Figure 6 Main plots for EM

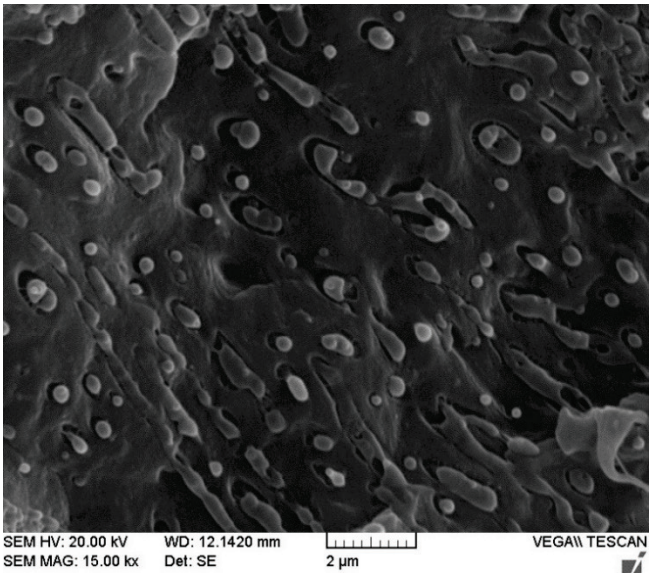

Figure 7 FESEM image taken from fractured surface sample including 2wt.% TiO_2 nanoparticles

However, regarding the mechanical properties of the variables, namely EM, a variation of TiO_2 seems to have a significantly increasing effect, similar to Selvin's [13] finding about polystyrene/TiO_2 nanocomposites. The relative strength of the effect of different parameters may also be seen. The main effects plot for EM (Fig. 6) showed that LLDPE was the most important factor. The elastic modulus of polymer nanocomposites largely depends on the good dispersion of nanoparticles in the matrix. Fig. 7 shows field emission scanning electron microscopy (FESEM) images taken from the samples' fractured surface. It can be observed from Fig. 7 that nanoparticles are well dispersed in the matrix. As a result, titanium oxide nanoparticles lead to an increase in the elastic modulus.

Fig. 8 illustrates the interaction plot between the three investigated parameters, namely LLDPE, TiO_2, and SEBS, for EM, respectively. One could see that the initial interaction happened between LLDPE and TiO_2 for EM, indicated by non-parallel lines (Fig. 8). Fig. 8 shows that, at the low levels of LLDPE (20 wt. %) and TiO_2 (0 wt. %), the interaction was highly significant, and that increasing both parameters produced a good interaction and increased the EM. However, the important interaction of LLDPE versus TiO_2 for EM showed that a high TiO_2 (2 wt. %) would result in an increase in the EM of PP/LLDPE/TiO_2 nanocomposites when LLDPE was under the high level (40 wt. %), while the effect of TiO_2 was reduced at the low level of LLDPE (20 wt. %). These data for EM suggested that the ideal TiO_2 of PP/LLDPE/TiO_2 nanocomposites varied with LLDPE. The models with high TiO_2 show large EM when LLDPE is high, and the models with low TiO_2 indicate small EM when LLDPE is low.

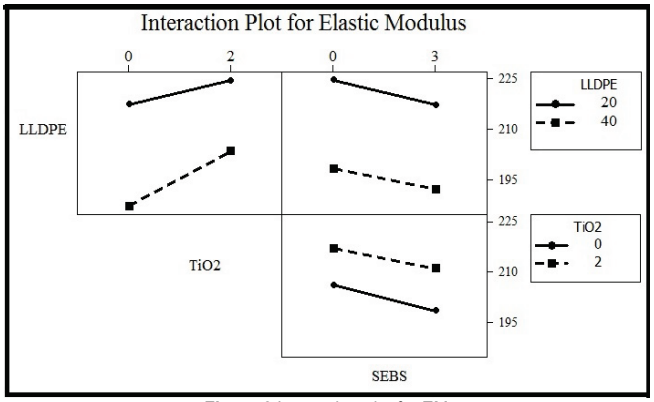

Figure 8 Interaction plot for EM

3.5 Optimal Ranges to Achieve the Best Tensile Properties

Mini-tab uses a contour plot to obtain the optimal areas of tensile properties. Contour or level plots are a method to present a three-dimensional surface on a two-dimensional plane. It graphs two predictor variables X Y on the y-axis and a response variable Z as contours. In this graphs, darker regions indicate higher responses values. They are beneficial for the creation of a favorable response. They present the contribution of two parameters simultaneously, and another parameter is retained at its middle level.

Fig. 9 presents the contour plot of the ultimate tensile strength as a function of TiO_2*LLDPE, SEBS*LLDPE, and TiO_2*SEBS. In any of these three modes, the third factor has been fixed in the middle level. Fig. 9 shows that to achieve the best ultimate tensile strength, low amounts of LLDPE (Less than 25 wt. %) and average amounts of titanium dioxide nanoparticles and SEBS should be used. B using this

combination, the ultimate tensile strength of more than 32 MPa can be achieved. Based on Fig. 9, the presence of high values of LLDPE (more than 35 wt.%) led to a significant reduction in the ultimate tensile strength.

Fig. 10 depicts the contour plot of the elastic modulus as a function of TiO_2*LLDPE, SEBS*LLDPE, and TiO_2*SEBS. In any of these three modes, the third factor has been fixed in the middle level. It is clear that, to achieve the best elastic modulus, low amounts of LLDPE and SEBS and high amounts of titanium dioxide nanoparticles should be used. By using this combination, the elastic modulus of more than 220 MPa can be achieved. Based on Fig. 9, the presence of high values of TiO_2 led to a significant increase in the elastic modulus.

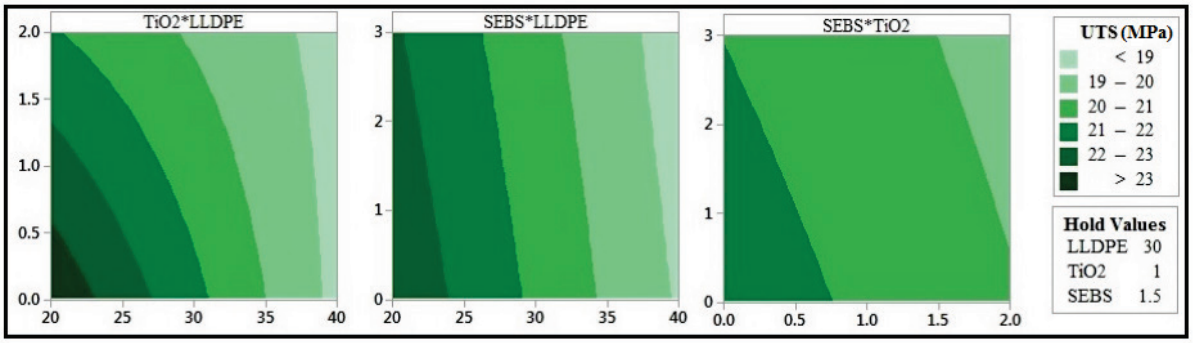

Figure 9 The contour plots of ultimate tensile strength

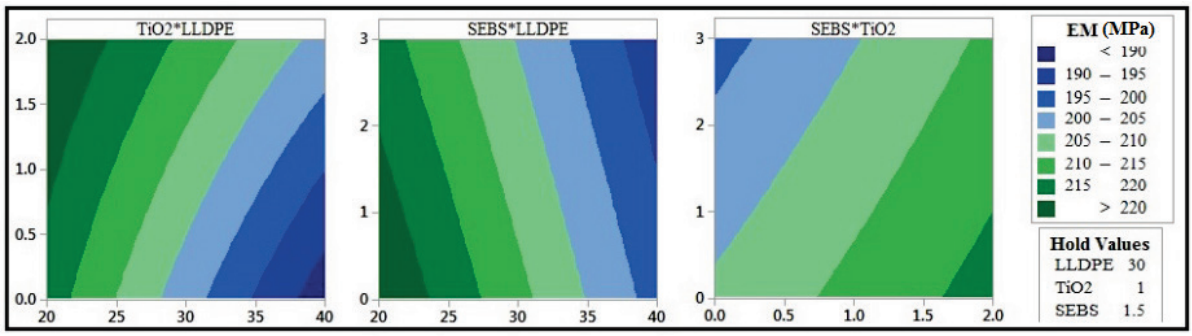

Figure 10 The contour plots of elastic modulus

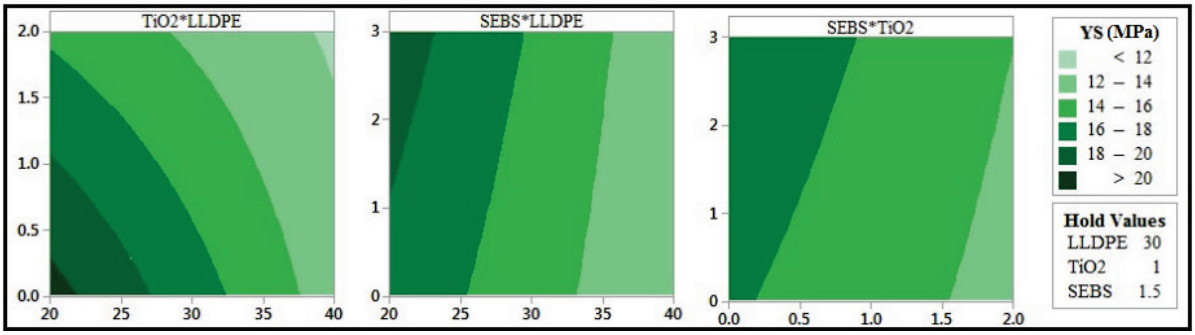

Figure 11 The contour plots of yield strength

Fig. 11 presents the contour plot of yield strength as a function of TiO_2*LLDPE, SEBS*LLDPE, and TiO_2*SEBS. In any of these three modes, the third factor has been fixed in the middle level. It is observed from Figure 11 that to achieve more than 20 MPa for yield strength, the smallest amount of polyethylene (about 20 wt.%) with the highest amount of nanoparticles and compatibilizer should be combined. Based on Fig. 11, the presence of high values of LLDPE (more than 25 wt.%) led to a significant reduction in yield strength.

4 CONCLUSIONS

An optimization method, in which the factorial design, mathematical modelling and contour plots were used for the prediction of the mechanical properties of PP/LLDPE/TiO_2 nanocomposites, has been studied. The following results were obtained:

- It was observed that the most important factors were LLDPE and TiO_2, which influenced YS, UTS, and EM, while SEBS was relatively less significant.
- From the main effects and interaction plot, one sees that by adding SEBS from low to high levels, there was a

6.76% increase in YS, whereas an increase in LLDPE led to a decrease in YS by 31.7%. An increase in LLDPE and SEBS decreased the UTS to 16.63% and 2.40%, respectively. Moreover, an increase in TiO_2 and LLDPE×TiO_2 (from a low to a high level) resulted in 2.57% and 5.85% increases in EM, respectively.

- The optimized ranges of variables on the tensile properties were found by using the contour plot. The results show that the most improved tensile properties were obtained in the low level of LLDPE and SEBS and the middle level of titanium dioxide nanoparticles.

5 REFERENCES

[1] Zapata, P. A., Rabagliati, F. M., Lieberwirth, I., Catalina, F., & Corrales, T. (2014). Study of the photodegradation of nanocomposites containing TiO_2 nanoparticles dispersed in polyethylene and in poly (ethylene-cooctadecene). *Polym Degrad Stabil*, 109, 106-114. https://doi.org/10.1016/j.polymdegradstab.2014.06.020

[2] Chen, J. H., Zhong, J. C., Cai, Y. H., Su, W. B., & Yang, Y. B. (2007). Morphology and thermal properties in the binaryblends of poly (propylene-co-ethylene) copolymer andisotactic polypropylene with polyethylene. *Polymer, 48*(10), 2946-2957. https://doi.org/10.1016/j.polymer.2007.03.037

[3] Owpradit, W. & Jongsomjit, B. (2008). A comparative study on synthesis of LLDPE/TiO_2 nanocomposites using different TiO_2 by in situ polymerization with zirconocene/dMMAO catalyst. *Mater Chem Phys, 112*(3), 954-961. https://doi.org/10.1016/j.matchemphys.2008.07.050

[4] Chaichana, E., Jongsomjit, B., & Praserthdam, P. (2007). Effect of nano-SiO_2 particle size on the formation of LLDPE/SiO_2 nanocomposite synthesized via the in situ polymerization with metallocene catalyst. *Chem Eng Sci, 62*(3), 899-905. https://doi.org/10.1016/j.ces.2006.10.005

[5] Zapata, P. A., Palza, H., Cruz, L. S., Lieberwirth, I., Catalina, F., Corrales, T., & Rabagliati, M. (2013). Polyethylene and poly (ethylene-co-1-octadecene) composites with TiO_2 based nanoparticles by metallocenic in situ polymerization. *Polymer, 54*(11), 2690-2698. https://doi.org/10.1016/j.polymer.2013.03.048

[6] Palza, H., Reznik, B., Kappes, M., Hennrich, F., Naue, I. F. C., & Wilhelm, M. (2010). Characterization of melt flow instabilities in polyethylene/carbon nanotube composites. *Polymer, 51*(16), 3753-3761. https://doi.org/10.1016/j.polymer.2010.06.016

[7] Palza, H., Vergara, R., & Zapata, P. A. (2011). Composites of polypropylene melt blended with synthesized silica nanoparticles. *Compos Sci Technology, 71*(4), 535-540. https://doi.org/10.1016/j.compscitech.2011.01.002

[8] Tong, Y., Li, Y., Xie, F., & Ding, M. (2000). Preparation and characteristics of polyimide–TiO_2 nanocomposite film. *Polym Int, 49*(11), 1543-1547. https://doi.org/10.1002/1097-0126(200011)49:11<1543::AID-PI535>3.0.CO;2-B

[9] Giang, V., Thai, H., Huynh, D., Trung, H., Lam, D. T., & Tuan, M. V. (2013). Effect of titanium dioxide on the properties of polyethylene/TiO_2 nanocomposites. *Compos B-Eng, 45*(1), 1192-1198. https://doi.org/10.1016/j.compositesb.2012.09.058

[10] Norio, N. & Toyoharu, H. (2008). Preparation of TiO_2 nanoparticles surface-modified by both carboxylic acid and amine: dispersibility and stabilization in organic solvents. *Colloids Surf A*, 317, 543-550. https://doi.org/10.1016/j.colsurfa.2007.11.036

[11] Daneshpayeh, S., Ashenai Ghasemi, F., Ghasemi, I., & Ayaz, M. (2015). Predicting of mechanical properties of PP/LLDPE/TiO2 nanocomposites by response surface methodology. *Compos. Part. B*, 84, 109-120. https://doi.org/10.1016/j.compositesb.2015.08.075

[12] Garcia, M., Vilet, G. V., & Jain, S. (2004). Polypropylene/ SiO_2 nanocomposites with improved mechanical properties. *Rev Adv Mater Science, 6*(2), 169-175.

[13] Selvin, T. P. & Kuruvilla, J. (2004) Mechanical properties of titanium dioxide filled Polystyrene microcomposites. *Mater let, 58*(3-4), 281-289. https://doi.org/10.1016/S0167-577X(03)00470-1

[14] Wacharawichananat, S., Thongyai, S., & Tipsri, T. (2009). Effect of mixing conditions and particle sizes of titanium dioxide on mechanical and morphological properties of Polypropylene/Titanium dioxide composites. *Iran Polymer journal, 18*(8), 607-616.

[15] Altan, N. & Yildirim, M. (2010). Mechanical and Morgholigical properties of Polypropylene and High density polyethylene matrix composites reinforced with surface modified nano sized TiO_2 particles. *World Acad Sci Eng Technol, 4*(10), 252-257.

[16] Premphet, K. & Horanont, P. (2000). Phase structure of ternary polypropylene/elastomer/filler composites effect of elastomer polarity. *Polym, 41*(26), 9283-9290. https://doi.org/10.1016/S0032-3861(00)00303-7

[17] Abughalia, M., Hassan, A., & Yussuf, A. (2011) Mechanical and Thermal properties of Calcium Carbonate filled PP/LLDPE Composite. *J Appl Polym Sci, 121*(4), 2413-2421. https://doi.org/10.1002/app.33570

[18] Gang, L., Feng, T. Y., Yuan, Y. F., Cheng, Z. L., Xing, Z. Z., & Ji, X. Q. (2005). Effect of nanoscale SiO_2 and TiO_2 as the fillers on the mechanical properties and aging behavior of Linear Low Density Polyethylene/Low Density Polyethylene blends. *J Polym Env, 13*(4), 339-348. https://doi.org/10.1007/s10924-005-5528-x

[19] Altan, M. & Yildirim, H. (2012). Mechanical and Antibacterial Properties of Injection Molded Polypropylene/ TiO_2 Nano-Composites: Effects of Surface Modification. *J Mater Sci Technol, 28*(8), 686-692. https://doi.org/10.1016/S1005-0302(12)60116-9

[20] Guo, H. & Li, X. (2012). Preparation and Properties of Transparent SEBS/Titania Nanocomposite Films via Functionalization of SEBS and Sol-Gel Process. *Polym Compos, 20*(1/2), 155-160. https://doi.org/10.1177/0967391112020001-230

[21] Xue, B., Li, F., Xing, Y., Sun, M., Liu, D., & Jiang, Y. (2011). Preparation of Cu/OMMT/LLDPE nanocomposites and synergistic effect study of two different nano materials in polymer matrix. *Polymer Bulletin, 67*(8), 1463-1481. https://doi.org/10.1007/s00289-011-0466-3

[22] Montgomery, D. C. (2011). *Design and Analysis of Experiments*. John Wiley & Sons, New York.

[23] Box, G. P. G., Hunter, J. S., & Hunter, W. G., (2005). *Statistics for Experimenters: Design, Innovation and Discovery*. John Wiley & Sons, USA.

Authors' contacts:

Sajjad DANEAHPAYEH
Faculty of Mechanical Engineering,
Shahid Rajaee Teacher Training University,
Shabanloo St., Lavizan, Tehran, Iran
Tel: +9821-22970060
sajad_danesh66@yahoo.com

Faramarz ASHENAI GHASEMI
Corresponding author
Faculty of Mechanical Engineering,
Shahid Rajaee Teacher Training University,
Shabanloo St., Lavizan, Tehran, Iran
Tel: +9821-22970060
f.a.ghasemi@sru.ac.ir
faramarz_ashenai_ghasemi@yahoo.com

Ismail GHASEMI
Department of Polymer Processing,
Iran Polymer and Petrochemical Institute (IPPI),
15 km Tehran-Karaj Highway, Pajuhesh Science and Technology Park,
Pajuhesh Boulevard, Tehran 14977-13115, Iran
Tel: +9821-44787050/
I.Ghasemi@ippi.ac.ir

ISSN 1846-6168 (Print), ISSN 1848-5588 (Online)
https://doi.org/10.31803/tg-20181006143504

Original scientific paper

INVESTIGATION OF THE MECHANICAL PERFORMANCE OF FIBER-MODIFIED CERAMIC COMPOSITES USING FINITE ELEMENT METHOD

Majid AHMADI, Seyed Hadi SEYEDIN, Seyed Vahid SEYEDIN

Abstract: Ceramic materials are widely used in impact safekeeping systems. Ceramic is a heterogeneous material; its characteristics depend considerably both on specifications of its ingredients and the material structure completely. The finite element method (FEM) can be a useful tool for strength computation of these materials. In this paper, the mechanical properties of the ceramic composites are investigated, and the mechanical performance modeling of fiber-fortified ceramic matrix composites (CMC) is expressed by the instance of aluminum oxide fibers in a matrix composite based on alumina. The starting point of the modeling is an infrastructure (primary cell) that contains a micromechanical size, the statistical analysis characteristics of the matrix, fiber-matrix interface, fiber, and their reciprocal influences. The numeral assessment of the model is done using the FEM. The numerical results of composite elastic modulus were computed based on the amount of the added fibers and the porosity was evaluated for empirical data of samples with a similar composition. Various scanning electron microscope (SEM) images were used for each sample to specify the porosity. Also, the unit cell method presumed that the porous ceramic substance is manufactured from an array of fundamental units, each with the same composition, material characteristic, and cell geometry. The results showed that when the material consists of different pores and fibers, the amount of Young's modulus reduces with the increment of porosity. The linear correlation model of elasticity versus porosity value from experimental data was derived by MATLAB curve fitting. The experimental data from the mechanical test and numerical values were in good agreement.

Keywords: ceramic composite; elasticity; fiber; Finite Element Method (FEM); mechanical performance; thermal stress

1 INTRODUCTION

Engineering materials are divided into three technical sections; ceramics, metals, and polymers. Composite is a mixture of various materials from one or more of these parts. One of the phases is often harder, discontinuous, and stronger named as the reinforcement. The less rigid and weaker phase is continuous termed as the matrix. The combination results in different premier properties are not displayed by unique materials. The main advantageous property of composites is mechanical efficiency. Composites contain reinforcement (particles, fibers, flakes, and fillers) embedded in a matrix (metals, polymers, or ceramics). The matrix retains the reinforcement to form the desirable shape while improves all mechanical properties. The important advantageous parameters of fiber-reinforced composites are specific modulus and strength, respectively [1].

Ceramic pieces are broadly used in strike safekeeping systems; the finite element method (FEM) is generally used for strength calculation. As ceramic is a heterogeneous material, its properties depend extremely both on characteristics of the material structure and on its components entirely [2]. Aluminum silicate is used in metallurgical, pottery, glass, and ceramic industries for its resistance or durability. These materials contain refractory soils or clay content. The layered clay stone increases refractories resistance in high-temperature compositions that have a large granule or particle size distribution (PSD) with high porosity and heterogeneous microstructure. Fiber-modified composites use has been extended in the world due to ductility, durability, high strength, stiffness, and impact resistance. The major objective of the fiber addition is to enhance the mechanical characteristics, strength in particular [3].

Ceramic matrix composites (CMCs) can be substituted rather than other materials in various applications in which the higher expenses are offset by an increment in performance. They are prone to catastrophic failure due to the lack of stiffness. To benefit from CMCs and minimize problems like a partial failure, modeling and computational software such as finite element analysis (FEA) are fundamental for investigating stuff efficiency non-destructively at the operating conditions and temperatures. FEA is able to define mechanical characteristics, such as inter-laminar shear properties and shear forces, crack deflection, and congested damage failure [4, 5]. A new concept was developed by Tranquart et al. to model complex materials such as CMCs on the Yarn's scale for identifying bending moment diagrams and qualitative data for life cycle anticipation, as well as material design and structure optimization. A novel general finite elements approach (GFEA) such as the novel numerical modeling approach of the CMC yarn, as a suitable modeling scale, has been offered recently. This model depends on a pattern-based explanation of the micro-scale put into a GFEM-like framework. A multi-scale and multi-physics macroscopic structure (model) of both the engineering or mechanical action or behavior and the age of self-treatment CMC structures was offered by Genetetal and accredited on the stuff level. The mechanical model considers the fracture or crack networks, as well as its relation with fiber-matrix interrupting through fracture and inelastic stresses or strains. All the simulations have been accomplished through the conventional software package in mechanical engineering such as ABAQUS/Standard FEA [6, 7].

Composites are superior to all other known structural materials in distinct hardness fatigue strength, resistance, high-temperature durability, and other properties. The expected combination of properties can be fitted in advance

and realized in making a specific material. Many modern technologies need materials, such as metals, ceramics, metal alloys, and polymeric materials with unique combinations of properties that cannot be carried out. The required composite materials for underwater, aerospace, and transportation applications have unique properties. Most of the composites typically have one construction in common, a binder or matrix mixed with a fortified material. A composite is a material developed from two or more distinct phases, matrix and dispersed. If the fibers are directionally oriented and continuous, the material is called an advanced composite. The composite material properties depend on the stiffness of bonds and the physical-mechanical features of their components. A specific advantage of composites is the capability of their components to be utilized fully. Such materials may take specified valuable properties that are not found in the components. To obtain the optimal characteristic in composites, their components are selected to have strongly various but perfect properties. The basis or matrix of composites may consist of metals or alloys (metallic composites), carbon, polymers, and ceramics (non-metallic composites) [8]. Technologically, the most substantial composites are generally those in which the dispersed phase is in the form of a fiber. Indeed, the powerful fibers embedded in a softer matrix produce products with great strength-to-weight proportions. The matrix materials transmit the load to the fibers that absorb the stress.

Also, the linear behavior of ordinary composites and its frame and structure can be described analytically by Classical Laminate Theory (CLT). By investigating elastic mechanical characteristics (Young's moduli parameter, shear modulus of rigidity, and Poisson's ratios), as well as influence of moisture and thermal impact, CLT can effectively compute the stress-strain relations in composite become laminated up to fracture initiation. Through thickness, both the vertical and shear forces are ignored in CLT, thus supposing composite plates to be extremely wide and long that causes neglecting edge effects. Finite element modeling (FEM) dominates these issues and can perform the stress investigation of structures more carefully. Computational or numerical simulation results are being generally used in the design, production, and investigation of several composites and structures. The important parameter in increment of industrial competitiveness is saving or reducing the design age. The capability to finish designs by a proper software on the computer effectively reduces the reliance on long-time methods and costly physical experiments. Composites can be nearly optimized for suitable and special uses. Most commercial FE software possess user-friendly composite mathematical modeling capabilities, which can accurately obtain elastic action through anisotropic or orthotropic constructional modeling. Unlike CLT, FE models allow accurate and regular stress analyses through the accomplishment of an appropriate computerized sample model, leading to the anticipation of stress concentrations [9].

The arrangement or orientation of the fibers, the fiber density, and their distribution all have a significant influence on the resistance and other performances of fiber-modified composites. With regards to direction, two extremes are possible: (1) a parallel arrangement of the fiber longitudinal axis in a single direction; and (2) an accidental adjustment. Mechanical reactions of this unique composite depend on multiple parameters, such as strain-stress behaviors of the matrix phases, fiber, the phase volume fractions, and the direction a load or the stress is enforced to it [10]. In recent years, ceramic material has become increasingly substantial, especially for unique uses that need great strength. Ceramics show superior behavior at high temperatures in general. The difficulty of using ceramics is their fragile harm behavior. A single deficiency or defect can cause fragile damage in the whole structure [11].

Fiber-reinforced or -modified composites have great mechanical performance, such as high unique strength and hardness. Particularly, laminated composite structures have widely been used, where the in-plane properties are substantial [12].

In past decades, the finite element method as an efficient tool has become a broadly accepted computational technique not only in computational mechanics but also in certain engineering majors. The approach has been extended to solve easy linear equations in mechanics of solid bodies along with severe non-linear problems in almost all fields of applied physics or mathematics; and more recently, in many other branches of general science.

Some packages that can be used are FLUENT, ABAQUS, ADINA, ANSYS, NASTRAN, and LUSAS. Finite element method gives a proximate distribution of the needed size in the considered field that is not possible to be specified analytically. A proximate solution is derived by dividing the total area (bodies) to the minor elements. Then, the related physical rules are applied to each element and total elements of the set of solutions to solve the existing problems [13]. One of the novel numerical simulation methods is finite element analysis (FEA) that can evaluate the fracture probability caused by the characteristics and performance of flaw distribution. It is considered an effective tool to facilitate and increase the use of ceramics in components and members; the FEA can also forecast the distribution of ceramic rigidity. Specifically, the needed data on the microstructure distribution (i.e., relative density, porosity, and grain size) are used as the input parameters [14]. Also, the finite element method is done to model the piezo-laminated plate panel as an appropriate composite structure and show the static and dynamic analysis of structural vibrations subjected to an external force. The piezo-laminated structure modeling is based on the assumptions of first-order shear deformation theory (FSDT) [15]. In general, the purpose of the numerical model is to investigate the effect of substantial parameters on the behavior of the fiber composite. This grid frame or substructure (elementary cell) takes fiber, the fiber-matrix interface, the single components matrix, and their particular harm behavior into an account. It is selected in such a way that a macrostructure property for the complete structure can be made by a proper number of substructures. The model has been performed in a finite element method code to research the effect of separate component factors on the behavior of the total.

In a finite element method modeling, several analyses can be done; for instance, dynamic and static analysis, which later could be modeled and involved forced vibrations. In general, a static linear elastic analysis is the easiest and default one but with limited use due to its closed scope [16]. Modeling of the accidental fiber distribution of a fiber-resistant composite via simulation software is of high importance to investigate the approaching failure behavior of the material on the limitation of micro-scale. Fiber-reinforced composites are typically recognized as ordinal materials with three structural levels: macro-scale, mesoscale, and micro-scale. The micro-scale defines the adjustment of composite fibers in the fiber bundle. The mesoscale typically relates to the fabric/lamina shape or geometry, and the macro-scale composite refers to engineering the structural action of the stuff. In a multi-scale modeling and simulation of composite stuff, micro-scale concepts (including both numerical-analysis and mathematical methods) are usually applied to anticipate the effective rigidity and strength performance of axial symmetry of a composite material or transversely isotropic fundamental properties of composites, which are used as theoretical tools for technical structure design [17, 18]. Recently, a finite element analysis (FEA) modeling has been performed for the long fiber- modified ceramic matrix woven composites (LFMCWCs) sample. For instance, this method has been validated to investigate the grinding process of a 2.5D woven quartz such as fiber-reinforced silicon dioxide ceramic matrix (SiO_2/SiO_2) composite. Concerning the grinding tests, their results were directly confirmed for the precision of the FEA method [19].

The strength of these studies is their uniqueness, using various materials and composites, as well as FEM use as a useful tool to analyze and predict the mechanical performance of composites, which is a cost-effective and time-saving approach. However, the past research weaknesses are testing only a few limited materials and some simulations without comparing with experimental data, in particular, microstructure SEM images that are very vital for investigating mechanical performance.

In the present research, only one composite has been modeled with a total detailed account of its physical morphology along with its thermo-physical performances. The composite morphology at micro-scale has been made as close to reality as possible with measurements from SEM micrographs for the geometric details, such as the fiber radius and length. A commercial FE code of ABAQUS has been applied to create the computational model. The real microstructure with fiber distribution has been specified via an SEM image, for example. The science of image analysis has then been done on the main image to determine the fibers based on various color threshold modules, histograms and algorithms. From this image, the data such as the distribution of distances between neighboring fibers and the fiber radius extracted based on image pixels in a black and white image via MATLAB image processing toolbox. The obtained statistical parameters were utilized and employed mesh grids to generate a finite element analysis that was used to anticipate the effective mechanical property and compare it with the experimental data, such as volume fraction, porosity, and elasticity. This study focuses on the mechanical performance of ceramic composites as well as the comparison of experimental data and simulation results.

1.1 Methodology

The present study deals with technical performances of the elastic theory originated from FEA of the total representative volume elements in fiber-modified composites. The fibers are put orderly in the square array that is known as the uni-directional composite. An example of a uni-directional fiber composite is shown in Fig. 1.

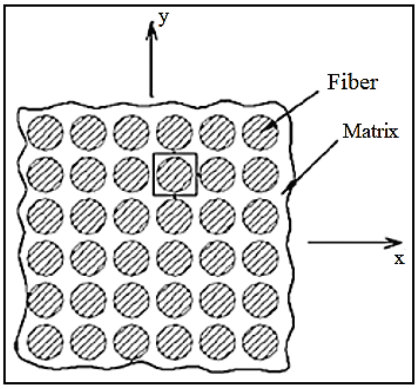

Figure 1 The schematic image of the unit cells.

It is supposed that the fiber and matrix material is usually linearly elastic. Typically, a unit cell is employed for the analysis. The measure of the fiber volume in proportion to the whole volume of the composite is served from the cross-sectional areas of the fiber associated with the total cross-sectional area of each unit cell. This fraction of composite is considered as a substantial parameter in a composite that is named the fiber volume fraction (VF).

2 EXPERIMENTAL METHOD

Some samples were made using the layered claystone, clay, and bauxite in the amounts defined by the Jahad Daneshgahi Corporation according to scientific principles [21, 24]. Samples with the addition of 1% wt. content of low alumina-based fibers (with the aspect ratio of $l/d \approx 17$), were added to the composition in order to evaluate the results of numerical modeling to the empirical data. The material was blended in the ball mill with water to enable better distribution of components, proper fibers in particular. The obtained composition was dried within 24 hours at 100 °C and then pressed between pressures of 35000 kPa to 55000 kPa to create two various porosities. Other samples were thermally operated at about 1200 °C and then were tested via the compaction and the Brazilian tests [20] to get the values of elasticity modulus (E) and strength (F). The test was done via the modern-hydraulic testing system (Instron testing system, Model 1362) with a load cell of 5000 N and 100 kN through a data logger. The calculated values of modulus were served to evaluate the numerically obtained values [21]. The whole samples were experimented using the scanning

electron microscope (SEM), and captured images were employed to determine their porosity [22].

Porosity values were measured based on the various threshold level of darkness of the obtained images via the image processing method. Different SEM images of each sample were used to determine the porosity of various samples. This method is appropriate since the pore, absorbs more light, and it takes place as part of the image darker than of the solid material. Given the porosity of the material and the proper method for determining the number and share of pores, given in Fig. 2, the microstructure images were captured using an SEM system, (the Zeiss DSM-960A model, operated at the range of 21 kV).

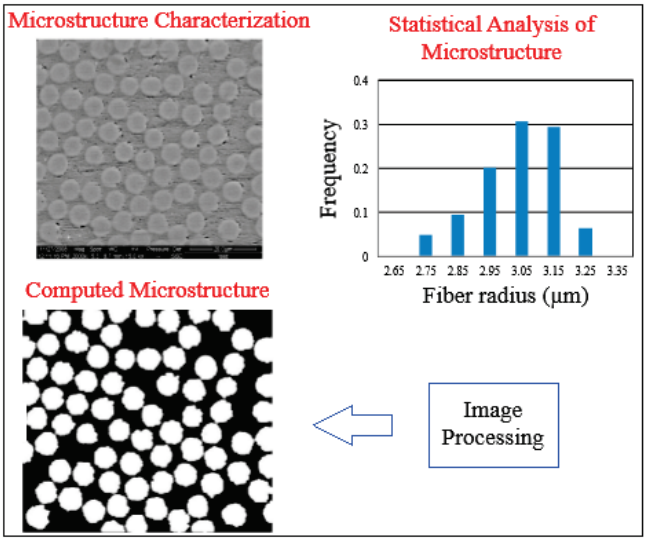

Figure 2 The digital image for micromechanical modeling of an accidental descriptive volume element in a composite. The SEM image is taken from [22].

2.1 The Explanation of the Finite Element Analysis

The unit cell approach supposes that the porous ceramic has been made of an array of fundamental elements or units, each with the same composition, cell shape or geometry, and material characteristics. A plate cubic cell is investigated as a descriptive volume element to model and simulate the real microstructures of porous ceramics. This simulation supposes that: a) the ceramic matrix is investigated as being isotropic; b) the elastic performance of the ceramic composite is linear [6, 25].

Total 3D finite element (FE) simulations were generated using ABAQUS 2018, FE software package. Total material data was used for FE simulation and the matrix:

For fibers: the first Young's modulus E_1 = 145000 MPa and Poisson's ratio of ν_1 = 0.25; the second Young's modulus E_2 = 10000 MPa with Poisson's ratio of ν_2 = 0.20.

3 RESULTS AND DISCUSSION

The mesh geometry was generated by computational cell elements derived from image processing of the material SEM, and certain calculations were done based on the combination of the material. Moreover, the volume fraction of the fibers was chosen while making the material and fixed on 1% volume. The fiber dimensions were obtained by evaluating short fibers via the image processing program. According to Fig. 1, the average fiber length was 0.1344 mm, and the average fiber radius was 0.003 mm. Thus, the formula for calculating the volume of the single cylindrical fiber was computed as follows:

$$V_f = \pi r^2 l = \pi(0.003)^2 \times 0.1344 = 3.8\times10^{-6}\ \text{mm}^3 \quad (1)$$

The material volume was computed from total fiber constituents using the simple equation based on the cell volume of 0.0000038 mm^3 and edge length of 0.068 mm. Since the fiber length is 0.1345 mm and also the unit cell can be big enough, the fiber can fit in each cell. The presumption that eight fibers belong to one elementary cell provides a cube with the dimensions of 0.14 mm × 0.14 mm, and the depth of 0.14 mm; also, the fiber radius is r = 0.003425 mm, and the length is l = 0.137388 mm. They are the same for entire fiber volume fractions. The calculated volume fractions of elementary cells for various fibers have an error range of 0.04-0.1 in proportion to various fiber volumes in ceramic.

All fibers were randomly put into a matrix, which included 4 and 8 fibers. The schematic representation of fiber has been shown in Fig. 3.

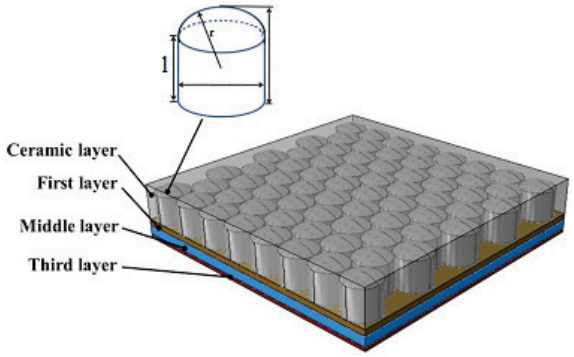

Figure 3 The schematic diagram of the designed ceramic composite system.

To investigate the effect of porosity on mechanical characteristics, the elementary cell was produced with fibers without pores and cells that were put into the pores.

The schematic representation of the mesh grid according to the unit cell has been shown in Fig. 4.

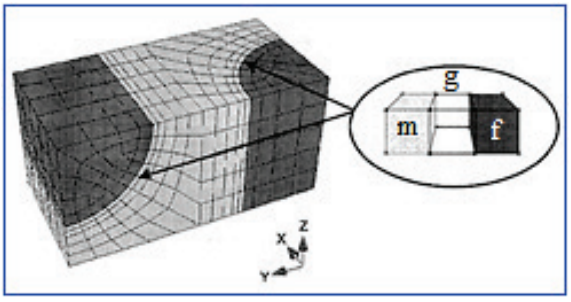

Figure 4 Schematic representation of the finite element unit cell

Fig. 5 shows the unit cell: a) the fibers with pores (porous fibers); and b) the fibers without pores. It can be realized that the existing contact between matrix and fibers is the surface to surface contact type with a friction factor of 0.1. In the software, it is determined that the surface to surface contact is as of the finite sliding and the friction formulation as of the penalty.

3.1 Calculation of Mechanical Properties by Analytical Solution

The mechanical performance of the lamina is computed using the following equations of Elasticity Theory, as well as Halphin-Tsai's formulae; Linear Young's Modulus equation in the fiber for each direction is as follows:

$$E = \frac{\sigma}{\varepsilon} \tag{2}$$

σ is the stress, and ε is the strain in each direction (x, y or z).

$$\nu_{12} = -\frac{\varepsilon_2}{\varepsilon_1} \tag{3}$$

ε_1, ε_2 are the strains in various directions (x, y, z).

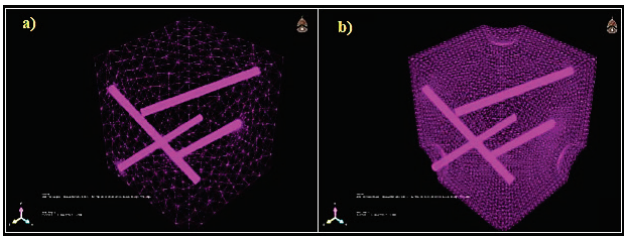

Figure 5 Elementary cells: a) with fibers and pores; and b) with fibers without pores.

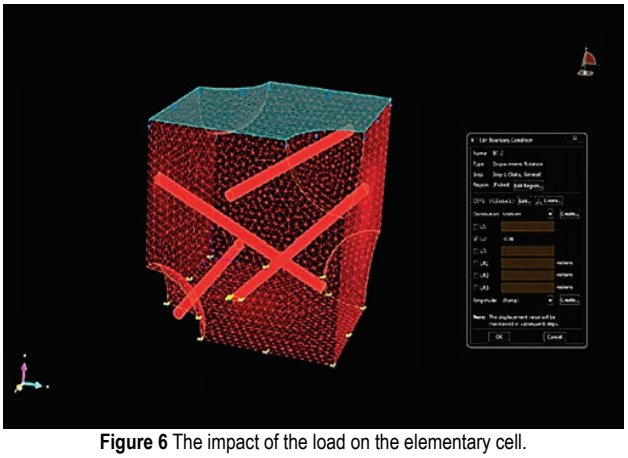

Figure 6 The impact of the load on the elementary cell.

Experimental data for pure Al_2O_3 used to simulate the alumina ceramic are summarized in Tab. 1. It should be noted that the physical properties of the material (Density ρ, Specific heat C_p, Thermal conductivity λ, Young's modulus E, Poisson's ratio ν, and thermal expansion factor α) have been reported in Tab. 1 according to the density (without pores) from the Tab. 1.

Table 1 Physical properties of alumina (Al_2O_3).

ρ (g/cm^3)	Cp (J/g·K)	Λ (W/m·K)	E (GPa)	ν	A (1/K*106)
3.989	0.78	29	390	0.22	9.1

Fig. 6 shows the matrix with 8 fibers. This model of elementary mesh grid cell is originated from the matrix in which it does not have any pores.

3.2 Comparison of Experimental and Calculated Parameters of Elastic Modulus

To evaluate the achieved numerical simulation results, the derived data were tested and analyzed via a mechanical experiment. The obtained values of elastic modulus for various combinations are divided into two main parts: one with only pores, and one with fibers and pores simultaneously, which are shown in Fig. 7. The experimental data were also added to the data diagram and fitted with the model extended in this study. When the material consists of pores and fibers, the quantity of Young's modulus reduces with the increment of porosity. The value of Young's modulus in the improved material with fiber has greater amount as compared to the material without fiber including the same porosity. Poisson's ratio, generally, decreased with an increasing fiber volume fraction according to Eq. (4).

$$\nu = \nu_f V_f + \nu_m V_m \tag{4}$$

In this equation, ν_f is Poisson's ratio of fiber, and ν_m is Poisson's ratio of a matrix.

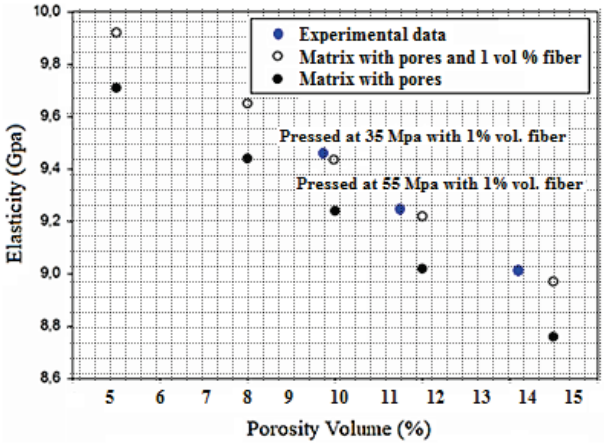

Figure 7 Young's modulus of elasticity versus the porosity volume.

Fig. 8 shows the linear regression model of the elastic modulus obtained by the experimental data.

This linear correlation was calculated by MATLAB software of version R2014b as follows:

$$E = -0.08871\varepsilon + 10.27 \tag{5}$$

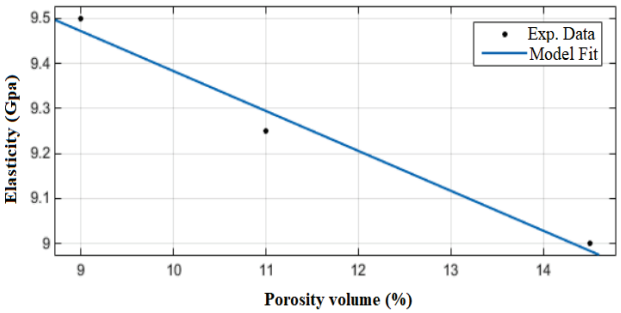

Figure 8 Linear curve fitting model of elasticity versus porosity value (%).

In this equation, E is elastic modulus (GPa), and ε is porosity volume (%). Eq. (5) signifies that with increasing porosity volume, the modulus of elasticity decreases. The experimental data shows good consistency with the linear model. Also, the statistical parameters verify the accuracy of the experimental results. The quality of fitness is presented in Tab. 2.

Table 2 Statistical data calculated by MATLAB software.

Statistic parameter	Calculated value
SSE	0.003024
R-Square	0.975800
Adjusted R-Square	0.951600
RMSE	0.054990

Compared to the experimental values derived from mechanical experiment, it presents good consistency of experimental and calculated values in the model.

Schematic flowchart for preparing samples of each experiment is shown in Fig. 9.

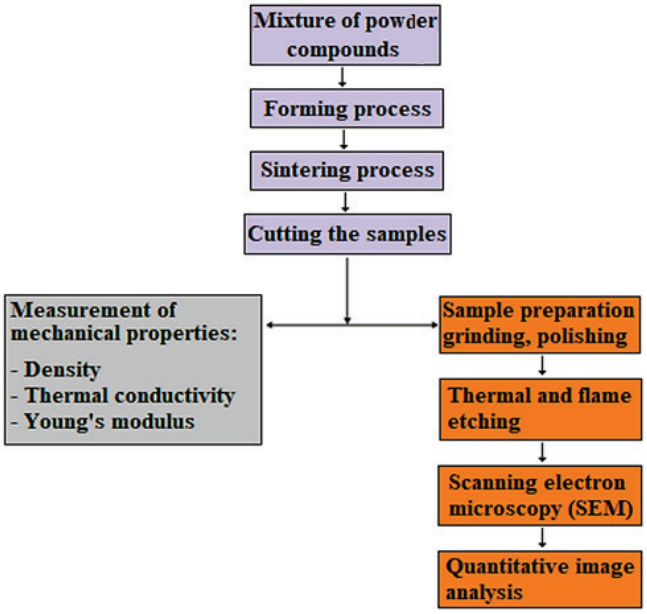

Figure 9 Schematic flowchart describing the experimental procedure of samples.

In the present research, the finite element analysis has been done to anticipate the engineering and mechanical properties of the fibers in the field of a fiber-modified ceramic composite. The simulation results were validated with the results obtained from the experimental data. In addition, it was found that the mechanical properties of a ceramic composite such as E, ε, σ, and v are strong functions of volume fraction in the fibers. The results showed that any change in the dimension or volume and porosity of the fibers could influence the mechanical properties of a composite.

4 CONCLUSION

The finite element method, as a useful model, is a powerful tool to investigate the different properties of composite materials. The effect of resistance, stiffness, and reinforcement distribution in mechanical properties of composite material is considered by checking the finite element analysis and micromechanics approach.

In this study, the geometry of the mesh was obtained through calculating elements of unit cells, which had been obtained from image processing; it is used for the analysis of the material SEM images, as well as certain calculations based on the material performance. The information obtained from the mechanical analysis test was employed to evaluate the achieved simulation results. The experimental data was also added to the data diagram, and the information fitted the FEM simulation model was extended in this research. The results showed that when the material consists of pores and fibers, the index of Young's modulus reduces with the increment of the porosity. The value of Young's modulus of either enhanced or fortified material, including fibers has greater values compared to the material without fiber with the same porosity. The linear model of the elastic modulus, which was obtained by the experimental data and was compared to empirical values originated from a mechanical test, signifies good consistency with those computed values of the mathematical simulation model.

The numeral model was extended based on the investigation of mechanical behavior, parallel to measured porosity properties, and a linear mathematical model was derived for elasticity modulus with appropriate accuracy by experimental data. The number of entire fibers was prepared in each experiment in the cube related to the combination of the material. The used materials were examined mechanically and by means of simulation results in order to get the key values of elastic modulus, physical and engineering properties, as well as the structure, which was tested by the image processing analysis of the SEM images. The number and size of the pores and porosity were the basis for calculating the proper elementary cube for computer simulation. Finally, the experimental and simulation data were in good agreement.

Acknowledgments

This research has been guided and supported by a professional mechanical engineer, Seyed Hassan Alhoseini.

5 REFERENCES

[1] James Paul, K. & Sd. Abdul Kalam. (2016). Mechanical Properties of Okra Fiber Reinforced Composites Using Fem,

International *Journal of Advanced Research in Mechanical Engineering & Technology (IJARMET), 2*(2).
[2] Shchurova, E. I. (2016). Modeling of the Ceramics Structure for the Finite Element Analysis. Procedia Engineering, 150, 179-184. https://doi.org/10.1016/j.proeng.2016.06.744
[3] Sadik, C., El Amrani, I. E., & Albizane, A. (2014). Recent advances in silica-alumina refractory: A review. *Journal of Asian Ceramic Societies, 2*(2), 83-96. https://doi.org/10.1016/j.jascer.2014.07.006
[4] Choi, A. H., Heness, G., & Ben-Nissan, B. (2014). Using finite element analysis (FEA) to understand the mechanical properties of ceramic matrix composites. In Advances in Ceramic Matrix Composites, 286-311. https://doi.org/10.1533/9780857098825.2.286
[5] Choi, A. H., Heness, G., & Ben-Nissan, B. (2018). Using finite element analysis (FEA) to understand the mechanical properties of ceramic matrix composites. In *Advances in Ceramic Matrix Composites* (pp. 375-400). https://doi.org/10.1016/B978-0-08-102166-8.00016-5
[6] Boccaccini, A. R. & Fan, Z. (1997). A new approach for the Young's modulus-porosity correlation of ceramic materials. *Ceramics International, 23*(3), 239-245. https://doi.org/10.1016/S0272-8842(96)00033-8
[7] Farooqi, J. K. & Sheikh, M. A. (2006). Finite element modelling of thermal transport in ceramic matrix composites, Computational Materials Science 37, 361-373. https://doi.org/10.1016/j.commatsci.2005.11.001
[8] Callister, W. D. & Rethwisch, D. G. (2011). *Materials science and engineering* (Vol. 5, pp. 344-348). NY: John Wiley & Sons.
[9] Reiner, J. & Vaziri, R. (2018). *Structural Analysis of Composites with Finite Element Codes: An Overview of Commonly Used Computational Methods*, Comprehensive Composite Materials II, Vol. 8. https://doi.org/10.1016/B978-0-12-803581-8.10050-5
[10] Ismar, H., Schröter, F., & Streicher, F. (2000). Modeling and numerical simulation of the mechanical behavior of woven SiC/SiC regarding a three-dimensional unit cell. *Computational Materials Science, 19*(1-4), 320-328. https://doi.org/10.1016/S0927-0256(00)00170-1
[11] Kakani, S. L. & Kakani, A. (2010). *Material Science*, New Age International Pvt Ltd Publishers.
[12] Tao Zeng, Lin-zhi Wu, & Li-cheng Guo. (2004). Mechanical analysis of 3D braided composites: a finite element model. *Composite Structures*, 64, 399-404. https://doi.org/10.1016/j.compstruct.2003.09.041
[13] Dimitrijević, M. M., Tomić, N., Međo, B., Jančić-Heinemann, R., Rakin, M., & Volkov-Husović, T. (2014). Modeling of the mechanical behavior of fiber-reinforced ceramic composites using (FEM). *Science of Sintering, 46*(3), 385-390. https://doi.org/10.2298/SOS1403385D
[14] Ozaki, S., Aoki, Y., Osada, T., Takeo, K., & Nakao, W. (2018). Finite element analysis of fracture statistics of ceramics: Effects of grain size and pore size distributions. *Journal of the American Ceramic Society, 101*(7), 3191-3204. https://doi.org/10.1111/jace.15468
[15] Sharma, A. (2018). The finite element based study on active attenuation of structural vibration using porous ferroelectric ceramics. In *AIP Conference Proceedings* (Vol. 1975, No. 1, p. 030007). AIP Publishing. https://doi.org/10.1063/1.5042177
[16] Pedro Colmar Gonçalves da Silva Vellasco, Luciano Rodrigues Ornelas de Lima, Luís Alberto Proença Simões da Silva. (2017). *Finite Element Modelling, Modelling Steel and Composite Structures*, Chapter 3, 209-211. https://doi.org/10.1016/B978-0-12-813526-6.00003-9
[17] Wenzhi Wang, Yonghui Dai, Chao Zhang, Xiaosheng Gao & Meiying Zhao. (2016). Micromechanical Modeling of Fiber-Reinforced Composites with Statistically Equivalent Random Fiber Distribution. *Journal of Materials (MDPI)*. https://doi.org/10.3390/ma9080624
[18] Samadi, F. & Missagh Shamshiri, G. S. (2019). Numerical Modeling for Simulation of Contaminant Migration of Leachate in Soil Media. arXiv preprint arXiv:1905.02280.
[19] Yuguo Wang, Haoji Wang, Jinhua Wei, Bin Lin, Jingyu Xu, & Sheng Fang. (2019). Finite element analysis of grinding process of long fiber reinforced ceramic matrix woven composites: Modeling, experimental verification and material removal mechanism. Ceramics International, 45(13), 5920-15927. https://doi.org/10.1016/j.ceramint.2019.05.100
[20] Andreev, G. E. (1991). A review of the Brazilian test for rock tensile strength determination. Part I: calculation formula. *Mining Science and Technology, 13*(3), 445-456. https://doi.org/10.1016/0167-9031(91)91006-4
[21] Dimitrijević, M. M., Veljović, D., Posarac-Marković, M., Jančić-Heinemann, R., Volkov-Husović, T., & Zrilić, M. (2012). Mechanical properties correlation to processing parameters for advanced alumina-based refractories. *Science of Sintering, 44*(1), 25-33. https://doi.org/10.2298/SOS1201025D
[22] See http://thermalceramics.com/products/categories/bulk
[23] Yang, Z. (2010). Effect of Interphase on the Prediction of Mechanical Properties for Unidirectional Composites. *Ph.D. Thesis*, Harbin Institute of Technology, Harbin, China.
[24] Bunshah, R. F. (2001). *Handbook of hard coatings, Deposition Technologies, Properties*. New York: Noyes Publication.
[25] Dimitrijevic, M., Heinemann, R. J., Husovic, T. V., Posarac, M., & Majstorovic, J. (2011). Morphological analysis of surface degradation of advanced alumina based refactories subjected to thermal shock. *Procedia Engineering*, 10, 2153-2157. https://doi.org/10.1016/j.proeng.2011.04.356

Authors' contacts:

Majid AHMADI
Department of Mechanical Engineering,
Science and Research Branch,
Islamic Azad University (SRBIAU),
Daneshgah Blvd, Simon Bulivar Blvd, Hesarak area, Tehran, Iran

Seyed Hadi SEYEDIN
Corresponding author
Department of Chemical Engineering,
Science and Research Branch,
Islamic Azad University (SRBIAU),
Daneshgah Blvd, Simon Bulivar Blvd, Hesarak area, Tehran, Iran
sh.seyedin@iran.ir

Seyed Vahid SEYEDIN
Department of Software Engineering,
Tehran South Branch, Islamic Azad University,
Deh haghi (Ahang) Ave, Abuzar Blvd, Afsariyeh Highway, Tehran, Iran

ISSN 1846-6168 (Print), ISSN 1848-5588 (Online)
https://doi.org/10.31803/tg-20190707102048

Original scientific paper

APPLICATION OF A LOGARITHMIC MODEL ON A STRESS - DEFORMATION INTERDEPENDENCE OF THE RECYCLED TIRES

Anđelko CRNOJA, Željko KOS, Oleg POPOV

Abstract: During the last two decades, technological development has led to an extreme increase in transport and connected industries. This has significantly increased the production of automobile tires, which have their life span after which they go to waste. It is therefore necessary to extricate new products from recycled raw materials. For a product to be created, it is necessary, especially in civil engineering, to examine and determine all the properties of this material (pressure, traction, stress resistance, etc.). The results obtained by the research in this paper are mathematically processed by applying a logarithmic model. The aim of this process is to predict stress deformation in terms of tensile force. The model obtained is significant with accuracy of 87.21% and has a very high accuracy of the deformation estimation in relation to the applied stress. Independent variables were granulometric composition, binder (glue) and specific mass.

Keywords: deformation; logarithmic model; recycled rubber; stress

1 INTRODUCTION

For a long time, it was deliberated how to recycle the vehicle tire to create new products in many areas of human activity and because of the rubber properties, the same applies for civil engineering and construction industry. After the establishment of technological recycling processes, we started investigating the effects on human health. One of the main reasons for the recycling process is the procedure for disposal's harmful impact on the environment, nature and human health as it is complicated and the waste is environmentally hazardous [1]. Certain authors tell us about the performance of certain rubber components on human health and its association with the occurrence of certain diseases [2-6]. The beginnings of recycling were in the United States in the 1960s and in Europe, recycling of tires began in the 1980s [7]. The first products that were produced from recycled vehicle tires were developed by the construction industry, and were mainly rubber floors for sports grounds. Different methods are being developed today and different technological processes are sought – those that can produce products widespread in different sectors of the economy, especially in civil engineering as an engine of the overall economy. It is very important to know the properties of each material so that its behavior can be determined in different situations. When performing the test, the measurement procedures should be carried out according to the applicable norms in order to be comparable and useful. Such results should be dealt with from various aspects to obtain relevant and correct information that is especially important when new products in construction industry are developed and that tells us what material it is and what kind of properties it has. The aim of this study is to show results and to direct further research towards proving that the products from recycled automotive tires have potential and that such waste from the environment can and should become a source of raw materials for wider application. It should be noted that the geographical location of the recycling facility is in the north-western Croatia [8]. Used tires are mostly collected from a wider area. This is important because every production facility has different technology, access, quality, granulometric composition, quantity and type of binders (glues) used, and other parameters that are specific to the individual manufacturer, reflecting the quality of the raw material to produce samples/products. The geographic position of producers and collectors of spent car tires in the world is an important fact because the various climatic impacts, traffic management arrangements, etc., are determining quality of tire and tire composition for a wider area of tire use.

2 MATERIAL AND METHODS

2.1 Basic Features of the Application of a Mathematical Logarithmic Model

The tests were carried out on the axial device for the application of tensile force in terms of the test of resistance to stretching. Test details can be found in Fig. 1.

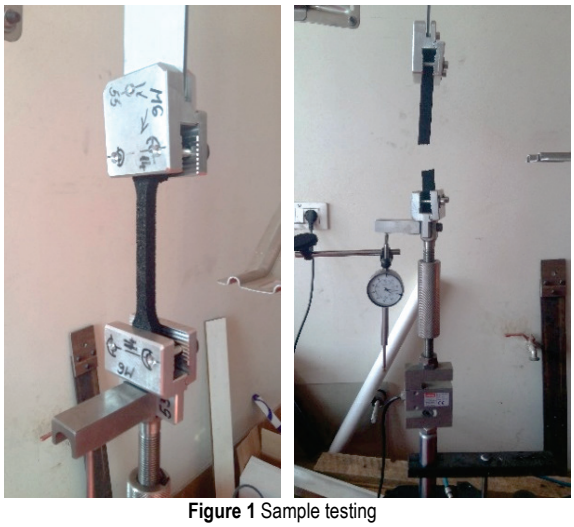

Figure 1 Sample testing

The results were processed using a logarithmic model. Such a model is applied when we have multiple independent variables each of which is subject to logarithm. Then, control of the model is done in terms of its correctness, significance, etc. Such actions are needed to prove its realistic application. The proposed model predicts with certain accuracy the deformation of the real sample in relation to the assumed stress provided that the known values for the specific mass and binder amount are known. The minimum accuracy must be 80% to make the model applicable and acceptable. In such conditions we get a mathematical expression so that the mentioned sizes can be calculated.

2.2 Main Characteristics of the Test Samples

The samples were manufactured according to the valid norm [9] and as such were tested on the axial device. Load appliance is manual, and monitored and read through measuring devices. The following figure shows the test specimen according to HRN EN ISO 527-4: 2008 (for testing of the tensile strength of polymeric materials) [9]. The detailed dimensions of the sample are shown in Fig. 2.

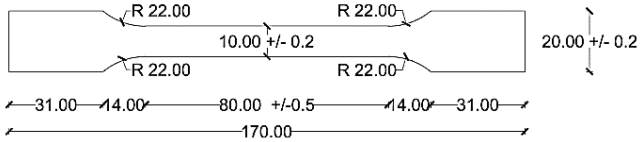

Figure 2 Test sample

Samples were prepared according to the following different characteristics:

1) Specific mass
2) Granulometric composition
3) The amount of binders
4) Geometric Characteristics (Sample Thickness).

The specific mass ranges from min 585 kg/m^3 to max 1100 kg/m^3.

The granulometric composition is divided into 3 groups, namely:

1) A granulate of 0.5-2.0 mm
2) A granule of 2.0-3.5 mm
3) Granulate mix (0.5-2.0-35% + 2.0-3.5-65%).

Plan of experiment is listed in Tab. 1.

Table 1 Plan of the experiment

Sample thickness	Granulometric composition	Number of experiments
10 mm	0.5 – 2	3
10 mm	2 – 3.5	3
10 mm	0.5-2(35%) + 2-3.5(65%)	3
15 mm	0.5 – 2	3
15 mm	2 – 3.5	3
15 mm	0.5-2(35%) + 2-3.5(65%)	3
20 mm	0.5 – 2	3
20 mm	2 – 3.5	3
20 mm	0.5-2(35%) + 2-3.5(65%)	3
Total		27

The amount of binder (polyurethane adhesive) ranges from 29.6 to 67 kg/m^3 of the sample. A single manufacturer may use a different type of binder within the material structure. The tested samples are based on polyurethane-based glue, while other binders such as epoxy can be used, etc., which is especially important in civil engineering, because of the economical acceptance, e.g. production of construction panels for improvement of soundproofing properties on light metal structures and construction panels for making roadside sound barriers.

2.3 Results of Samples Testing

Twenty-seven samples were tested with different properties. The changing variables are the granulometric composition, the specific weight, and the amount of the binder. In Fig. 3 we can see a graphic representation of the stress ratio and the associated deformation of a particular sample. In the same figure it can be noticed that there are significant differences in values and that the influence of individual variables in the sample on the results of the test is visible.

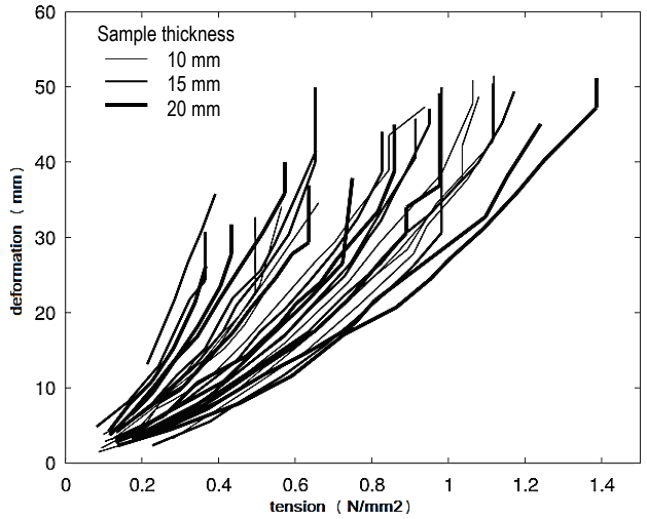

Figure 3 Test results - stress and deformation relationship

3 APPLICATION OF THE MATHEMATICAL MODEL

Based on the results presented, we created a database and used the Statistical Package (SPSS) program with the application of a multiple logarithmic model.

In the model shown in Tab. 2, we see that all variables are logarithmized. It should be emphasized that the respective variables are independent of each other, which is one of the conditions for applying the chosen model. The variables that are considered are the following:

1) log(δ) - logarithm variable "stress"
2) log(ρ) - logarithm variable "specific mass"
3) log(pu) - logarithm variable "polyurethane glue – binder".

The model interprets the accuracy of 87.21% (R^2 = 0.87212527) in relation to the given results. This means that

with an accuracy of 87.21% we can predict the deformation results in relation to the predicted stress if we apply this model. It should be noted that other independent variables, such as specific mass and amount of binder, must remain invariable, otherwise the model is not valid and cannot be applied.

Table 2 The logarithm results of the test result database

Regression Summary for Dependent Variable: log deformation (Database) R = .93387647, R^2 = .87212527 Adjusted R^2 = .87059077 $F(3.250)$ = 568.35 p						
	b*	Std. Err. - of b*	b	Std. Err. - of b	$t(250)$	p-value
Intercept			1.49231	0.015047	99.1744	0
log(δ)	1.015547	0.024731	1.29961	0.031649	41.0636	0
log(ρ) (t/m^3)	−0.304961	0.02444	−1.28938	0.103332	−12.478	0
log(pu) g/m^2	−0.083137	0.02291	−0.13434	0.03702	−3.6289	0.000345

3.1 Testing Models of Expectation or Significance

Testing the significance of the model is carried out to determine the level of significance of the test. The test provides the information with which reliability is performed. If the data is such that the probability value of $p < 0.05$ we say that the results are acceptable.

Table 3 The test results of the logarithm results-significance base

Analysis of Variance; DV: log deformation (Database)					
	Sums of - Squares	df	Mean - Squares	F	p-value
Regress.	26.65913	3	8.886378	568.3461	0
Residual	3.90888	250	0.015636		
Total	30.56801				

According to Tab. 3, the value of factor p is less than 0.05, and we conclude that the model is correct and reliable.

3.2 Model Multicollinearity Test

Multicollinearity testing is performed to determine the correlation of independent variables, or to show us what is the interdependence of the same.

Table 4 The results of the logarithm test results base-multicollinearity

Variables currently in the Equation; DV: log deformation (Crnoja database 25.05.2019.)	
	Tolerance
log(δ)	0.836293
log(ρ) (t/m^3)	0.856332
log(pu) g/m^2	0.97453

For multicollinearity analysis it is important that all factors are greater than 0.20. If we look at the model in Tab. 4, we see that the condition is fulfilled, and the conclusion is that there is no multicollinearity problem.

3.3 Testing the Model for the Presence of Heteroscedasticity

The presence of heteroscedasticity does not lead to the estimates obtained by the least squares method being biased, but causes the ratings to have no minimal variation, i.e. are not effective. Hence, if there is heteroscedasticity, no prediction based on the original model's ratings will be effective. The variation of the forecast, apart from the variation of residuals, includes the variation of parameter estimates. Therefore, it must be ensured that the model has no presence of heteroscedasticity [10].

The condition that there is no heteroscedasticity is that the factor $p > 0.05$. In Tab. 5, we see that the condition is fulfilled, and we conclude that the model is correct and reliable.

Table 5 The results of logarithm test results base-heteroscedasticity

Spearman Rank Order Correlations (Spreadsheet 14) MD pairwise deleted Marked correlations are significant at $p < .05000$				
	Valid - N	Spearman - R	$t(N-2)$	p-value
Residuals & log(δ)	254	0.032002	0.508281	0.611701
Residuals & log(ρ)	254	0.024431	0.387948	0.698382
Residuals & log(pu)	254	0.002687	0.042648	0.966016

4 MATHEMATICAL MODEL RESULTS

After making the logarithmic mathematical model and performing the tests to verify the correctness of the applied model, we conclude that it can be applied with a very high accuracy to predict deformation with known stress. The condition is that the independent variables of the specific mass and amount of polyurethane adhesive are known and unchangeable. This is ensured by the technological process of production for a given product. Based on the above-mentioned requirements, the model defined the mathematical expression that we can use to make such calculations. By studying the results of the multiple logarithmic model, we came to the following mathematical expression:

Logarithmic form of equation:

$$\log\varepsilon = 1.49 + 1.2996\log\delta - 1.289\log\rho - 0.134\log pu \qquad (1)$$

Basic form of equation:

$$\varepsilon = 31.07\delta^{1.30}\rho^{-1.29}pu^{0.134} \qquad (2)$$

Where: ε – deformation, δ – stress (MPa), ρ – specific mass (t/m^3), pu – glue g/m^2 (kg).

After defining the mathematical expression to determine the value of the deformation value in relation to the given load, it is necessary to note the significant influence of certain areas in the test zone curve. These are the minimum and maximum values that have a significant impact on the actual model. The actual model represents the test case from which the model base was created. This means that the impact of the accuracy error we have noted initially depends to a great extent on these values. In Tab. 6, we see the above values that have a significant impact on the mathematical model predicting the deformation size.

Table 6 Overview of the influential minimum and maximum from the model base

Standard Residual: log log deformation (Database) Outliers						
Number of observation	Observed - Value	Predicted - Value	Residual	Standard - Pred. v.	Standard - Residual	Std.Err. - Pred.Val
50 . . . |* . . .	0.59	0.30	0.28	-2.83	2.26	0.03
56 . . . | . * . .	1.51	1.09	0.43	-0.42	3.42	0.02
66 . . . * . . .	0.51	0.76	-0.25	-1.41	-2.02	0.02
89 . . . |* . . .	0.69	0.42	0.27	-2.48	2.15	0.02
124 . . * . | . . .	0.37	0.86	-0.49	-1.12	-3.90	0.01
125 . . *. | . . .	0.74	1.15	-0.40	-0.23	-3.22	0.01
126 . . . * | . . .	0.91	1.25	-0.34	0.08	-2.73	0.01
127 . . . * | . . .	1.06	1.38	-0.31	0.47	-2.50	0.01
128 . . . *| . . .	1.20	1.48	-0.28	0.79	-2.25	0.01
129 . . . * . . .	1.28	1.54	-0.26	0.97	-2.07	0.01
Minimum . . * . | . . .	0.37	0.30	-0.49	-2.83	-3.90	0.01
Maximum . . . | . * . .	1.51	1.54	0.43	0.97	3.42	0.03
Mean . . . |* . . .	0.89	1.02	-0.14	-0.62	-1.08	0.02
Median . . . *| . . .	0.83	1.12	-0.27	-0.33	-2.16	0.01

Tab. 6 shows significant deviations of model values compared to actual measured values. As regards minimum and maximum, explanation of the occurrence is relatively easy. We can notice that due to the nature of the test the initial and final measurement are in the zone that is most difficult to measure; the biggest error is in the initial deformation estimation and in the phase of plastic deformation or in the area of material breakdown.

The measurements were performed by a simple manual stress method and the problem of recording the initial deformation and deformation in the zone of plastic deformation and breakdown of the material is extremely difficult and subject to the subjective impression on the spot at the time of measurement.

5 CONCLUSION

The model is significant and shows with very high precision the behavior of the material when it comes to the stresses in real terms and the actual material that can be obtained as a raw material on a certain geographical micro location.

The accuracy of the applied multiple logarithmic model is 87.21%. Therefore, we can conclude that the model is significant and applicable and has a very high accuracy of the deformation estimation in relation to the applied stress.

The research will continue in the direction of examining other properties such as the elasticity module etc. from which information would be obtained that would be useful for certain computer modelling when creating new products in a wide range of human activities including civil engineering and construction industry.

The results obtained by applying a multiple logarithmic model can be applied in defining and solving certain problems that require a response to the question of how deformation is and is allowed if there is a certain stress effect.

6 REFERENCES

[1] European Tyre & Rubber Manufacturers' Association. (2015). End of life tyre report, http://www.etrma.org/uploads/Modules/Documentsmanager/elt-report-v9a---final.pdf

[2] Marsili, L., Coppola, D., Bianchi, N., Maltese, S., Bianchi, M., & Fossi, M. C. (2014). Release of Polycyclic Aromatic Hydrocarbons and Heavy Metals from Rubber Crump in Synthetic Turf Fields: Preliminary Assessment for Athletes. *Journal of Environmental and Analytical Toxicology, 5*(2), 1000265. https://doi.org/10.4172/2161-0525.1000265

[3] Swedish Chemicals Inspecorate (2006). Synthetic turf from a chemical perspective – a status report 3/06 KEMI-Kemkalieinspektionen. Sundbyberg, Order. No. 510 834 July 2006. e-mail: kemi@cm.se

[4] World Health Organization International Agency for Research on Cancer - IARC (2010). Monographs on the Evaluation of Carcinogenic Risks to Humans 1983. VOLUME 92 Some Non-heterocyclic Polycyclic Aromatic Hydrocarbons and Some Related Exposures, Lyon, France, 868.

[5] Simon, R. (2010). Review of the Impacts of Crumb Rubber in Artificial Turf Applications. *UC Berkeley: Laboratory for Manufacturing and Sustainability*. Retrieved from https://escholarship.org/uc/item/9zp430wp

[6] Birkholz, D. A., Belton, K. L., & Guidotti, T. L. (2012). Toxicological Evaluation for the Hazard Assessment of Tire Crumb for Use in Public Playgrounds. *Journal of the Air & Waste Management Association, 53*(7), 903-907. https://doi.org/10.1080/10473289.2003.10466221

[7] Watterson, A. (2017). Artificial Turf: Contested Terrains for Precautionary Public Health with Particular Reference to Europe? *International Journal of Environmental Research and Public Health*. https://doi.org/10.3390/ijerph14091050

[8] http://gumiimpex.hr

[9] HRN EN ISO 527-4:2008

[10] Nešić, N. (2014). Otkrivanje posledice prisustva heteroskedastičnosti. Univerzitet u Novom Sadu, Prirodnomatematički fakultet, Departman za matematiku i informatiku. Master rad, 90. (in Serbian)

Authors' contacts:

Anđelko CRNOJA, PhD student
Odessa State Academy of Civil Engineering and Architecture,
Didrihsona 4, 65029 Odessa, Ukraine
Tel: 00385992755466
E-mail: acrnoja@hotmail.com

Željko KOS, PhD
Corresponding author
University North,
31b, Jurja Krizanica, 42000 Varazdin, Croatia
Tel: 0038598757989
E-mail: zkos@unin.hr

Oleg POPOV, PhD, Assistant Professor
Department of Technology of Building Production,
Odessa State Academy of Civil Engineering and Architecture,
Didrihsona 4, 65029 Odessa, Ukraine
Tel: 00380503339753
E-mail: oleg.a.popov@gmail.com

ISSN 1846-6168 (Print), ISSN 1848-5588 (Online)
https://doi.org/10.31803/tg-20190728144720

Original scientific paper

POWER REGULATION BY COUPLE HALF WAVE LPWM RECTIFIER AT THREE-PHASE LOADS

Erol CAN

Abstract: The paper presents an application of power control by couple half wave LPWM rectifiers processing at the energy distribution line. The switching method with the components of semiconductor for alternating energy control in the energy distribution line is used on alternating energy sources. In three-phase power line and load, power control and regulation are done with the proposed modulation correction index (MCI). Therefore, the simulation model of 3-phase energy distribution is established after the relationships between the energy sources and the circuit elements are determined by the circuit analysis method. The controls of the current and the voltage are done by trying at the different loads in the line at the simulation. According to the modulation correction index (MCI), currents of unbalanced loads are balanced by the proposed method on the power line. Then, the balance currents and powers that MCI provides are calculated. Finally, a power line of 15 km at length that is created by connecting the model of RLC is tested. Obtained results show the effectiveness of the proposed method.

Keywords: balance currents; circuit analysis; modulation correction index; LPWM half rectifiers; simulation of power control

1 INTRODUCTION

As well as the production of energy, the distribution and use of existing energy is of great importance. Therefore, many studies have been conducted on energy production and distribution [1-3]. Direct current (DC) energy in power lines and different loads is controlled by converting it into changing energy with pulse width modulation (PWM) inverters [4-9]. Therefore, the DC power source is derived from either renewable energy sources or alternating current (AC) sources. The DC energy from the AC source is converted back into AC current to control the power line. The quality of the converted energy from the DC current decreases since the current and voltage contain a high amount of harmonic distortion [10-12]. Multi-level inverters are used to eliminate or reduce these unwanted effects. This increases the cost of the system and the complexity of the system while it makes it difficult to find the faults that can be on the device. In addition, for some loads on the line controlled by the multi-level inverter, the quality of the current can be drawn to the desired level while the voltage of the generated energy cannot be obtained at the desired level [13, 14]. Thus, the paper presents a model of power control by inverse half rectifier processing method that uses the modulation correction index at an energy distribution line. On the line, there are two AC-source half-wave PWM rectifiers for each phase control current and voltage. Two GTO and two IGBT switches created are used on these half-wave rectifiers. This provides a mixed switches structure at the PWM rectifiers while it is intended for demonstrating the availability of different accessible switch preferences when performing energy control on the line. In the proposed control method, the effective values of the alternating current and voltage of the load are controlled by PWM on the load with dividing as the pulse width. Therefore, the modulation index values of PWM control the effective values of the current and voltage on the load without disturbing the sinus structures. In this study, the structure of the proposed line model is described with making the circuit analysis of the power line. After the design of the power line model, three-phase line operation is performed in MATLAB Simulink for different load cases in the application phase.

Then, obtained results of the simulation are verified in experimentation. The current and voltages of different loads without changing the sinus structure of current and voltage vary depending on the modulation index on the line. In the simulation conducted for unbalanced loads, the impedance of the third phase is half of the other phase impedances while the two phases are equal to each other. Imbalance current of the line with the low impedance value is balanced by regulating the modulation index value. These modulation index values are named as modulation correction index (*MCI*) for balancing the power and current values in the first time. The imbalances due to different load conditions in the line are solved with different Modulation Correction Index values. These values are given in tables. When the results are analyzed, the value of the voltage controlled on the load has lower distortion than that of the previous line studies with inverters [15, 16]. In addition, these results can be obtained in a less complicated and inexpensive way using the proposed model. In addition, according to the results, the power distribution line is simulated for efficient power distribution and control without losing a lot of time and money. Then, the results are validated in experimentation. By taking this model into consideration, applications can be performed in less time and with less error rate. As the missing and difficult sides of the power line in the simulation can be determined, the accidents and errors that may occur are reduced and the loss of life and property is eliminated at the experimentation. According to the results obtained, it is observed that energy distribution and control are done effectively.

2 DESIGN OF THE PROPOSED MODEL

At three-phase power lines, six alternating energy sources are as V_s, four of semiconductor switches are for every phase, one resistive load is for every phase, and parallel RL loads are connected in series to the resistive load for each phase. Four semiconductor switches used for each phase are 2-IGBT and 2-GTO at the applications. Linear Pulse Width Modulation method (LPWM) is used to control switches because LPWMs determine the operating time of the switches. The comparison of the triangular signals and the direct signal to generate LPWMs is as in Fig. 1b. Fig. 1a shows the power circuit. The power line seen in Fig. 1a consists of three balanced phases. The accounts to be made for a phase are valid for every phase at the line. The switches S3 and S4 provide a negative voltage of half-wave with the second Vs source on the load, while the switches S1 and S2 provide a positive voltage of half-wave with the first V_s source on the load. In this case, the sinus voltage and the sinus current are formed by dividing according to the duty ratio of the LPWM on the load as in Eq. (1). α is phase difference. ωt is electrical angle as radians.

$$V_s = U_m \cdot \sin(\omega t) \tag{1}$$

D is the duty rate at which the PWMs are used to provide alternating sources over the load.

The alternating voltage that occurs on the line by two sources can be expressed as in Eq. (2).

$$V_s = DU_m \cdot \sin(\omega t) \tag{2}$$

The Z5 consists of a series of inductive (L) and resistive (R) loads. The unit of R is expressed in ohm, the unit of L in Henry, and the unit of Z6 in ohm.

Z_6 can be expressed as in Eq. (3).

$$\frac{1}{Z_6} = \frac{1}{j\omega L} + \frac{1}{R} \tag{3}$$

The Z_A is impedance of the first phase in ohm. Z_A can be expressed as in Eq. (4).

$$Z_A = Z_6 + R_1 \tag{4}$$

The I_1 is current of the first phase in ampere. I_1 can be expressed as in Eq. (5).

$$I_1 = \frac{DU_m \cdot \sin(\omega t)}{Z_A} \tag{5}$$

The Z_B is impedance of the second phase in ohm, The Z_C is impedance of the third phase in ohm. In the case of a balanced line, for voltages that have difference as the alpha-degree of phase, the current of the second and third phases of the line is found as in Eq. (6) and in Eq. (7).

$$I_2 = \frac{DU_m \cdot \sin(\omega t + \alpha)}{Z_B} \tag{6}$$

$$I_3 = \frac{DU_m \cdot \sin(\omega t + 2\alpha)}{Z_C} \tag{7}$$

If the B phase impedance is equal to half of the other phases, the operating times of the PWMs can be adjusted by calculating the Modulation Correction Index (MCI) to compensate for the current of the three phases.

D_1 is modulation index for C phase; D_2 is modulation index for B phase (MCI) and is calculated as shown below.

$$\frac{D_1 U_m \cdot \sin(\omega t + 2\alpha)}{Z_C} = \frac{D_2 U_m \cdot \sin(\omega t + \alpha)}{Z_B} \tag{8}$$

$$\left.\begin{aligned} Z_C &= 2Z_B \\ U_m \cdot \sin(\omega t + \alpha) &= U_m \cdot \sin(\omega t + 2\alpha) \end{aligned}\right\} \tag{9}$$

$$\frac{D_1 U_m \cdot \sin(\omega t + 2\alpha)}{Z_C} = \frac{D_2 U_m \cdot \sin(\omega t + \alpha)}{2Z_C} \tag{10}$$

$$2D_1 = D_2 \tag{11}$$

$$\left.\begin{aligned} MCI &= D_1 - D_2 \\ MCI &= D_1 - \frac{D_1}{2} \\ MCI &= \frac{D_1}{2} \end{aligned}\right\} \tag{12}$$

The modulation index of the unbalanced line according to the calculated MCI value should be increased as half the modulation index value of the C phase. The length of the power distribution line shall be determined as series resistance (R_L), inductance (L_L), capacitor (C_C) loads to be connected serially to the circuit in Fig. 1.

The Z_W represents the line length impedance. Z_W is described as in Eq. (13).

$$Z_W = j\omega L_L + R_L + \frac{1}{j\omega C_C} \tag{13}$$

Impedance (Z_L) of the power distribution line can be found as in Eq. (14).

$$Z_L = Z_A + Z_W \tag{14}$$

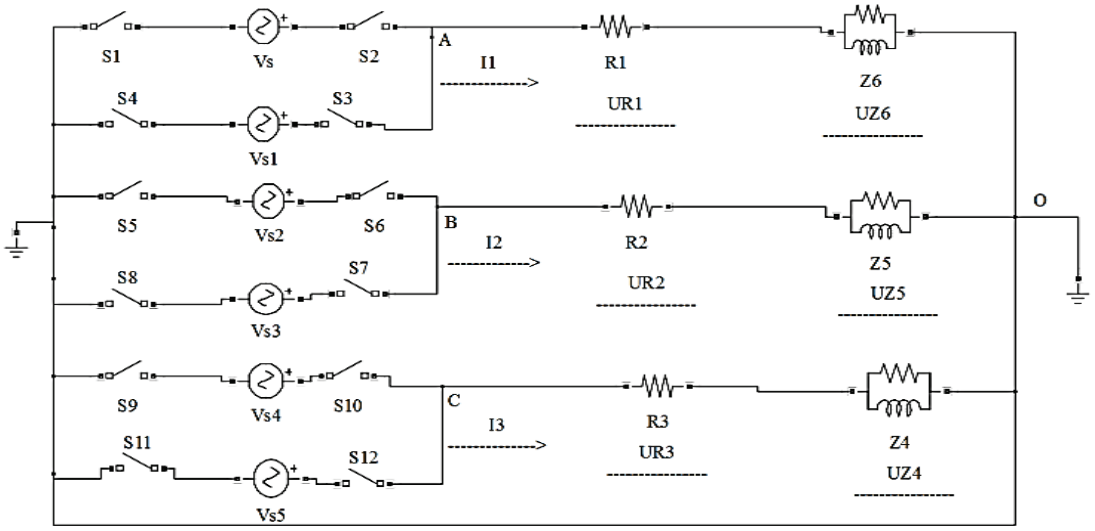

a)

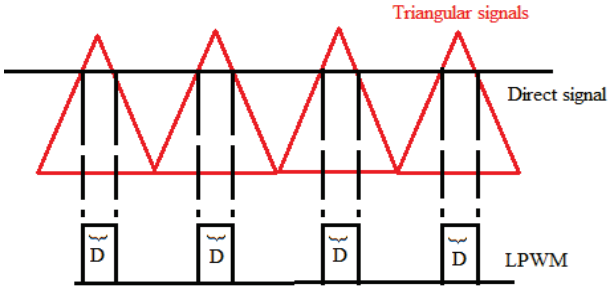

b)

Figure 1 a) the power line of circuit model, b) LPWM

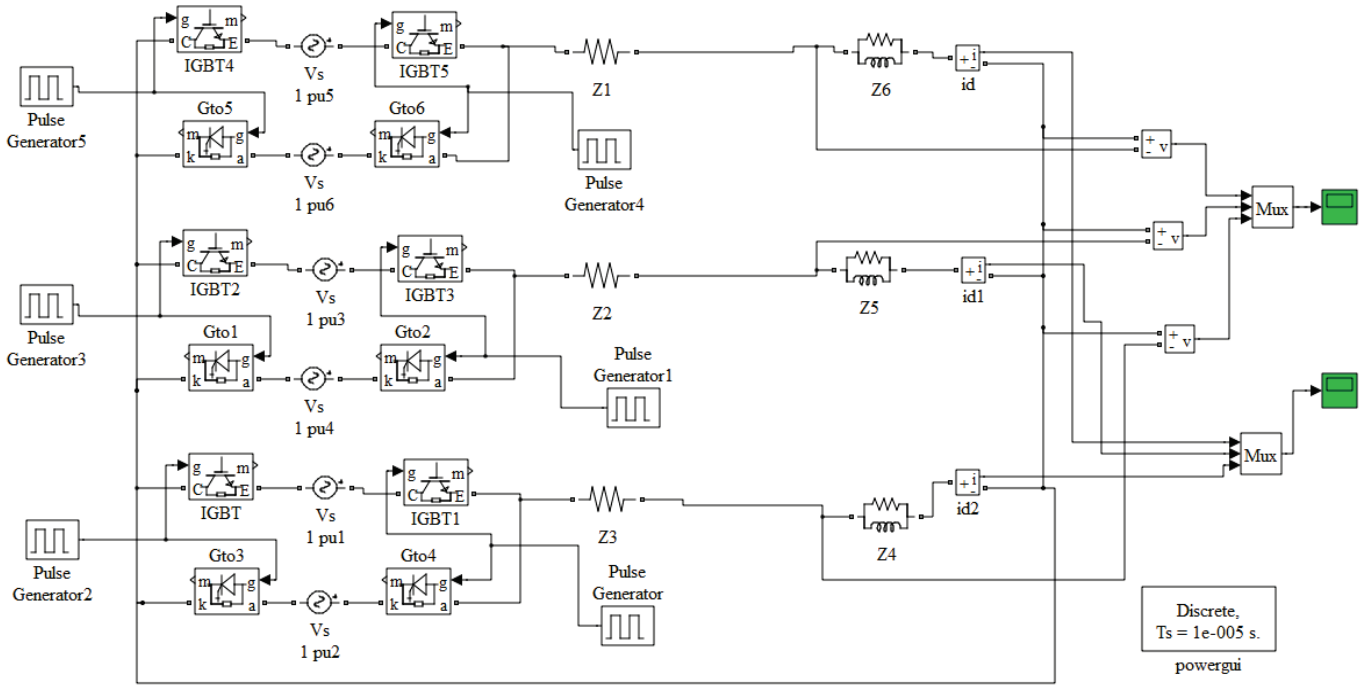

Figure 2 Balanced power line

3 POWER LINE APPLICATION

The impedances of each phase are equal to each other for the application in Fig. 2. Z1 = Z2 = Z3 = 10 ohm, Z6 = Z5 = Z4 = 10 + j0.1, V_s = 220 volt, Modulation index = 0.95, Switching frequency is 100 kHz.

The circuit in Fig. 2 provides a three-phase alternating voltage at 60 Hz of frequency to the power line. The voltage

and distortion value of voltage are given in Fig. 3, while the current is as in Fig. 4.

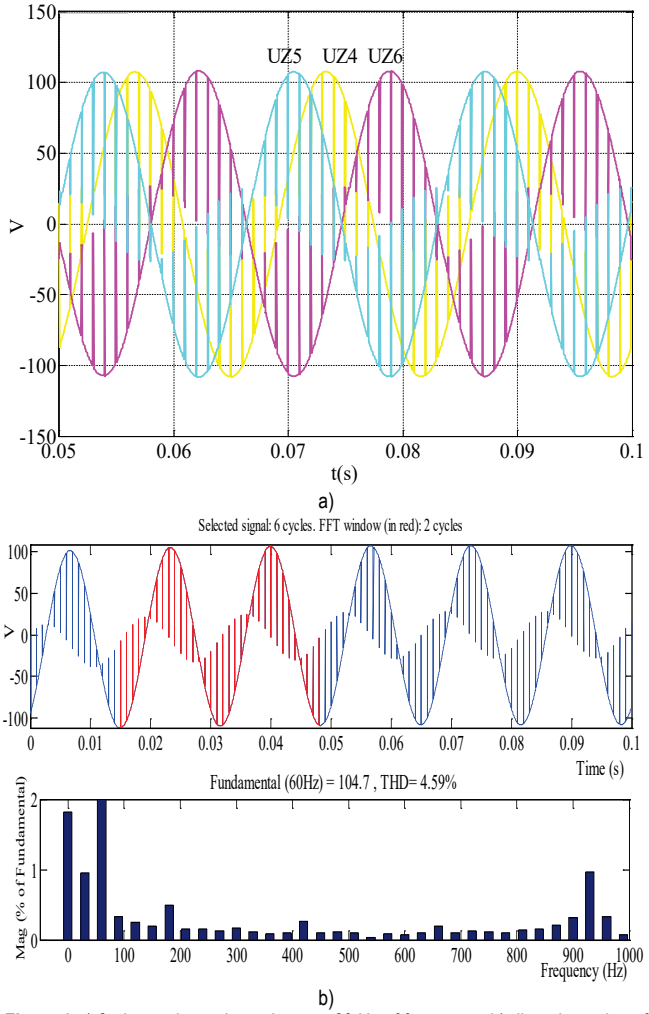

Figure 3 a) 3-phase alternating voltage at 60 Hz of frequency, b) distortion value of voltage

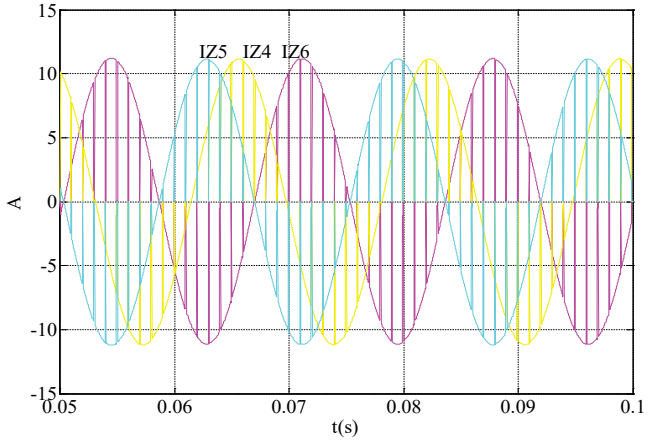

Figure 4 3-phase alternating current at 60 Hz of frequency for balanced load

For the balanced three-phase loads that are Z4, Z5, Z6 in Fig. 3a, a three-phase alternating voltage with 60 degree of the phase difference is provided on load. These voltages are formed on the load according to arranging the modulation index value. In Fig. 3b, the THD value of the voltage on the load is 4.49%. 104.7V is created with 0.95 of modulation index on load. While the THD values of the voltage supplied to the load with PWM inverters can exceed 100%, a level of 4.59% can be achieved for the proposed method. In the simulation, the current obtained is given at the 0.8 of modulation index in Fig. 4.

For the balanced three-phase load that is ZA, ZB, ZC in Fig. 4, a three-phase alternating current with 60° of the phase difference is provided on load. 10.7 A is created with 0.95 of modulation index on load. If loads in Fig. 2 are changed as $Z1 = Z3 = 10$ ohm and $Z2 = 5$ ohm; Z5 and Z4 are $10 + j0.1$, $Z6 = 5 + j0.05$. D is 0.8. Then, three phases are unbalanced. Model is performed according to unbalanced loads; loads currents are shown in Fig. 5.

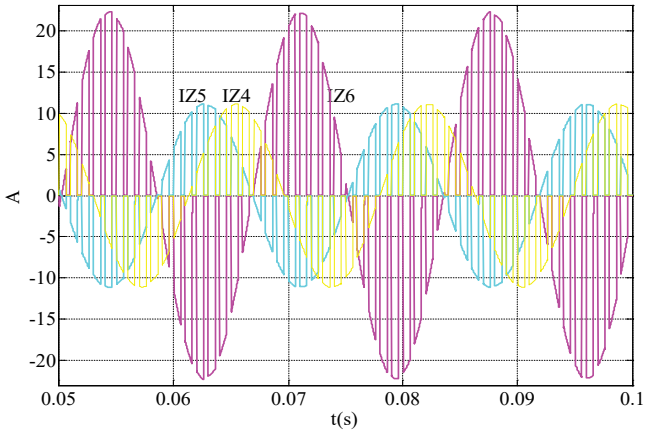

Figure 5 Unbalanced loads of currents

The load at less impedance value generates more current. Currents of IZ5 and IZ4 are 12 A at the maximum while Currents of IZ6 is 24A at the maximum. The difference in impedances of the loads is half. Therefore, the load with a low impedance of the modulation index must be twice the load with high impedance. Fig. 6 shows the balanced loads with the effective value of their current.

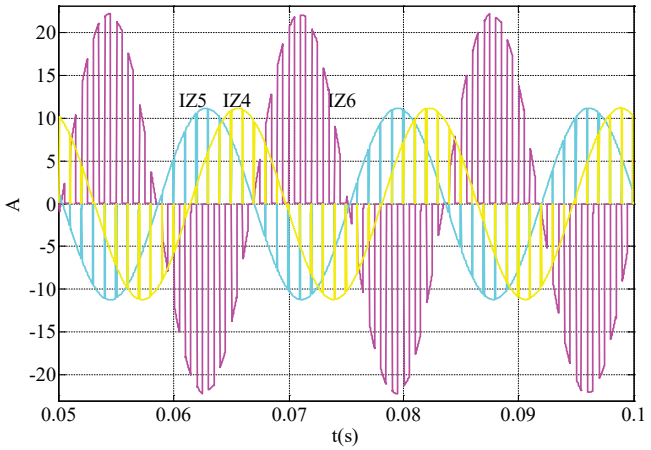

Figure 6 The balanced loads with the effective value of their current

MCI is 0.5 according to Eq. 11. Therefore, when the modulation index for IZ6 is made to 0.45, the modulation

index for IZ4 and IZ5 is 0.9. Then, IZ4 = IZ5 = IZ6 = 10.8A for effective value of the current [7].

When the three-phase line is supplied with 220 volts; balancing currents and MCIs are given in Tab. 1 for different line imbalances. When the three-phase line is supplied with 330 volts; balancing currents and MCIs are given in Tab. 2 for different line imbalances. Z is 10 ohms as impedances.

Table 1 Correction currents and MCIs of 3-phase lines fed with AC sources of 220V

D	ZA	ZB	ZC	MCI	$I_{max}-I_{ef}$ for I_{ZA} and I_{ZC}	$I_{max}-I_{ef}$ for I_{ZB}	I_{ef} for I_{ZA} and I_{ZC} with MCI
0.8	Z	0.9Z	Z	0.89	22A-17.6A	24.4A-19.6A	19.6A
0.8	Z	0.8Z	Z	0.99	22A-17.6A	27.5A-22A	22A
0.7	Z	0.9Z	Z	0.776	22A-15.4A	24.4A-17.08A	17.08A
0.7	Z	0.8Z	Z	0.875	22A-15.4A	27.5A-19.25A	19.25A
0.7	Z	0.7Z	Z	0.99	22A-15.4A	31.42A-22A	22A
0.7	Z	0.6Z	Z	X	22A-15.4A	36.6A-25.66A	X
0.6	Z	0.9Z	Z	0.666	22A-13.2A	24.4A-14.66A	14.66A
0.6	Z	0.8Z	Z	0.756	22A-13.2A	27.5A-16.65A	16.65A
0.6	Z	0.7Z	Z	0.857	22A-13.2A	31.42A-18.85A	18.85A
0.6	Z	0.6Z	Z	0.99	22A-13.2A	36.66A-22A	22A
0.6	Z	0.5Z	Z	X	22A-13.2A	44A-26.4A	X
0.6	Z	0.4Z	Z	X	22A-13.2A	55-33A	X

Table 2 Correction currents and MCIs of 3-phase lines fed with AC sources of 330V

D	ZA	ZB	ZC	MCI	$I_{max}-I_{ef}$ for I_{ZA} and I_{ZC}	$I_{max}-I_{ef}$ for I_{ZB}	I_{ef} for I_{ZA} and I_{ZC} with MCI
0.8	Z	0.9Z	Z	0.89	33A-26.4A	36.6A-19.6A	29.4A
0.8	Z	0.8Z	Z	0.99	33A-26.4A	41.25A-33A	33A
0.7	Z	0.9Z	Z	0.776	33A-23.1A	36.6A-25.62A	25.62A
0.7	Z	0.8Z	Z	0.875	33A-23.1A	41.25A-28.87A	28.87A
0.7	Z	0.7Z	Z	0.99	33A-23.1A	47.3A-33A	33A
0.7	Z	0.6Z	Z	X	33A-23.1A	54.9A-38.49A	X
0.6	Z	0.9Z	Z	0.666	33A-19.8A	36.6A-21.99A	21.99A
0.6	Z	0.8Z	Z	0.756	33A-19.8A	41.62A-24.97A	24.97A
0.6	Z	0.7Z	Z	0.857	33A-19.8A	47.13A-28.27A	28.27A
0.6	Z	0.6Z	Z	0.99	33A-19.8A	54.99A-33A	33A
0.6	Z	0.5Z	Z	X	33A-19.8A	66A-39.6A	X
0.6	Z	0.4Z	Z	X	33A-19.8A	82.5A-44A	X

Table 3 Balancing currents and balancing powers for three-phase system with 220 volt input

Impedance (Ohm)	MI	MCI	Pb(VA)	I_b(A)
0.9Z	0.8	0.89	440	2
0.8Z	0.8	0.99	968	4.4
0.9Z	0.7	0.776	309	1.68
0.8Z	0.7	0.875	847	3.85
0.7Z	0.7	0.99	1452	6.6
0.6Z	0.7	X	X	X
0.9Z	0.6	0.666	321,2	1.46
0.8Z	0.6	0.756	759	3.45
0.7Z	0.6	0.857	1243	5.65
0.6Z	0.6	0.99	1936	8.8
0.5Z	0.6	X	X	X
0.4Z	0.6	X	X	X

In Tab. 1, the imbalances generated in the impedances ranging from 10 ohm to 4 ohm on the line are controlled by the modulation index that is from 0.8 to 0.6. While the effective value of the line current is balanced twice in the 0.8 modulation index, the effective value of the line current can be set at three times for the 0.7 of modulation index value. In the case of 0.6 modulation index, the effective value of the line current can be compensated four times. For the 0.9Z value of ZB at the 0.8 of the modulation index, the MCI value is 0.89. For the 0.8Z value of ZB at the 0.8 of the modulation index, the MCI value is 0.99. At the 0.7 of the modulation index, the MCI value is 0.776 for the 0.9Z value of ZB while the MCI value is 0.875 for the 0.8Z value of ZB. The line can be balanced in nine of twelve trials, while the line cannot be balanced in three cases. Although a current of 25.6 A is required for the compensation of the line, the maximum current that the line can achieve is 22A at 0.99 of modulation index. Current imbalance of the 6 ohm of the impedance controlled by 0.7 modulation index cannot be compensated. Thus, MCI is shown with X. Although a current of 26.4 A is required for the compensation of the line, the maximum current that the line can achieve is 22A at 0.99 of modulation index. Current imbalance of the 5 ohm impedance controlled by 0.6 modulation index cannot be compensated. So, MCI is shown with X for it.

Although a current of 33 A is required for the compensation of the line, the maximum current that the line can achieve is 22 A at 0.99 of modulation index. Current imbalance of the 4 ohm impedance controlled by 0.6 modulation index cannot be compensated. Thus, MCI is shown with X for it. In Tab. 2, the imbalances generated in the impedances ranging from 10 ohm to 4 ohm are controlled on the line from 0.8 modulation index to 0.6 modulation index. The line can be balanced in nine of twelve trials, while the line cannot be balanced in three cases. Tab. 3 shows the balancing current and balancing power generated by arranging of the MCI to compensate for the three-phase power line, which has 220V of the input voltage source. Tab. 4 has the balancing current and balancing power generated by arranging of the MCI to compensate for the three-phase power line, which has 330V of the input voltage source. The balance current (I_b) is the difference between the high phase

current and the low phase current values. This value can be expressed as follows.

$$I_b = I_{ZA} - I_{ZB} \tag{14}$$

$$I_b = I_{ZA} - I_{ZB} \tag{15}$$

The balance power (P_b) can be found as in Eq. (16) while U_i is input voltage for the line.

$$P_b = U_i \cdot I_b \tag{16}$$

For the impedance of 0.9Z at Tab. 2, a compensation power of 440 VA and a balancing current of 2 A are provided with a 0.89 *MCI* value when a compensation power of 968VA and a balancing current of 4.4 A are provided with a 0.99 of *MCI*. The first greatest balancing power and current are 1936 VA and 8A that are provided with 0.99 of *MCI* at the 0.6Z of impedance, while the second greatest balancing power and current are 1452 VA and 6.6 A that are provided with 0.99 of *MCI* at 0.7Z of the impedance. When the impedance value (Z) is 10 ohm, the balancing current and power cannot be provided with 0.6 of modulation index to the system supplied with 220 volts for 0.5Z and 0.4Z impedance values. When the impedance value (Z) is 10 ohm, the balancing current and power cannot be provided with 0.7 of modulation index to the system supplied with 220 V for 0.6Z of the impedance values.

Table 4 Balancing currents and balancing powers for three-phase system with 330 volt input

Impedance (Ohm)	*MI*	*MCI*	P_b(VA)	I_b(A)
0.9Z	0.8	0.89	880	4
0.8Z	0.8	0.99	1936	8.8
0.9Z	0.7	0.776	618	336
0.8Z	0.7	0.875	847	7.7
0.7Z	0.7	0.99	2904	13.2
0.6Z	0.7	X	X	X
0.9Z	0.6	0.666	642	2.92
0.8Z	0.6	0.756	1518	6.9
0.7Z	0.6	0.857	2486	11.3
0.6Z	0.6	0.99	3872	17.6
0.5Z	0.6	X	X	X
0.4Z	0.6	X	X	X

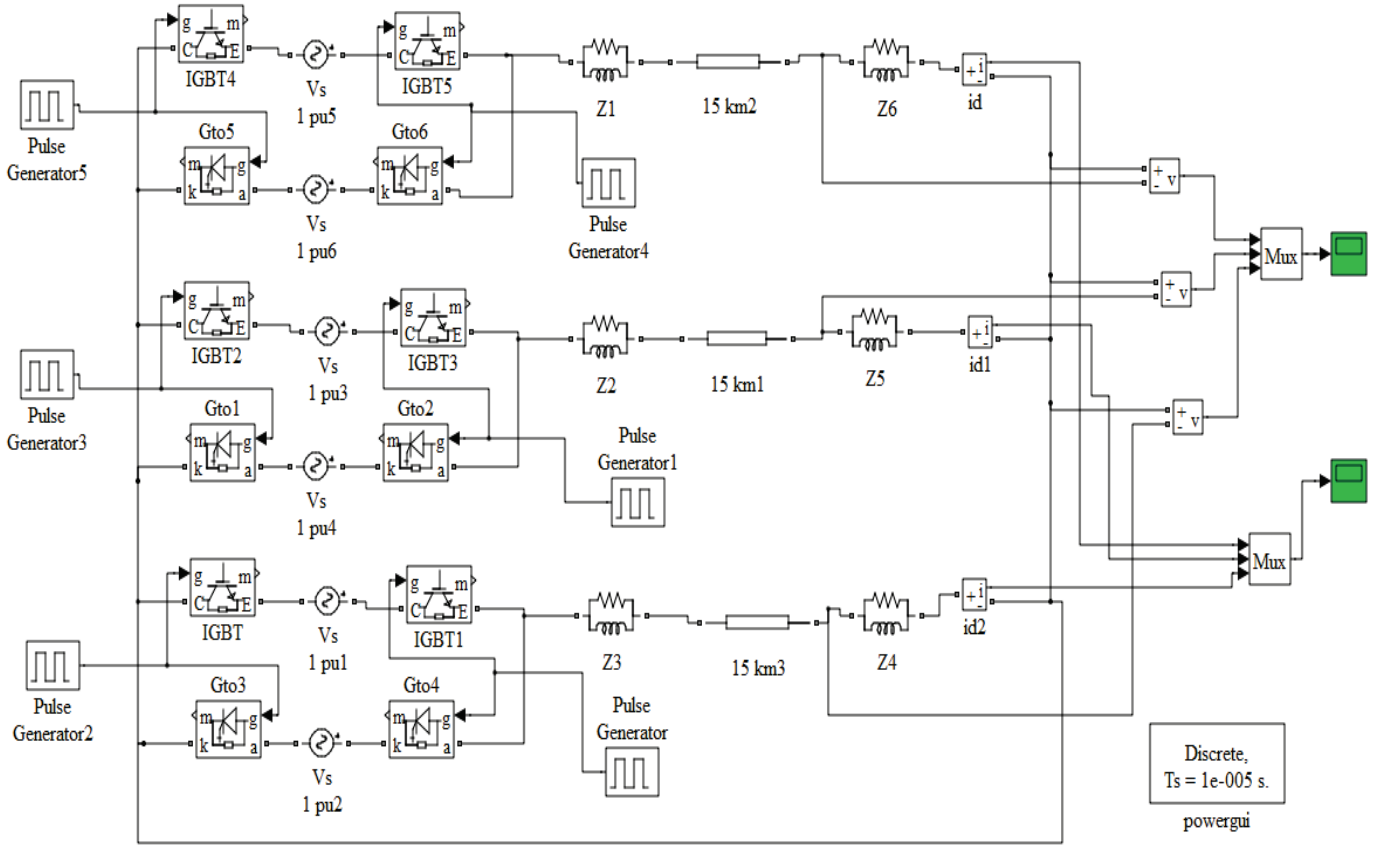

Figure 7 Regulated power line of 15 km

For the impedance of 0.9Z at Tab. 4, a compensation power of 880 VA and a balancing current of 4 A are provided with a 0.89 *MCI* value when a compensation power of 968VA and a balancing current of 8.8 A are provided with a 0.99 of *MCI*. The first greatest balancing power and current are 3872 VA and 8 A that are provided with 0.99 of *MCI* at the 0.6Z of impedance, while the second greatest balancing power and current are 2904 VA and 13.2 A that are provided with 0.99 of *MCI* at 0.7Z of the impedance. As the unbalanced phase impedance decreases, the applied *MCI* and the balancing current increase, which leads to an increase in the balancing power. When the

impedance value (Z) is 10 ohm, the balancing current and power cannot be provided with 0.6 of modulation index to the system supplied with 330 V for 0.5Z and 0.4Z impedance values. In line with the model in Figure 1, a line length of 15 km in Fig. 7 can be obtained if a serial RLC circuit is added to the series. Z1 = Z2 = Z3 = Z4 = Z5 = Z6 = 10 + *j*0.1.

R, *L*, *C* values for the impedance of the line (Z_w) are respectively as 0.143 ohm, 102×10^{-2} H, $C = 1510\times10^{-8}$. Regulated power line of 15 km is in Fig. 7.

Parallel RL loads connected in series at the beginning and end of the 15 km long line in Fig. 7 are energized by alternating power sources that are controlled by switches with 0.9 of modulation index. The three-phase alternating voltage that occurs at the end of the power line is as in Fig. 8a, while the harmonic distortion of the voltage on the load is as in Fig. 8b.

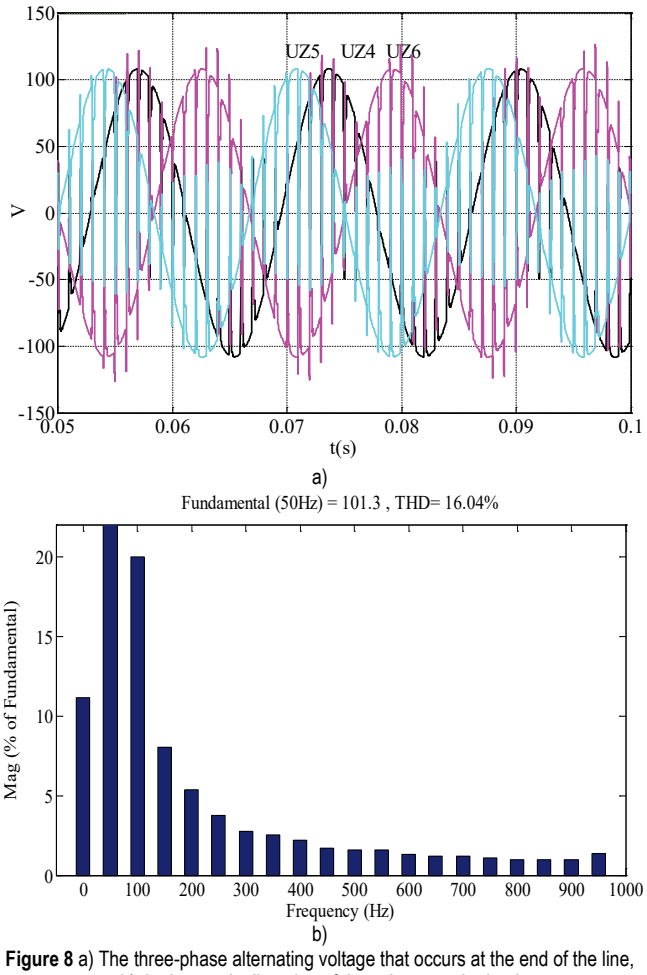

Figure 8 a) The three-phase alternating voltage that occurs at the end of the line, b) the harmonic distortion of the voltage on the load

On the power line, 101 volts of the alternating voltage at the maximum value is formed on loads. The effective value of the voltage is 90.9 V because the modulation index is 0.9. Although there is no filtering element on the line, the distortion of the load voltage is 16%. If the load on such a line is provided with alternating voltage by conventional inverter methods, this value will exceed 100%. When Parallel RL loads connected in series at the beginning and end of the 15 km long line are energized with alternating source, a three-phase alternating current that occurs on the load is presented in Fig. 9.

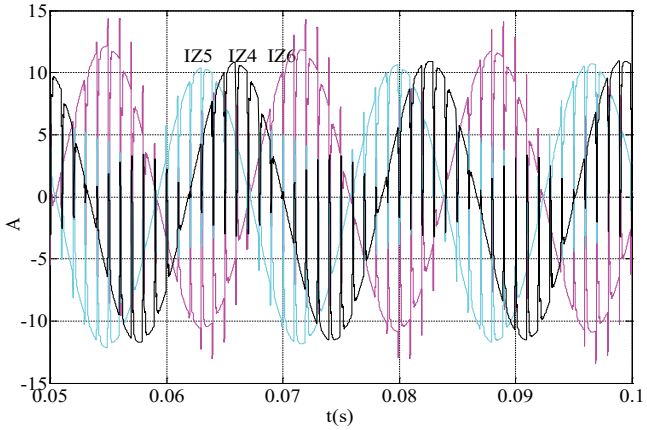

Figure 9 A three-phase alternating current of the 15 km long line

On the power line, a 12-volt alternating current at the maximum value is formed on loads. The effective value of the voltage is 10.2 A because the modulation index is 0.9. According to the results, the power distribution line is simulated for efficient power distribution and control without losing a lot of time and money. By taking this model into consideration, applications can be performed in less time and with less error rate. As the missing and difficult sides of the power line in the simulation can be determined, the accidents and errors that may occur are reduced, and the loss of life and property is eliminated.

4 CONCLUSION

The paper presented power control by inverse half rectifier processing method at energy distribution line in the simulation. The three-phase power line was controlled by semiconductor switches in reverse and parallel connected sources for each phase. First, the circuit model and mathematical equations of the line were created. In mathematical equations, the effect of the modulation index of the control signals applied to the switches to the power occurring on the load was shown. In unbalanced loads, it was shown how to calculate the values of *MCI* to equalize the effective value of the current. The current and voltage of the line were measured at different loads in the line. The balancing current and power were calculated by measuring for different modulation indices and line impedances. Obtained results and the effect of modulation index on the results were discussed. Unbalanced load current imbalances were eliminated by equalizing the effective values of the currents. As the unbalanced phase impedance decreases, the applied *MCI* and the balancing current increase, which leads to an increase in the balancing power. According to the results obtained, the design and application of the line has been successfully achieved.

5 REFERENCES

[1] Krauter, S. (2018). Simple and effective methods to match photovoltaic power generation to the grid load profile for a PV based energy system. *Solar Energy*, *159*, 768-776. https://doi.org/10.1016/j.solener.2017.11.039

[2] Niu, B., Hwangbo, H., Zeng, L., & Ding, Y. (2018). Evaluation of alternative power production efficiency metrics for offshore wind turbines and farms. *Renewable Energy*, *128*, 81-90. https://doi.org/10.1016/j.renene.2018.05.050

[3] Exel, L. & Frey, G. (2018). Modeling and simulation of local flexibilities and their effect to the entire power system. *Computer Science-Research and Development*, *33*(1-2), 6. https://doi.org/10.1007/s00450-017-0346-7

[4] Matsumori, H., Shimizu, T., Takano, K., & Ishii, H. (2018). Three-Phase AC Filter Inductor Design for Three-Phase PWM Inverter for Conversion Efficiency Improvement at Low Load. *Electrical Engineering in Japan*, *203*(1), 37-49. https://doi.org/10.1002/eej.23053

[5] Ananda, A. S. (2018). Performance Analysis of Series-Passive Filter in 5-Phase PWM Inverter Drive and Harmonic Study Using Simulink/Matlab. In *Advances in Power Systems and Energy Management* (pp. 139-146). Springer, Singapore. https://doi.org/10.1007/978-981-10-4394-9_14

[6] Kumar, M. (2018). Time-Domain Characterization of Digitized PWM Inverter with Dead-Time Effect. *IEEE Transactions on Circuits and Systems I: Regular Papers*. https://doi.org/10.1109/TCSI.2018.2827950

[7] Mukherjee, S., Giri, S. K., Kundu, S., & Banerjee, S. (2018). A Generalized Discontinuous PWM Scheme for Three-Level NPC Traction Inverter with Minimum Switching Loss for Electric Vehicles. *IEEE Transactions on Industry Applications*. https://doi.org/10.1109/TIA.2018.2866565

[8] Takahashi, H., Obara, H., & Fujimoto, Y. (2018, March). Dead time compensation for three-level flying capacitor inverter with phase shift PWM. In *Advanced Motion Control (AMC), 2018 IEEE 15th International Workshop on* (pp. 229-233). IEEE. https://doi.org/10.1109/AMC.2019.8371093

[9] Sivakumar, P., & Arutchelvi, M. S. (2018). Modified composite power control strategy for grid connected wind-PV systems with unbalanced nonlinear current. *International Transactions on Electrical Energy Systems*, e2587. https://doi.org/10.1002/etep.2587

[10] Can, E., & Sayan, H. H. (2016). SSPWM three phase inverter design and experimented on unbalanced loads. *Tehnički vjesnik*, *23*(5), 1239-1244. https://doi.org/10.17559/TV-20150730222021

[11] Can, E. & Sayan, H. H. (2017). The increasing harmonic effects of SSPWM multilevel inverter controlling load currents investigated on modulation index. *Tehnički vjesnik*, *24*(2), 397-404. https://doi.org/10.17559/TV-20151020134629

[12] Can, E. (2018). The modeling and analysis of a power transmission line supplied by a solar power plant. *Tehnički glasnik*, *12*(3), 124-130. https://doi.org/10.31803/tg-20180521111744

[13] Singh, S. N. & Singh, G. K. (2017). Modelling, design and stability analysis of an improved SEPIC converter for renewable energy systems. *International Journal of Electronics*, 1-19.

[14] Pan, L., et al. (2017). One-cycle control for three-phase single-capacitor Z-source inverter with unity power factor. *International Journal of Electronics*, 104(4), 635-658. https://doi.org/10.1080/00207217.2016.1242161

[15] Raj, N., Jagadanand, G., & George, S. (2016). A Modified Charge Balancing Scheme for Cascaded H-Bridge Multilevel Inverter. *Journal of Power Electronics*, *16*(6), 2067-2075. https://doi.org/10.6113/JPE.2016.16.6.2067

[16] Zheng, C. F., Zhang, B., Qiu, D. Y., Zhang, X. H., & Xiao, L. M. (2015). Wavelet PWM Technique for Single-Phase Three-Level Inverters. *Journal of Power Electronics*, *15*(6), 1517-1523. https://doi.org/10.6113/JPE.2015.15.6.1517

Author's contacts:

Erol CAN, PhD, Assoc. Prof.
Aviation Electric Electronics, School of Civil Aviation,
Erzincan Binali Yıldırım University,
Fatih Avenue, 24100 Erzincan, Turkey
cn_e@hotmail.com

ISSN 1846-6168 (Print), ISSN 1848-5588 (Online)
https://doi.org/10.31803/tg-20190211142404

Original scientific paper

INFLUENCE OF AN UNEVEN SURFACE ON THE VIBRATION OCCURRENCE AFFECTING THE TRACTOR OPERATOR

Željko BARAČ, Ivan PLAŠČAK, Tomislav JURIĆ, Pavo BALIČEVIĆ, Vinko DUVNJAK, Mladen JURIŠIĆ, Goran HEFFER, Monika MARKOVIĆ

Abstract: The paper presents a study of the influence of an uneven surface and number of tractor hours on vibration that is transmitted to the operator's hand-arm system during operation. The study was conducted on the asphalt, gravel and grass traversal during 2015 and 2016. The results indicate that the movement of a tractor on different agrotechnical surfaces generates vibrations of varying intensity that affect the hand-arm system of the operator. The highest vibration values were recorded on the asphalt, while the least vibrations were measured on the grass. The measured maximum vibration values are lower than the permissible 5 $m \cdot s^{-2}$ in the direction of all three axes, making it possible to assume that they are not harmful to the health of the operator.

Keywords: agrotechnical surfaces; hand-arm system; vibration

1 INTRODUCTION

There are numerous negative effects of vibration on the operator. However, since vibration is closely intertwined with other occupational hazards, a clear causal link between the impact of vibration and health damage cannot be established. A wealth of research shows that constant short-term exposure to high vibration can cause stomach and chest pain, lack of air, nausea and dizziness, whereas constant long-term exposure can result in psychomotor, physiological, and psychological disorders [1]. The structure of an agricultural tractor consists of a fixed connection between the axes and the tractor, which is especially unfavorable regarding the transmission of mechanical vibration to the operator's workplace. Mechanical vibration is transmitted through the operator's seat, the floor of tractor cabs, steering wheels, control and driving levers. The negative impact of mechanical vibration decreases the operator's concentration affecting his/her central nervous system and potentially causing occupational diseases of the spine and stomach [1, 2]. Vibration is an oscillatory body movement which can be straight or angular depending on the motion path. The increase in speed of agrotechnical practices has created new problems relating to the dynamic behavior of machinery and exposure of the operator's body to vibration. An increased speed of agrotechnical practices intensifies mechanical vibration, which consequently affects the operator [3].

Electrical and pneumatic hand-held tools can cause hand-arm vibration [4]. Depending on the intensity, frequency, and exposure period, the changes can be temporary (i.e. reversible) or permanent. Working in a cold environment increases injury risk. When exposed to vibration, it is necessary to avoid hand hypothermia (e.g. keep the hands warm using gloves or a source of heat). Furthermore, it is necessary to measure vibration in an objective way to determine the real danger to human health, as well as to develop mechanisms and equipment to protect the operator from the negative impact of vibration [5]. Authors [6] point out that cardiovascular disorders result from vibration exposure in which case operators often complain about occasional pain in hands or white fingers, which is a sign of hypothermia. Neurological disorders occur when hands and arms are exposed to vibration causing tingling and numbness of the hand or the whole arm. A muscle and the peripheral nervous system disorder affecting the hand or arm is a consequence of vibration exposure that produces irreversible changes in hand bones and wrist joints. Workers exposed to long-term vibration generally complain of muscle weakness and tingling in hands and arms. Additionally, vibration decreases the firmness of grip strength, which is considered a direct consequence of mechanical damage to peripheral nerves. Cardinale and Wakeling [7] argue that constant exposure to high vibration frequencies can significantly impair one's health. The operator's hand-arm system is the most susceptible to vibration within the frequency range of 6-16 Hz [8, 9, 10].

Fahy and Thompson [11] point out that the transfer of vibration to the operator's body occurs when the body is leaning against a vibrating surface (e.g. when in a seated position on a vibrating chair; in a standing position on a vibrating floor; in a lying position on a vibrating surface). Bogadi-Šare [12] claims that the operator exposed to general vibrations can develop osteoarticular diseases. The changes in the lumbar vertebrae in 90 % of the general population aged between 55 and 60 can be confirmed by x-ray, whereas the same can be confirmed among 100 % of the vibration-exposed population aged between 45 and 50. Zeng [13] claims that constant vibration exposure accompanied by the aging of the agricultural population presents a significant risk to their health. Therefore, a modification of vehicle design should facilitate a decrease in vibration created by agrotechnical practices. Pobedin et al. [14] point out that vibration reduction can be achieved by adding a vibration muffler into the tractor cab. Authors [15] claim that modern tractors are often equipped with parts that reduce the

vibration transferred to the driver (e.g. low-pressure tyres, air sprung seat and cab, and front axle suspension).

Barač et al. [16] measured the vibration that affects the operator's hand-arm system when working with a sprayer and mulcher. The lowest vibration values were measured on a sprayer in the direction of the *x*, *y* and *z* axes. Barač et al. [17] researched the impact of various agrotechnical surfaces (asphalt, gravel and grass surface) on the level of vibration that affect the hand-arm system. The results show that the lowest vibration values were obtained for the grass surface in the direction of all axes, whereas the highest values were obtained on the asphalt and gravel surfaces in the direction of x and y axes, and the y axis, respectively.

The aim of the research is to establish the level of mechanical vibration that affects the operator's hand-arm system on various agrotechnical surfaces in relation to an increased amount of the tractor's work hours. It is expected that the increase in work hours will result in a heightened level of vibration that affects the hand-arm system of the driver of an agricultural tractor.

2 MATERIALS AND METHODS

The research was performed on a *Landini Powerfarm 100* tractor through a two-year period. Over the first and second research year (2015 and 2016), the tractor reached 5 800 and 6 800 hours of work, respectively. The measurements were conducted on the agricultural fields and access roads of the School of Agriculture and Veterinary Medicine in Osijek to establish the values of vibration influencing the hand-arm system of the operator (in the direction of the *x*, *y* and *z* axes). The tractor moved along gravel, asphalt, and grass surfaces. The measurement of vibration was repeated three times, which produced the mean value of vibration used for further research. Each measurement lasted for 30 minutes.

Vibration level measurement was performed in accordance with the standards [18, 19, 20], which define the limits of vibration exposure, their effects on the operator's health, and include the guidelines for measurements at the workplace. The measurements were performed with a measuring device *MMF VM30*. A sensor was mounted on the steering wheel with the coordinates set in the direction [20]: *x* axis: longitudinally (along the axis of motion – forward (positive) / backward (negative); *y* axis: laterally (at the right angle to the motion direction); and *z* axis: vertically, upward (positive) / downward, vertically to the surface (negative). The weather conditions in 2015 were as follows: air temperature ranged between 29° C and 31 °C; relative humidity ranged from 62 % to 64 %; the impact of wind was minimal. The weather conditions in 2016 were similar.

The directives [21] and OG [22] contain both the limit values and critical values for the exposure of the hand and arm and they are as follows:

- The limit value for daily exposure based on the reference time of eight hours is 5 $m \cdot s^{-2}$;
- The critical value for daily exposure based on the reference time of eight hours is 2.5 $m \cdot s^{-2}$.

3 RESULTS AND DISCUSSION

Compared to the results obtained in 2015, the results for 2016 show a slight vibration deviation in the direction of all three axes measured on all three types of surfaces (gravel, asphalt, and grass surface) (Tab. 1).

Table 1 Mean values ($m \cdot s^{-2}$)

Surfaces	*x* axis		*y* axis		*z* axis	
	Year					
	2015	2016	2015	2016	2015	2016
Asphalt	0.079	0.081	0.071	0.073	0.069	0.071
Gravel	0.060	0.063	0.071	0.074	0.037	0.070
Grass	0.020	0.023	0.069	0.073	0.040	0.044

The highest mean vibration values were measured in the direction of *x* and *z* axes on the asphalt surface in 2015 and 2016. The highest mean vibration values in 2015 were obtained in the direction of the y axis on the asphalt and gravel road, while the highest mean values were measured on the gravel road in 2016. The lowest vibration values in the direction of the x axis were measured as follows: in 2015 and 2016 when the tractor moved along a grass surface; in 2015 in the direction of the y axis along a grass surface; in 2016 on the asphalt and grass surface in the direction of the z axis; in 2015 on the gravel road; in 2016 on the grass surface.

Comparable results were obtained by the authors [23], who measured the vibrations produced by framesaws and bandsaws. The authors established that the obtained vibration level does not carry any health risk to the operator positioned on the framesaw stand even after an eight-hour exposure period. However, a one-hour exposure results in decreased working conditions, which can afflict workers' wellbeing and their efficiency. Deboli et al. [24] measured the vibrations on four tractors equipped with several types of tyres on three different surfaces, i.e. gravel road, asphalt, and a combination between asphalt and gravel road. In the last case, two tyres drove along the gravel road, and the other two along the asphalt road. Irrespective of the tyre type, the lowest vibration was obtained when the tractor moved along the asphalt surface. The vibration level in this case did not reach the allowed limit values, which is in accordance with the results of our research. The results of the descriptive statistics related to the mean values of the obtained vibration in the direction of the *x* and *z* axes on the asphalt surface (Tab. 2) show that the standard error was higher in the second year of measurement (2) compared to the first year (1), whereas it remained the same in the direction of the y axis for both years. Furthermore, the variance analysis of the mean values for the obtained vibration impacting the hand-arm system of the driver in the direction of all three axes (*x*, *y* and *z*) on the asphalt surface shows no statistically significant difference between the measurements in both the first and second year.

Tab. 3 shows the descriptive statistics related to the mean values of the obtained vibration in the direction of *x* and *y* axes on the gravel surface. It is discernible that a higher standard error occurs in the second (2) year of measurement compared with the first year (1). Variance analysis of the mean values of vibration in the direction of the *x*, *y* and *z* axes on the gravel surface shows no statistically significant

difference concerning the mean value of the obtained vibration in both the first and second measurement year.

The highest standard error related to the obtained vibration was measured in the direction of the *x* and *z* axes on the grass surface in the second (2) measurement year (Tab. 4). A higher standard error in the direction of the y axis was determined in the first (1) measurement year. The variance analysis of the mean values of vibration in the direction of the *x*, *y* and *z* axes on grass impacting the hand-arm system did not reveal any statistically significant differences between the first (1) and second (2) measurement year.

Table 2 Descriptive statistics and variance analysis for occurred vibrations on asphalt surface

	N	$\overline{x}$	σ	*C.V.* (%)	*st. error*	*F*	*Sig.* (95 %)
x axis							
2015	3	0.07967	0.004509	5.65	0.002603	0.129	0.738
2016	3	0.08100	0.004583	5.65	0.002646		
Total	6	0.08033	0.004131	5.14	0.001687		
y axis							
2015	3	0.07133	0.006110	8.56	0.003528	0.161	0.709
2016	3	0.07333	0.006110	8.33	0.003528		
Total	6	0.07233	0.005574	7.70	0.002275		
z axis							
2015	3	0.06900	0.005568	8.06	0.003215	0.243	0.648
2016	3	0.07133	0.006028	8.45	0.003480		
Total	6	0.07017	0.005345	7.61	0.002182		

Table 3 Descriptive statistics and variance analysis for occurred vibrations on gravel surface

	N	$\overline{x}$	σ	*C.V.* (%)	*st. error*	*F*	*Sig.* (95 %)
x axis							
2015	3	0.06033	0.002517	4.17	0.001453	1.391	0.304
2016	3	0.06300	0.003000	4.76	0.001732		
Total	6	0.06167	0.002875	4.66	0.001174		
y axis							
2015	3	0.07100	0.004583	6.45	0.002646	0.519	0.511
2016	3	0.07400	0.005568	7.52	0.003215		
Total	6	0.07250	0.004848	6.68	0.001979		
z axis							
2015	3	0.03667	0.032146	87.66	0.018559	2.326	0.202
2016	3	0.07000	0.020000	28.57	0.011547		
Total	6	0.05333	0.030111	56.46	0.012293		

Table 4 Descriptive statistics and variance analysis for occurred vibrations on grass surface

	N	$\overline{x}$	σ	*C.V.* (%)	*st. error*	*F*	*Sig.* (95 %)
x axis							
2015	3	0.02067	0.003055	14.77	0.001764	0.985	0.377
2016	3	0.02333	0.003512	15.05	0.002028		
Total	6	0.02200	0.003286	14.93	0.001342		
y axis							
2015	3	0.06900	0.006557	9.50	0.003786	0.768	0.430
2016	3	0.07333	0.005508	7.51	0.003180		
Total	6	0.07117	0.005913	8.30	0.002414		
z axis							
2015	3	0.04000	0.002000	5	0.001155	1.920	0.238
2016	3	0.04400	0.004583	10.41	0.002646		
Total	6	0.04200	0.003847	9.15	0.001571		

4 CONCLUSION

The following conclusions can be drawn based on our two-year research:

- The level of vibration that impacts the hand-arm system for all agrotechnical surfaces in the direction of the *x*, *y* and *z* axes was higher in the second (2) measurement year compared to the first (1) measurement year, which is in accordance with the specified hypothesis;
- The highest levels of vibration were obtained for the asphalt surface in the direction of the *x* and *z* axes (in 2015 and 2016), as well as in the direction of the y axis for the asphalt and gravel surfaces in 2015, and for the gravel surface in 2016;
- The lowest vibration levels were obtained as follows: for the grass surface in the direction of the *x* axis in 2015 and 2016; in the direction of the *y* axis in 2015; in the direction of the z axis in 2016. The lowest level for the asphalt surface was obtained in the direction of the *y* axis in 2016 (the same result was obtained for the grass surface). The lowest level for the gravel surface was obtained in the direction of the *z* axis in 2015;
- The research shows that different agrotechnical surfaces (i.e. asphalt, gravel and grass surfaces) produce vibration of various intensity levels that are transmitted to the hand-arm

system of the agricultural tractor operator. Irrespective of the higher vibration values obtained in the second measurement year, they did not exceed the allowed vibration limit values (5 m s^{-2}) affecting the hand-arm system. Therefore, it is assumed that they will not harm the operator's health over an eight-hour work period.

5 REFERENCES

[1] Brkić, D., Vujčić, M., Šumanovac, L., Lukač, P., Kiš, D., Jurić, T., & Knežević, D. (2005). *Exploitation of agricultural machinery*. Faculty of Agrobiotechnical Sciences Osijek.

[2] Goglia, V., Gospodarić, Z., Košutić, S., & Filipović, D. (2003). Hand-transmitted vibration from the steering wheel to drivers of small four-wheel drive tractor. *Applied Ergonomics, 34*(1), 45-49. https://doi.org/10.1016/S0003-6870(02)00076-5

[3] Servadio, P., Marsili, A., & Belfiore, N. P. (2007). Analysis of driving seat vibrations in high forward speed tractors. *Biosystems engineering, 97*(2), 171-180. https://doi.org/10.1016/j.biosystemseng.2007.03.004

[4] Stegić, M. (2009). *Vibration Theory of the Linear Discrete Mechanical Systems*. University textbook, Faculty of mechanical engineering and naval architecture, Zagreb.

[5] Poplašen, D. & Kerner, I. (2013). Vibrations transmitted to the hands and arms. *Safety, 55*(4), 389-391. Retrieved from https://hrcak.srce.hr/112849

[6] Goglia, V., Suchomel, J., Žgela, J., & Đukić, I. (2012). Forestry workers` exposure to vibration in the context of directive 2002/44/EC. *Journal of the Forestry Society of Croatia, 5-6,* 283-289. Retrieved from https://hrcak.srce.hr/index.php?show=clanak&id_clanak_jezik=126217

[7] Cardinale, M. & Wakeling, J. (2005). Whole body vibration exercise: are vibrations good for you. *British Journal of Sports Medicine, 39*(9), 585-589. https://doi.org/10.1136/bjsm.2005.016857

[8] Goglia, V. & Beljo-Lučić, R. (1998). Some problems of measuring and evaluation whole body and hand-arm transmitted vibrations. *Proceedings of the 26th International Symposium on Agricultural Engineering, Actual Tasks on Agricultural Engineering*, Opatija, 61-68.

[9] Goglia, V., Žgela, J., Suchomel, J., & Đukić, I. (2011). Exposure to hang-arm Transmitted vibration at forest nursery and thinning. *Human Resources Management and Ergonomics, 5*(1), 45-55. Retrieved from https://frcatel.fri.uniza.sk/hrme/archi.html

[10] Suchomel, J. & Slancik, N. (2005). Influence of some ergonomic criterions on modeling and optimization technology in forestry. *Proceedings of the International Conference Management of human potential in enterprises*, Žilina, 354-359.

[11] Fahy, F. & Thompson, D. (2015). *Fundamentals of Sound and Vibration*, Second Edition. University textbook, Institute of Sound and Vibration Research, University of Southampton, Southampton. Retrieved from https://books.google.hr/books?hl=hr&lr=&id=znd3CAAAQBAJ&oi=fnd&pg=PP1&dq=11.%09Fahy,+F.,+Thompson,+D.+Fundamentals+of+Sound+and+Vibration,+Second+Edition.+Institute+of+Sound+and+Vibration+Research,+University+of+Southampton,+Southampton,+2015.&ots=BP1zI0Wbpa&sig=HSHPF7daxNGN6GM-XRd_gKP3U6I&redir_esc=y#v=onepage&q&f=false

[12] Bogadi-Šare, A. (1993). Whole body vibration syndrome – a medical problem requiring more attention. *Archives of Industrial Hygiene and Toxicology, 44*(3), 269-279. Retrieved from https://hrcak.srce.hr/index.php?show=clanak&id_clanak_jezik=216606

[13] Zeng, X. (2016). *Modeling predictors of whole body vibration exposure among Saskatchewan farmers: A key step in low back disorder prevention*. University of Saskatchewan, Saskatoon. Retrieved from https://harvest.usask.ca/handle/10388/7389

[14] Pobedin, A. V., Dolotov, A. A., & Shekhovtsov, V. V. (2016). Decrease of the vibration load level on the tractor operator working place by means of using of vibrations dynamic dampers in the cabin suspension. *Proceedia Engineering, 150*, 1252-1257. https://doi.org/10.1016/j.proeng.2016.07.136

[15] Gomez-Gil, J., Gomez-Gil, F. J., & Martin-de-Leon, R. (2014). The influence of tractor-seat height above the ground on lateral vibrations. *Sensors, 14*(10), 19713-19730. https://doi.org/10.3390/s141019713

[16] Barač, Ž., Vidaković, I., Zimmer, D., & Ermenić, V. (2017). The relationship of agrotechnical interventions on the level of vibrations produced and their influence on the system hand-arm of the operator of the tractor. *Proceedings of the 52*th *Croatian and 12th international symposium on agriculture, Dubrovnik,* 628-631. Retrieved from https://www.cabdirect.org/cabdirect/abstract/20173178505

[17] Barač, Ž., Plaščak, I., Jurišić, M., Zimmer, D., Vidaković, I., & Laslo, J. (2017). The influence of different agricultural surfaces on produced vibration that affect the system hand-arm of operator. *Proceedings & abstract of the 10th International Scientific/Professional Conference Agriculture in Nature and Environment Protection*, Vukovar, 187-190. Retrieved from https://www.cabdirect.org/cabdirect/abstract/20173257533

[18] HZN (1999). Mechanical vibration and shock – Evaluation of human exposure to whole-body vibration – Part 1: General requirements, HRN ISO 2631-1. Croatian Standards Institute, Zagreb, 1999.

[19] HZN (2008). Mechanical vibration – Measurement and evaluation of human exposure to hand-transmitted vibration – Part 1: General requirements, HRN ISO 5349-1, Croatian Standards Institute, Zagreb.

[20] HZN (2008). Mechanical vibration – Measurement and evaluation of human exposure to hand-transmitted vibration – Part 2: Practical guidance for measurement at the workplace, HRN ISO 5349-2, *Croatian Standards Institute*, Zagreb, 2008.

[21] EC (2002). Council Directive on the minimum health safety requirements regarding the exposure of workers to the risks arising from physical agents (vibration), *J Eur Commun*, EEC 89/391, 2002/44. Retrieved from https://eur-lex.europa.eu/legal-content/HR/TXT/?uri=CELEX:02002L0044-20081211

[22] OG 155/2008. Rule book on protection from the risk of exposure to vibration at work. Ministry of economy, entrepreneurship and crafts, *Republic of Croatia*, Zagreb.

[23] Đukić, I. & Goglia, V. (2007). Noise and vibration in using framesaws and bandsaws. *Scientific journal of wood technology, 58*(1), 19-22. Retrieved from https://hrcak.srce.hr/index.php?show=clanak&id_clanak_jezik=19667

[24] Deboli, R., Calvo, A., Preti, C., Palietto, G. (2008). Whole body vibration (wbv) transmitted to the operator by tractors equipped with radial tires. *International conference Innovation Technology to Empower Safety, Health and Welfare in Agriculture and Agro-food Systems*, Ragusa, 1-10. Retrieved from http://www.ragusashwa.it/CD_2008/lavori/TOPIC7/poster/DEBOLI-1.pdf

Authors' contacts:

Željko BARAČ, MSc, Research Assistant
Corresponding author
Faculty of Agrobiotechnical Sciences Osijek,
Vladimira Preloga 1, 31000 Osijek, Croatia
zbarac@fazos.hr

Ivan PLAŠČAK, PhD, Associate Professor
Faculty of Agrobiotechnical Sciences Osijek,
Vladimira Preloga 1, 31000 Osijek, Croatia
iplascak@fazos.hr

Tomislav JURIĆ, PhD, Full Professor
Faculty of Agrobiotechnical Sciences Osijek,
Vladimira Preloga 1, 31000 Osijek, Croatia
tjuric@fazos.hr

Pavo BALIČEVIĆ, PhD, Full Professor
Faculty of Agrobiotechnical Sciences Osijek,
Vladimira Preloga 1, 31000 Osijek, Croatia
pbalicevic@fazos.hr

Vinko DUVNJAK, PhD, Scientific Adviser
Agricultural Institute Osijek,
Južno predgrađe 17, 31000 Osijek, Croatia
vinko.duvnjak@poljinos.hr

Mladen JURIŠIĆ, PhD, Full Professor
Faculty of Agrobiotechnical Sciences Osijek,
Vladimira Preloga 1, 31000 Osijek, Croatia
mjurisic@pfos.hr

Goran HEFFER, PhD, Full Professor
Faculty of Agrobiotechnical Sciences Osijek,
Vladimira Preloga 1, 31000 Osijek, Croatia
hgoran@fazos.hr

Monika MARKOVIĆ, PhD, Assistant Professor
Faculty of Agrobiotechnical Sciences Osijek,
Vladimira Preloga 1, 31000 Osijek, Croatia
mmarkovic@fazos.hr

ISSN 1846-6168 (Print), ISSN 1848-5588 (Online)
https://doi.org/10.31803/tg-20190226095826

Original scientific paper

THE EFFECTS OF DIELECTRIC VALUES, BREAST AND TUMOR SIZE ON THE DETECTION OF BREAST TUMOR

Nuşin UNCU, Emine AVŞAR AYDIN

Abstract: Although breast cancer is the second main cause of female deaths after lung cancer, early diagnosis plays a crucial role to diminish the death rate. Many techniques have been improved to detect the cancerous cells. At different microwave frequencies, the malignant cells indicate different electrical characteristics as compared to the normal cells. According to these frequencies, the breast tissue is more permeable than other tissues such as the brain and muscle. Due to this property of the breast tissue, microwaves can be used for the detection of breast cancer. In this study, the breast prototype was modelled using the CST STUDIO SUITE electromagnetic simulation software with respect to different breast size, tumor size and dielectric values tested at a range of the 0-3.0 GHz frequency. The objective of this paper is to investigate the effects of each factor and the interactions of factors on detecting cancer cells using the factorial analysis. The results indicate that the factors such as fat and skin permittivity, tumor and breast sizes are more effective in the detection of breast tumor. Although the effect of fibro permittivity is not significant alone, there are considerable interaction effects of a large breast size and small tumor size through low-to-high values of fibro permittivity. Furthermore, the combinations of a breast radius smaller than almost 8.5 cm with a high level tumor radius and breast radius larger than 8.5 cm with a low level tumor radius are desirable for lessening the return loss value.

Keywords: dielectric properties; factorial design; factor effects; microwave breast cancer detection

1 INTRODUCTION

Breast cancer is one of the main reasons of female death worldwide [1-5]. It is a key factor that the tumor be recognized in the early stages for a higher survival rate. In the last decade, the Microwave Imaging System [6-10] has been the focus of many researchers because of some drawbacks of the existing breast cancer detection techniques which are the magnetic resonance imaging (MRI), X-ray mammography, and ultrasound. Among these breast cancer imaging techniques, the MRI cost is very high and it also only has the advantage of screening evaluation before surgical operation. The X-ray mammography has hazardous radiation, false positives and painful breast compression. The microwave-based breast cancer imaging is one of the most promising methods for detecting breast cancer during its early development. This method relies on the differences in the dielectric properties of benign and malignant breast tissues which are skin, fat, fibro glandular, tumor [1, 2].

Dielectric properties of a material are obtained by measuring its ability to interact with electromagnetic energy [11]. The electric and magnetic forces generated by electromagnetic (EM) fields can cause changes in the interaction results. In addition to that, these properties tell us a lot about the mechanism of interaction of electromagnetic fields with various biological systems, including biopolymers, membranes and cells.

An EM field primarily acts upon components within the materials in biological tissues. These materials have a net electric charge and/or electric dipole moment. The main source of electric dipole moments in tissues belongs to polar molecules. The other additional sources are protein structures, muscles, fat, etc. Due to the fact that the electrical properties of a tissue are determined by such a wide variety of components, as reflected in different dielectric dispersions, these properties exhibit significant variations.

The thermal phenomena of conduction, convection and radiation play only a secondary role in temperature equilibrium, when an object is exposed to microwaves. The reason for this is that the release of heat is so instantaneous.

In a research study, the data from 15 patients showed that the values of dielectric properties for malignant breast tissues at 1-2 GHz are 3-5 times higher than the normal breast tissues [1]. In another study, 12 measurements indicated that dielectric properties of malignant breast tissues are roundly 10 times greater than the normal breast tissues since malignant tissues have a lot of water and are also more active in relation to the normal tissues.

Malignant tumors have higher relative permittivity and conductivity values than the normal breast tissue. These values can be as high as 10 times for adipose fat, but drop to a contrast of around 10%, mainly in conductivity, for fibro glandular (FG) tissue. This contrast has posed a challenge for the microwave imaging community as FG tissue is where most breast tumors originate [12]. Understanding the mechanisms that result in the high permittivity and hyper-conductivity of tumors is therefore a crucial part of breast cancer imaging. There have been many factors with difference in dielectric properties between the normal and malignant tissues.

One of factors is necrosis [13]. It is usually found in malignant breast tissue. Necrosis leads to the breakdown of cell membranes and thus a larger fraction of tissue can carry current at low frequencies, which decreases the capacitance of the tumor.

The second factor is the charging of the cell membrane [13]. In breast carcinoma, fat lobules are replaced with fibroblastic proliferation and epithelial cells are accompanied by a variety of alterations at the transformed cell surface. Cancer cell membranes have a reduced potential and have the ability to absorb positive ions because they have a higher negative surface charge. As a result, the conductivity of the

malignant tissue is increased because of the displacement and rotations of this mobile charge by the microwave field.

The relaxation times which are a third factor in malignant tissues are larger than those in the normal tissues resulting from the increased motional freedom of water [13]. The last one is sodium concentration and water content [13]. The sodium concentration in cancer cells is higher than that in normal cells. The high sodium concentration alone yields higher permittivity and conductivity values for malignant tissue. This higher sodium concentration also affects the cell membrane potential and causes the malignant tissue to retain more fluid. This retained fluid is in the form of bound water, which has higher permittivity and conductivity values. Malignant tissue therefore has a higher water content ratio than that of normal tissue, which coincides with higher values of permittivity and conductivity than normal breast tissue at the same microwave frequency.

The understanding and development of medical microwave techniques needs knowledge of the microwave dielectric properties of human tissues. There have been many data on the dielectric properties of female human normal/malignant/benign and surrounding breast tissue.

Dielectric properties of breast carcinoma and the surrounding tissues were measured [14]. The experiments were performed at the frequencies from 100 kHz to 100 MHz at 37 °C using an automatic network analyzer and an end-of-the-line capacitive sensor. Using a computer program, the cole-cole parameters were found by curve fitting. Tissues were divided into three main categories. These were the central part of the tumor, the tumor surrounding tissue, and the peripheral tissue. Tumor specimens were taken from seven different patients. From each specimen, depending on its size, 2-6 samples in the form of thin disks were excised. The number of samples was 28. The duration of all measurements was 4 h after the surgery. As seen from Table 1, measurements showed significant differences in dielectric properties between the samples taken from different locations. Surgical pathology reported the following diagnoses: A-infiltrating ductal carcinoma without metastases, B-infiltrating ductal carcinoma, C-infiltrating ductal carcinoma with focal papillary component, D-infiltrating carcinoma consistent with lobular carcinoma, E-infiltrating lobular carcinoma, F-infiltrating ductal carcinoma, G-infiltrating lobular carcinoma.

Using a resonant cavity technique, complex permittivity of in vitro diseased and non-diseased human female breast tissues were measured at 3.2 GHz [15]. Both dielectric properties and water contents of these tissues were found. Experimental data were compared with the models predicted from mixture equations.

Hitherto, breast cancer detection studies were carried out using dielectric properties; however the effect of dielectric properties has not been investigated. A 3D-breast was modeled by using the CST STUDIO SUITE electromagnetic simulation software and analyzed by using different dielectric properties and different breast and tumor sizes based on experimental design analyses results in the frequency range from 0 GHz to 3 GHz.

Design of Experiment (DOE) techniques have been used extensively in many different scientific fields. These techniques are beneficial for getting accurate statistical inferences for revealing the effects of factors on a process with less experimenting rather than considering all the combinations of factors. One of the DOE technique applications is found in [16] for analytical chemistry. In another study [17], a considerable decrease of patient dissatisfaction was given for the emergency room. [18] applied the factorial design technique to see the effects of prophylactic antiemetic interventions on the risk of postoperative nausea and vomiting of the surgery patients. Another case study on the effect of treatment factors on the quality of life of patients with breast cancer is found in [19]. In this study, 2^k factorial design is used to reveal the effects of factors and their interactions on the success of detecting breast tumor.

The outline of the paper starts with the introduction section. It is followed by illustrating the factors considered in breast cancer detection and applying simulation and the general factorial design. In the third section, significant effects of factors and their interaction graphs are given. Finally, further suggestions on the improvement of breast cancer detection are explained in the conclusion part.

Table 1 Computer fitted dielectric parameters of breast carcınoma and the surrounding tissues in the frequency range from 100 kHz to 100 MHz [14]

Specimen Location	Sample No.	ε_δ	ε_∞	τ (μs)	α	σ_{DC} (ms/cm)	Diagnosis
A	1	6090	50	0.633	0.326	2.20	Infiltrating ductal carcinoma metastases
	2	8260	50	0.595	0.311	3.03	
	3	3720	50	0.267	0.283	6.47	
	4	5170	50	0.288	0.239	6.91	
	5	3440	50	0.238	0.238	7.12	
	6	5710	50	0.263	0.277	6.60	
B	1	3330	50	1.30	0.380	3.3	Infiltrating ductal carcinoma
	2	5510	30	0.33	0.250	5.70	
C	1	793	20	0.579	0.232	0.82	Infiltrating ductal carcinoma
	2	482	30	0.603	0.281	0.38	
	3	3310	30	0.557	0.310	3.05	
D	1	2740	30	0.269	0.358	3.89	Infiltrating lobular carcinoma
	2	3285	30	0.3202	0.275	5.75	
	3	2320	30	0.259	0.278	6.49	
	4	1253	319	0.670	0.400	3.52	
E	1	3125	167	0.525	0.223	1.02	Infiltrating lobular carcinoma
	2	7060	30	1.605	0.362	4.99	
	3	13100	30	1.396	0.349	6.59	
	4	3080	50	0.45	0.298	3.90	
F	1	8830	30	1.408	0.360	2.78	Infiltrating ductal carcinoma
	2	10170	30	1.210	0.340	2.73	
	3	180	10	0.684	0.149	0.120	
G	1	288	10	0.983	0.10	0.161	Infiltrating lobular carcinoma
	2	298	10	1.008	0.075	0.130	
	3	675	10	1.391	0.163	0.444	
	4	7930	50	1.216	0.367	5.33	
	5	5490	50	0.768	0.379	4.15	
	6	8660	50	1.415	0.331	5.16	

2 SIMULATION MODEL OF BREAST TUMOR

A hemisphere breast model was designed as showed in Fig. 1 according to the dielectric properties of tissues which are permittivity (ε) and conductivity (σ). Microwave imaging was carried out by transmitting a sequence of

electromagnetic waves through the breast model and measuring the scattered field on the breast.

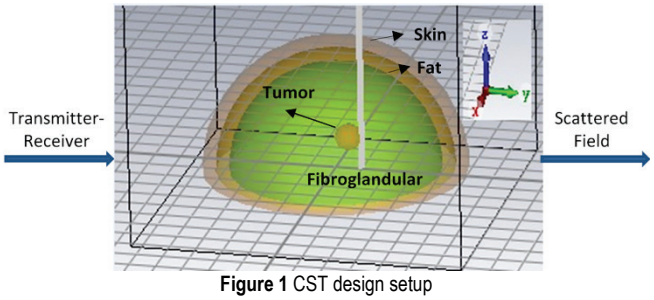

Figure 1 CST design setup

The design points that are the combinations of 10 factors values ranging from their lower values to upper values given in Tab. 2 are generated by experimental design methods by using the Design Expert 7.0 Trial Version. Design space is used in the CST simulation model for assessing the return loss values (*S11*). In order to find the input-output relationship, main effects and interactions of factor effects on detecting breast tumor, *S11* values obtained from the simulation are entered as experimental design output values. The flow of the method application in this study is given in Fig. 2.

Table 2 Lower and upper bounds for factor values

Factor	Name	Low Level	High Level
A	Skin ε	30	40
B	Skin σ	3	9
C	Fat ε	1	10
D	Fat σ	0	1
E	Fibro ε	40	50
F	Fibro σ	1.70	12
G	Tumor ε	40	56
H	Tumor σ	3	15
J	Breast Radius (cm)	2.5	10
K	Tumor Radius (mm)	1	10

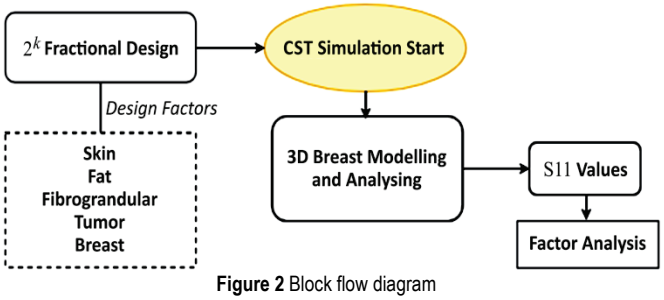

Figure 2 Block flow diagram

3 RESULTS

2^k factorial design is used with *V* Resolution in this study. It means that each factor has two levels. In this experiment, there are ten factors, and in order to lessen the number of experiments, we can exclude some design points by using the resolution property of the factorial design technique. Hence, the fractional factorial is used and $2^{10-3} = 128$ experiments are conducted. The analysis of variance (ANOVA) results in Tab. 3 show that our model with a *p*-value less than 0.0001 represents the design space significantly. The *p*-values of the factors *A*, *C*, *J* and *K* are less than 0.05 and they can be concluded as having significant effects with the confidence of 0.95. Thus, *Skin ε*, *Fat ε*, *BreastRadius* and *TumorRadius* are obtained as main concerns in the detection of breast cancer.

Table 3 Analysis of the variance for the main effects

Source of Variation	Sum of Squares	*d.o.f*	Mean Square	*F* Value	*p*-value Prob > *F*
Model	3349.53	55.00	60.90	12.56	< 0.0001
A-Skin ε	39.77	1.00	39.77	8.20	0.0055
B-Skin σ	17.34	1.00	17.34	3.58	0.0626
C-Fat ε	68.71	1.00	68.71	14.17	0.0003
D-Fat σ	0.28	1.00	0.28	0.06	0.8093
E-Fibro ε	13.24	1.00	13.24	2.73	0.1029
F-Fibro σ	0.08	1.00	0.08	0.02	0.8985
G-Tumor ε	10.19	1.00	10.19	2.10	0.1516
H-Tumor σ	7.22	1.00	7.22	1.49	0.2264
J-BreastRadius	299.76	1.00	299.76	61.81	< 0.0001
K-TumorRadius	576.77	1.00	576.77	118.92	< 0.0001

The graphs of the each significant factor's main effect on the value of *S11* is illustrated in Fig. 3. The factors *BreastRadius* (*J*) and *TumorRadius* (*K*) seem to be more influential than others on the change of the *S11* value in terms of their slopes of the lines. However, the difference is that while the *S11* value decreases through low-to-high values of BreastRadius *(J),* the low-to-high values of the *TumorRadius (K)* increase.

In order not to illustrate all of the two factor interactions, only significant interaction effects of *AJ, BD, CE, CJ, CK, EJ, EK,* and *JK* are given in Tab. 4. The interactions of factors are important to be considered to demonstrate the effect of two factors together on the value of *S11*. Hence, the significance of two factors may result as lesser or greater than each factor alone.

Table 4 Analysis of the variance for significant interaction effects

	Source of Variation	Sum of Squares	*d.o.f*	Mean Square	*F* Value	*p*-value Prob > *F*
Interactions	Model	3349.53	55.00	60.90	12.56	< 0.0001
	AJ	44.98	1.00	44.98	9.27	0.0032
	BD	19.92	1.00	19.92	4.11	0.0464
	CE	24.20	1.00	24.20	4.99	0.0286
	CJ	75.75	1.00	75.75	15.62	0.0002
	CK	64.90	1.00	64.90	13.38	0.0005
	EJ	40.47	1.00	40.47	8.34	0.0051
	EK	48.40	1.00	48.40	9.98	0.0023
	JK	1838.38	1.00	1838.38	379.05	< 0.0001

In Fig. 4, the graphs of interactions from Tab. 4 are demonstrated. In the AJ interaction graph, *Skin ε* has no significant effect on the *S11* value for the small size *BreastRadius*. However, for the large size *BreastRadius*, the *S11* value increases through the low-to-high values of *Skin ε.* In the *BD* interaction graph, the *S11* value increases at the high value of *Fat σ* through the low-to-high values of *Skin σ* . In the interaction graphs of *CE, CJ* and *CK*, the *S11* value increases through the low-to-high values of Fat *ε* for the high value *Fibro ε,* for the large size of *BreastRadius and* the small size of *TumorRadius,* respectively. Similarly, in the graph of *EJ* and *EK* interactions, *S11* decreases for the large size of

BreastRadius and the small size of *TumorRadius* through the low-to-high values of Fibro *ε*.

Finally, in the last graph, while *BreastRadius* is smaller than 8.5 cm, *S11* values for the large size *TumorRadius* are less than for the small size. However, this interpretation becomes reverse after the 8.5 cm size *BreastRadius*. However, the values of *S11* for the large size *TumorRadius* are greater than the small size.

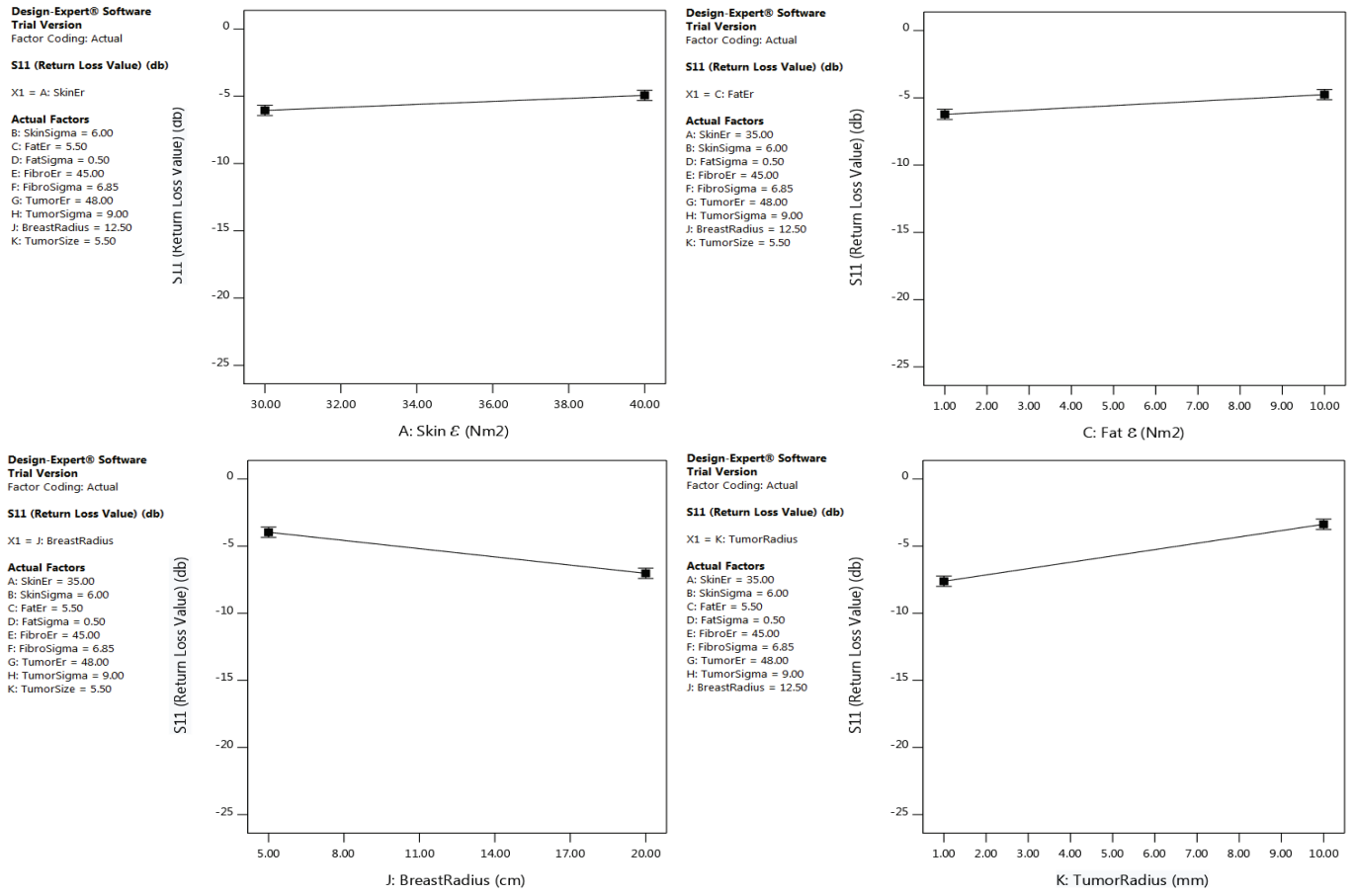

Figure 3 Significant factors' main effects on the detection of breast cancer

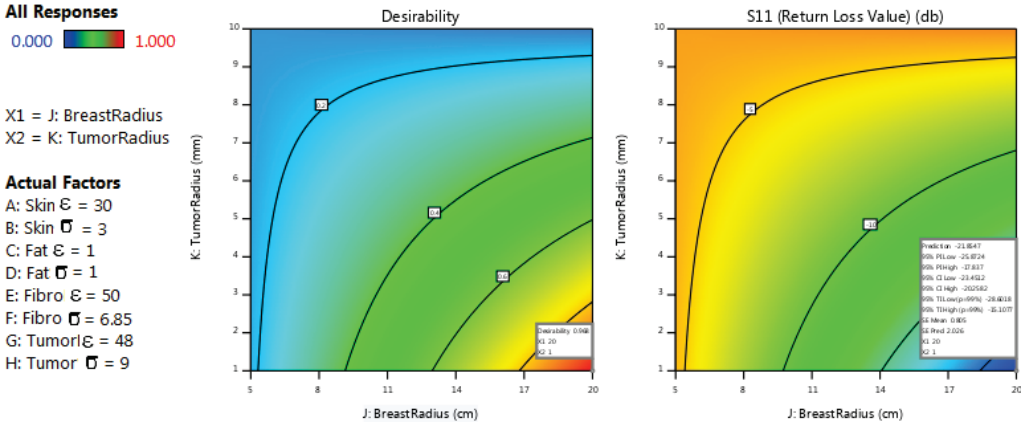

Figure 5 Desirability and optimum surface contours of *S11*

By using the numerical optimization tool of the Design Expert, the minimum value of *S11* is found. In order to have a minimum *S11* value, the optimal design points are given in Fig. 5.

The desirability graph based on two most effective factors on breast tumor detection is demonstrated in Fig. 5. The desired value of *S11* is -21.8547. It is seen that the S11 value decreases at the given values of factors in Fig. 5, and the increasing values of breast radius size and decreasing values of tumor size considerably help the detection of breast tumor.

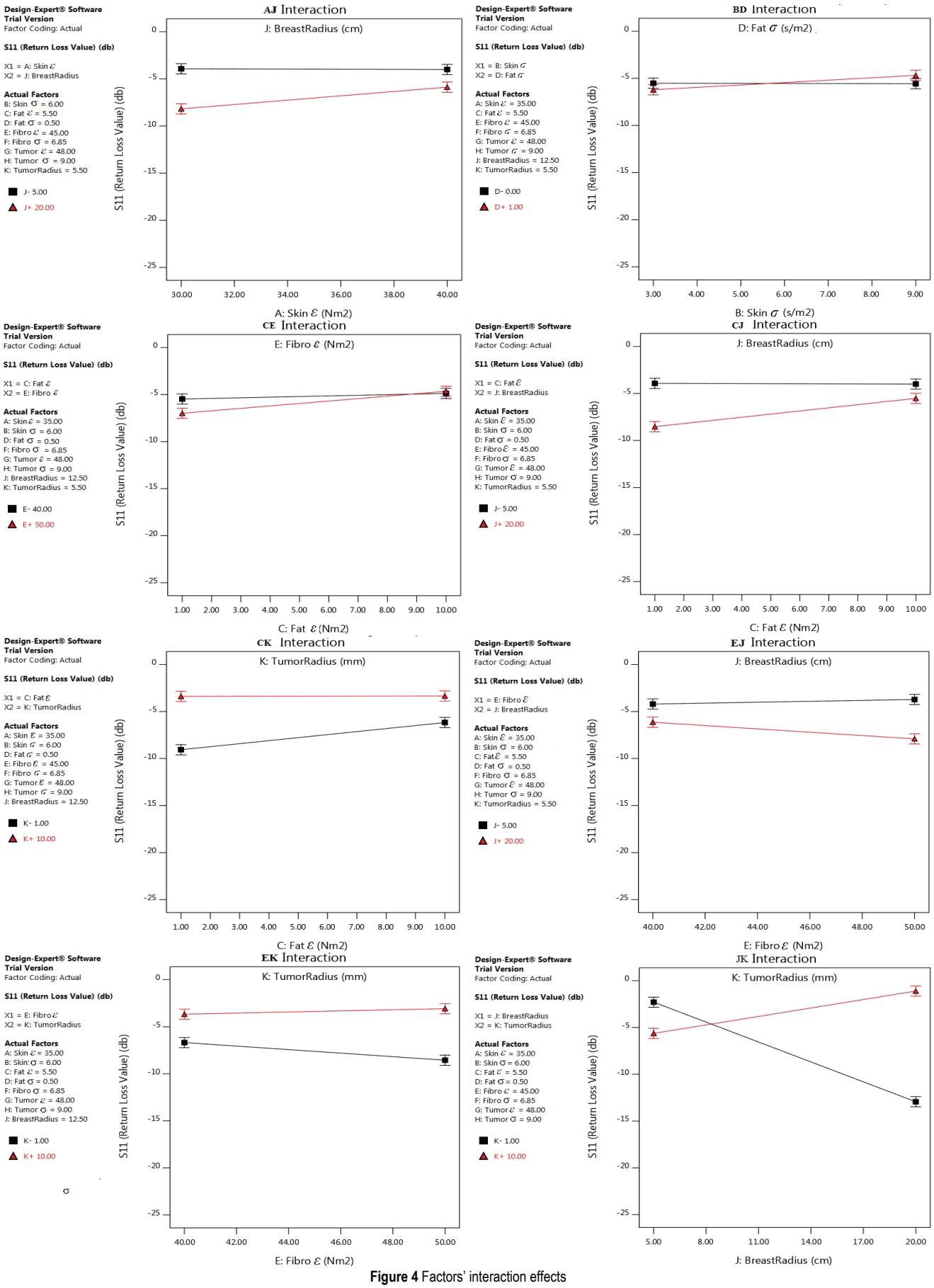

Figure 4 Factors' interaction effects

4 CONCLUSION

Breast cancer is one of the most widespread cancers among females. Various research groups have focused on microwave breast imaging techniques that are non-invasive and harmless to women. The microwave breast imaging technique relies on the differences in the dielectric properties of benign and malignant breast tissues which are skin, fat, fibro glandular, tumor. Breast cancer detection studies were carried out by using dielectric properties of skin, fat, fibro glandular, and tumor tissues. However, the effect of dielectric properties has not been investigated. A 3D-breast was modeled by using the CST STUDIO SUITE electromagnetic simulation software and analyzed by using different dielectric properties and different breast and tumor sizes based on experimental design analyses' results in the frequency range from 0 GHz to 3 GHz.

The results of this study show that some factors do not have significant effects on the detection of breast tumor as it was considered in previous studies. The main factors such as fat and skin *permittivity*, breast and tumor size seem to be important factors among others. Moreover, interaction effects are crucial for observation. However, the effects of some factors change based on low or high the values of others are. For instance, although the effects of the factors *fibro permittivity, skin and* fat *conductivity* are not significant alone, their interaction effects are meaningful. Particularly, through the low-to-high values of fibro permittivity with a large size breast and a small size tumor, the return loss value seems to decrease. The effect of the low-to-high values of skin and fat conductivity together increases the return loss value.

In future experiments, the design points can be constructed by using only the significant factors in order to lessen the number of factors and increase the precision of the model. For further studies, a phantom model will be carried out by using the results of this study.

5 REFERENCES

[1] Kwon, S. & Lee, S. (2018). Corrigendum to "Recent Advances in Microwave Imaging for Breast Cancer Detection". *International Journal of Biomedical Imaging*, 2018, 1-1. https://doi.org/10.1155/2018/1657073

[2] Kim, T., Oh, J., Kim, B., Lee, J., Jeon, S., & Pack, J. (2008). A study of dielectric properties of fatty, malignant and fibro-glandular tissues in female human breast. 2008 Asia-Pacific Symposium on Electromagnetic Compatibility and 19th International Zurich Symposium on Electromagnetic Compatibility. https://doi.org/10.1109/APEMC.2008.4559850

[3] Song, H., Men, A., & Jiang, Z. (2017). Breast tumor detection using empirical mode decomposition features. *IEEE Access,* 1-1. https://doi.org/10.1109/ACCESS.2017.2737633

[4] Kurrant, D. J. & Fear, E. C. (2011). Regional Estimation of the Dielectric Properties of the Breast: Skin, Adipose, and Fibroglandular Tissues. *Proceedings of the 5th European Conference on Antennas and Propagation (EUCAP)*, 2164-3342.

[5] Chen, Y., Kosmas, P., & Martel, S. (2013). Microwave breast tumor detection and size estimation using contrast-agent-loaded magnetotactic bacteria. *2013 35th Annual International Conference of the IEEE Engineering in Medicine and Biology Society (EMBC)*. https://doi.org/10.1109/EMBC.2013.6610790

[6] Tayel, M. B. & Hasan, H. T. (2017). An analytical metalens design approach of CST studio analysis for breast minimum full electric field coverage. *2017 12th International Conference on Computer Engineering and Systems (ICCES)*. https://doi.org/10.1109/ICCES.2017.8275384

[7] Yousefnia, M., Ebrahimzadeh, A., Dehmollaian, M., & Madannejad, A. (2018). A Time-Reversal Imaging System for Breast Screening: Theory and Initial Phantom Results. *IEEE Transactions on Biomedical Engineering, 65*(11), 2542-2551. https://doi.org/10.1109/TBME.2018.2807799

[8] Wang, L. & Peng, H. (2017). Holographic Microwave Imaging for Breast Cancer Detection Based on Compressive Sensing. *Volume 3: Biomedical and Biotechnology Engineering*. https://doi.org/10.1115/IMECE2017-70063

[9] Delbary, F., Brignone, M., Bozza, G., Aramini, R., & Piana, M. (2010). A Visualization Method for Breast Cancer Detection Using Microwaves. *SIAM Journal on Applied Mathematics, 70*(7), 2509-2533. https://doi.org/10.1137/090774720

[10] Wang, L. (2018). Microwave Sensors for Breast Cancer Detection. *Sensors, 18*(2), 655. https://doi.org/10.3390/s18020655

[11] von Hippel, A. R. (1954). *Dielectric and Waves*. MIT Press. New York, 284p.

[12] Nikolova, N. (2011). Microwave Imaging for Breast Cancer. *IEEE Microwave Magazine, 12*(7), 78-94. https://doi.org/10.1109/MMM.2011.942702

[13] Sha, L., Ward, E., & Stroy, B. (n.d.). A review of dielectric properties of normal and malignant breast tissue. *Proceedings IEEE SoutheastCon 2002 (Cat. No.02CH37283)*. https://doi.org/10.1109/.2002.995639

[14] Surowiec, A., Stuchly, S., Barr, J., & Swarup, A. (1988). Dielectric properties of breast carcinoma and the surrounding tissues. *IEEE Transactions on Biomedical Engineering, 35*(4), 257-263. https://doi.org/10.1109/10.1374

[15] Campbell, A. M. & Land, D. V. (1992). Dielectric properties of female human breast tissue measured in vitro at 3.2 GHz. *Physics in Medicine and Biology, 37*(1), 193-210. https://doi.org/10.1088/0031-9155/37/1/014

[16] Sudha, T., Divya, G., Sujaritha, J., & Duraimurugan, P. (2017). Revıew of Experımental Desıgn in Analytıcal Chemıstry. *Indo American Journal of Pharmaceutical Research*, 550-565.

[17] Moore, C. H. (1994). Experimental Design in Healthcare. *Quality Management in Healthcare, 2*(2), 11- 26.

[18] Apfel, C. C., Korttila, K., Abdalla, M., Kerger, H., Turan, A., M. D., Vedder, I., Zernak, C., Danner, K., Jokela, R., Pocock, S.J., Trenkler, S., Kredel, M., Biedler, A., Sessler, D. I., & Roewe, N. (2004). A Factorial Trial of Six Interventions for the Prevention of Postoperative Nausea and Vomiting. *The New England Journal of Medicine, 350*(24), 2441-2451. https://doi.org/10.1056/NEJMoa032196

[19] Aslan, I. (2015). Design of Experiment (DOE) Case Studies in Healthcare. *International Review of Social Sciences, 3*(7), 287-303.

Author contact:

Nuşin UNCU, Assistant Prof.
Adana Alparslan Türkeş Science and Technology University,
Department of Industrial Engineering,
Balcalı Mahallesi, Çatalan Caddesi No: 201/1,
01250 Sarıçam-Adana/Turkey
nuncu@atu.edu.tr

Emine AVŞAR AYDIN, Assistant Prof.
Corresponding author
Adana Science and Technology University,
Department of Aeronautics Engineering,
Balcalı Mahallesi, Çatalan Caddesi No: 201/1,
01250 Sarıçam-Adana/Turkey
+90-05318436781
eaydin@atu.edu.tr
rasvaenime@gmail.com

ISSN 1846-6168 (Print), ISSN 1848-5588 (Online)
https://doi.org/10.31803/tg-20180908135420

Original scientific paper

DESIGN AND CONSTRUCTION OF THE PRESSURE SWIRL NOZZLE AND EXPERIMENTAL INVESTIGATION OF SPRAY CHARACTERISTICS

Seyed Hadi SEYEDIN, Majid AHMADI, Seyed Vahid SEYEDIN

Abstract: This paper focuses on the structure and performance of the pressure swirl nozzle and the study of liquid atomization. In this study, the atomizer has been designed and some experiments have been performed on it. Since image processing is an efficient method for measuring the size of the droplet and since it considerably reduces the total measuring time and eliminates the subjective observer's error in sizing and counting spray drops, a digital camera has been used for capturing images and image processing has been done by the MATLAB software. The results show that by increasing the atomization air pressure, the spray angle increases and the droplet's size decreases. It is concluded that the spray angle is a function of the atomization air pressure and orifice diameter. Moreover, when the distance from the spray centre line increases, the droplet's average velocity decreases.

Keywords: atomization; droplet size; image processing; pressure swirl nozzle; spray

1 INTRODUCTION

The prediction of droplet size distributions for atomization nozzles is important for the process design and the improvement of industrial spraying processes [1]. In one of the recent researches, the spray flow structure, droplet Sauter mean diameter, and droplet impingement energy were characterized at predefined axial distances and pressure drops. It was found that the spray cone produced by the pressure swirl nozzles changes from a hollow cone to a full cone as the axial distance increases. The droplet's size initially decreases with the increasing of the axial distance but subsequently increases in the investigated range of the axial distance, while the droplet impinging Weber number decreases monotonously [2]. An experimental study on the spray characteristics, including mass flow rate, spray flux distribution, spray cone angle and drop size spectrum, was conducted. Based on the experimental data, the curves of the flow rate and spray cone angle versus the nozzle pressure drop were obtained. Several typical spray flux distributions were derived and the results indicated that the flux distribution changes significantly even with small pressure changes. Thus, it was proposed that the instability of the spray flux distribution should be considered in the pressurizer [3]. In a new study, the spray cone-angle of the full cone nozzles is measured by the evaluation of images recorded with a camera by using the IMAGE J software. Correlations for the coefficient of discharge, spray cone angle and Sauter mean diameter are suggested on the basis of the experimental results. [4] made an important contribution by making the full linear stability analysis of a helical column of fluid in zero gravity and they successfully compared their prediction with the experimental data collected through high-speed imaging.

The droplet size distribution is one of the most important parameters of spray nozzles. The hollow conical spray is made up of large droplets. According to the experiments, the recirculation zone contains the smallest droplets. In recent researches, the Eulerian model has been developed to model liquid sheet atomization with high Weber and Reynolds numbers. The model considers a single phase of the liquid–gas mixture to represent the turbulent mixing of the liquid sheet with the ambient gas [5]. Various measuring techniques such as laser doppler anemometry (LDA), phase doppler particle analysis (PDPA) and computational fluid dynamic (CFD) have been applied for modelling the turbulent mixing of the liquid sheet with the ambient gas. The size of most spray drops is in the range of (10-1000) microns. The technique of real-time image sensing and processing is the one of the most promising methods to size and count such small drops. By using this technique, one can store real-time images of the spray drops in a computer through a video camera. Subsequently, the stored information can be analysed automatically. The main advantage of the technique is that the measurement and analysis can be performed in a very short time. Furthermore, the subjective human error, which is almost unavoidable in manual sizing and counting, can be eliminated so that it is possible to analyse sprays in various environments by appropriate image processing. Despite these advantages, there are some basic problems related to the system, resolution and light diffraction. On the other hand, this is a rapid and available method in comparison to the LDA and PDPA techniques [6]. In a new paper on a better understanding of the injector performance, the characteristics of the pressure-swirl atomizer were experimentally investigated and data were correlated to the Reynolds numbers (*Re*) [7].

Image processing is not a quantitative method but it can give us a good idea about the spray pattern and droplet size. Nowadays, a high-speed photographic system can be built up by using almost only the conventional devices. A simple set was successfully used to carry out tests on a group of pressure swirl nozzles. The camera does not need to have high speed shutter capabilities. As a matter of fact, even special high-speed shutters enable to "stop" the spray image because of the droplet's velocity stream. The shutter is kept open while the trigger is pressed. The photo is taken in the

darkness or by a black sheet at the back of spray. Moreover, an investigation of spray characteristics such as the liquid breakup length and spray cone angle of a charge-injected electrostatic pressure-swirl nozzle has been conducted. The liquid breakup length decreased, while the spray angle increased with an increase in the applied voltage and injection pressure. An empirical equation to predict the breakup length for the electrostatic pressure-swirl nozzle has been suggested. The experimental result was within the range of the predicted equation [6, 8].The above-mentioned two techniques are deducing the particle size information from the optical signals scattered from an individual particle or a group of particles. In measuring volume, it is assumed that all particles are spheres. Thus, basically, only the spherical particles should be processed with other techniques for accurate measurement. On the other hand, in principle, various non-spherical particles can be processed through the image processing technique because it is based on direct visualization and wide application is possible. Moreover, the measurement accuracy of the image processing techniques is relatively insensitive to the optical properties of the particles in comparison with the other techniques and optical alignment is much easier [9]. In some cases, the simulation program can be used in combination with calculation models to predict the drop size depending on the hollow cone nozzle's geometry and the volume flow for the atomization of Newtonian fluids [10]. In a new paper, the viscous flow through the swirl chamber of a pressure-swirl atomizer has been studied theoretically [11]. Additionally, the thermal effects on the spray cone formation of a pressure swirl nozzle in spray cooling have been investigated experimentally by particle image velocimetry (PIV) [12].

The main purpose of the image processing is to develop a simple appropriate algorithm to size and count the number of spherical spray drops in the image frames, and emphasis was placed on eliminating undesirable objects from the image. Such objects included odd-shaped foreign materials and drops in contact or overlapping and parts of single drops cut off by the image frame boundaries [6]. Therefore, this paper investigates the pressure swirl nozzle property and the application of a new image processing method for determining the droplet size distribution and droplet velocity distribution. The pressure of the liquid and gas mixture is measured in a mixing chamber by a pressure gauge.

1.1 Usage and Performance of Pressure Swirl Nozzle

Pressure-swirl nozzles are used in a broad range of industrial uses, e.g. washing, cooling system, combustion chamber, heavy fuel injection, painting and food processing, etc. Their spray characteristics are approximately linked to the internal flow which predetermines the values of the liquid sheet formed at the outlet and discharge orifice. Pressure-swirl atomizers are easy to make and prepare good atomization. They are frequently used in different applications where a large surface area of droplets is needed or a surface must be coated by a liquid, e.g. combustion, fire suspension or air conditioning. In principle, the pumped liquid is injected via tangential ports into a swirl chamber where it gains a swirl motion, under which it leaves the exit orifice as a conical liquid sheet which consequently breaks up into small droplets due to aerodynamic forces. The centrifugal motion of the swirling liquid makes a low-pressure area in the swirl chamber centre and generates an air core along the centreline. The flow pattern inside the atomizer is rather complex; it is a two-phase flow with secondary flow effects. There is a strong link between the resulting spray characteristics and internal flow conditions; however, not all aspects of the internal flow are well realized [16]. Moreover, the pressure swirl and air-blast atomizers are the two types of atomizers used in gas-turbine engines [17]. In recent years, some researchers studied the characteristics of atomization for pressure-swirl atomizers of two various geometries. The important effect of atomizer construction on the atomization process has been observed. Furthermore, a guided experimental study reported that they aimed to intensify the process of atomization and improve the properties of the spray [18].

2 ATOMIZER DESIGN AND CONSTRUCTION

The two phases of atomizing including the following stages and different sections of the atomizer have been shown in Fig. 1.

(1) Primary mixing of liquid and gas in the distributer
(2) Secondary mixing in the mixing chamber
(3) Severe mixing in the spiral tube
(4) Liquid film formation in the cone cap
(5) Final atomization in the output of the nozzle tip.

Section (1) consists of two concentric tubes. Along the internal tube, there are some holes to mix the liquid feed and atomizer gas. The liquid feed (water or vacuum gasoil) and the atomizer gas (air or steam) enter into the internal tube and annular space, respectively, and mix together through the holes existing on the internal tube. Then, the two-phase mixture enters the section (3) which consists of a cylindrical spiral surrounded by a connecting tube. This spiral produces a homogeneous mixture by circulatory movement and hard mixing at the opening of the orifice. Thus, the homogeneous mixture is atomized to a hollow conical spray after passing the circular orifice. The orifice size and design have a main role in the droplet size and droplet velocity at the nozzle outlet. The parameters for the design of the pressure swirl atomizer and operational variables are summarized in Tab. 1.

Table 1 Summary of the design parameters for the pressure swirl nozzle.

Design data	Spray Angle 60°
Length of the distribution tube	0.14 m
Number of holes in the distribution tube	15
Holes diameter	0.00075 m
Length of the connecting tube	0.8 m
Length of spiral	0.8 m
Orifice shape	conical
Cone angle	60o
Orifice hole diameter	0.001 m
Orifice hole depth	0.005 m
Pressure of mixture	2 bar
Maximum liquid flow rate	6.5 L/h
Maximum gas flow rate	205 L/h

The schematic drawing of the pressure swirl nozzle and its design characteristics are shown in Fig. 1. Here the pressure swirl atomizer is designed for gas oil having the maximum flow rate of 6.5 L/s, the average injection pressure of 2.5 bar and a half spray cone angle of 30°, and the material is made from stainless steel for the prevention of corrosion.

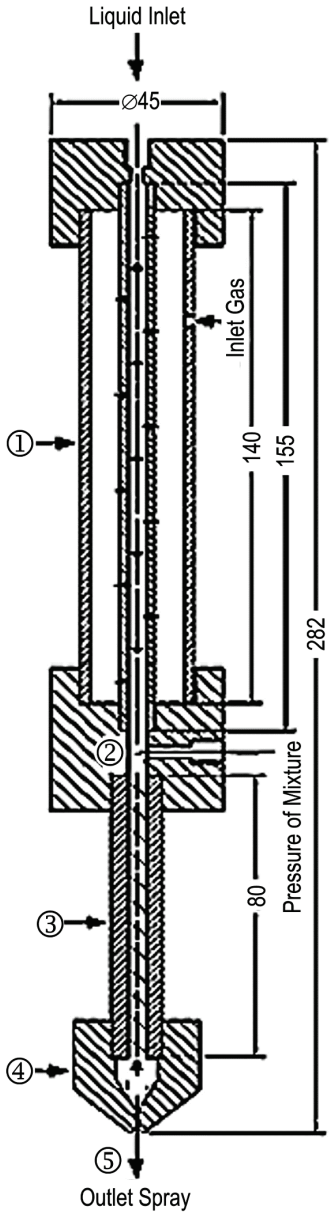

Figure 1 The schematic drawing of the pressure swirl nozzle (1) Distributer tube (2) Mixing chamber (3) Spiral part (4) Nozzle conical cap (5) Nozzle orifice

3 THE EXPERIMENTAL SET-UP

The experimental set-up is shown in Fig. 2 .The air with high pressure exits from the compressor, passes through the tube and enters into the liquid pressure vessel. In Fig. 2, the schematic images of various equipment used in the pressure swirl nozzle's performance analysis are shown.

When the sprayed stream exits the nozzle orifice, the images of produced droplets are captured by a digital camera. After the investigation and modification of images, they are processed by a R2014a version of the MAT LAB software.

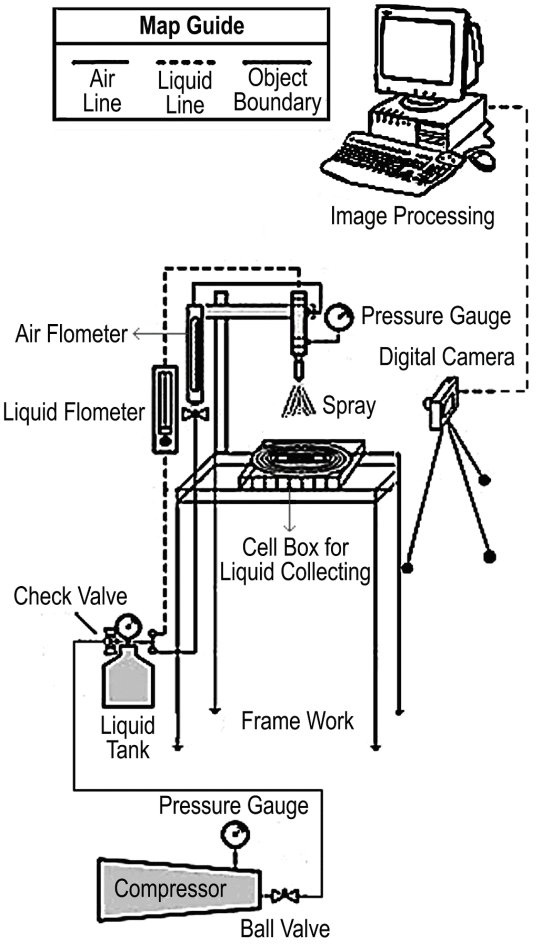

Figure 2 The schematic representation of the pressure swirl nozzle and the performance analysis system

4 PHOTOGRAPHY AND IMAGE PROCESSING METHOD

In this study, a digital camera is used. Furthermore, for the sharper spray image, a black plastic retain is used at the back of the nozzle. This part is useful for visualizing the transparent spray droplets.

Before image processing, the following steps for image preparing must be conducted:

1) Shooting (taking a photograph) from the nozzle spray
2) Preparing and modifying the image for better resolution
3) Checking images and obtaining the necessary information.

The schematic image of spray droplets after photography is shown in Fig. 3

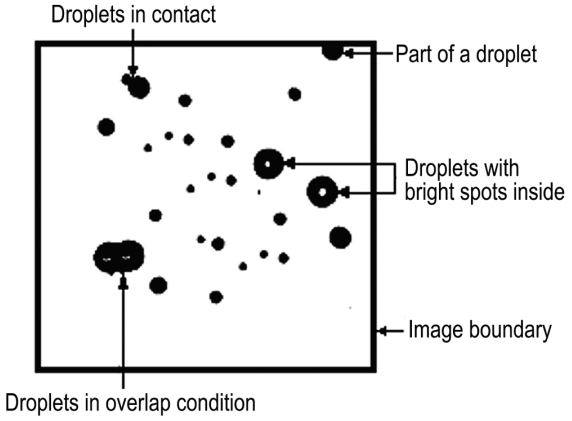

Figure 3 The model image of spray droplets containing undesirable objects

4.1 Calculation of the Mean Droplet Velocity (MDV)

For calculating MDV, the first shooting from the spray by means of a high speed camera (Casio Exilim-1200 frame per second) was done. Film or video frames were then extracted by a computer. After this step, the movement of droplets from one frame to the next one was computed based on the pixel unit and it was converted to the metric unit. Droplet displacement value was then divided by time (seconds) to calculate the velocity droplet by using the Eq. (1):

$$V = \frac{x_2 - x_1}{pix \times 100} \times 1200 \text{ m/s} \quad (1)$$

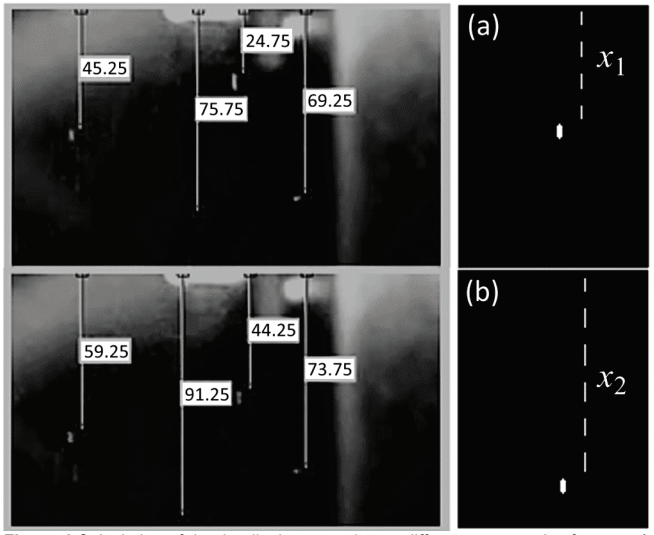

Figure 4 Calculation of droplet displacement in two different consecutive frames: a) Previous frame. b) Next frame, captured by Casio Exilim Pro EX-F1 high speed digital camera, 6.0 MP, 1200 fps

In Eq. (1), x is the droplet distance that transfers based on the pixel in the digital image. The *pix* is the number of pixels that is equivalent to 1 cm and this formula is divided by 100 for converting to the meter unit (SI). They are calculated by the MATLAB image processing toolbox based on the pixel unit. It takes the time of 1/1200 second for the droplet to move from one frame to another frame; therefore, the equation is multiplied by 1200. To our knowledge, velocity is displacement divided by time (meter per second, here Δt = 1/1200 and $\Delta x = x_2 - x_1$). Moreover, the mean velocity of droplets is calculated by the average velocity of droplets, in each area of the frame. Droplet displacement in two consecutive frames for measuring velocity is shown in Fig. 4.

4.2 Calculation of the Mean Droplet Size (MDS)

The high quality digital images were captured from the spray for MDS calculation. The original images were converted to black and white (BW) images. Each white colour has a pixel value equal to 1 and each black colour has the pixel value equal to 0 (i.e., an image includes the 0 and 1 matrix). The droplet shape is assumed to be elliptic. Therefore, by having the area of (A) and ellipse eccentricity of (e) for a droplet in a black and white image, the diameter of the droplet is calculated by using the MATLAB software and image processing toolbox. The droplet is more spherical in shape as the parameter of (e) approaches to 1.

$$A = \pi ab \,, \quad e = \sqrt{1 - \left(\frac{b}{a}\right)^2} \quad (2)$$

In Eq. (2), a and b are half of the large and small diameters of the oval object. The droplet shape is shown in Fig. 5, and it is near the elliptic shape.

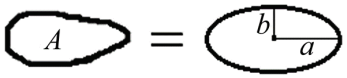

Figure 5 Droplet surface is approximately equivalent to the oval area

In Fig. 6, two models of connectivity for calculating the droplet size by means of the image processing method has been presented. The droplets are white and the image background has the black colour (BW image). The 0 and 1 matrix for image processing is presented in Fig. 6 (SE is the structure element in MATLAB).

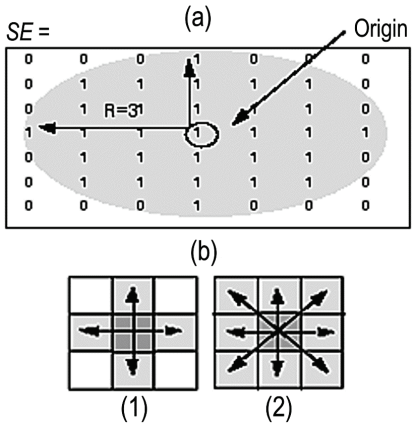

Figure 6 (a) The 0 and 1 matrix of the BW image. (b) Two types of pixels' connectivity in the MATLAB Software for image processing, 4th and 8th connectivity [14]

The initial image includes RGB image and grey levels (between 0 and 1) must be converted to the BW image. Each image must be bmp (2D format) before processing. Therefore, there is a matrix from the image including 0 and 1. Non-isolated droplets (i.e. droplets in overlap condition, or droplets in contact) are all eliminated and the holes (empty spaces) of drops are filled by the same pixels.

For segregation or better separation of pixels and proper image investigation, the Sobel function in MATLAB is used. In Fig. 7, the Sobel modification method for accurate analysis is shown. After this step, the image processing operation starts and the information is derived.

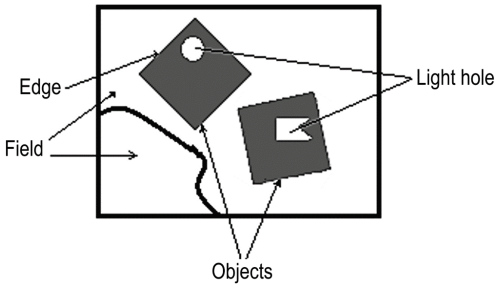

Figure 7 Image for displaying the Sobel method performance

The Sobel method is a linear algorithm of edge detecting, which determines the boundaries of the light and dark points of an image. The Sobel command is used in MATLAB as a function for image processing. The change in pixel gradients of an image is applied by the Sobel method for a complete separation of BW pixels before processing. In Fig. 8, different stages for preparing image (before processing) are shown. The main image changed into BW and the Sobel method is applied to separate the boundary between the dark and light spots in an image for better processing and more accurate results.

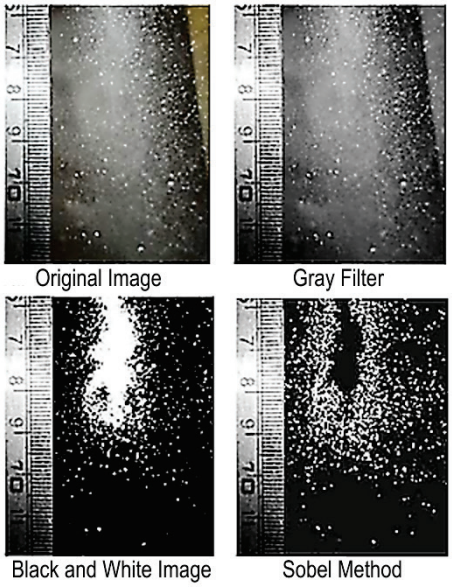

Figure 8 Better separation of a droplet in a BW image by the Sobel method

Thus, the length and width of the centre of each drop are derived from Eq. (3).

$$X = \frac{\sum_{i=1}^{n} x_i}{n},\ Y = \frac{\sum_{i=1}^{n} y_i}{n} \tag{3}$$

Where x_i and y_i are the length and width of the droplet pixels, respectively. n is number of pixels that include the droplet.

4.3 Determination of the Spray Angle

The number of pixels in the longitudinal and cross directions of spray cone should be measured. The spray angle was calculated by the MATLAB image processing toolbox (Fig. 9).

In Fig. 9, θ is the angle between the spray centre line and the external edge of the spray cone which represents the half spray cone angle, and it is calculated by the Eq. (4).

$$\theta = 2\arctan\left(\frac{a}{b}\right) \tag{4}$$

The spray angle, θ, depends on the air pressure and air flow rate. In dilute solutions, the air flow rate influence is more dominant than that of the liquid. Because the shear forces from the air flow are exerted on the liquid sheet in the nozzle head, where the mixture of air and liquid is spread out from the nozzle orifice, it atomizes into small droplets.

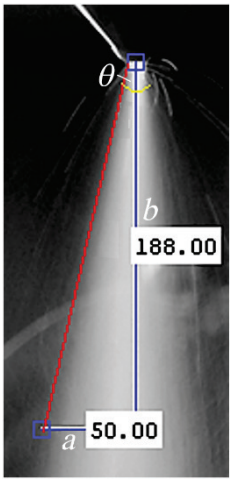

Figure 9 Determination of the spray angle by the MATLAB Image Processing toolbox. Longitudinal and cross distances from the spray centre are shown in the pixel unit.

The programming algorithm for image processing is shown in Fig. 10.

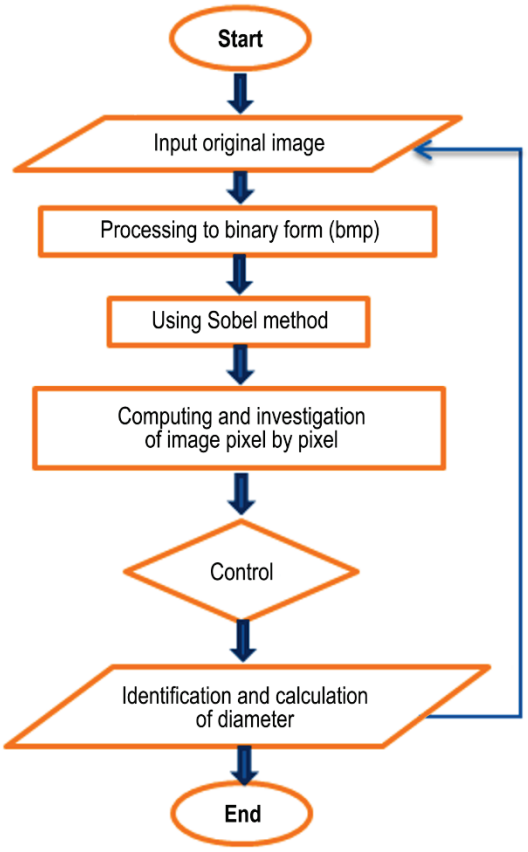

Figure 10 Flowchart for pattern recognition

5 RESULTS AND DISCUSSION

The droplet size and velocity distribution was obtained in different distances from the nozzle tip (8, 14 and 20 cm, respectively) through the cylindrical space beneath the nozzle orifice. The experimental values related to image processing will be discussed. Fig. 11 represents the radial evolution of the mean diameter at different distances from the tip of the nozzle.

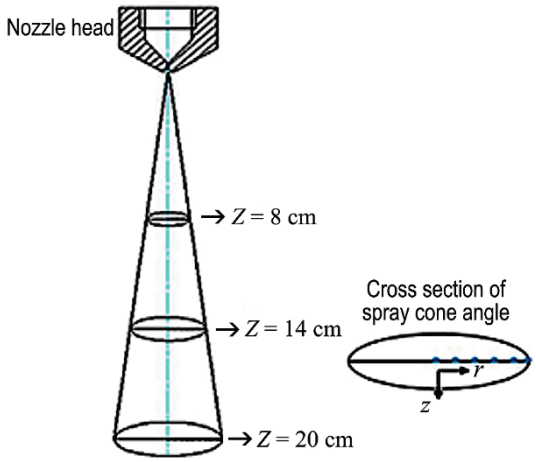

Figure 11 The sketch of the droplet position in each cross section of the spray.

The mean diameter of droplets at each point in the spray cross-section is calculated by the Eq. (5).

$$D_{10} = D_{\text{mean}} = \frac{\sum_0^i D_i}{N_i} \tag{5}$$

In which i is the measured point in the spray's cross-section, D_i is the sample diameter in each point of surface and N_i is the total number of sampled droplets in the spray area. The measurements gave a minimum droplet size at the spray axis and an increase of size towards the edges of the spray. Fig. 12 presents the experimental measurements by the image processing method in different distances. The droplets near to the central axis of the spray for the axial distance from the nozzle tip were very small. A possible reason could be the difficulty of measuring the smaller droplets with the image processing method. Moreover, in this method, the over-estimation of the mean diameter in the edge of the spray is observed. Fig. 12 shows that the calculated mean diameter increases regularly when increasing the distance from the tip of the spray nozzle and the experimental spacemen. Measurements also show a rising trend at the distance of 8 cm.

5.1 Results of the Mean Droplet Diameter

The droplet's mean diameter was calculated by the image processing method and the results are compared and presented in Fig. 13 and Tab. 2. It is concluded that the applied camera apparatus can measure the values of the mean diameter at threshold locations with difficulty (centre and edge) of the spray at this distance (8 cm). At the distances of 14 cm and 20 cm from the nozzle tip, the dispersion of the droplet's diameter is increased by increasing the radial position due to the vortex flow of the surrounding air (Fig. 12).

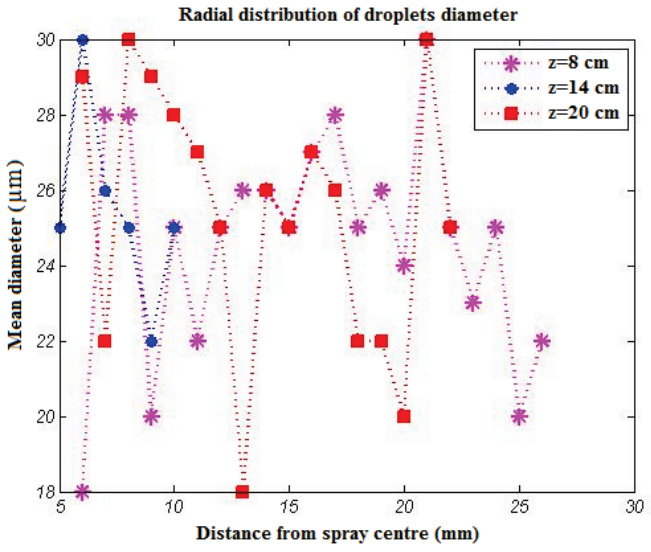

Figure 12 Droplet mean diameter in the radial coordinate, in different distances from the nozzle tip.

The experimental results for the mean diameter of the droplets are shown in Tab. 2. Moreover, Fig. 12 shows that as the spray cone section is set farther from the nozzle orifice,

the droplet mean diameter has some fluctuations in the droplet size.

Table 2 The mean diameter of the droplets in different distances from the nozzle tip

Distance (cm)	Mean Diameter (μm)
8	25.02
14	24.5
20	26.09

5.2 The Results of the Mean Droplet's Velocity

Due to the existence of air-cored vortex in the pressure swirl atomizer, the droplet number concentration is high at the region near the axis of the spray. Fig. 13 shows the radial distribution of the droplet mean velocity. At the centre of the spray cone, the droplet velocity is high and reduces towards the edge of the spray. A relatively uniform velocity distribution of droplets in the spray is observed. At the axial distance of 8 cm, the calculated mean velocity of the droplets at the centre is larger than the measured results at the edge of the spray. This is due to the over-estimation of the mean diameter which is depicted in Fig. 13. At the axial distance of 20 cm, the calculated mean velocity of the droplets at the centre of the spray is smaller than the measured results. This might be because of the uncertainty associated with the model implemented within the experimental results which may have out layer points. The mean velocity of droplets at each interval in the spray cross-section is calculated by the Eq. (6).

$$V_{\text{Avg}} = \frac{\sum_{i=1}^{N} v_i}{N} \tag{6}$$

The v_i is the droplet velocity, N is the number of droplets and V_{Avg} is the mean velocity in each area of the spray.

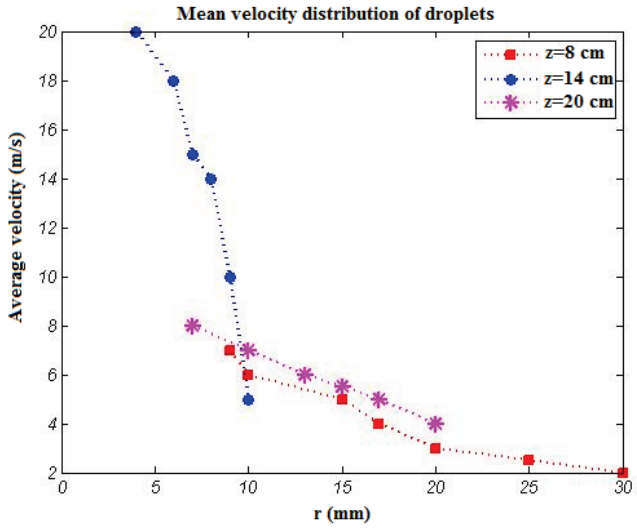

Figure 13 Droplet mean velocity distribution in the redial coordinate in various distances from the nozzle tip

The experimental results are based on the mean velocity at each section and are shown in Tab. 3 and Fig. 13. The results show that as the spray cone section is set farther from the nozzle orifice, the droplet mean velocity decreases. The liquid flow in the orifice centre is fast and near the orifice walls, and it decreases due to the wall effects. As a result of the mean droplet velocity, this velocity decreases. In the spray cone centre line, the velocity reaches the maximum. Since the spray jet is in the straight trajectory and away from the spray cone centre, the spray stream angle causes the droplets' movement in more distances than the one of a straight line and the mean droplet velocity decreases.

Table 3 The mean velocity of the droplets in different distances from the nozzle tip

Distance (cm)	Mean Velocity (m/s)
8	14.9
14	6.9
20	5.05

5.3 Calculation Number Density as Radial Distribution

Fig. 14 shows the predicted number density of the droplets at each cross-section. The number density distributions are defined by dividing the number of the droplets in each interval by the total number of droplets accommodated on the circle radius of the cone section. The number density is the percentage of the droplets' number to the whole number, in different intervals. It is considerable that the number of drops is more at the area near the spray centre, rather than other points, and is an indicator of the swirl motion of air-liquid mixture, which is counted as a feature of the nozzle. Moreover, at intervals of 14 and 20 cm, the distance of droplets increases from the spray cone centre and the number of drops reduces at that area, which is why the number density reduces as well.

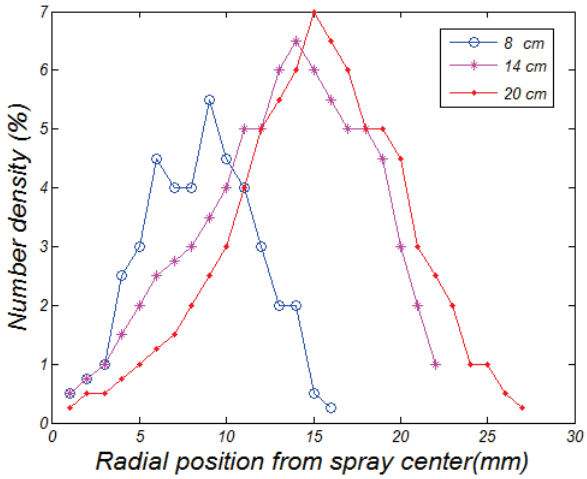

Figure 14 Radial distribution of the number density at different zones of the nozzle's output - image processing

In the distances of 14 and 20 cm, the number of drops on that surface is reduced and consequently the number density is reduced, i.e. the pressure swirl nozzle has a hollow cone spray pattern.

5.4 Air Pressure Changes and their Effect on the Pressure Swirl Nozzle

Fig. 15 shows the changes in the spray angle versus the air pressure for the pressure swirl nozzle system. The average value of the spray angle for this nozzle is about 41 degrees, for Lacava et al., it is 27 degrees and for Digvijay et al., it is 32 degrees. The percentages of the relative difference of the spray angle in this research in comparison with these two works (Lacava and Digvijay) are 33% and 21%, respectively [15, 16].

The reason behind this difference is the different structure of nozzles, equipment type and experiment operational conditions.

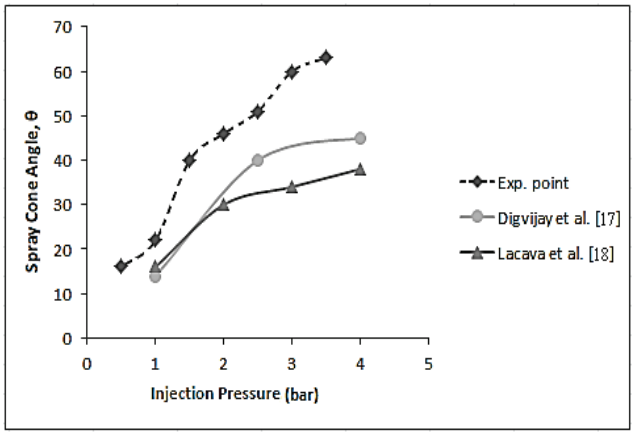

Figure 15 Effect of injection pressure on the spray cone angle

In this section, a simple experimental correlation is provided for determining the angle of the nozzle spray according to the curve in Fig. 15. Eq. (7) is used for determining the spray angle in pressure-swirl nozzles.

$$\theta = 1.1439\, p^{0.7058}\, d_0^{-0.452} \tag{7}$$

In this equation, pressure is in the bar and orifice diameter of the nozzle's head and it is measured in meters. The Reynolds number value was bigger than 2300, and the flow was fully turbulent. This equation follows the power law and it has been computed as the data fitting program by the MATLAB software and it is better to use it for low viscosity liquids and turbulent flows. The novelty of this work is the use of the precision digital camera and the image processing method for calculating the spray characteristic, which is an available, fast and inexpensive way and also an effective method for academic research work.

6 CONCLUSIONS

In this research, it was shown that the vortex flow of the surrounding air is responsible for the droplet size scattering near the edge of the spray. By increasing the distance of the droplets from the centre of the spray cone, the velocity of the output drops decreases due to the friction effect near the wall of the nozzle's orifice. The same results were obtained by increasing the distance from the nozzle's head. The average velocity of drops is reduced gradually by increasing the air pressure. By means of decreasing the droplet velocity, the number of collision is reduced and the average number of drops from the centre to the edges of the spray cone increases gently. Furthermore, near the edge of the spray cone, the drops' size varies as a result of the existing produced vortex in the surrounding air of the jet spray, resulting in the drop size distribution. The advantage of the image processing method is that it is cheap and available. The accuracy and quality of the images is related to the environmental conditions such as light and digital camera. The results showed that by increasing the atomization air pressure, the spray angle increases and it is predicted that the droplet size decreases because of an increase in droplet velocity and more collision of the droplets with each other and the orifice wall at the outlet of the nozzle. It is found that the spray angle is a function of air pressure and the orifice diameter of the nozzle's head. Moreover, by increasing the distance from the spray centre, the droplets' average velocity decreases because the outlet droplets' contact the edges of the nozzle orifice and air friction factor decrease their velocity.

Acknowledgement

The authors would like to thank Masoud Kambarani and Seyed Hasan Alhoseini for their assistance and guidance with the experimental set up and their contributions to the research.

Nomenclatures

V Velocity (m/s)
Pix Number of pixels equivalent to 1 cm
X Distance by the pixel unit (Pixels)
A Area (m^2)
a Half of a large diameter in oval
b Half of a small diameter in oval
n Number of pixels
x Length of drops based on the pixel
y Width of drops based on the pixel
θ Spray angle (Degree)
p Air pressure (bar)
d_0 Orifice diameter (mm)
D_{10} Mean diameter (μm)
N Number of droplets

7 REFERENCES

[1] Renze, P., Heinen, K., & Schönherr, M. (2011). Experimental and numerical investigation of pressure swirl atomizers. *Chemical Engineering & Technology*, *34*(7), 1191-1198. https://doi.org/10.1002/ceat.201100054

[2] Xie, J. L., Gan, Z. W., Duan, F., Wong, T. N., Yu, S. C. M., & Zhao, R. (2013). Characterization of spray atomization and heat transfer of pressure swirl nozzles. *International Journal of Thermal Sciences*, *68*, 94-102. https://doi.org/10.1016/j.ijthermalsci.2012.12.015

[3] Lan, Z., Zhu, D., Tian, W., Su, G., & Qiu, S. (2014). Experimental study on spray characteristics of pressure-swirl

nozzles in pressurizer. *Annals of Nuclear Energy*, *63*, 215-227. https://doi.org/10.1016/j.anucene.2013.07.048

[4] Jain, M., John, B., Iyer, K. N., & Prabhu, S. V. (2014). Characterization of the full cone pressure swirl spray nozzles for the nuclear reactor containment spray system. *Nuclear Engineering and Design*, *273*, 131-142. https://doi.org/10.1016/j.nucengdes.2014.02.025

[5] Belhadef, A., Vallet, A., Amielh, M., & Anselmet, F. (2012). Pressure-swirl atomization: Modeling and experimental approaches. *International Journal of Multiphase Flow*, *39*, 13-20. https://doi.org/10.1016/j.ijmultiphaseflow.2011.09.009

[6] Kim, H. H., Ogata, A., & Kim, J. H. (2009, June). High speed camera observation of electrospray. In *Electrostatics Joint Conf., Boston, MA*. https://doi.org/10.1016/j.jaerosci.2011.01.007

[7] Lee, E. J., Oh, S. Y., Kim, H. Y., James, S. C., & Yoon, S. S. (2010). Measuring air core characteristics of a pressure-swirl atomizer via a transparent acrylic nozzle at various Reynolds numbers. *Experimental thermal and fluid science*, *34*(8), 1475-1483. https://doi.org/10.1016/j.expthermflusci.2010.07.010

[8] Laryea, G. N., & No, S. Y. (2004). Spray angle and breakup length of charge-injected electrostatic pressure-swirl nozzle. *Journal of Electrostatics*, *60*(1), 37-47. https://doi.org/10.1016/j.elstat.2003.11.001

[9] Jiang, Y., Jeon, H. Y., Tian, L., & Bode, L. E. (2010). Measuring particle size distribution using LED-illumination. *International Journal of Multiphase Flow*, *36*(3), 193-201. https://doi.org/10.1016/j.ijmultiphaseflow.2009.11.004

[10] Nonnenmacher, S. & Piesche, M. (2000). Design of hollow cone pressure swirl nozzles to atomize Newtonian fluids. *Chemical Engineering Science*, *55*(19), 4339-4348. https://doi.org/10.1016/S0009-2509(00)00043-9

[11] Wimmer, E. & Brenn, G. (2013). Viscous flow through the swirl chamber of a pressure-swirl atomizer. *International Journal of Multiphase Flow*, *53*, 100-113. https://doi.org/10.1016/j.ijmultiphaseflow.2013.02.003

[12] Xie, J. L., Gan, Z. W., Wong, T. N., Duan, F., Yu, S. C. M., & Wu, Y. H. (2014). Thermal effects on a pressure swirl nozzle in spray cooling. *International Journal of Heat and Mass Transfer*, *73*, 130-140. https://doi.org/10.1016/j.ijheatmasstransfer.2014.01.077

[13] www.mathworks.com, MATLAB software Help. Version R2014b. Developed by Mathworks Co.

[14] Kulshreshtha, D. B., Dikshit, S., & Channiwala, S. A. (2011). Experimental investigations of air assisted pressure swirl atomizer. *Indian Journal of Science and Technology, 4*(2), 126-130. https://doi.or/10.17485/ijst/2011/v4i2/29947

[15] Sapee, S. (2015). Computational Fluid Dynamics Study on Droplet Size of Kerosene Fuel. *Journal of Advanced Research in Fluid Mechanics and Thermal Sciences, 16*, 1-14.

[16] Malý, M., Sapík, M., Jedelský, J., Janáčková, L., Jícha, M., Sláma, J., & Wigley, G. (2018). Internal flow characteristics in scaled pressure-swirl atomizer. In *EPJ Web of Conferences, 180*, p. 02059. EDP Sciences. https://doi.org/10.1051/epjconf/201818002059

[17] Garai, A., Pal, S., Mondal, S., Ghosh, S., Sen, S., & Mukhopadhyay, A. (2017). Experimental investigation of spray characteristics of kerosene and ethanol-blended kerosene using a gas turbine hybrid atomizer. *Sādhanā, 42*(4), 543-555. https://doi.org/10.1007/978-981-10-7449-3_9

[18] Maly, M., Jedelsky, J., Slama, J., Janackova, L., Sapík, M., Wigley, G., & Jicha, M. (2018). Internal flow and air core dynamics in Simplex and Spill-return pressure-swirl atomizers. *International Journal of Heat and Mass Transfer*, *123*, 805-814. https://doi.org/10.1016/j.ijheatmasstransfer.2018.02.090

Authors' contacts:

Seyed Hadi SEYEDIN
Department of Chemical Engineering,
Science and Research Branch,
Islamic Azad University,
Daneshgah Blvd, Simon Bulivar Blvd, Tehran, Iran

Majid AHMADI
Corresponding author
Department of Mechanical Engineering,
Science and Research Branch,
Islamic Azad University,
Daneshgah Blvd, Simon Bulivar Blvd, Tehran, Iran
majidahmadi.iau@iran.ir

Seyed Vahid SEYEDIN
Department of Software Engineering,
Tehran South Branch,
Islamic Azad University,
Azarshahr Street, North Iranshahr Street,
Karimkhan-e-Zand Avenue, Tehran, Iran

ISSN 1846-6168 (Print), ISSN 1848-5588 (Online)
https://doi.org/10.31803/tg-20190513114458

Original scientific paper

CUTTING PERFORMANCE OF DEEP CRYOGENIC TREATED AND NITRIDED HSS CUTTING TOOL INSERTS

Sanja ŠOLIĆ, Zdravko SCHAUPERL, Vlado TROPŠA

Abstract: High speed steel (HSS) is a very important industrial tool material and has been constantly improved for different wear resistance applications and cutting tools, i.e. drills, milling cutters, hobs and for the cutting tools in which the economical cutting speed is too low for choosing the carbide tools. The properties of HSS depend significantly on the parameters of the conducted heat treatment. In this paper, the influence of deep cryogenic treatment in combination with nitriding of metallurgical powder metallurgy HSS on the wear resistance was measured. Additionally, the cutting performance in a single point cutting tool machinability test at the configuration of the dry low-speed turning of steel was investigated. The results showed that deep cryogenic treatment itself, and in combination with nitriding, resulted in the reduction of the wear rate. The results of the single point cutting tool machinability test showed that deep cryogenic treated and nitrided HSS inserts performed worse than the classically heat-treated inserts and deep cryogenic treated HSS inserts exhibited approximately the same flank wear as the nitrided ones.

Keywords: deep cryogenic treatment; cutting tools; high speed steel; nitriding; wear resistance

1 INTRODUCTION

High speed steel (HSS) is a very important industrial tool material and has been constantly improved for different wear resistance applications and cutting tools, i.e. drills, milling cutters, hobs and for the cutting tools in which economical cutting speed is too low for choosing the carbide tools. When cutting, the tool moves through the material of the workpiece by removing the chip from its surface. The tribological conditions that appear in the contact between these two surfaces in mutual motion are very demanding. The contact temperature of steel machining can range from 900 °C to 1300 °C [1-3]. According to Holmberg et al. [1], 80% of the heat produced in the machining process is caused by the mechanical deformation of the chip, 18% by friction between the chip and the upper surface of the tool and only 2% is created on the tool tip. Of the heat eliminated, about 75% is eliminated by the chip, 5% is absorbed by the workpiece and 20% is conducted through the tool, but note that these values change depending on the processing conditions, mostly speed and feed. Generally, there are four main mechanisms of tool wear that are present in metal cutting tools, namely abrasive wear, adhesive wear, delamination wear and wear due to chemical instability, including diffusion, solution and electrochemical wear [2, 3].

Abrasive wear takes place on tool surface and is caused by hard particles, usually carbides, oxides and some silicates in the work material, and it is responsible for the tool flank face wear. Abrasive wear appears in the same amount regardless of the cutting speed and cutting temperature. The adhesive wear of cutting tools is the result of the formation of micro-welded joints between the chip and the tool face and the breaking of joints by the shearing force which tears out particles of tool material and adheres it to the chip or the workpiece. Adhesive wear occurs in low cutting speeds at the flank face of the tool when contact temperatures are not very high. Delamination wear occurs when HSS tools soften due to annealing during machining. It is the result of the plastic deformation of the surface which leads to subsurface crack nucleation, propagation and fallout of wear particles from the tool surface. Wear due to chemical instability occurs with high cutting speeds and high cutting temperatures [2].

The properties of high-speed steels depend significantly on the parameters of conducted heat treatment [4].

Authors in [5] reported that using different heat treatment parameters with different additional heat treatment and thermo-chemical processes increases tool steel properties and its wear resistance and can be adjusted for specific application. The application of deep cryogenic treatment (DCT) in the heat treatment of high speed steel tools has resulted in increased wear resistance and dimensional stability of the treated material [6, 7]. Combining DCT with various austenitization temperatures results in a different volume of retained austenite which affects the hardness and fracture toughness [8, 9] of certain tools, but it can also affect the enhancement in wear resistance regardless of the hardness [10, 11].

In the recent years, numerous authors have studied the influence of deep cryogenic treatment on a variety of HSS and tool steel properties. Authors in [8] compared the wear behaviour of a vacuum heat treated and the deep cryogenic treated at −196 °C ESR AISI M2 HSS in combination with four different tempering temperatures. The presented results showed that in general, DCT samples had better wear resistance compared to the vacuum heat treated samples with improvement in their fracture toughens and hardness. Authors in their review [12] concludes that the improvement gained by DCT is mainly due to the complete elimination of the retained austenite and the formation of nanometre sized carbides dispersed in the tempered martensitic structure. Authors [13] investigated the influence of different heat treatment parameters (austenitizing temperature, cooling rate, holding time, heating rate, and tempering temperature) which all directly influence the effect of DCT on tool steel

properties. The results showed that the most significant parameters in terms of mechanical properties are austenitizing and tempering temperatures. A low austenitizing temperature combined with a high tempering temperature improves fracture toughness, bending strength and elongation, while the high austenitizing and low tempering temperatures improve hardness and wear behaviour.

Authors in [14] analysed the influence of DCT with different austenitizing and tempering temperatures on fracture toughness, hardness and wear resistance of PM lower C, high W and Co cold work tool steel, high C and V PM cold work tool steel and PM HSS. They reported that in the case of low carbon cold-work tool steel, the DCT results greatly improved in fracture toughness, while maintaining high hardness, which can be linked to the formation of finer needles such as martensite and martensitic transformation accompanied by plastic deformation of the primary martensite. On the other hand, for high C cold-work tool steel, the DCT has a negative effect, while for high-speed steel, the DCT has virtually no impact on its properties. They also reported an alteration in fracture toughness/Rockwell hardness ratio which affects wear resistance of cold-work tool steel. It was concluded, however, that hardness is still a major parameter affecting abrasive wear resistance.

The application of DCT to HSS cutting tools has been enhanced in the recent years due to its effect in the prolonging of tool life, dimension stability and stress relief. Authors in [15] reported that the M2 HSS twist drills tool life increased for approximately 280 % when drilling steel, taking the total failure of tools as a criterion for determining the tool service life. Authors in [16] reported a 77 % and 126 % improvement tool life of DCT and tempered M2 tool steel drills.

Authors in [17] investigated the combined impact of the cryogenic temperature with tempering on the mechanical properties and wear resistance of the W9 HSS. They concluded that all varieties of DCT influenced the wear resistance and hardness of W9 HSS. The performance of the W9 HSS taps during the tapping test was not notably influenced by the DCT temperature. It was shown that tool life was the longest when treated in the temperature range of −196 to −160 °C with subsequent tempering, and it was concluded that for treatment effectiveness and cost efficiency, the deep cryogenic treatment at −160 °C could be the optimal choice.

Authors [5] investigated the impact of different time and temperature DCT parameters and the combination of DCT and plasma nitriding on the wear performance of powder–metallurgy HSS considering the wear resistance and resistance to galling under dry sliding conditions. They concluded that DCT improves the microstructure of PM HSS generating the finer needle-like martensitic structure, which results in higher hardness and better wear resistance properties, especially considering friction, and galling resistance against stainless steel which considerably improves with longer cryogenic treatment times. They also concluded that plasma nitriding improves tribological properties of PM HSS and reduces the effect of austenitizing temperature, but the results indicated that if combined with DCT, it could eliminate the advantageous influence of deep-cryogenic treatment.

It is clear that an optimized combination of cryogenic treatment temperature and time, cooling rate, and subsequent tempering would make the best of sub-zero treatment while balancing the cost and performance of the material.

The purpose of this paper is to study the influence of deep cryogenic treatment, in combination with nitriding, of powder metallurgy high speed steel on the wear resistance and cutting performance in a single point cutting tool machinability test at the configuration of the dry low-speed turning of steel.

2 MATERIALS AND METHODS

The material used in this study was a high speed steel produced by powder metallurgy, grade PM S390 MC. The chemical composition of steel is presented in Tab. 1.

Table 1 Chemical composition of the PM S390 MC high speed steel

% C	% Si	% Mn	% Cr	% Mo	% V	% W	% Co	% Fe
1.64	0.60	0.30	4.80	2.00	4.80	10.40	8.00	rest

For wear resistance-testing, disc shaped samples were prepared with the dimensions of ∅22×4 mm. For the purpose of a single point cutting tool machinability test or turning test, 20 cutting tool inserts were prepared according to the ISO 13399, CNMA 120408, Fig. 1, with the dimensions shown in Tab. 2.

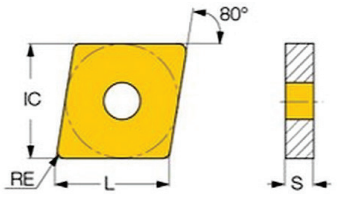

Figure 1 Insert CNMA 120408 [18]

Table 2 CNMA 120408 insert dimensions

Grade	*L*, mm	*IC*, mm	*S*, mm	*RE*, mm
CNMA 120408	12.9	12.7	4.76	0.8

The heat treatment was performed in an Ipsen vacuum furnace with the preheating parameters 650 °C / 30 min, 850 °C / 20 min, 1050 °C / 15 min before the heating to the austenitization temperature. The heating rate to the austenitization temperature of 1130 °C was 5 °C/min and the austenitization lasted 6 min, after what samples were quenched in the nitrogen flow, p = 1050 mbar. The heat treatment parameters are presented in Tab. 3.

Table 3 Heat treatment parameters

Batch	Austenitization, °C/min	Deep cryogenic treatment, °C/h	Tempering, °C/h	Nitriding, °C/h
HT	1130 / 6 min	-	520 / 520 / 490 / 2 h	
HTN	1130 / 6 min	-	520 / 520 / 490 / 2 h	490 / 2.5 h
DCT	1130 / 6 min	−196 °C / 24 h	520 / 2 h	
DCTN	1130 / 6 min	−196 °C / 24 h	520 / 2 h	490 / 2.5 h

After quenching, part of the test samples were soaked in liquid nitrogen at a controlled speed and left for 24 h, followed by single tempering. Other samples were tempered three times. Part of the vacuum and deep cryogenic treated samples were plasma nitrided (95% H_2 and 5% N_2). Nitriding in the duration of 2.5 hours was carried out at a temperature of 490 °C in a Metalplas Ionon BDAG GRUPPE BALCKE-DÜRR AG apparatus. After heat treatment, thorough analysis of the microstructure and mechanical properties was performed on samples and the results were published in [19].

Wear resistance of specimens was determined by simulating two-body abrasive wear by alternating the sliding motion by using ball-on-flat contact with the Al_2O_3 ball as a counter-body with a hardness of 1200 HV and a diameter of ∅10 mm. Wear tests were performed under dry sliding conditions at an average sliding speed of 0.024 m/s with a frequency of 5 Hz and amplitude of 2.4 mm, maximum contact pressure of 1300 MPa (F_N = 10 N) and total sliding distance of 30 m, Fig. 2. Test results were evaluated in terms of the samples' wear rate (mm^3/Nm) and average coefficient of friction. Testing was performed at room temperature (22 °C) and relative humidity of 40 %.

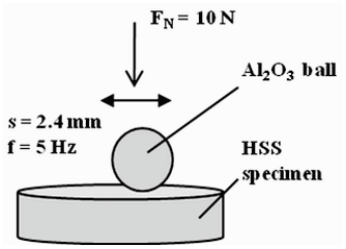

Figure 2 Schematic diagram of ball-on-flat wear test

The single point cutting tool machinability test was performed at the CNC turning machine SBL 500 TRENS with the parameters presented in Tab. 4. The material of the workpiece used in this test was annealed X210Cr12 steel with a hardness of 240 HB.

Table 4 Turning parameters

	Cutting speed, m/s	Depth of cut, mm	Feed, mm
Turning X210Cr12 steel with HSS tools	30	0.5	0.1

For every heat treatment batch, five HSS tool inserts were used with two cutting edges. Tool wear was measured after every two minutes of turning by measuring the flank wear, *VB*, by using the Tescan Vega TS5136LS scanning electron microscope. The criterion for the end of tool life was the catastrophic failure of five 2-minute cycles of turning, i.e. a total of 10 minutes. *VB* was the width of the flank wear track at the edge of the flank, Fig. 3. The results represent the mean value of ten measurements.

3 RESULTS AND DISCUSSION

The results of the abrasion wear testing show that DCT and nitriding resulted in lower wear rates of the high-speed steel specimens tested against alumina ball counter-body. The results are presented in Figure 4. Deep cryogenic treatment resulted in a 23.6 % reduction of the wear rate. Nitriding resulted in an approximately 18.4 % reduction of the wear rate and in combination with DCT 25.6 % respectively.

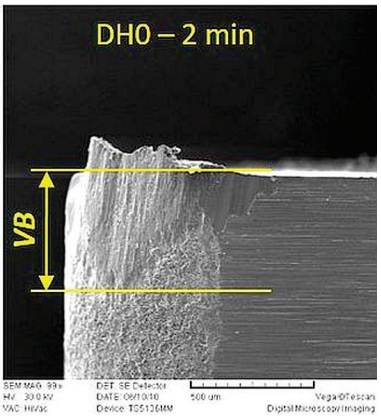

Figure 3 Flank wear of the tool, *VB*

The results show that nitriding after deep cryogenic treatment did not significantly influence the reduction in wear rate as it influenced the wear rate after heat treatment. Regarding the coefficient of friction, DCT samples had a bit higher coefficient of friction, approximately 4 % higher than classically heat-treated samples. Through nitrogen diffusion layer formation [19, 20], plasma nitriding reduced friction coefficient of the analysed steel in classic heat-treated samples (HTN) and DCTN samples for 8 % and 11 %, respectively.

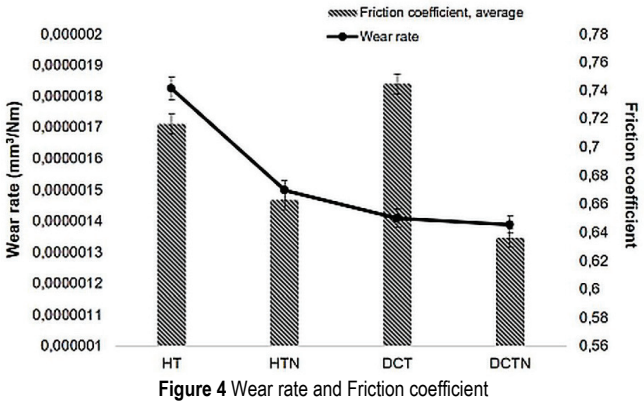

Figure 4 Wear rate and Friction coefficient

Fig. 5 presents the values of the average flank wear of the cutting tool inserts measured every two minutes of turning. The results show that after two minutes, heat treated (HT) inserts had the highest value of average flank wear, but after four minutes of turning, the cryogenically treated and nitrided (DCTN) tool inserts had higher flank wear values than the heat treated (HT) ones. The heat-treated inserts (HT) and cryogenically treated and nitrided (DCTN) inserts had total tool failure after eight minutes of turning with flank wear values above 1.2 mm. The DCT inserts and heat-treated and nitrided (HTN) inserts exhibited similar wear behaviour with slightly lower flank wear values for the heat-treated and nitrided (HTN) tool inserts. When compared with the

laboratory wear test results, it can be observed that the DCT samples had a lower wear rate than the HTN samples and that the DCTN samples exhibited the lowest wear rate of all samples, and in the machinability test, the DCTN tool inserts had the poorest wear behaviour. Similar results were reported in [5], where it was concluded by the authors that plasma nitriding enhances the tribological properties of powder metallurgy HSS, but if combined with the DCT, it might reduce the advantageous effect of the deep-cryogenic treatment and the reasons for that are not clear at present.

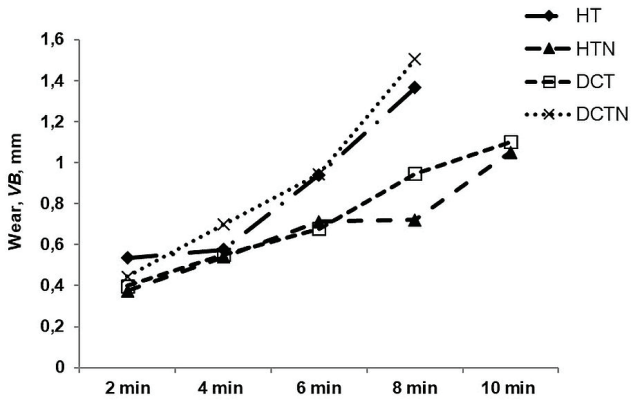

Figure 5 Average flank wear of differently heat treated HSS cutting tool inserts

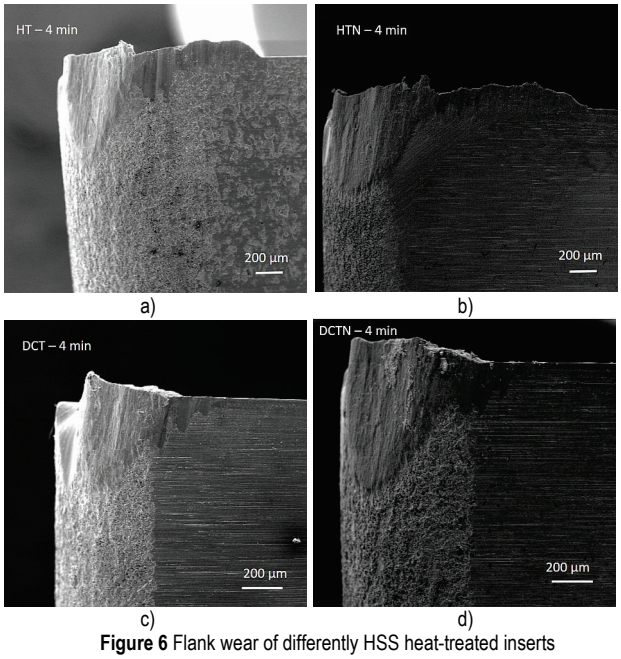

Figure 6 Flank wear of differently HSS heat-treated inserts
a) Classically heat treated HSS; b) Classically heat treated and nitrided HSS
c) Deep cryogenic treated HSS; d) Deep cryogenic treated and nitrided HSS

Although the laboratory tests gave the results on wear behaviour of the cryogenically treated and nitrided HSS, they cannot predict the behaviour of HSS tools under the realistic wear condition, e.g. cutting processes which involve high temperatures at the tool – chip contact, high stress on the tool surfaces and intense interaction between the tool and the workpiece. It is clear that at the cutting speed of 30 m/min diffusion and oxidation, wear mechanisms were also pronounced at a higher rate and they contributed to the intensity of the cutting tool insert flank face wear.

Fig. 6 shows wear of the cutting inserts flank face and the formation of a build-up edge of the flank face in all four cutting inserts can be observed. The build-up edge is formed as a result of indirect adhesion wear [21].

Adhesion wear is one of the tool wear mechanisms that can be present in a wider range of cutting temperatures. It can be produced by two different ways. Direct adhesion wear is caused by the integration of tool particles to the chips, and indirect or secondary adhesion wear is caused by an integration of a fragment of the workpiece material to the tool. This affects tool wear in the way that tool geometry is altered by material integration and when these fragments are removed, they can extract tool particles causing tool wear [21]. As observed in Fig. 6 d, the highest build-up edge after four minutes of turning is present at the DCTN insert even though DCTN samples had the lowest coefficient of friction in the laboratory wear test. This is also in accordance with [5], where it was concluded after the laboratory wear tests performed on samples, that plasma nitriding in combination with DCT might eliminate the advantageous effect of DCT, leading to reduced galling resistance. Galling resistance reduction also had a large influence on the results in the machinability test performed within this research since galling is a very intense form of adhesion wear. Adhesion wear leads to the formation of a build-up edge of the tool flank face intensifying the wear of the cutting tool.

4 CONCLUSION

Properly optimized and conducted heat treatment can notably affect the properties of high-speed steels. The heat treatment parameters of HSS are chosen depending on the required specific properties of the particular tool. With different combinations of deep cryogenic treatment parameters and nitriding, it is possible to affect the mechanical properties (hardness and fracture toughness) of certain components, but it can also increase wear resistance regardless of the changes in hardness values.

In this paper, the influence of nitriding in combination with deep cryogenic treatment on the abrasion wear resistance and coefficient of the friction of high-speed steel produced with powder metallurgy was investigated. In addition to that, its behaviour under the realistic wear condition, i.e. the cutting process, was observed, by performing the single point cutting tool machinability test and measuring the flank wear every two minutes. The results showed that deep cryogenic treatment resulted in a 23.6 % reduction of the wear rate and nitriding in an approximately 18.4 % reduction of the wear rate, in combination with the deep cryogenic treatment of 25.6 % respectively. The results show that nitriding after deep cryogenic treatment did not influence significantly the reduction in the wear rate as it influenced the wear rate when conducted after the heat treatment. Regarding the coefficient of friction, deep cryogenic treatment samples had an approximately 4 % higher coefficient of friction than the classically heat-treated samples. Plasma nitriding reduced the friction coefficient of

the analysed steel in the classically heat-treated samples and deep cryogenic treated samples for 8 % and 11 %, respectively. Regarding the behaviour of HSS in the machinability test, the heat-treated (HT) inserts and deep cryogenic treated and nitrided (DCTN) inserts exhibited a total tool failure after eight minutes of turning with flank wear values above 1.2 mm.

DCT inserts and heat-treated and nitrided (HTN) inserts exhibited similar wear behaviour through the machinability test with slightly lower flank wear values for the heat-treated and nitrided (HTN) tool inserts. When compared to the laboratory wear test results, it can be observed that the DCT samples had a lower wear rate than the HTN samples and that the DCTN samples exhibited the lowest wear rate of all samples and in the machinability test, the DCTN tool inserts had the poorest wear behaviour.

Based on the results of the machinability test, it can be concluded that when high-speed steel is subjected to conditions in the real cutting process, classical heat treatment and nitriding have the same effect as DCT and in combination with DCT, plasma nitriding eliminates the advantageous effect of the deep-cryogenic treatment.

5 REFERENCES

[1] Holmberg, K. & Matthews, A. (1994). *Coatings Tribology*, Elsevier Science B. V., Amsterdam.

[2] Soković, M., Barišić, B., & Sladić, S. (2009). Model of quality management of hard coatings on ceramic cutting tools. *Journal of Materials Processing Technology*, 209, 4207-4216. https://doi.org/10.1016/j.jmatprotec.2008.11.026

[3] Šolić, S. (2011). Influence of the microstructure on the tribological properties of cutting tools, doctoral thesis, Zagreb, UniZg, FAMENA. (in Croatian)

[4] Šolić, S., Schauperl, Z., Godec, M. & Tropša, V. (2017). Microstructural changes in heat treatment of PM high-speed steels. *Tehnički glasnik, 11*(4), 166-170.

[5] Podgornik, B., Majdic, F., Leskovšek, V., & Vizintin, J. (2012). Improving tribological properties of tool steels through combination of deep-cryogenic treatment and plasma nitriding. *Wear*, 288, 88-93. https://doi.org/10.1016/j.wear.2011.04.001

[6] Meng, F., Tagashira, K., Azuma, R., & Sohma, H. (1994). Role of eta-carbide precipitations in the wear resistance improvements of Fe–12Cr–Mo–V–1.4C tool steel by cryogenic treatment. *ISIJ International*, 34, 205-210. https://doi.org/10.2355/isijinternational.34.205

[7] Meng, F., Tagashira, K., Azuma, R., & Sohma, H. (1994). Role of eta-carbide precipitation's in the wear resistance improvements Fe-12Cr-Mo-V-1,4C tool steel by cryogenic treatment. ISIJ International, 34(2), 205-210. https://doi.org/10.2355/isijinternational.34.205

[8] Leskovšek, V., Kalin, M., & Vižintin, J. (2006). Influence of deep-cryogenic treatment on wear resistance of vacuum heat-treated HSS. *Vacuum*, 80, 507-518. https://doi.org/10.1016/j.vacuum.2005.08.023

[9] Leskovšek, V. & Ule, B. (1998). Improved vacuum heat-treatment for fine-blanking tools from high speed steel M2. *Journal of Material Processing Technology*, 82, 89-94. https://doi.org/10.1016/S0924-0136(98)00023-5

[10] Molinari, A., Pellizzari, M., Gialanella, S., Straffelini, G., & Stiasny, K. H. (2001). Effect of deep cryogenic treatment on the properties of tool steel. *J. Mater. Process. Technol., 118*, 350-355. https://doi.org/10.1016/S0924-0136(01)00973-6

[11] Mohan Lal, D., Renganarayanan, S., Kalanidhi, A. (2001). Cryogenic treatment to augment wear resistance of tool and die steels. *Cryogenics*, 41, 149-155. https://doi.org/10.1016/S0011-2275(01)00065-0

[12] Baldissera, P. & Delprete, C. (2008). Deep Cryogenic Treatment: A Bibliographic Review**.** *The Open Mechanical Engineering Journal*, 2, 1-11. https://doi.org/10.2174/1874155X00802010001

[13] Oppenkowski, A., Weber, S., & Theisen, W. (2010). Evaluation of factors influencing deep cryogenic treatment that affect the properties of tool steels. *J. Mater. Process. Technol.*, 210, 1949-1955. https://doi.org/10.1016/j.jmatprotec.2010.07.007

[14] Podgornik, B., Paulin, I., Zajec, B., Jacobson, S., & Leskovšek, V. (2016). Deep cryogenic treatment of tool steels. *Journal of Materials Processing Technology*, 229, 398-406. https://doi.org/10.1016/j.jmatprotec.2015.09.045

[15] Silva, F. J., Franco, S. D., Machado, A. R., Ezugwu, E. O., Souza, A. M. J. (2006). Performance of cryogenically treated HSS tools. *Wear*, 261, 674-685. https://doi.org/10.1016/j.wear.2006.01.017

[16] Firouzdor, V., Nejati, E., & Khomamizadeh, F. (2008). Effect of deep cryogenic treatment on wear resistance and tool life of M2 HSS drill. *Journal of Materials Processing Technology*, 206, 467-472. https://doi.org/10.1016/j.jmatprotec.2007.12.072

[17] Yan, X. G. & Li, D. Y. (2013). Effects of the sub-zero treatment condition on microstructure, mechanical behavior and wear resistance of W9Mo3Cr4V high speed steel. *Wear, 302*(1-2), 854-862. https://doi.org/10.1016/j.wear.2012.12.037

[18] www.iscar.com

[19] Šolić, S., Cajner, F., & Leskovšek, V. (2012). Effect of Deep Cryogenic Treatment on Mechanical and Tribological Properties of PM S390 MC High-Speed Steel. *Materials Testing, 54*(10), 688-693. https://doi.org/10.3139/120.110380

[20] Kato, H. & Eyre, T. S. (1994). Sliding wear characteristics of nitrided steels. *Surf. Eng.*, 10, 65-74. https://doi.org/10.1179/sur.1994.10.1.65

[21] Gómez-Parra, A., Álvarez-Alcón, M., Salguero, J., Batista, M., & Marcos, M. (2013). Analysis of the evolution of the Built-Up Edge and Built-Up Layer formation mechanisms in the dry turning of aeronautical aluminium alloys. *Wear*, 302(1-2), 1209-1218. https://doi.org/10.1016/j.wear.2012.12.001

Authors' contacts:

Dr. sc. **Sanja ŠOLĆ,** Assistant Professor
University North, Department of Mechanical Engineering
J. Križanića 31b, 42 000 Varaždin, Croatia
E-mail: sanja.solic@unin.hr

Dr. sc. **Zdravko SCHAUPERL,** Full Professor
University of Zagreb, Faculty for Mechanical Engineering and Naval Architecture,
Ivana Lučića 5, 10000 Zagreb, Croatia
E-mail: zdravko.schauperl@fsb.hr

Dr. sc. **Vlado TROPŠA,** Associate Professor
University North, Department for Mechanical Engineering
J. Križanića 31b, 42000 Varaždin, Croatia
E-mail: vlado.tropsa@unin.hr

ISSN 1846-6168 (Print), ISSN 1848-5588 (Online)
https://doi.org/10.31803/tg-20190226231838

Original scientific paper

THE INFLUENCE OF PRINTING, LAMINATION AND HIGH PRESSURE PROCESSING ON SPOT COLOR CHARACTERISATION

Renata TOMERLIN, Mario TOMIŠA, Damir VUSIĆ

Abstract: The food industry has recognized the important role that multi-layered, flexible packaging materials play and it uses them extensively within the packaging processes. Trends within food processing and packaging continuously encourage manufacturers to develop new technologies which extend a product's shelf-life. The samples that were the subject of research described in this paper are retort stand-up pouches made of multi-layered flexible material, the layers of which have been bonded with a laminating process that aims to both extend a product's shelf-life and stability, permitting the final processing of the finished product under aggressive regimes. It is intended that packaging, when subjected to graphic reproduction and high pressure processing, shall remain unchanged in all aspects, in particular the visual aspect that is the subject of the research. The samples were printed on polyester film (PET) using a rotogravure printing technique and laminated on aluminum (Al), oriented polyamide (OPA) and finally on inner polypropylene (PP) layers. The sample was monitored for the *Vegeta Blue* spot colorimetric difference in the CIE L*a*b* space throughout the individual graphic reproduction phases and the final high pressure processing (HPP) of the finished product. The goal is to determine the size of the spot color colorimetric difference (ΔE^*) in relation to the defined formula and the established standard. On the basis of measured results, guidelines and recommendations for the correction and quality assessment of spot color reproduction throughout the entire process were defined, with the goal to minimize any deviation to the lowest possible level.

Keywords: CIE L*a*b*; colorimetric difference; food packaging; high pressure processing; spot color

1 INTRODUCTION

The packaging of a product was originally considered as anything that held, protected and stored its contents. It has evolved throughout history from its initial role to that of a key element and driver of a marketing mix. Simplicity has led to complexity and, aside from retaining the basic functional features, packaging has now acquired a number of new attributes. It communicates and is unique in its shape, is easily recognizable, uses intelligent materials and colors, applies unique coding and is interactive, biodegradable and, in some instances, edible. All of this and much more make up today's food packaging. Its design and attractiveness draw consumer attention to a shelf and encourage the purchase and consumption of products [1, 2]. As color and form are the most recognizable design elements, each retail chain brand strives to achieve the spot color standardization that forms the dominant element of its visual identity. Throughout the packaging process, from its initial inception, i.e. the designer's idea, through production and final placement on the shelf, special attention is paid to the colorimetry and reproduction quality of all elements defining the visual design, especially those involving the spot color reproduction defined and permitted within the CIE $L^*a^*b^*$ color space.

The packaging industry is one of the global leaders in industrial production and food packaging is the main segment within the whole packaging industry.

Numerous new food packaging products appear on the market every year and face high levels of competition and increased consumer demands. Every food product includes a food packaging system, and this has become an increasingly influential factor when a consumer decides to purchase a particular product when there is a choice of various brands of the same type of the product. Just as with food, food packaging must meet high quality and safety standards and comply with all legal requirements and regulations to achieve success on the market [3].

The composite multi-layer flexible packaging material was used to manufacture the samples used in the research presented in this paper, which included not only the different types of polymeric materials but also a layer of aluminum that provides an adequate barrier and adds container strength for all of the production processes to which the packaging shall be subjected. The packaging material is composed as follows (Fig. 1):

- Polyester PET 12 μ
- Aluminum Al 9 μ
- Oriented polyamide OPA 15 μ
- Polypropylene PP 75 μ.

The composition of this packaging material is suitable for High Pressure Processing (HPP). High pressure processing (HPP) is an industrially tested technology that offers a more natural, environmentally friendly alternative for pasteurization or shelf life extension of a wide range of food products [4]. Commercial high pressure and low temperature methods achieve inactivation of vegetative microorganisms by subjecting vacuum-sealed food in flexible packaging to treatment at hydrostatic pressures of 600 MPa (or less) and initial temperatures lower than 40 °C for one to fifteen min. depending upon product application. A food product with packaging is subjected to treatment at 300, 400 and 500 MPa pressures for a defined time period of 5 and 10 minutes. Pressures above 400 MPa at ambient temperature inactivate the vegetative flora (bacteria, virus, yeasts, molds and parasites) present in food, extending the products shelf life importantly and guaranteeing food safety. High Pressure Processing respects the sensorial and nutritional properties of food, because of the absence of heat

treatment, and maintains its original freshness throughout the shelf life [5].

Figure 1 Multi-layered Stand-up Pouch Material

2 FLEXIBLE MULTI-LAYERED FOOD PACKAGING

Food packaging experienced its greatest expansion and flourishing in the second half of the 20th century. This is partly due to the development and discovery of new polymer materials and partly due to increased food production as a result of population growth, urbanization, lifestyle changes, female employment and increasingly pronounced hygiene habits [6].

Packaging material is any material from which packaging is made, such as: glass, plastic, paper, cardboard, wood, metal multi-layered mixed materials and other materials [7].

Multi-layered mixed flexible material plays an important role within the packaging material segment. Multi-layered packaging is predicted to grow at an annual rate of 4.1%, meaning an increase from 27.4 million metric tons in 2017 to 33.5 million metric tons in 2022. The financial market share of flexible packaging material is growing annually by 4.3% and by 2022 this is expected to amount to 283 billion USD [8].

Historically, polymer materials have only been used as a packaging material for a short period of time and, from their initial mass use in the 1950s onto the present day, their properties have constantly improved, changed and been enhanced. Packaging materials are almost exclusively made from plastomers. A considerably smaller amount of duromers and elastomers are used as an auxiliary material for sealing lids and fasteners [9].

The polymers most commonly used in plastic packaging include:

- Polyethylene (PE),
- Polypropylene (PP),
- Styrene homo- and copolymers [polystyrene, (PS), styrene-acrylonitrile (SAN) and acrylonitrile butadiene styrene (ABS),
- Polyvinylchloride (PVC)
- Polyamide (PA)
- Polyethylene terephtalate (PET) and
- Polycarbonate (PC) [9].

Usually, these are divided into flexible and rigid packaging materials. Everything that has a thickness of up to 250 μ (0.010 inch) is considered a flexible material or film, and everything thicker is considered a rigid polymer. However, in practice, this is not the most effective method of division as the stiffness of a material depends on the type of polymer. Therefore, for example, PVC (polyvinylchloride) or cellulose nitrate will already be rigid at 70 – 80 μ, whereas LD PE (low density polyethylene) will not be rigid even at 300 μ [10].

Polymers are very rarely used in their original form, and in order to achieve good characteristics to be a packaging material, different additives are added during their production to improve their properties. In addition to the combination of different polymers, multi-layered flexible packaging is combined with other materials (e.g. paper and aluminum) that aim to increase endurance, packaging resistance and barrier properties.

Currently, a new EU Directive is being developed, and it is known as the SUP Directive (*Single-Use Plastics*). This Directive shall also partly cover the packaging materials primarily intended for snack products, beverage industry and in general all food intended for direct consumption without further processing [11]. A great deal of pressure has been applied to manufacturers of plastics and polymer materials relating to the adequate disposal and recycling of materials with a view to reducing marine pollution in seas, marinas and the environment in general. Regardless of its negative reputation and poor image, plastic has a number of benefits over other packaging materials and it is impossible to imagine life without it.

Only 1.5% of all oil and gas consumed in Europe is used as a raw material for the production of plastic packaging, while 90% is used for heating, transportation and energy production. If food is packaged with other packaging materials, the associated energy consumption would be doubled and greenhouse gas emissions would be almost tripled. This would also be accompanied by a 360% increase in packaging weight. It is the lightest packaging material. More than 50% of all European products are packed in plastic that only accounts for 17% of the total packaging weight of all products on the market. Furthermore, this weight has been reduced by 28% over the previous 10 years. Lightweight packaging means lighter loads and fewer trucks required to deliver the same amount of products, thus reducing energy consumption for transportation, CO_2 emissions and transportation costs [12].

From the perspective of companies and consumers (users), packaging must achieve several goals:

- Identify a brand,
- Contain the product's description and valid information,
- Facilitate smooth transportation and product protection,
- Facilitate storage for the consumer and
- Enable easy consumption of the product [13].

All of this is possible with multi-layer flexible packaging as certain polymer materials provide an excellent printing substrate, look extremely attractive on the shelf and offer a range of options for additional effects, such as various lacquers, partial matte or glossy finishing, a metallic effect if a printed surface is laminated on an aluminum surface without white primer, etc. Additionally, handling, production and transportation of this type of packaging material is simple and allows for storage in ambient temperatures for an

extended shelf life, provided of course that the packaging remains hermetically sealed and secured. A relatively new form of packaging on the Croatian market are stand-up pouches made of flexible multi-layered materials, suitable for sterilization and high pressure processing and practical for use and application. Stand-up pouches can take various forms, depending on the molding tool on the forming machine and the staples used, and they can include possible variants such as a sealing strip or laser perforations or indentations for easier opening. Depending on the combination of packaging materials, these may be transparent or contain an aluminum layer, but the latter are not suitable for heating in a microwave oven.

The retort stand-up pouches are the actual subject matter of this research. It defines the colorimetric difference of the *Vegeta Blue* spot color in the CIE $L^*a^*b^*$ space applied to the packaging design to detect the phase of the process that causes the greatest colorimetric difference in relation to the defined standard and color formula. When shopping, customers are inclined to select certain products according to their individual habits and memorized characteristics. The main feature of Vegeta branded products is their recognizable blue color. *Vegeta Blue* is a color that should be kept within a strictly defined tolerance range ($\Delta E^* \leq 1$), regardless of the type of packaging material, printing technique or finishing process). This is not a simple task at all, as it requires selecting an adequate supplier that understands the specifics of the printing technique, its alignment within the graphic preparation and design process and permanent quality control and measurement of colorimetric values within the CIE $L^*a^*b^*$ space throughout the entire graphic and technological process.

3 RESEARCH METHODOLOGY

This chapter describes the methodology used in this research and the impact of the individual phases of the graphic and technological process on the *Vegeta Blue* spot colorimetric difference. Standard values for the *Vegeta Blue* spot color were prescribed in Podravka Packaging Development Dpt., coordinated with the supplier. The results of the measurement of the CIE $L^*a^*b^*$ color values and their colorimetric difference per processing stages were compared and colorimetric differences were observed compared to the defined standard and the set *Vegeta Blue* spot color formula. The measurement was taken after printing, lamination and high pressure processing. It indicated the stage at which the greatest colorimetric difference outside the tolerance area occurred and whether it could have an impact on consumer perception.

The graphical and technological process is divided into several stages. The first of these is the graphical design stage, which in some instances implies solely the application of visual elements to the already existing form and packaging material, and in certain situations this may mean designing a new form mainly in rigid plastic, glass, or metal packaging, which also requires the development of a new label, a *shrink sleeve* foil or another final package decoration. In such situations, this design process is more time-consuming and complex and requires the connectivity of designers, marketing experts, development engineers and specialist expertise from suppliers of certain packaging materials. Primary packaging is in most instances characterized by applied printing. In order to achieve excellent printing results, graphical preparation, customized to specific printing techniques and characteristics, is required. The printing phase is followed by lamination processes, die-cutting forming and sealing the retort stand-up pouch in this case. In addition to the processes listed above, the packaging that is the subject of this research is also exposed to the processing of a finished product, which in this instance means exposure to high pressure processing during which unwanted changes to the packaging material can occur, and that manifest in the form of de-lamination of the packaging material, separation of individual layers or changes in a polymer, which in turn can affect colorimetric difference and subsequently consumer perception.

3.1 Design, Graphic Preparation and Printed Form Production

For the purposes of the research presented in this paper, a design has been applied to the already existing technical drawing of the retort stand-up pouch produced by the Company Aluflexpack Novi from Umag. Packaging design usually begins with a good, clear and detailed *brief* for the agency and the designer. Since it was necessary to apply the *Vegeta Blue* spot color on as large area of the pouch that was the subject of this research as possible, the design was completed in the Podravka Design Studio and it included the tailoring of an already existing design to new dimensions. The *Brief* is usually drafted by the marketing team with expert support from development specialists, who mostly reduce the ideas of designers and marketing into a practicable and feasible framework.

The stand-up pouch constructed from a multi-layered packaging material onto which the design was applied has a total volume of 500 ml and measures 140×240 mm. The format of the packaging that is the subject of research is part of the standard Aluflexpack Novi product range and formatted components of this shape are currently included in production. In addition to the design, a color measuring atlas has been applied on the back of the bag, which will be used in future studies relating to process of colorimetric difference.

The design and graphical preparations were completed in Adobe Illustrator CC. Color separation was completed in Esko ArtPro, Version 16.0.0 in Company Anilox. Separation for printing was performed by using seven colors (cyan, magenta, yellow, black, *Vegeta Blue*, reflex blue and white). A test print was performed on an Epson Stylus Pro WT7900 ink jet printer, which uses a Micro Piezo TFP head for printing. The printer color management software is GMG RIP and GMG FlexoProof, Ver.5.8.1.312. A test print using digital technology (GMG *proof*) was performed for quality control of all design elements. Podravka, which in this instance commissioned the design, received the final color separation and digital print, for quality control purposes. A

signed digital print serves as a guarantee for the packaging supplier that all is in order and that the next stage of the process, namely the engraving of printed forms, can be embarked upon.

Separation was engraved from the application Collage, which was also used for installation and to define the following parameters:

- Lineature, (70 L/cm – 101 L/cm, depends on color),
- Individual separation angles, (33° – 60°, depends on the color),
- Tool angle, (110° – 130°, depends on the color),
- Reproduction curve.

Preliminary prepared cylinders were then engraved on electronic engraving machines. The engraving was performed on an Ohio Gravure Tec. Inc. USA, Gravostar Spectrum Engraving Machine. The process was tailored to the parameters of the selected substrate and machine on which the printing was performed. In order for the print cylinders to be sufficiently durable to withstand printing on printing machines, they were finally processed with hard chrome plating, where a protective layer of chromium, several micro millimeters thick, was applied. Final quality control was performed by a visual inspection of the finished printed forms and the pattern was printed on a test print machine utilizing the original inks and consumer substrate (PET 12 μ) at the Aluflexpack Novi Print Shop by simulating the parameters of the printing machine. A test print was performed on a manually processed printing press. The test print, when obtained as described above, showed if there were any visible defects and if any corrections on print forms were necessary. The test print with engraved print forms was performed on Rotogravure Proofing Press, a test print machine produced by JM Heaford of the UK, on a HA 3500×1800 (Fixed Drum / Hydraulic Rotation) Model.

3.2 Printing and Finishing

The samples that are the subject of this paper have been printed by using the rotogravure printing technique. Rotogravure printing is a direct, intaglio printing technique. The print face is hollowed out in its printed form and the blank spaces are foremost [14]. The printing ink is applied on the entire print form during printing and later, a doctor blade removes the printing ink from the blank spaces (Fig. 2). By pressing the printing form onto the substrate, the printing ink is transferred to the substrate. The printing surface of the PET foil should be treated to be suitable for printing, which has a significant influence on surface tension and enables the ink to connect with the printing substrate [15].

This printing technique allows the reproduction of very small details, small font-sized text, excellent photographs and product views. The usual perception of rotogravure printing within the printing industry is that it is used in the printing of top class brand packaging which must be high-quality. Quality remains the main feature of the printing technology, but in recent years, the producers of printing forms, i.e. engraving companies, have sought to reduce costs and automate the process. New, fast engraving heads use robotic arms and are fully automated, replacing human labor and they have led to significantly shorter delivery times, often no longer than a few days [16].

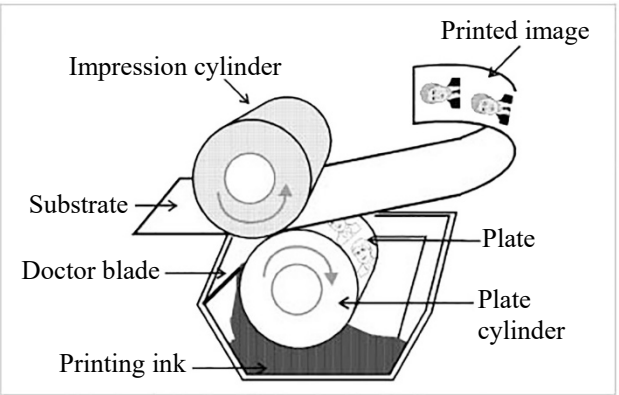

Figure 2 Rotogravure Printing Schematic [17]

Aside from the high prices of the printing forms, rotogravure printing is also known for evaporation ink finishing. Most printing that utilizes this technique involves inks based on organic solvents. The vapors from organic solvents are harmful to human health and highly flammable. For these reasons, the plants and facilities where rotogravure printing machines are used require special construction and safety measures [14]. Companies operating within the EU are subject to stringent legislation and must be equipped with special types of air purification and solvent recovery devices.

The Aluflexpack Novi Print Shop in Umag printed design samples on the Schiavi Pulsar Printing Machine, 10 group, 1.240 mm wide with a maximum speed of 350 m/min, utilizing a rotogravure printing technique on transparent, 12 μ thick polyester (PET). Aluflexpack Novi utilizes a cutting edge solvent recovery plant and has been awarded the BRC (the British Retail Consortium) and ISO (the International Organisation for Standardisation) production certification.

Siegwerk printing inks (thermal-resistant ink), specifically intended for printing packaging that can later be processed by various methods applied to finished products, were used. Resistances of this ink series are archived by using completely resistant pigments according to ISO 2836. The printed samples were measured for the values of *Vegeta Blue* and were compared with the set standard values and pre-defined color formula. After the printing phase was completed, the laminating process was performed on the Rotomec Rotoconvert Machine with three unwinders (a triplex in a single pass) 1.230 mm wide, with a maximum speed of 300 m/min. A Henkel agent and a catalyst were used for lamination. A flexible retort stand-up pouch consists of four different materials: PET, Al, OPA and PP. After lamination, each material has to pass though the cross-linking of materials and solvent evaporation phase which aim to eliminate the problem of residual odor within the packaging material and any de-lamination and migration problems. The Totani BH-60DLLS machine was used to form, seal on three sides (laterally and on the bottom) and die-cut the stand-up pouches, operating at a maximum speed of 1.000 pouches/min.

3.3 High Pressure Processing (HPP)

The processes that may cause unnecessary changes in the packaging's properties and appearance do not always end upon the completion of the graphical and technological process. The packaging, as an integral part of the product, is subject to various food processing regimes, the aggressive parameters which can affect the packaging material's properties.

The application of food high pressure processing in the food industry has developed as an alternative to conventional thermal processes, such as pasteurization and sterilization, aiming to achieve a microbiologically safe product that does not undergo any sensory, physical or nutritional value changes.

High Pressure Processing is a cold pasteurization process in which the final packaged product is exposed in a given chamber to high isostatic pressure (300–600 MPa / 43 500–87 000 psi), which is applied by water (Fig. 3) [18].

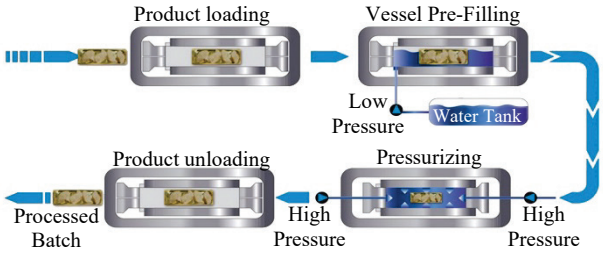

Figure 3 High Pressure Processing [5]

4 MEASUREMENT RESULTS

The evaluation of the measured samples within this research was performed on 25 samples for the printing and lamination, and on 24 samples for high pressure processing stages. The total quantity of produced samples was 1000 pieces. High pressure processing was carried out at the University of Zagreb's Faculty of Food Technology and Biotechnology, using a 2 L volume device manufactured by the Stansted Fluid Power. It applied pressures of 300, 400 and 500 MPa for a defined period of 5 and 10 minutes. The processing temperature remained constant at 22 ± 1 °C. The pressure rising rate was set at 5 MPa/s and the release at a maximum of 20 MPa/s. Four samples were processed in each of the pressure and temperature regimes stated above (300, 400 and 500 MPa, during 5 and 10 minutes), totaling 24 samples.

Changes in colorimetric values were monitored throughout the printing phase by using a measuring device utilizing the standard formula with the CIE $L^*a^*b^*$ colorimetric values for the *Vegeta Blue* spot color. The color was measured with a Hunter Associates Lab. Inc. Device, Type: ColorQuest XE, in Aluflexpack Novi's Print Shop. The device was calibrated to accord with the ISO/IEC 17025:2005 and BS EN ISO 9001:2000 Standards. By measuring the samples after each process stage, starting with printing, the influence of each individual phase on CIE $L^*a^*b^*$ components in the color space was determined. It was defined at what stage in the process and under which processing regimes, the greatest colorimetric difference occurred and what the most significant differences within the CIE $L^*a^*b^*$ color space were. The average colorimetric difference for each phase was defined in the statistical analysis of the measured values and it was expressed by applying the method of the median mean. Parallel curves were also shown after each measurement stage demonstrating the colorimetric difference values compared to the set color (Figs. 4 and 5).

The measurement was performed on three standard light sources: D65./10°, A.../10° and F11./10°. Aluflexpack Novi's Print Shop had previously recorded the CIE $L^*a^*b^*$ *Vegeta Blue* spot color values that are the subject of the research and the defined formula. For the purposes of this research, the color formula was to a lesser extent modified in its composition and it did not use the original values.

The following standard measuring values were set for *Vegeta Blue* under three different light sources:

Table 1 Standard Colorimetric values for the Vegeta Blue color

Light source	L^*	a^*	b^*
D65./10°	52.44	−25.05	−33.41
A.../10°	46.06	−31.96	−45.96
F11./10°	46.62	−16.28	−41.82

Following the measurement and evaluation of all samples, comparisons of deviations for each process phase were made. The largest colorimetric difference of the *Vegeta Blue* spot color appeared after the lamination phase. Measurement results were subjected to a statistical analysis and expressed as a median mean which represented the center of mass for the set of 25 pouch samples for printing and lamination and 24 for the high pressure processing stage.

The measured values were obtained by using the following formula:

$$\Delta E_{CMC} = \sqrt{\left(\frac{\Delta L}{lS_L}\right)^2 + \left(\frac{\Delta C}{cS_C}\right)^2 + \left(\frac{\Delta H}{S_H}\right)^2} \quad (1)$$

No color tolerance system is perfect, but CMC and CIE94 equations best represent the color differences in the way our eyes see them (Tab. 2) [20].

Table 2 Colorimetric Difference Evaluation Criteria for the Measured Colors

Tolerance Method	Matching with Visual Perception (%)
CIELAB	75 %
CIELCH	85 %
CIECMC	95 %

Table 3 Average Colorimetric Difference Values for the Vegeta Blue spot color

Stage of the process	Source of light	Colorimetric difference CMC2:1
Printing	D65./10°	0.23
	A.../10°	0.23
	F11./10°	0.30
Lamination	D65./10°	1.56
	A.../10°	1.71
	F11./10°	1.43
HPP	D65./10°	1.94
	A.../10°	2.28
	F11./10°	2.10

The presented Figs. 4 and 5 show the spectral curves of the measured *Vegeta Blue* spot color regarding the performed stage of the process. The right part of the picture shows the L diagram with two wavelengths of color in two phases and the ab diagram shows the color difference between the two phases. The colorimetric difference after printing is within the tolerance limits and amounts to D65./10° light source CMC2:1 = 0.23. After lamination, a greater colorimetric difference occurred, the color surpassed the determined tolerance range and the colorimetric difference under the same conditions equaled to D65./10° CMC2:1 = 1.56 (Fig. 4). After high pressure processing, an even higher colorimetric difference of *Vegeta Blue* occurred and the average value on the measured samples equaled to D65./10° CMC2:1= 1.94. With lamination, *Vegeta Blue* became darker and crossed into the area of yellow-red. This clearly shows that HPP also influences the *Vegeta Blue* spot color deviations.

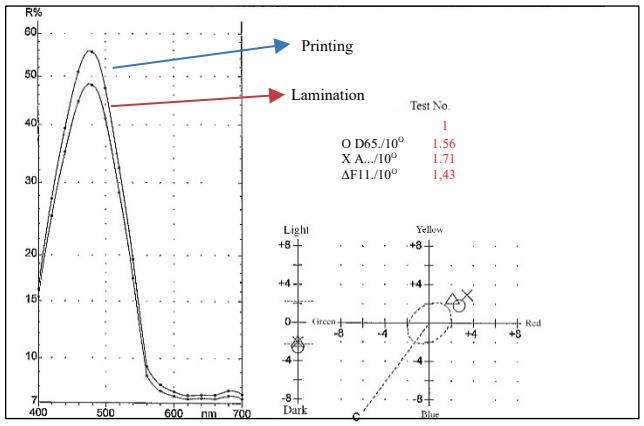

Figure 4 Printing vs Lamination

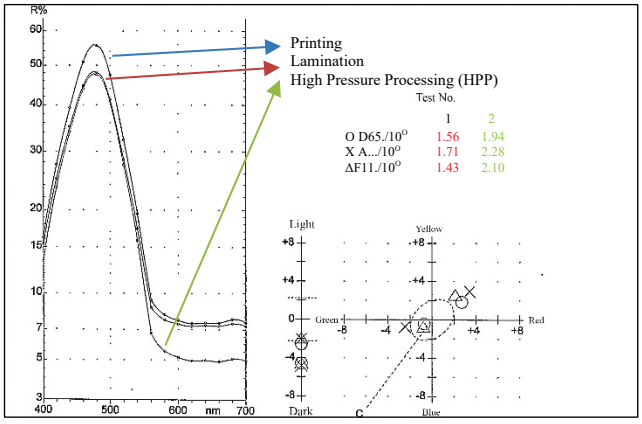

Figure 5 Print vs Lamination vs High Pressure Processing (HPP)

The unacceptable colorimetric difference occurs after the lamination process. By laminating the transparent polyester layer (PET) onto the aluminum surface, a change occurs in all parts of the CIE $L^*a^*b^*$ color system. The problem that arises when the transparent polyester is laminated onto the aluminum surface is inconsistent graphic reproduction, which could be prevented by adjustments to the color recipe. Food packaging is made of different packaging materials and with different printing techniques. Together with different packaging manufacturers and their specific features (printing inks, machine type, substrate, lamination agents, varnishing etc.), the challenge of maintaining color uniformity within the CIE $L^*a^*b^*$ space is sometimes insurmountable. The colorimetric values on a multi-layer flexible packaging containing aluminum and on the packaging containing only transparent polymer materials are not identical. To achieve the identical print, which would mean that the spot color is within the tolerance area, it is necessary to redefine the spot color input formula for every substrate. This, of course, makes the process more complicated and more expensive for print shops, but for the manufacturers of brands that are recognizable by their specific, protected color, the goals is to maintain identical colorimetric values. Specific features of individual packaging materials require that the maximum allowed tolerance area and the standard colorimetric values for the spot color be defined. During the measuring and evaluation of samples, it was noticed that a rather small deviation of the *Vegeta Blue* spot color, which occurred after lamination (ΔE = 1.56), was more visible than greater deviations of some other colors. After high pressure processing, according to the measured values, *Vegeta Blue* was darker (Fig. 5).

5 CONCLUSION

In order to achieve the desired final effect on the graphical and technological process used for the manufacturing of packaging and marketing of an on-shelf product that attracts customers, every company is faced with a long, complex and well-managed process. It is necessary to define the packaging material's type and composition for every product, which depends on the product's properties, desired shelf life, production lines used for packaging, handling and method of use in addition to a whole range of other factors. Once the material type has been defined, it is also necessary, based on other parameters, to define the printing technique which will be used in the printing of packaging. The choice of printing techniques is largely dependent on the price, volume of the packaging ordered, target quality, further processing of the completed product, etc. Once the printing technique, the packaging material and the print shop that will produce the packaging have been defined, all input parameters have to be agreed upon: the color, separation and allowed colorimetric difference tolerance. If more parameters are defined at the very beginning of the graphical and technological process, the chance of an error and undesired results is reduced to a minimum. For printing, it is recommended to select a packaging manufacturer who applies a standardized and controlled process, which largely facilitates monitoring of packaging through each of the stages and results in a colorimetric difference not exceeding the tolerance area agreed between the ordering party and the packaging manufacturer. Standardization and monitoring of all stages of such a process is the only way packaging can be produced within the defined area of a tolerated colorimetric difference, and meet the goal of the acceptable difference generally invisible to consumers' eyes.

Increasingly aware and informed consumers now have numerous requirements which they expect from packaging, and these requirements have to be met. Packaging no longer has only a protective or storage function. It is a 'silent seller' on the shelf, contributing to distinction, increasing recognition and is interactive, easy to handle and provides a range of additional benefits such as laser perforation, re-sealable options, microwave heating or direct consumption. It must comply with the guidelines on sustainable development, environmental protection, etc. At first sight, what the consumer ranks the highest is the color perception and an emotional link with the brand. In order to achieve attractiveness in a shop and draw the initial attention of the consumer, which only lasts a few seconds, a multidisciplinary approach and a highly complex implementation process are necessary.

The goal of the research presented in this paper was to determine the value of the *Vegeta Blue* spot colorimetric difference that appears on packaging during printing, processing and high pressure processing of the completed product. The *Vegeta Blue* spot color was measured after these stages and compared with the set standard in order to achieve better qualitative properties for the final product and improve its attractiveness on the shelf. Based on the measurement results, the process stages that provide the highest impact on color deviation were determined. The formula for the *Vegeta Blue* spot color with its allowed tolerance area ($\Delta E \leq 1$) was defined as the measurement starting point.

The results were the measured values for the *Vegeta Blue* spot color. High pressure processing (HPP) causes deviations in the CIE $L^*a^*b^*$ values of spot color and it increases deviation that is a result of the lamination process. The measurement has shown that the spot colorimetric difference that occurs during the processing phase is lower than the difference that occurs during the lamination stage. During high pressure processing, a change in process colors was also identified (cyan, magenta, yellow and black), in the colors of the dish presented as a part of the design. The changes to process colors were not the subject of the research presented in this paper, but the Company Anilox measured these values against the atlas of the colors applied, specifically to enable further research. It is exactly the process colors for which deviations resulting from sterilization and high pressure processing can be prevented during the graphic preparation and print form design stages.

This Paper has defined the *Vegeta Blue* spot color value of the colorimetric difference in the CIE $L^*a^*b^*$ color space for printing, lamination and HPP stages. This paper also proposes guidelines to achieve colorimetric difference within the previously defined tolerance ranges for individual colors, and determines those parts of the technological process that have the greatest effect on color deviations.

Every project relating to the inception and creation of packaging is unique and the same rules do not apply to all packaging materials. Complexity and a multi-disciplinary approach add creativity and challenges to each new project. All stages require excellent correlation and communication among the designer, the ordering party and the packaging manufacturer. Within the commissioning company itself, the involvement of several different teams and experts is also necessary in order to prevent any problems on production lines or later during the handling and processing of a product. The fact that industrial production is not the same as the small manufacturing plants of family proprietorships should not be forgotten. Industry seeks to eliminate manual work, machines have high capacities and under ideal conditions, the output control of the packaging manufacturer becomes the input control of the ordering party, but all this presumes error-free packaging items. The shelves in shops today are overcrowded, full of special offer packaging and novelties. It is impossible to determine which of the packaging properties is the most important for the consumer, whether the consumer makes his/her decision consciously or based on emotions linked to a familiar brand. The task for every manufacturer of recognized trademarked products is to achieve uniformity of spot color on different packaging materials, with different printing techniques and with different suppliers. The parameters which influence changes in spot colors are the subject of this paper and they are really numerous in products marketed in several different types of packaging material. There is a difference between printing on a mono material with a white background and a multi-layer flexible material composed with aluminum or metallized foil. For the *Vegeta Blue* spot color, just like for all other world famous brands, the intended goal is to reach colorimetric values that will be within the desired tolerance area. There are several software solutions which will facilitate the standardization process, but every ordering party should be aware that it is impossible to achieve laboratory conditions in the production plant. It is easy to manage and control standardization with one supplier, on a defined type of packaging material, with a defined type of printing inks, the lamination agent that is always the same, printing forms made with identical parameters and always by the same manufacturer. All this cannot guarantee a perfect result, but any colorimetric difference in such cases has been reduced to a minimum. The reality of food companies is unfortunately slightly different from the described ideal conditions. All manufacturers, for a variety of reasons, use the services of several packaging manufacturers and in such situations, standardization, and subsequently the control of colorimetric values and other packaging characteristics, become more complex and difficult in practice.

The relating research provides a good basis for further research in the area of process color and other packaging material deviations, within the area of printing techniques and processing procedures and other processing methods applied to a finished food product.

6 REFERENCES

[1] Kotler, P. & Armstrong, G. (2012). *Principles of Marketing.* 14th Ed. Upper Saddle River, New Jersey: Pearson Prentice Hall.

[2] Govers, P. C. M. & Schoormans, J. P. L. (2005). Product personality and its influence on consumer preference. *Journal of Consumer Marketing, 22*(4), 189-197. https://doi.org/10.1108/07363760510605308

[3] Young, T. K., Byungjin, M., & Kyung, W. K. (2014) General Characteristics of Packaging Materials for Food System. In Jung, H.H. (Eds.) *Innovations in Food Packaging*, 13-20. Elsevier Ltd. https://doi.org/10.1016/B978-0-12-394601-0.00002-3
[4] Welti-Chanes, J., López-Malo, A., Palou, E., et al. (2005). Fundamentals and Applications of High Pressure Processing of Foods. *Novel Food Processing Technologies.* New York: CRC Press.
[5] HPP Technology: What is High Pressure? (5th February 2018). Retrived from https://www.hiperbaric.com/en/ high-pressure
[6] Galić, K., Ciković, N., & Berković, K. (2000). *Analiza ambalažnog materijala*. Zagreb, Hrvatska: Hinus d.o.o.
[7] Značenje pojmova iz Pravilnika o ambalaži, Savjetodavna služba HOK-a, (5th May 2018). Retrived from http://infos.hok.hr/faq/f_tehnicka_pitanja/f9_zastita_okoline/znacenje_pojmova_iz_pravilnika_o_ambalazi
[8] The Future of Packaging: Long Term Strategic Forecasts to 2028, Smithers Pira. (2018, October 5th). Retrived from https://www.smitherspira.com/industry-market-reports/ packaging/packaging-long-term-strategic-forecasts-to-2028
[9] Vujković, I. A. (1997). *Polimerna i kombinovana ambalaža*. Novi Sad, Srbija: Poli.
[10] Briston, J. H. (1990). *Plastics Film*. 3rd Ed. Essex, United Kingdom: Longman Scientific & Technical.
[11] Proposal for a Directive of the European Parliament and of the Council, (28th May 2018). Retrived from http://ec.europa.eu/environment/circular-economy/pdf/single-use_plastics_proposal.pdf
[12] Plastics - the Facts 2016. (18th Dec. 2017). Retrived from https://www.plasticseurope.org/en/resources/publications/3-plastics-facts-2016
[13] Bassin, S. B. (1988). Value-Added Packaging Cuts through Store Clutter, *Marketing News*, September 26th, pp. 21.
[14] Bolanča, S. (2013). *Tisak ambalaže.* Zagreb, Hrvatska: Sveučilišna naklada.
[15] Valdec, D., Miljković, P., & Auguštin, B. (2017). The influence of printing substrate properties on color characterization in flexography according to the ISO specifications, *Tehnički glasnik, 11*(3), 73-77.
[16] Anyadike, N. (2003). *Introduction to Flexible Packaging*. Surrey, UK: Pira International Ltd.
[17] Oldenzijl, R., Gaitens, G. and Dixon, D. (2010). Conduct Radio Frequencies with Inks, Radio Frequency Identification Fundamentals and Applications Design Methods and Solutions, Cristina Turcu (Ed.), ISBN: 978-953-7619-72-5, InTech, Retrived from: http://www.intechopen.com/books/ radio-frequencyidentification-fundamentals-and-applications-design-methods-and-solutions/conduct-radio-frequencies-withinks. https://doi.org/10.5772/7982
[18] Food Safety, High Pressure Processing of Foods, Authority of Ireland, (September 2015). Retrived from https://www.fsai.ie/ publications_high_pressure_processing/
[19] Kuehni, R. G. (2003). *Color space and its divisions: color order from antiquity to the present*. New Jersey: John Wiley & Sons. https://doi.org/10.1002/0471432261
[20] A Guide to Understanding Color, x-Rite Pantone. (2016). Retrived from https://www.xrite.com/-/media/xrite/files/ whitepaper_pdfs/l10-001_a_guide_to_understanding_color_ communication/l10-001_understand_color_en.pdf

Authors' contacts:

Renata TOMERLIN, MSc
Podravka d.d. (plc),
Ante Starčevića 32,
48000 Koprivnica, Croatia
E-mail: renata.tomerlin@podravka.hr

Mario TOMIŠA, PhD, Assoc. Prof.
University North,
Trg dr. Žarka Dolinara 1,
48000 Koprivnica, Croatia
E-mail: mario.tomisa@unin.hr

Damir VUSIĆ, PhD, Assoc. Prof.
University North,
Jurja Križanića 31b,
42000 Varaždin, Croatia
E-mail: damir.vusic@unin.hr

ISSN 1846-6168 (Print), ISSN 1848-5588 (Online)
https://doi.org/10.31803/tg-20190328155758

Original scientific paper

ADVANTAGES AND DISADVANTAGES OF RAMAN SPECTROSCOPY IN TESTING PAPER BANKNOTES

Gordana JAUKOVIĆ

Abstract: This paper presents advantages and disadvantages of Raman spectroscopy when used for testing banknotes, i.e. in case study I, 1 and 5 dinars banknotes from a private collection dating from 1876 of numismatic value were analyzed, and in case study II, 1000 dinars banknote from circulation together with its counterfeit. In both cases banknotes were analyzed by using Raman spectrometer DXR Raman microscope at the Faculty of Physical Chemistry, with a laser of wave-length 780 nm at 12 mW of power. Specters were recorded under microscope using 50X lens in a range 1800-60 cm^{-1}. Analyses from case study I on both specimens showed spectrum characteristic for fluorescence appearance, therefore intensive signal of fluorescence covered Raman signal. In case study II, it was established that Raman spectroscopy can reliably detect a counterfeit banknote. Research, comparisons and analyses regarding original and counterfeit 1000 dinars note were performed on red banknote surfaces.

Keywords: banknotes counterfeiting; forensics; numismatics; printing inks; protective elements; Raman spectroscopy; spectrum

1 INTRODUCTION

The need for multidisciplinary examination of objects with cultural-historic value emerged in order to preserve and protect them from counterfeiting. In this paper, we are focused on historical banknotes and banknotes form circulation, as an issue of importance for numismatic museums, private collectors and researchers responsible for the care of numismatic collections. The scientific detection of forgeries is an important task for numismatic researchers around the world since they are responsible for determining the authenticity as well as the historical and monetary value of their collections. Complexity of this issue is further increased by influence of time that increases transformation and degradation of pigments and binders. Banknotes and postage stamps have complex composition; thus, several methods should be used for their identification [1, 2]. One of the approaches used in identification of materials is physical-chemical analysis, such as Raman spectroscopy. Raman spectroscopy can give qualitative, quantitative and structural information on different materials [3]. Numerous studies have been devoted to evaluating the efficiency of several analytical techniques for the detection of forgeries of banknotes form circulation [3-5]. Gaining insight into microchemical and microphysical nature of banknotes is invaluable for clarifying issues regarding the source of materials, production techniques, exchange and trade, and many other social cultural elements. Since multidisciplinary approach in examining banknotes is at its beginnings, the results of this and other similar research could contribute in finding the best solution for framework of the future comprehensive database of cultural heritage (library of pigments and materials used in the production of banknotes) [1-5].

2 EXPERIMENTAL PART

2.1 Materials and Methods

This paper is focused on examination of pigments used in banknotes to obtain characteristic Raman spectra that serve for the authenticity assessment. For the first time in the Republic of Serbia, in 2015, the Raman spectroscopy was used to evaluate the applicability of this method for the analysis of banknotes. The results of the study were applied in two case studies; first case study was conducted on two specimens of historical banknotes from 1876, and the other examination was done in the second case study on a banknote from circulation and its counterfeit. Measurements were performed at Laboratory for micro-Raman spectroscopy at the Faculty for Physical Chemistry in Belgrade. Banknotes were examined by Raman spectrometer DXR Raman microscope (Thermo Scientific) with a laser of wave-length 780 nm at 12 mW of power. Spectra were recorded under microscope using 50× lenses in a range 1800-60 cm^{-1}. During recording, a 10 s exposition with 10 repetitions was used.

2.2 Case Study I – 1 Dinar and 5 Dinars Banknotes of Year 1876 – Money of Central Treasury: A Historical Money Description

According to archive documents, specimens of banknotes from 1876 were printed in State Printing Works in Belgrade, but the paper was bought from supplier *Le Franc* and imported from Paris. Archive documents indicate that expected results should refer to spectra of "Berlin" blue, known in materials technology literature under the official name "Prussian blue" or "Paris blue" [6]. Paper surface was covered with yellowish net – impregnation [6, 7]. Dinar banknotes from the end of the 19th century had watermark containing figures and words denoting value, which is visible in Fig. 1a) and 1b). Law articles regarding punishments for counterfeiters were printed in textual form.

a) b)

Figure 1 Watermark as a protective element in denominations of: a) 1 dinar and b) 5 dinars from 1876. Central part has figures "1" and "5", with word "DINAR" printed in Cyrillic capital letters.

2.2.1 Evaluation of Banknotes by Raman Spectroscopy – Denominations of 1 and 5 Dinars from 1876

Banknotes in denominations of 1 and 5 dinars from 1876 Fig. 1a) and 1b) were evaluated by Raman spectrometer DXR Raman microscope (Thermo Scientific) with a laser of wave-length 780 nm at 12 mW of power. Spectra were recorded under microscope using 50× lens in the range 1800-60 cm^{-1}. During recording, a 10 s exposition with 10 repetitions was used. Spectra were corrected regarding fluorescence through use of fifth degree polynomial in a software package. In case of banknote specimens from 1876 it was impossible to identify certain pigments used in banknote manufacturing due to pronounced fluorescence. The spectrum characteristic for appearance of fluorescence was noticeable in both specimens, regardless of recorded point (both in clear paper and pigment itself) and variations of experiment conditions. The fluorescence originates (Fig. 2) from paper used for banknote manufacturing, and it was visible due to laser radiation from visible part of electromagnetic spectrum. That makes the intensive signal of fluorescence cover Raman signal, disabling pigment analysis with DXR Raman microscope. Therefore, to get reliable information, it would be necessary to implement different methods such as FTIR spectroscopy, since it is also a noninvasive method [4].

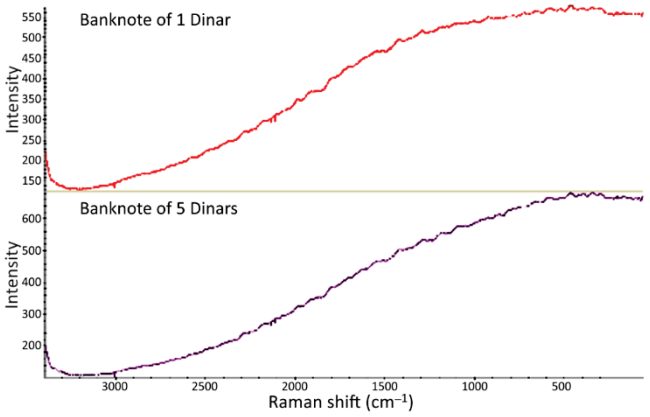

Figure 2 Pronounced fluorescence on samples of 1- and 5-dinars banknotes from 1876

2.3 Case Study II – Circulation Banknotes, 1000 Dinars Denomination and Its Counterfeit

Circulation banknotes, 1000 dinars denomination (Fig. 3) and its counterfeit, were evaluated in same conditions as in the first case study by Raman spectrometer DXR Raman microscope (Thermo Scientific) with a laser of wave-length 780 nm at 12 mW of power. Spectra were recorded under microscope using 50× lens in the range 1800-60 cm^{-1}. During recording a 10s exposition with 10 repetitions was used. Spectra were corrected regarding fluorescence through the use of fifth degree polynomial in a software package.

Figure 3 Marked regions of 1000 dinar banknote where Raman spectra were recorded

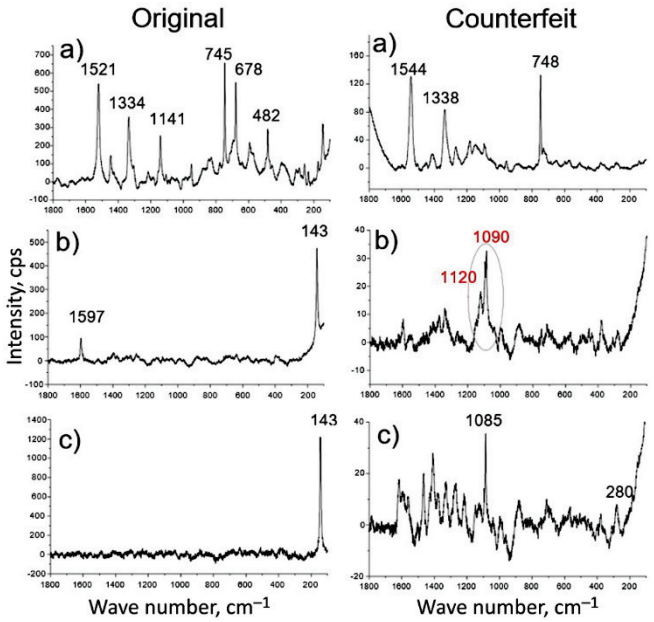

Figure 4 Raman spectra from region 1 on original and counterfeit banknote

Spectra from region 1 recorded in original and counterfeit banknote are presented in Fig. 4. Spectrum a) in original banknote based on stripes 1521, 1334, 1141, 745, 678 and 482 cm^{-1} can be attributed to spectrum of blue phthalocyanic pigment, since during recording with 780 nm laser it shows resonant effect. Resonant amplification of intensity of that pigment can cause masking stripes of other, possibly present pigments [8]. Spectra b) and c) in original banknote show intensive stripe at 143 cm^{-1} originating from TiO_2 in anatase form. Besides that, noticeable stripe in spectrum b) is stripe at 1597 cm^{-1} that could arise from vibrations of aromatic rings of orange diazo pigments of pyrazoline [9, 10]. In the same region of counterfeit banknote the spectrum received was of green phthalocyanic pigment, spectrum a), with most intensive stripes at 1544, 1338 and 748 cm^{-1} [11]. Unlike original banknote, counterfeit produced stripes of cellulose, i.e. of paper, spectrum b). In

spectrum c) of counterfeit banknote most intensive stripe noticeable is at 1085 cm^{-1} arising from white pigment – chalk [11].

During recording of spectrum in region 2 of original banknote (Fig. 5) intensive fluorescence occurred, so just a single spectrum was recorded (after correction) with noticeable weak stripes at 1586, 1560 and 1364 cm^{-1} of red pigment (alizarin) [8]. In the same region of counterfeit banknote green phthalocyanic pigment, spectrum a), was identified as well as chalk, spectrum b).

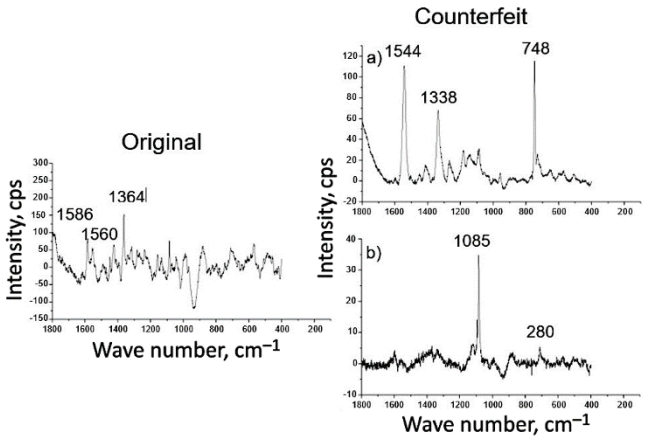

Figure 5 Raman spectra of region 2 in original and counterfeit banknote

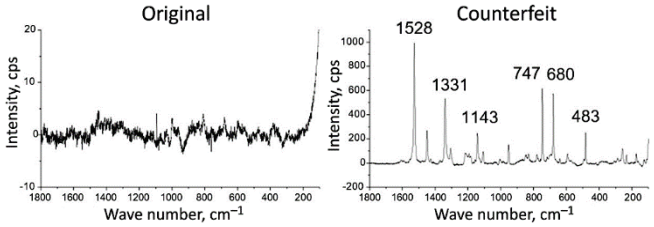

Figure 6 Raman spectra of region 3 in original and counterfeit banknote

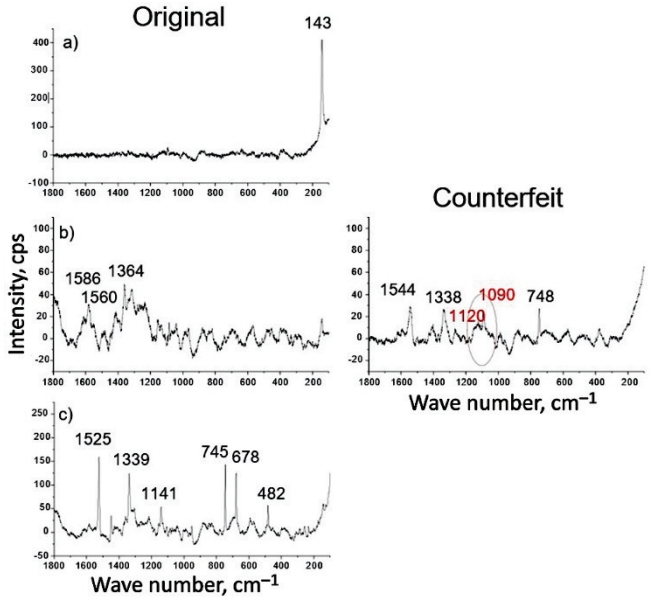

Figure 7 Raman spectra of region 4 in original and counterfeit banknote

In region 3 of original banknote (Fig. 6) spectrum that would enable identification of pigments was not received, while counterfeit banknote produced very good spectrum of blue phthalocyanic pigment.

In region 4 of original banknote (Fig. 7) TiO2 was identified in anatase form, spectrum a), naphthol red pigment (alizarin), spectrum b), while spectrum c) corresponds to blue phthalocyanic pigment. From counterfeit banknote received was spectrum of green phthalocyanic pigment, with pronounced stripes of cellulose at 1120 and 1090 cm^{-1}.

3 CONCLUSION

The results of the measurements are given in Figs. 2, 4, 5, 6 and 7. Our measurements successfully confirmed that there are advantages and disadvantages in examining banknotes with the Raman spectroscopy. Within the first case study, the analyzed specimens of historical banknotes gave unsuccessful measurements due to the spectrum characteristics. In addition, appearance of fluorescence was noticeable in both samples due to the yellowish impregnation. Recommendation for further analysis is employment of other noninvasive techniques such as FTIR. In the examination of specimens in the second case study we concluded that the Raman spectroscopy is a successful and easily obtained method applicable in forensic evaluation of circulating banknotes and counterfeits.

Acknowledgement

Many thanks to Dr Danica Bajuk-Bogdanović, research associate at the Faculty of Physical Chemistry, for assistance in recording and interpreting Raman spectra. This research was conducted in 2015 within the curriculum of PhD studies History and Philosophy of Science and Technology at the University of Belgrade.

4 REFERENCES

[1] del Hoyo-Melendez, J. M., Gondko, K., Mendys, A., Krol, M., Klisinska-Kopacz, A., Sobczyka, J., & Jaworucka-Drath, A. (2016). A multi-technique approach for detecting and evaluating material inconsistencies in historical banknotes. *Forensic Science International*, 266, 329-337. https://doi.org/10.1016/j.forsciint.2016.06.018

[2] Badovinac, I. J., Orlic, N., Lofrumento, C., Dobrinic, J., & Orlic, M. (2010). Spectral analysis of postage stamps and banknotes from the region of Rijeka in Croatia. *Nuc. Instrum. Meth. A*, 619, 487-490. https://doi.org/10.1016/j.nima.2009.10.174

[3] Skenderović-Božičević, M., Gajović, A., & Zjakić, I. (2012). Identifying a common origin of toner printed counterfeit banknotes by micro-Raman spectroscopy. *Forensic Science International*, 223, 314-320. https://doi.org/10.1016/j.forsciint.2012.10.007

[4] Itrić, C. & Modrić, D. (2017). Banknote characterization using the FTIR spectroscopy. *Tehnički glasnik, 11*(3), 83-88.

[5] Bruna, A., Farinella, G. M., Guarnera, G. C., & Battiato, S. (2013). Forgery detection and value identification of euro banknotes. *Sensors, 13*(2), 2515-2529. https://doi.org/10.3390/s130202515

[6] Hadži-Pešić, J. (1995). Novac Srbije 1868–1918. Beograd: Narodna banka Jugoslavije, Zavod za izradu novčanica i kovanog novca; Stojanović Ž. 1996. Papirni novac Srbije i Jugoslavije 1876–1996, Beograd. (in Serbian)
[7] Poznovija, M. (1991). Tehnologija sito-štampe I, Novi Sad: Zavod za izdavanje udžbenika; Radosavljević V. 2000. Konzervacija i restauracija arhivske i bibliotičke građe i muzejskih predmeta od tekstila i kože. Beograd: Arhiv Srbije i Arhiv Vojvodine. (in Serbian)
[8] de Almeida, M. R., Correa, D. N., Rocha, W. F. C., Scafi, F. J. O., & Poppi, R. J. (2013). Discrimination between authentic and counterfeit banknotes using Raman spectroscopy and PLS-DA with uncertainty estimation. Microchemical Journal, 109, 170-177. https://doi.org/10.1016/j.microc.2012.03.006
[9] Nadim, C. S., Zumbuehl, S., Delavy, F., Fritsch, A., Kuehnen, R. (2009). Synthetic organic pigments of the 20th and 21st century relevant to artist's paints: Raman spectra reference collection. *Spectrochimica Acta Part A*, 73, 505-524. https://doi.org/10.1016/j.saa.2008.11.029
[10] Schulte, F., Brzezinka, K.-W., Lutzenberger, K., Stege, H., & Panne, U. (2008). Raman spectroscopy of synthetic organic pigments used in 20th century works of art. J. Raman Spectrosc. 39, 1455-1463. https://doi.org/10.1002/jrs.2021
[11] Caggiani, M. C., Cosentino, A., Mangone, A. (2016). Pigments Checker version 3.0, a handy set for conservation scientists: A free online Raman spectra database. Microchemical Journal, 129, 123-132. https://doi.org/10.1016/j.microc.2016.06.020

Author's contact:

Gordana JAUKOVIĆ, PhD student of Belgrade University,
Senior Associate, National Bank of Serbia,
Communication Department, Unit for Exhibitions and Education,
12 Kralja Petra St, 11 000 Beograd, Serbia
gordana.jaukovic@nbs.rs
gordana.jaukovic@gmail.com

ISSN 1846-6168 (Print), ISSN 1848-5588 (Online)
https://doi.org/10.31803/tg-20190817135410

Preliminary communication

VORTEX COOLED AIR TURNING OF INDUCTION-HARDENED RACEWAY ON THE WIND TURBINE-BEARING RING

Mladen BOŠNJAKOVIĆ, Olivera MAGLIĆ, Dragomir MOŠKUN, Zoran CRNAC

Abstract: In the turning process of hard materials with CBN cutting inserts, metalworking fluid is not advisable as it results in poorer quality of finished surface and shortening of the tool life. Dry machining, otherwise, develops excessive heat, residual stresses in the workpiece material due to thermal stress, and therefore causes possible problems of achieving tolerances on larger workpieces. During the dry turning of induction hardened raceway on the wind turbine-bearing ring of 1500 mm in diameter, problems with achieving tolerances occurred. The vortex-cooled air implementation during turning resulted in achieving designing tolerances of the workpiece, with better surface roughness and with less tool wear. The result was 50% lower cost of cutting inserts and small operating costs associated with air consumption. The vortex-cooled air implementation makes it possible to extend the tool life of CBN cutting inserts and thus higher cost-effectiveness of machining.

Keywords: cost-effectiveness of machining; turning; vortex-cooled air

1 INTRODUCTION

The industrial world is slowly moving toward dry machining as the technology of the future. Development of environmental awareness, concern for human health, and law regulations force industrial production to avoid using cutting fluids and turn to develop and improvement of dry machining.

Drivers for the implementation of a dry cutting are in particular companies with series production in the field of automobile manufacturers and their suppliers. But the transformation from wet to dry cutting comes along with major problems, strong heating of the workpiece during dry cutting, higher tool wear, and finally, thermally caused dimension and form deviations [1]. F. Klocke et al. developed a model to predict and compensate the thermoelastic workpiece deformation [2].

Problems arising from the dry cutting process are specific to each process and each combination of tool-workpiece materials. To apply dry cutting, the most significant changes in the design of manufacturing systems are linked to cooling, additional equipment and adaptation of cutting processes to the new restrictions [3]. Requirements for high dimensional accuracy are still a limiting factor for the application of dry machining. The cooling during the process is necessary when there is strong adhesion between the tool and workpiece or when tool wears is too intensive, or when it is not possible to control the thermal deformation of the workpiece.

A necessary precondition for implementation of dry machining is an acceptable substitution of the functions of cooling and lubricating agents. In first investigations, regular compressed air was used, and its performance was inferior to water and oil [4]. Implementation of cold compressed air obtained better results. Nandy and others had shown that the use of a cold compressed air maximizes tool lifetime and machining productivity, giving the opportunity to use higher machining parameters related to dry machining [5, 6].

Cutting fluids could be replaced by cold compressed air, to cool and to remove chips from cutting area. Compared to cutting fluids, this technique significantly cut production costs, and it is not harmful to the environment and human health [7]. Applying cold air to the tool interface of these modern tooltip will also extend their tool life reducing the cost of metal-cutting.

With regard to the workpiece type, implementing dry machining instead of conventional wet machining will get savings of total costs for 17%. This will happen due to the elimination of cutting fluids, cleaning of the machine, maintenance and removing cutting fluids [8].

Cho and other investigated influence of cold compressed air at −4 °C to −25 °C pressure of 4 bar and showed that lowering the air temperature will increase surface quality and decrease residual stress [9].

Cooling with cold compressed air is usually performed by vortex tube.

The vortex tube is known as the Ranque-Hilsch vortex tube. It is a device that enables separation of hot and cold air during the flow of compressed air through an inlet nozzle tangential to the vortex chamber. Vortex tube was invented in 1933 by a French metallurgist and physicist Georges Ranque and improved by German physicist Rudolf Hilsch.

Although the basic work principle of the vortex tube is known, details of the process are still investigated, recently with Computational fluid dynamics (CFD) simulation [10]. Besides that, the influence of the geometry of the vortex tube to fluid stream parameters is also investigated.

The vortex tube is a simple device, which does not have moving parts and simultaneously produces a hot and cold stream of air at two ends from the source of compressed air.

It consists of a long tube that has a tangential nozzle at one end and valve at the other end, as shown in Fig. 1. Compressed air is introduced in the tube by a tangential nozzle that creates a vortex of the inlet air stream (in some cases over million rounds per minute) [11].

Air vortex is moving toward an adjustable valve at the hot end that controls the volume of the airflow and the temperature existing at the cold end. By adjusting the valve, you control the "cold fraction", which is the percentage of the total input of compressed air that exits the cold end of the Vortex Tube.

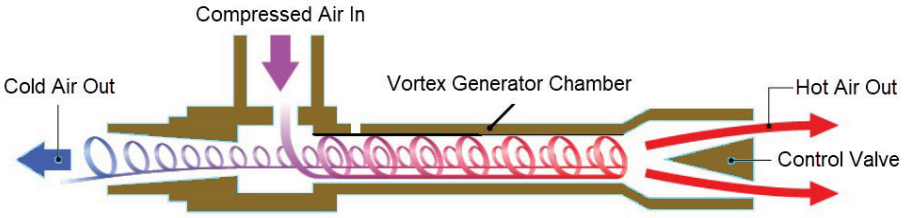

Figure 1 Scheme presenting Ranque-Hilsch tube

The adjustable valve leaks smaller part of the swirling air along the wall of the tube (20% to 40%), and central part of air vortex is directed in the opposite direction creating inner vortex through outer air vortex. Inner vortex transfers heat to outer vortex near the wall and, with a significant decrease of temperature, air exits on the cold end of the tube. Outer vortex near tube wall exits on the opposite end with a temperature higher than the temperature of inlet air. Vortex tube has many possible industrial applications and could be used as a cooling device at CNC machines, in refrigerators, heating processes, etc. High applicability of vortex tube is based on its simplicity, compactness and the fact that the system has a small mass and works in quiet mode. These tubes do not have moving parts, so they do not break or wear which makes them simple for maintenance.

Application of cold air will decrease the temperature at the cutting area during machining; it will decrease the temperature of tool, chip and workpiece due to intense heat removal by convection which emphasizes the importance of convection coefficient for tool temperature modelling. Convection coefficient for cutting fluids based on water is in the range from 103 to 104 W/(m^{2}K). Convection coefficient for cold air was investigated for the first time by Liu and Chou [12] and in simulation, it has values in range 50-5000 W/(m^{2}K), while in the experiment it is about 160 W/(m^{2}K) with applied air of temperature up to −15 °C and 860 W/(m^{2}K) for cooling with air with temperature up to −25 °C.

2 MATERIAL AND METHODS

2.1 Problem Definition

Example of machining without using cutting fluid is turning on a big vertical turning machine with maximal diameter 4270 mm with an embedded CNC control system. Although the machine is equipped with an emulsion cooling system, the manufacturer of the CBN (cubic boron nitride) inserts recommends turning without coolant. In accordance with this recommendation, induction hardened ring raceways for big axial bearings were performed.

Final machining of hardened raceway bearing was tried with PCBN (polycrystalline cubic boron nitride) insert without emulsion cooling because due to high temperature in cutting area cooling liquid evaporated and the insert would be damaged.

Machining of material 42CrMo4 was experimentally investigated by Sutter et al [13]. They determined that at cutting speed around 20 m/s, the temperature measured near the tool-chip interface achieved a maximal value of 870 °C for 42CrMo4. The increase of the cutting speed from 10 m/s to 65 m/s raises continuously the chips' temperature and influence the location of the maximal temperature.

Table 1 Workpiece basic data

Description	Values
Item name	Inner ring
Number of workpieces	27
Material designation	42CrMo4V
Material condition	Rolled ring, hardened and tempered at 800-900 MPa
Machining type	Final machining of induction hardened raceway with 56 HRC ±2 HRC for ball ⌀50

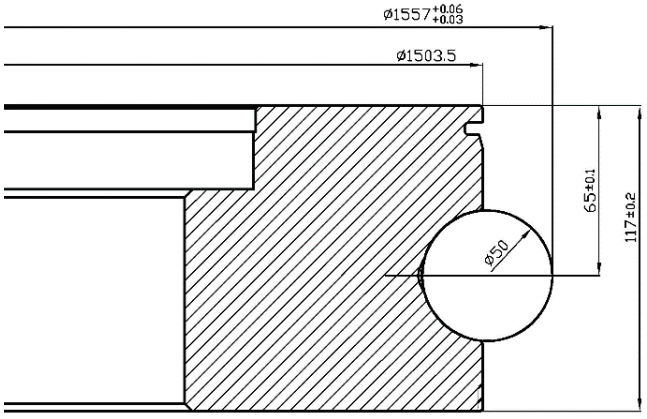

Figure 2 Scheme of inner ring

The dimension of the critical machined surface is measured by stick micrometer on balls ⌀50 which are set at 180º on a rolling raceway.

Two persons perform measuring – a worker on the machine and inspector. Results are recorded in the control list due to mounting ring in the axial bearing.

The problem that was noticed 24 hours after the final machining is the change in measure over balls for 0.1 mm to 0.2 mm which make impossible to mount two rings in the axial bearing. Rings had to be re-machined.

Requirements to the technology department were to find a solution for how to:

- decrease stress in the ring which is caused by thermal expansion due to higher ring temperatures during machining,
- perform dimensions in given tolerances,
- decrease tool costs.

All of these requirements should be realized with very limited funding resources.

2.2 Suggested Solution

Analysis of literature and taking into account economic and other limiting factors resulted in the proposal of application of cold air for cooling of the tool and workpiece. Installing a cold air nozzle is simple and requires only the installation of compressed air hose on the column of the machine. Accordingly, a SARA vortex tube was purchased.

Table 2 Vortex tube data

Description	Values
Supplier	SARA
Air pressure at the inlet	3 to 5 bars
Cold air outlet	lowest −48 °C
Hot air outlet	do 100 °C
Air consumption at 7-8 bar	270 l/min
Price of the device	€409 + VAT

Figure 3 Vortex tube

Table 3 Basic machine data

Description	Values
Machine	Vertical turning machine (See Fig. 3)
Year of production	1984.
Max. workpiece diameter	2500 mm
Max workpiece height	2000 mm
Total turning height	900 mm
Cooling system	Exist

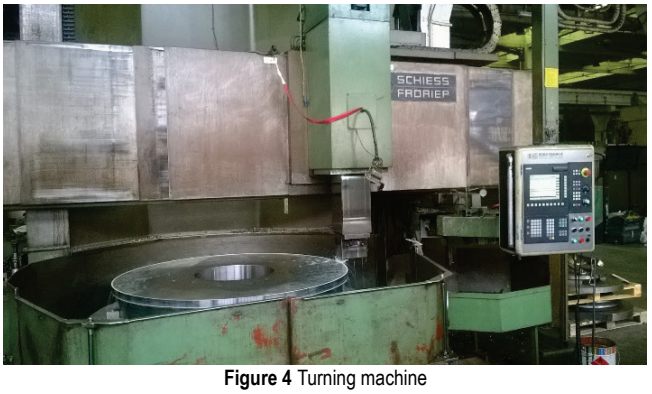

Figure 4 Turning machine

Optimal machining parameters according to the recommendations from literature presents a combination of low feed rate and low depth of cut with higher cutting speed, which is beneficial for reducing cutting temperatures, machining force and surface roughness (Tab. 4).

Table 4 Basic data for insert and final cutting parameters

Description	Values
Insert type	RCGX Full Face PCBN grade Insert size 0900700T-25VM 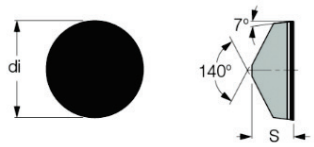
Tool holder	CRDCN 3225P 09-A 
Spindle speed	$n = 13$ min^{-1}
Feed rate	$s = 0{,}1$ mm/rev
Depth of cut	$a = 0{,}1$ mm
Pass interval	Raceway machining length $l = 83$ mm, number of passes $i = 7$ Insert machining time for 1 pass $t_1 = 63.85$ min Total insert machining time for $i = 7 \cdot t_1 = 446.95$ min

Table 5 Cooling data

Description	Values
Air pressure on input in a vortex tube	6 to 8 bars
Measuring instrument	 Rothewald Infra-Red digital thermometer with Laser Pointer
Temperature measuring range	−50 °C to 750 °C
Measured temperature	−11 °C (see Fig. 5)
Measuring accuracy	about ±2%

Figure 5 Temperature measurement of cold air on vortex tube outlet in workshop condition

Application of spot cooling of the tool with cold air during final machining of induction hardened raceway gave is shown in Figs. 6 and 7.

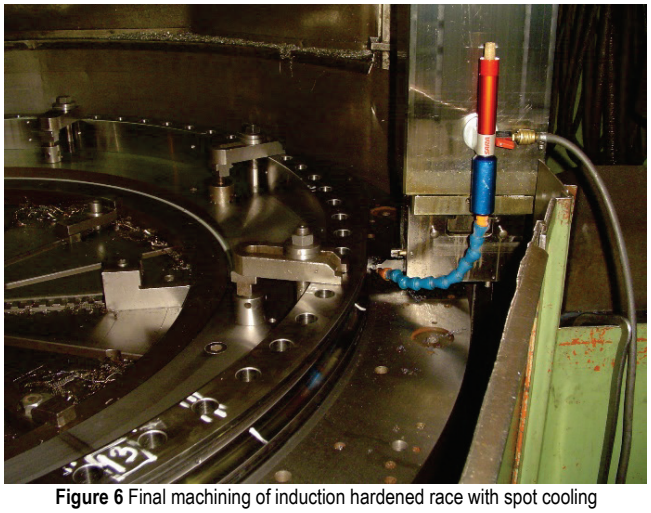

Figure 6 Final machining of induction hardened race with spot cooling

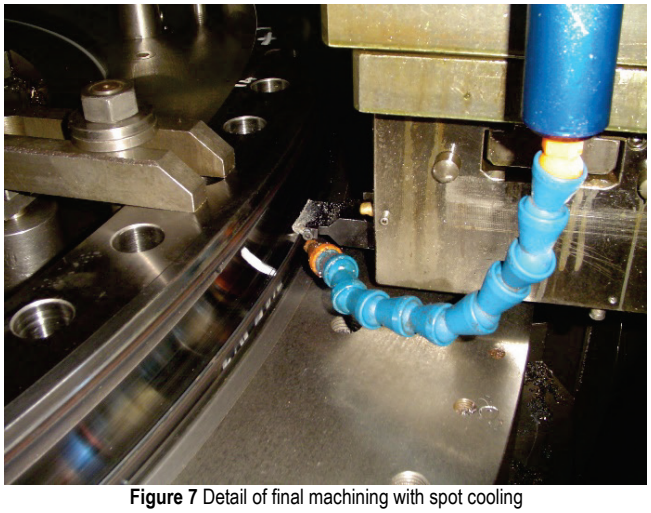

Figure 7 Detail of final machining with spot cooling

3 DISCUSSION

The following results have been obtained:

- First, it was noticed that there is no characteristic color of the machined chip.
- There is no characteristic point of burnout chips on cutting edge due to the fact that cold air decreases temperature in point of contact for cutting edge and raceway.
- During machining without cooling only one side of the insert was used for machining of one raceway (1 ring), and after the application of spot cooling, one side of the insert performed machining on two raceways (2 rings). That was a surprising result because the insert is expansive (135 €/piece) and it has only two sides (round insert which could be set in two positions). The durability of the insert was increased for 100% during machining of induction hardened raceway with one pass time of about 1 hour.
- The number of workpieces was 27 inner and 27 outer rings. It means that with spot cooling one insert machined 4 rings instead of only two; therefore, to machine the rings 14 inserts were spent instead of 28 inserts without cooling. This allows for significant savings. That is important information for the machining plan because ordering 20 inserts (minimum) costs less related to orders of only one insert which could cost from €160 to €215.
- When machined with spot cooling, the quality of surface finish is improved due to minimized heat input (also, material accumulation on the insert tip is less).
- Finally, decreasing of raceway roundness after final machining from 0.2 to 0.1 mm and changes in measure over balls is less than 0.1 mm, which means that there is no reason for additional machining of both rings before mounting.

The increase in operating costs due to cooling air consumption is not significant. For cost of 0.02 €/m^3 of the compressed air and consumption 0.27 m^3/h, the compressed air cost is €0.4 for an hour of the machine work.

4 CONCLUSION

Air spot cooling during turning of hard materials could extend tool life of CBN cutting inserts up to 100%, which could lead to significant savings at tool purchasing. Heat input in the hardened area had been significantly decreased, which decreased dimensional change measured 24 hours after final machining of the raceway. The quality of surface finish was improved, too.

In accordance with obtained results, the vortex tube air-cooling systems proved to be effective at dissipating the heat from the tool tip, proving that air-cooling is an effective method of cooling tool tip.

5 REFERENCES

[1] Dyck, M. (2007). *Beitrag zur Analyse thermisch bedingter Werkstückdeformationen in Trockenbearbeitungsprozessen*. Dr.-Ing. Dissertation wbk Institute of Production Science, Karlsruhe.

[2] Klocke, F., Kneer, R., Burghold, M., Deppermann, M., Peng, B., & Puls, H. (2018). Modelling and Compensation of Thermoelastic Workpiece Deformation in Dry Cutting. In: *Thermal effects in complex machining processes*. Lecture Notes in Production Engineering. *Springer*, Cham, Switzerland, 63-94. https://doi.org/10.1007/978-3-319-57120-1

[3] Aydin, M., Karakuzu, C., Uçar, M., Cengiz, A., & Çavuşlu, M. A. (2013). Prediction of surface roughness and cutting zone temperature in dry turning processes of AISI304 stainless steel using ANFIS with PSO learning. *International Journal of Advanced Manufacturing Technology, 67*(1-4), 957-967. https://doi.org/10.1007/s00170-012-4540-2

[4] Weinert, K., Inasaki, I., Sutherland, J. W., & Wakabayashi, T. (2004). Dry machining and minimum quantity lubrication. *CIRP Annals - Manufacturing Technology*, *53*(2), 511-537. https://doi.org/10.1016/S0007-8506(07)60027-4

[5] Sharma, V. S., Dogra, M., & Suri, N. M. (2009). Cooling techniques for improved productivity in turning. *International Journal of Machine Tools and Manufacture, 49*(6), 435-453. https://doi.org/10.1016/j.ijmachtools.2008.12.010

[6] Nandy, A. K., Gowrishankar, M. C., & Paul, S. (2009). Some studies on high-pressure cooling in turning of Ti-6Al-4V. *International Journal of Machine Tools and Manufacture,*

49(2), 182-198. https://doi.org/10.1016/j.ijmachtools.2008.08.008
[7] Duspara, M., Kosec, B., Stoić, M., Kramar, D., & Stoić, A. (2013). Application of vortex tube for tool cooling. *Journal of Production Engineering, 16*(2), 41-44.
[8] Lahres, M., Doerfel, O., & Neumüller, R. (1999). Applicability of different hard coatings in dry machining an austenitic steel. *Surface and Coatings Technology*, *120-121*, 687-691. https://doi.org/10.1016/S0257-8972(99)00359-X
[9] Choi, H. Z., Lee, S. W., & Jeong, H. D. (2002). The cooling effects of compressed cold air in cylindrical grinding with alumina and CBN wheels. *Journal of Materials Processing Technology*, *127*(2), 155-158. https://doi.org/10.1016/S0924-0136(02)00117-6
[10] Abdelghany, S. T. (2018). Three-Dimensional Computational Investigation of the Power Separation and Flow Anatomy in the Vortex Tube. *Journal of Scientific and Engineering Research, 5*(1), 197-212.
[11] Pinar, A. M., Uluer, O., & Kirmaci, V. (2009). Optimization of counter flow Ranque-Hilsch vortex tube performance using Taguchi method. *International Journal of Refrigeration*, *12*(6), 1487-1494. https://doi.org/10.1016/j.ijrefrig.2009.02.018
[12] Liu, J. & Kevin Chou, Y. (2007). On temperatures and tool wear in machining hypereutectic Al-Si alloys with vortex-tube cooling. *International Journal of Machine Tools and Manufacture,* 47(3-4), 635-645. https://doi.org/10.1016/j.ijmachtools.2006.04.008
[13] Sutter, G. & Ranc, N. (2007). Temperature fields in a chip during high-speed orthogonal cutting-An experimental investigation. *International Journal of Machine Tools and Manufacture*, *47*(10), 1507–1517. https://doi.org/10.1016/j.ijmachtools.2006.11.012

Authors' contacts:

Mladen BOŠNJAKOVIĆ, PhD, Assis. Prof.
Corresponding author
Technical Department, College of Slavonski Brod,
M. Budaka 1, 35000 Slavonski Brod, Croatia,
mladen.bosnjakovic@vusb.hr

Olivera MAGLIĆ, MSc
Technical Department, College of Slavonski Brod,
Dr. M. Budaka 1, 35000 Slavonski Brod, Croatia,
omaglic@vusb.hr

Dragomir MOŠKUN, MSc
Đuro Đaković Strojna obrada d.o.o.
dr. Mile Budaka 1, 35000 Slavonski Brod, Croatia
dmoskun@strojna-obrada.hr

Zoran CRNAC, MSc
Technical school,
E. Kumičića 55, 35000 Slavonski Brod, Croatia
zcrnac2@gmail.com

ISSN 1846-6168 (Print), ISSN 1848-5588 (Online)
https://doi.org/10.31803/tg-20190518181647

Preliminary communication

THE USE OF CEMENT CONCRETE PAVEMENTS FOR ROADS, DEPENDING ON CLIMATIC CONDITIONS

Iryna SOLONENKO

Abstract: The development of road network infrastructure is an important component of the economic development of the European Union. Updating of the road network contributes to the integration of the economies of countries into a coherent whole. The road network provides the free movement of citizens, the movement of goods and the effective implementation of various services. The increase in the length of the road network leads to an increase in the financial and material costs necessary to ensure its maintenance and repair. One of the ways to reduce costs is by strengthening the physic-mechanical and operational characteristics of the pavement due to the widespread use of cement concrete. The quality of the pavement of cement concrete depends largely on the rational selection of its composition. This allows a significant increase in the durability of road pavement. The purpose of the research was: the development of recommendations for the rational selection of the composition of the road pavement material of cement concrete, aimed at upgrading longevity, and taking into account its frost resistance grade. According to the goal, the following tasks were developed: the analyses of the climatic zones in which the road network of the European Union is located; the development of a research plan, a selection of the response function and influence factors; the study of physico-mechanical and operational characteristics of the researched material of road pavement; on the basis of the obtained data, the calculation of the complex of experimental-statistical models, which describe the physico-mechanical and operational characteristics of the road pavement material; on the basis of experimental statistical models, a method was proposed for selecting the rational compositions of the cement concrete pavement road material depending on the conditions of its application. The results presented in the article can be used in engineering and scientific practice for the selection of road pavement from cement concrete for highways.

Keywords: cement concrete; experimental statistical models; highway; road pavement; transport corridor; weather conditions

1 INTRODUCTION

The network of European roads has a considerable length. They ensure the stable development of the European Union (EU) countries. European roads are combined in a number of transport corridors. The main direction of traffic in these corridors: from north to south and from west to east. They enable the free movement of citizens and various goods and the performance of necessary services [1]. EU roads are directly adjacent to the road network of Belarus, Ukraine, Moldova and Russia. The distinctiveness of the roads of Ukraine and Moldova is the low quality of the road pavement, which is caused by the insufficient allocation of funds for their maintenance and repair.

As the analysis of the works [2, 3] shows, the condition of the roads mainly depends on the condition of the road pavement. The defects of road pavement (Fig. 1) significantly complicate the effective operation of vehicles, they reduce their speed and endanger traffic safety.

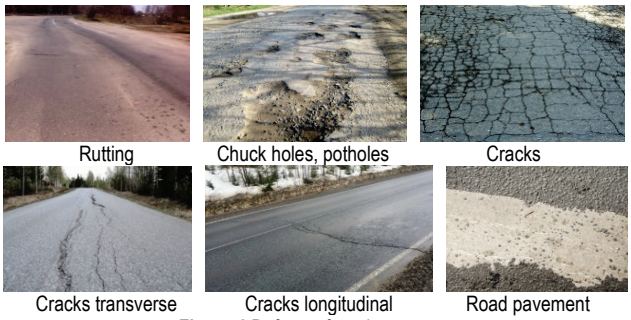

Figure 1 Defects of road pavement

The large length of EU roads (Tab. 1) requires significant funds for their maintenance and repair [4].

Table 1 The length of main roads, highways and specific sections of roads in the EU countries [4]

No.	Country	Main-line highway	Hard road pavement	Ground road pavement	General
1	Austria	2 223	200 000	0	202223
2	Belgium	1 763	120 514	33 498	155775
3	Bulgaria	801	43 649	440	44890
4	Great Britain	3 557	344 000	54 350	401907
5	Hungary	1 481	76 075	123 492	201048
6	Germany	12 917	644 480	0	657397
7	Greece	2 311	107 406	9 594	119311
8	Denmark	1 205	74 558	0	75763
9	Ireland	1 224	91 145	5 457	97826
10	Spain	16 583	683 175	0	699758
11	Italy	6 758	487 700	0	485458
12	Cyprus	254	8 564	4 442	13260
13	Latvia	0	14 707	57 737	72444
14	Lithuania	0	13 584	8 242	21 826
15	Luxembourg	152	2 899	0	3051
16	Malta	0	2 704	392	3 096
17	Netherlands	2 808	139 295	0	142103
18	Poland	1 566	292 134	131 863	425563
19	Portugal	2 992	71 294	11 606	85892
20	Romania	806	49 873	34 312	84 991
21	Slovakia	432	38 085	5 676	44193
22	Slovenia	618	38 985	0	39603
23	Finland	863	51 016	27 146	79025
24	France	11 882	1 028 446	0	1040328
25	Croatia	1 318	26 958	0	28276
26	Czech	1 250	130 671	0	131921
27	Sweden	2 050	579 564	0	581614
28	Estonia	115	10 427	47 985	58 527

An analysis of scientific publications [5, 6, 7] showed that a decrease in the operational costs of maintaining and repairing roads can be achieved by using cement concrete as a pavement material (Fig. 2).

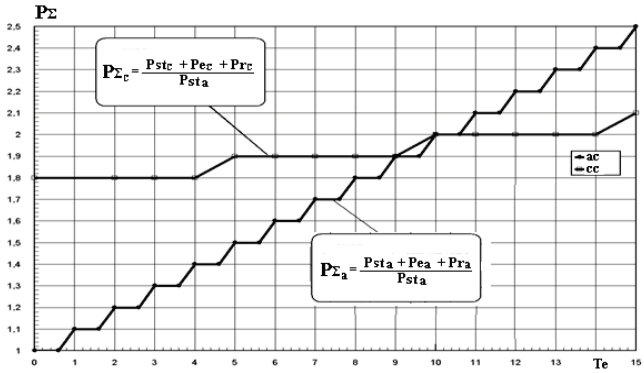

Figure 2 Relative construction cost ($P\Sigma$), maintenance and repair of roads bitominous with asphalt concrete and cement concrete (a - asphalt concrete, c - cement concrete, P_{st} - construction, P_e - content, P_r - repair, Te – road operation in time (in years), $P_{stc} = 1{,}8 \cdot P_{sta}$)

As it can be seen from Fig. 3, the total cost of construction and maintenance of highways made from cement concrete (c), after 10 years of operation, is lower than for the roads with asphalt concrete (a). Thus, the use of cement concrete coatings for the European Union countries reduces the cost of their maintenance and repair.

2 RESULTS AND DISCUSSION

An analysis of literary sources [7, 8, 9] showed that meeting the requirements on the durability of the cement concrete pavement for a highway can be achieved by a rational selection of its composition. The pavement is significantly affected by loads caused by traffic and climatic conditions.

The existing normative document EN 206-1 [10] (Tab. 2) does not take into account the frost resistance of the cement concrete pavement.

Table 2 Requirements for the material of the cement concrete pavement for roads (EN 206-1)

Characteristics	Demands
Water/cement (W/C)	0.45 ÷ 0.65
Class for compressive strength (MPa)	C 35/45 (45) ÷ C 40/50 (50)
Absorption of water, %	≥ 5
Frost resistance	-
Abrasion, mm	≥ 4
Air entrainment, %	4-7

With the purpose of studying the effect of the freeze-thaw temperature on the compressive strength and abrasion of the pavement material of cement concrete, researches have been conducted.

The purpose of the research was: the development of recommendations for a rational selection of the composition of the road pavement material of cement concrete, aimed at upgrading longevity, taking into account its frost resistance grade.

According to the goal, the following **tasks** were developed:

- the analyses of the climatic zones in which the road network of the European Union is located;
- the development of a research plan;
- the study of physico-mechanical and operational characteristics of the researched material of the road pavement;
- on the basis of the obtained data, the calculation of the complex of experimental-statistical models, which describe the physico-mechanical and operational characteristics of the road pavement material;
- on the basis of experimental statistical models, a method was proposed for selecting the rational compositions of the cement concrete pavement road material depending on the conditions of its application.

An analysis of the works [8, 9, 11] showed that the durability of the coating for highways made of cement concrete is significantly affected by the frost resistance of the material. The resistance of the pavement material to the effects of alternating temperatures is important for climatic zones with unstable negative temperatures (Fig. 2, Tab. 3). In these zones, throughout the entire winter period, repetitive cyclical freeze-thawing of the road pavement is happening.

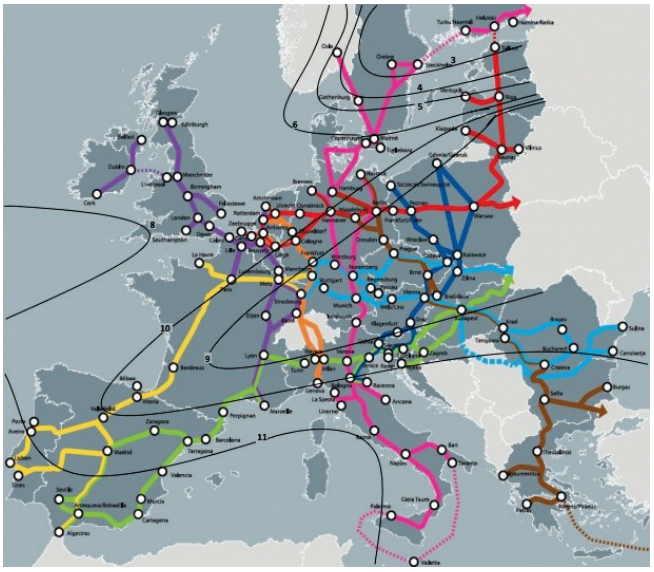

Figure 3 The location of the main roads of the EU countries in climatic zones

As it can be seen from Fig. 2, the roads of the European Union lie in different climatic zones. Therefore, different requirements for frost resistance should be imposed to the pavement material, depending on the climatic zones.

According to the works [7, 8, 9], an improvement in the frost resistance of cement concrete can be achieved by introducing an air-entraining additive into its composition, as well as a microsilica suspension filler. An increased resistance to the abrasion of the material is provided by the introduction of fibre material in the concrete. This composition allows the factors that influence the frost resistance of the pavement material to be determined (Tab. 4). The range of changes in the number of added components was determined on the basis of the recommendations of the MAPEI firm [12], an analysis of literature [11] and the personal experience of the author [9].

Table 3 Temperature range in winter time depending on the climatic zones

No. of zones	Celsius temperature (°C)	The number of freeze-thaw cycles	
		for 1 year	for 10 years
3	−40 … −34	4	40
4	−34 … −29	5	50
5	−29 … −23	5	50
6	−23 … −18	6	60
7	−18 … −12	8	80
8	−12 … −7	12	120
9	−7 … −1	20	200
10	−1 … +4	55	550
11	more +4	0	0

Table 4 Influencing factors and the range of their changes used in research

Impact factors			
x_1 –	air entraining agent additive Mapeplast PT-1		
x_2 –	polypropylene fiber MAPEFIBRE NS 12/ NS 18		
x_3 –	microsilicasuspension filler		
Range of factors change			
Levels of varying factors	x_1, l/m^3	x_2, kg/m^3	x_3, kg/m^3
Interval	0,142	0,3	7,5
Upper (+1)	0,285	0,6	15
Lower (−1)	0	0	0

The main characteristics of the additives and fillers used:
- air entraining agent additive Mapeplast PT-1 ("MAPEI"), its inclusion into the concrete mix provides an increase in the amount of the entrapped air (designed to increase the frost resistance of concrete);
- microsilica suspension, particle size 0.1-0.2 microns, specific surface area – 20 000 m^2/kg (designed to increase the strength of concrete and frost resistance, reduces abrasion and the permeability of concrete, etc.);
- polypropylene fibre - Mapefibre NS 12/NS 18 ("MAPEI"), diameter – 0.34 mm, fibre length 12-18 mm, density – 9,1×10-4 kg/m^3, tensile strength – 700 MPa, (increases the crack resistance of concrete and makes it resistant to abrasion).

The basic composition of the concrete mix for the manufacture of prototypes was determined by the method described in the article [9]:
- portland cement PC – I- H 500 - 470 kg/m^3;
- granite chippings (fractions 5÷20) - 1055 kg/m^3;
- sand (fineness modulus = 2.5) - 578 kg/m^3;
- superplasticizing admix Dynamon Easy 11 firms of "MAPEI" firms – 8.55 l/m^3;
- for adding water to the mix, distilled water was used.

The experiment plan is presented in Tab. 5.

At each point of the experiment plan, at least three experiments were conducted with the subsequent determination of the average value of the measurement result. To eliminate the influence of systematic errors caused by external conditions, the order of the experiments was randomized.

The experiments were conducted in the following sequence:
- the necessary amount of additives and fillers were added into the basic composition of the concrete mixture (Tab. 4);
- for each point of the experiment plan, the required number of samples was formed in the sizes of 0.1×0.1×0.1 meters and 0.07×0.07×0.07 meters [13];
- the obtained samples (Fig. 4a)) were maintained under the standard curing of a normal set for 28 days (t = 20 °C, W = 80%) [13];
- on the 28th day, samples of 0.07×0.07×0.07 meters were tested for an abrasion test (LKI-3 device) [14];
- the samples of 0.1×0.1×0.1 meters were tested for compressive strength [13];
- the part of the samples of 0.07×0.07×0.07 and 0.1×0.1×0.1 meters were tested for frost resistance in the freezer (in the freezing room temperature of −50 °C [15]);
- after testing for frost resistance (F50, F 100, F150, F 200), the samples (Fig. 4b)) were tested for the abrasion test and compressive strength [13, 14].

Table 5 The plan of the experiment and the compositions of the studied concretes

The plan of experiment				The composition of concrete		
No	x_1	x_2	x_3	PT-1, l/m^3	Fibre, kg/m^3	Microsilica suspension, kg/m^3
1	−1	−1	−1	0	0	0
2	−1	1	−1	0	0.60	0
3	0	0	−1	0.142	0.30	0
4	1	−1	−1	0.285	0	0
5	1	1	−1	0.285	0.60	0
6	−1	0	0	0	0.30	7.50
7	0	−1	0	0.142	0	7.50
8	0	0	0	0.142	0.30	7.50
9	0	1	0	0.142	0.60	7.50
10	1	0	0	0.285	0.30	7.50
11	−1	−1	1	0	0	15
12	−1	1	1	0	0.60	15
13	0	0	1	0.142	0.30	15
14	1	−1	1	0.285	0	15
15	1	1	1	0.285	0.60	15

a) b)

Figure 4 The material research: a) material samples prior to freezing and the thawing test; b) material samples after freezing and the thawing test (F 200)

The results of the experiments are presented in Tab. 6.

The convenience of the analysis for Tab. 6 is shown in a graphical form in the Figs. 5 and 6.

As it can be seen from the presented data (Fig. 5), the compositions used for the manufacture of the samples No. 1, 2, 3, 4 can be used as road pavement on the sections of roads that are not affected by the freeze-thaw.

Under the influence of the freeze-thaw temperature, the compressive strength of these samples decreases:
- for the sample No. 1 at: F50 – 3.1%, F100 – 8.1%, F150 – 9.5%, F200 – 14.2%;
- for the sample No. 2 at: F50 – 4.6%, F100 – 8.4%, F150 –11.8%, F200 – 15.6%;

- for the sample No. 3 at: F50 – 3.2%, F100 – 6.4%, F150 – 9.2%, F200 – 13.2%;
- for the sample No. 4 it comes down to: F50 – 1.9%, F100 – 5.4%, F150 – 8%, F200 – 9.3%.

The compressive strength of the remaining samples subjected to frost resistance tests, even after F200, was more than 50 MPa, which allows its use in all climatic zones.

Table 6 The results of the experiments on the compressive strength and abrasion under the cyclic effects of the freeze-thaw test (*F*)

The results of the experiments										
	$f_{ck.cube}$ (MPa)					G (kg/m^2)				
No	$f_{ck.cube0}$	$f_{ck.cube50}$	$f_{ck.cube100}$	$f_{ck.cube150}$	$f_{ck.cube200}$	G_0	G_{50}	G_{100}	G_{150}	G_{f200}
1	2	3	4	5	6	7	8	9	10	11
1	50.25	48.70	46.20	45.50	43.15	0.062	0.065	0.067	0.068	0.071
2	52.60	50.30	48.40	46.70	44.80	0.030	0.033	0.036	0.038	0.039
3	51.80	50.20	48.60	47.20	45.20	0.048	0.050	0.052	0.054	0.057
4	50.10	49.15	47.40	46.10	45.45	0.067	0.069	0.072	0.074	0.076
5	53.40	52.90	52.00	51.10	50.35	0.033	0.036	0.039	0.042	0.045
6	54.60	53.90	52.70	52.00	51.45	0.037	0.040	0.043	0.045	0.048
7	54.20	53.80	52.40	51.20	50.35	0.048	0.053	0.057	0.059	0.061
8	55.20	54.70	53.90	52.00	51.45	0.038	0.040	0.042	0.044	0.047
9	54.70	53.15	52.50	51.70	50.75	0.029	0.032	0.035	0.036	0.039
10	53.75	53.00	52.10	51.40	50.50	0.037	0.039	0.041	0.043	0.046
11	56.50	56.10	55.40	54.90	53.90	0.058	0.060	0.063	0.066	0.069
12	57.80	57.00	56.10	55.20	54.30	0.025	0.028	0.033	0.036	0.039
13	55.45	55.00	54.10	53.25	52.80	0.037	0.039	0.043	0.045	0.048
14	54.90	54.00	53.25	52.30	51.80	0.045	0.048	0.054	0.057	0.062
15	55.00	54.50	54.00	53.85	53.20	0.029	0.031	0.034	0.036	0.038

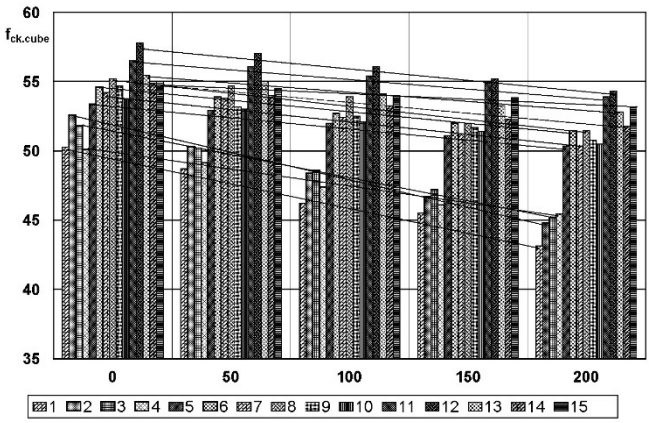

Figure 5 The results of the testing samples for abrasion before and after freezing and the thawing test (F0, F50, F 100, F150, F 200)

As it can be seen from Fig. 6, the abrasion of road pavement depends on the number of freeze-thaw cycles. An analysis of the data shown in (Fig. 6) proved that the samples of the material in which the loss of mass G was the following were the best in frost resistance:

- for the sample No. 2 at: F50 – 0.033 kg/m^2, F100 – 0.036 kg/m^2, F150 – 0.038 kg/m^2, F200 – 0.039 kg/m^2;
- for the sample No. 5 at: F50 – 0.036 kg/m^2, F100 – 0.039 kg/m^2, F150 – 0.042 kg/m^2, F200 – 0.045 kg/m^2;
- for the sample No. 9 at: F50 – 0.032 kg/m^2, F100 – 0.035 kg/m^2, F150 – 0.036 kg/m^2, F200 – 0.039 kg/m^2;
- for the sample No. 15 at: F50 – 0.031 kg/m^2, F100 – 0.034 kg/m^2, F150 – 0.036 kg/m^2, F200 – 0.038 kg/m^2.

The worst indicators have the following samples: No. 1, No. 4, No. 7, No. 11 and No. 14.

As it can be seen from Figs. 5 and 6, the dependence of the change in compressive strength and the loss of mass of the specimens at abrasion under the influence of freeze-thaw temperatures have the appearance close to linear. This means that it is possible to significantly reduce the number of experiments by limiting them only to the extreme values of freeze-thaw resistance tests (Fig. 6, $f = 0$ and $f = 200$) with their subsequent linear approximation.

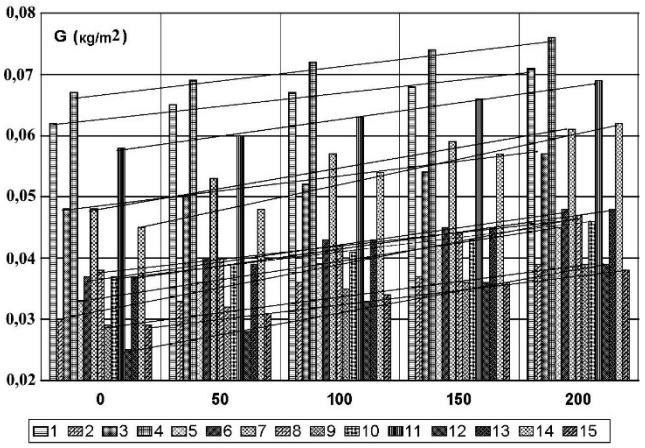

Figure 6 The results of the testing samples for compressive strength before and after freezing and the thawing test (F0, F50, F 100, F150, F 200)

The data used from Tab. 6 with the help of the Compex program [16] were obtained by ES-models in the form of a polynomial dependence of the form:

$$y = b_0 + \sum_{i=1}^{n} b_i x_i + \sum_{i=1}^{n} \sum_{k=i+1}^{n} b_{ik} x_i x_k + \sum_{i=1}^{n} \sum_{k=i+1}^{n} \sum_{l=k+1}^{n} b_{ikl} x_i x_k x_l + ..., \quad (1)$$

Where: y – the response function, b_0, b_{ik}, b_{ikl} – coefficients of the multiple regression equation, x_i – normalized value of the influence factor.

For the convenience of calculating mathematical models, the scale of the factors of influence was chosen so that the

value of the upper level was equal to +1, and the lower to –1. The origin of the coordinates of the influence factors was transformed and the transition to the normalized value of each factor was made:

$$x_i = \frac{\left(\tilde{x}_i - \tilde{x}_{i0}\right)}{I} \tag{2}$$

Where: x_i – normalized value; $\tilde{x}_i$ – natural value; $\tilde{x}_{i0}$ – main level; I – variability interval:

$$I = \left|\tilde{x}_i - \tilde{x}_{i0}\right| \tag{3}$$

The description of the methods for calculating the coefficients of regression models is beyond the scope of this article, but if necessary, you can refer to the works [16, 17].

The calculated mathematical models describing the change in the compressive strength ($f_{ck.cube0}$, $f_{ck.cube200}$) and abrasion (G_0, G_{200}) of the pavement material before and after the freezing thawing resistance test of the test samples (F 200) are presented in Tab. 7.

Table 7 Mathematical models describing the change in the compressive strength ($f_{ck.cube0}$, $f_{ck.cube200}$) and abrasion (G_0, G_{200}) of the pavement material before and after the freezing thawing resistance test

No	Response function	ES-models	
1	$f_{ck.cube0}$ (MPa) =	$54.49 - 0.46x_1 - 0.63x_1x_3 + 0.75x_2 - 0.53x_2x_3 + 2.15x_3 - 0.71x_3^2$	(4)
2	G_0 (kg/m^2) =	$0.04 + 0.002x_1x_2 - 0.002x_1x_3 - 0.01x_2 + 0.002x_2x_3 - 0.04x_3 + 0.004x_3^2$	(5)
3	$f_{ck.cube200}$ (MPa) =	$51.29 + 0.28x_1 - 0.85x_1x_3 + 0.24x_2 - 0.31x_2x_3 + 2.69x_3$	(6)
4	G_{200} (kg/m^2) =	$0.05 + 0.001x_1x_2 - 0.002x_1x_3 - 0.01x_2 + 0.003x_2^2 + 0.001x_2x_3 - 0.003x_3 + 0.006x_3^2$	(7)

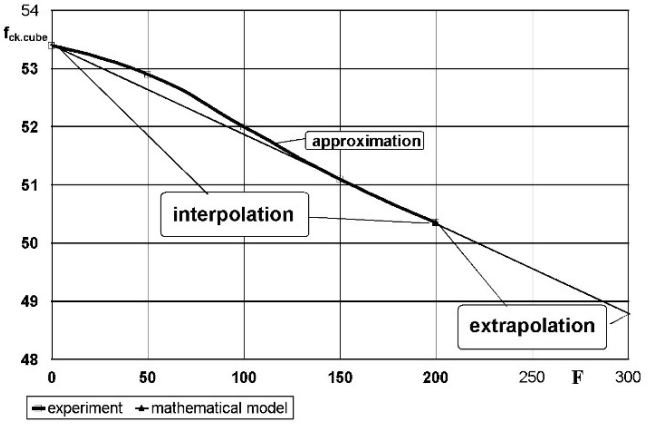

Figure 7 The example of using the mathematical models No. 1 and 3 for assessing the resistance of the sample No. 5 to the effect of the freeze-thaw cycles (F) on compressive strength

The obtained mathematical models allow us to determine the indicators of compressive strength and the abrasion of the road pavement material with a different combination of influence factors lying in predetermined intervals (Tab. 7).

To convert the results of the calculations using mathematical models into real physical quantities, a reverse transition from a standardized scale to a natural scale was made, using Eq. (2). The illustration of the use of mathematical models (for the sample No. 5) is presented in the Figs. 7 and 8.

The calculations of the compressive strength and abrasion with consideration of the freeze-thaw resistance for cement concrete pavements are made in the following sequence:

- the substituting formulas 4 ÷ 7 (Figs. 7 and 8) and the data of the influence factors (Tabs. 4 and 5) will determine the values - compressive strength ($f_{ck.cube}$) and abrasion (G), when exposed to the freeze-thaw temperature (at $F = 0$ and $F = 200$ cycles);
- through the obtained values, linear interpolation is performed and if necessary, extrapolation of the results is performed (Figs. 7 and 8);
- according to the Fig. 3 and Tab. 3, the number of freeze-thaw cycles for one year is determined;
- depending on the cycle life of automotive coating and the number of freeze-thaw cycles, resistance to alternating temperatures for the entire life time of the pavement is determined;
- deferring the values of freeze-thaw cycles along the ordinate axis (OF), we build the axis perpendicular to the intersection with the direct defining $f_{ck.cube}$, and similarly for G.

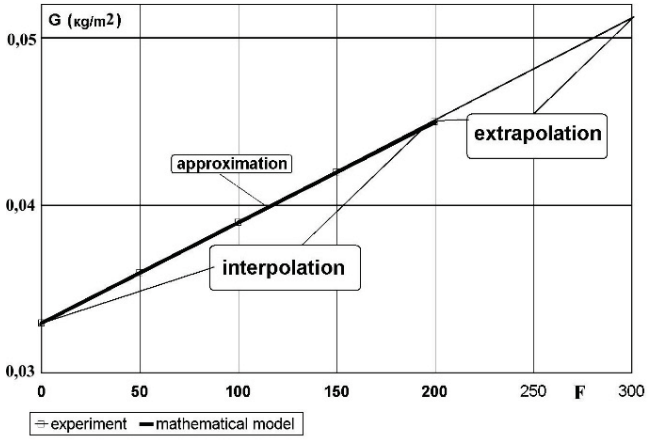

Figure 8 The example of using the mathematical models No. 2 and 4 for assessing the resistance of the sample No. 5 to the effect of freeze-thaw cycles (F) on abrasion

3 CONCLUSIONS

The researches have allowed the proposition of a method for determining the magnitude of changes in the compressive strength and weight loss of samples when the road pavement material is abraded under the influence of freeze-thaw temperatures.

An analysis of climatic zones in which the EU road network is located was carried out in order to determine the necessary freeze-thaw resistance of the road pavement material for each of them.

The study of changes in the properties of the pavement material depending on the number of freeze-thaw cycles has been carried out.

The recommendations for a rational selection of the composition of the pavement material of the cement concrete depending on the requirements for the freeze-thaw resistance were developed.

On the basis of the experimental statistical models obtained, a method is proposed for selecting the rational compositions of cement concrete road pavement materials, depending on the required freeze-thaw resistance.

When conducting research, additives and fillers from the MAPEI firm were used, which were kindly provided to the author by a representative of the company. If necessary, similar results can be obtained for the components from other manufacturer firms.

4 REFERENCES

[1] The European transport corridors [Electronic resource]. – Access mode: http://dergachev.ru/geop_events/210515-02.html#.XHZyGNDSjmZ (Available: 07 March 2019)

[2] The classification and description of typical road maintenance defects [Electronic resource]. – Access mode:http://www.steps.ru/article/klassifikatsiya_i_opisanie_tipichnyh_defektov_soderzhaniya_avtomobilnyh_dorog (Available: 09 March 2019)

[3] Shaikh Sameer J., Kanahya Bhutada, Sainath Poharkar, Devidas Chavade, & Kedarnath. (2018). Road Defects and Highway Maintenance. IOSR Journal of Mechanical and Civil Engineering (IOSR-JMCE), 15(2), Ver. II (Mar. - Apr.), 43-47. www.iosrjournals.org

[4] The length of highways in Europe [Electronic resource]. – Access mode: https://autotraveler.ru/spravka/road-length-in-europe.html#.XJFbDDpS__8. (Available: 05 March 2019).

[5] Solonenko, I. P. & Bratcheko, P. G. (2016). The harmonization of the regulatory framework of Ukraine with international requirements for road coverage. *The Sixth International Scientific and Practical Conference. Metrology, technical regulation, quality: achievements and prospects - OGATRK*, Odesa, 63-65.

[6] Vyrozhemskyi, V., Krayushkina, K., & Bidnenko, N. (2017). Durable high strength cement concrete topping for asphalt roads. *IOP Conference Series: Materials Science and Engineering*, 236, 012031. https://doi.org/10.1088/1757-899X/236/1/012031

[7] Pogorelov, S. N. & Semenyak G. S. (2016). Frost Resistance of the Steel Fiber Reinforced Concrete Containing Active Mineral Additives. Procedia Engineering, 150, 1491-1495. https://doi.org/10.1016/j.proeng.2016.07.088

[8] Delatte, N. J. (2014). *Concrete Pavement Design, Construction and Performance*, 2nd Ed., CRC Press, London. https://doi.org/10.1201/b17043

[9] Solonenko, I. P. (2015). The structure and properties of modified cement concrete coatings for highways, Dissertation. Sciences: spec. 05.23.05 *Construction materials and products* / I. P. Solonenko. OGASA. Odessa, 155 p.

[10] Concrete - Part 1: general of technological requirements, production and quality control. (EN 206-1) Per. from English Yu. S. Volkov. - Brussels, 2000. - 68 p.

[11] Mardani-Aghabaglou, A., Hosseinnezhad, H., Boyacı, O. C., Arıöz, Ö., Yaman, İ. Ö., & Ramyar, K. (2014). Abrasion resistance and transport properties of road concrete. Access mode: https://www.researchgate.net/publication/276334935_abrasion_resistance_and_transport_properties_of_road_concrete

[12] MAPEI. Agent additive for concrete and cement mortars. Access mode: http://ukrpolystroy.com.ua/shop/dobavka-mapei/

[13] DSTU B V.2.7-214:2009. Building materials. Concrete Methods of determining the strength of control samples. Kyiv, 2009, 35 p.

[14] DSTU B V.2.7-212:2009. Building materials. Concrete Methods of definition of erosion. Kiev, 2009, 8 p.

[15] DSTU B V.2.7-49-96:1997. Building materials. Concrete. The accelerated methods for determining frost resistance during multiple freezing and thawing. Kyiv, 1997, 10 p.

[16] Voznesensky, V. A. (1981). *The statistical Methods for Experimental Planning in Techno-Economic Research* / V. A. Voznesensky. 2nd ed. M.: Finance and Statistics, 263 p.

[17] Voznesensky, V. A. (1989). The numerical methods for solving construction and technological problems on a computer / V. A. Voznesensky, T. V. Lyashenko, B. L. Ogarkov. Kyiv: Vishcha School, 327 p.

Author's contact:

Iryna SOLONENKO, PhD, Head teacher
Odessa State Academy of Civil Engineering and Architecture,
4, Didrikhsona St., 65029 Odessa, Ukraine
Tel./Fax: +380974666579,
E-mail: odarina08@rambler.ru

ISSN 1846-6168 (Print), ISSN 1848-5588 (Online)
https://doi.org/10.31803/tg-20190328111708

Subject review

FINITE DIFFERENCE SOLUTION OF PLATE BENDING USING WOLFRAM MATHEMATICA

Katarina PISAČIĆ, Marko HORVAT, Zlatko BOTAK

Abstract: This article describes the procedure of calculating deflection of rectangular plate using a finite difference method, programmed in Wolfram Mathematica. Homogenous rectangular plate under uniform pressure is simulated for this paper. In the introduction, basic assumptions are given and the problem is defined. Chapters that follow describe basic definitions for plate bending, deflection, slope and curvature. The following boundary condition is used in this article: rectangular plate is wedged on one side and simply supported on three sides. Using finite difference method, linear equation system is given and solved in Wolfram Mathematica. System of equations is built using the mapping function and solved with solve function. Solutions are given in the graphs. Such obtained solutions are compared to the finite element method solver NastranInCad.

Keywords: Finite difference method; NastranInCad; Mathematica

1 INTRODUCTION

The article shows the implementation of the finite difference method in solving the plate bending problem. Due to the large number of equations, the system is solved using a computer. For these needs, appropriate symbolic programming software (Wolfram Mathematica, MATLAB, Mathcad, Sage, etc.) is selected and appropriate functions are used. In this paper, Wolfram Mathematica is used.

Bending of rectangular plates depends mostly on the ratio of plate thickness compared to other dimensions. Usually we differ the following:

1) small deflection thin plates,
2) large deflection thin plates,
3) thick plates.

If deflection of a thin plate comparing to plate thickness is relatively small, bending theory can be provided according to the following assumptions [1]:

1) There are no deformations in the middle cross section of the plate. This cross section is neutral during bending.
2) Points lined in neutral plane of a plate before deforming stay on a normal plane after bending.
3) Normal stress in transversal direction can be omitted.

With those assumptions plate deflection can be given as a function of two coordinates in the plate plane. This function complies with partial linear differential equations that together with boundary conditions define plate deflections. If some conditions cannot be satisfied, then additional conditions should be defined or some additions to formula should be given to define problem in a satisfactory way.

2 DEFLECTION AND CURVATURE OF A RECTANGULAR PLATE

The middle plane of a plate we define as *xy* plane. While the plate is bending, particles of *xy* plane are moved for a small displacement *w* and shape the middle plane of a plate (elastic plane). The change of deflection shown in Fig. 1 equals:

$$\partial w = \frac{\partial w}{\partial x}\partial x + \frac{\partial w}{\partial y}\partial y \tag{1}$$

Slope in this case is:

$$\frac{\partial w}{\partial n} = \frac{\partial w}{\partial x}\frac{\partial x}{\partial n} + \frac{\partial w}{\partial y}\frac{\partial y}{\partial n} = \frac{\partial w}{\partial x}\cos\alpha + \frac{\partial w}{\partial y}\sin\alpha \tag{2}$$

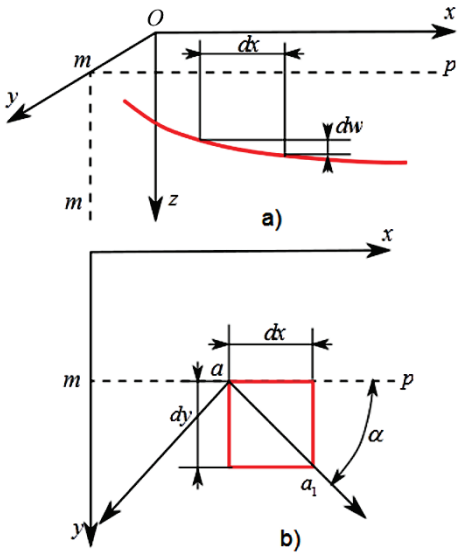

Figure 1 Slope of a middle plane [1]

When determining curvature of plate with small deflections, the slope in any direction is equal to the corresponding angle which tangent on a surface makes with axes *x* and *y* [1]. It follows:

$$\frac{1}{r_x} = -\frac{\partial}{\partial x}\left(\frac{\partial w}{\partial x}\right) = -\frac{\partial^2 w}{\partial x^2} \tag{3}$$

$$\frac{1}{r_y} = -\frac{\partial}{\partial y}\left(\frac{\partial w}{\partial y}\right) = -\frac{\partial^2 w}{\partial y^2} \tag{4}$$

For any direction:

$$\frac{1}{r_n} = -\frac{\partial}{\partial n}\left(\frac{\partial w}{\partial n}\right) = -\frac{\partial^2 w}{\partial n^2} \tag{5}$$

$$\frac{1}{r_n} = \frac{1}{r_x}\cos^2\alpha - \frac{1}{r_{xy}}\sin 2\alpha + \frac{1}{r_y}\sin^2\alpha \tag{6}$$

where:

$$\frac{1}{r_x} = -\frac{\partial^2 w}{\partial x^2},\ \frac{1}{r_y} = -\frac{\partial^2 w}{\partial y^2} \tag{7}$$

$$\frac{1}{r_{xy}} = \frac{\partial^2 w}{\partial x \partial y} \tag{8}$$

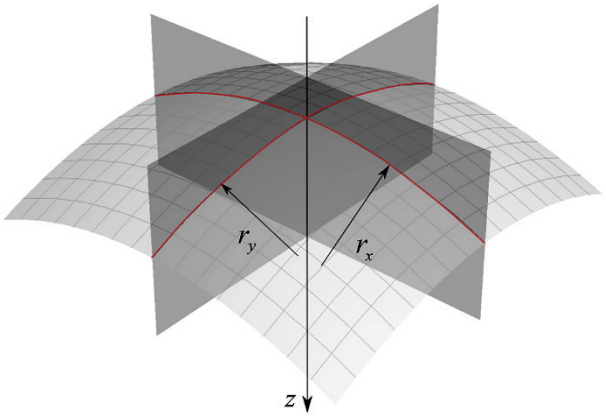

Figure 2 Curvature of a middle plane

3 RELATION BETWEEN BENDING MOMENTS AND CURVATURE

When bending the beam, the assumption is that the beam section is unformed and rotates around the neutral axis so that its position is normal in relation to the elastic line. Axis z is perpendicular to the middle plane and directed downwards (Fig. 3).

Elongations of elementary layer *abcd* are shown in Fig. 4:

$$\varepsilon_x = \frac{z}{r_x}, \tag{9}$$

$$\varepsilon_y = \frac{z}{r_y}. \tag{10}$$

Matching strains are:

$$\sigma_x = \frac{E_z}{1-\nu^2}\left(\frac{1}{r_x} + \nu\frac{1}{r_y}\right) \tag{11}$$

$$\sigma_y = \frac{E_z}{1-\nu^2}\left(\frac{1}{r_y} + \nu\frac{1}{r_x}\right) \tag{12}$$

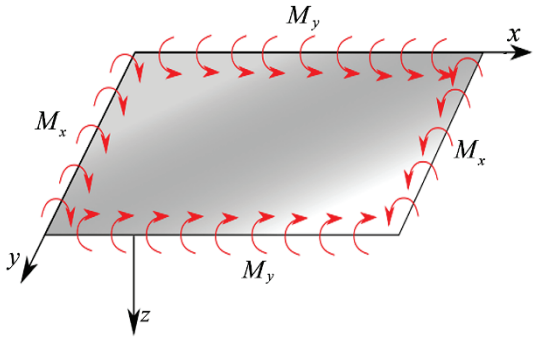

Figure 3 Pure bending [1]

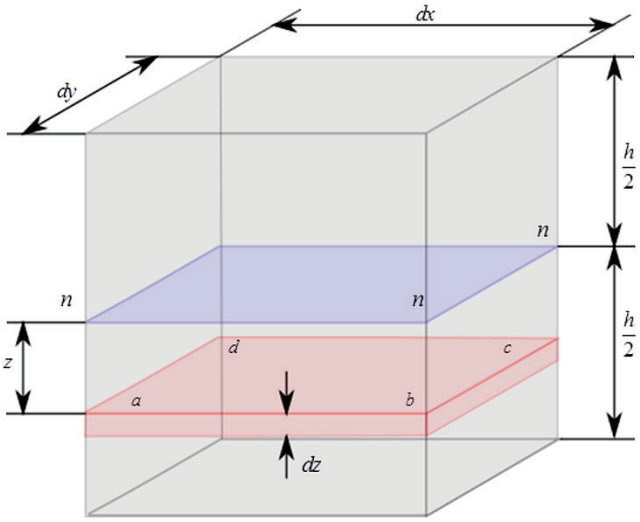

Figure 4 Differential element with elementary layer

Normal stresses can be replaced with moments:

$$\int_{-h/2}^{h/2} \sigma_x z \, \mathrm{d}y\mathrm{d}z = M_x \mathrm{d}y \tag{13}$$

$$\int_{-h/2}^{h/2} \sigma_y z \, \mathrm{d}x\mathrm{d}z = M_y \mathrm{d}x \tag{14}$$

Substituting (9) and (10):

$$M_x = D\left(\frac{1}{r_x} + \nu\frac{1}{r_y}\right) \tag{15}$$

$$M_y = D\left(\frac{1}{r_y} + \nu\frac{1}{r_x}\right) \tag{16}$$

Where D is flexural rigidity:

$$D = \frac{Eh^3}{12(1-\nu^2)} \tag{17}$$

4 DIFFERENTIAL EQUATIONS OF PLATE BENDING

We assume that the load on the surface is perpendicular to the surface and that the deflections are small compared to the thickness of the surface. At the borders we assume that the boundaries of the plates are free and these reactions are perpendicular to the plate, and the deformation of the central surface is neglected.

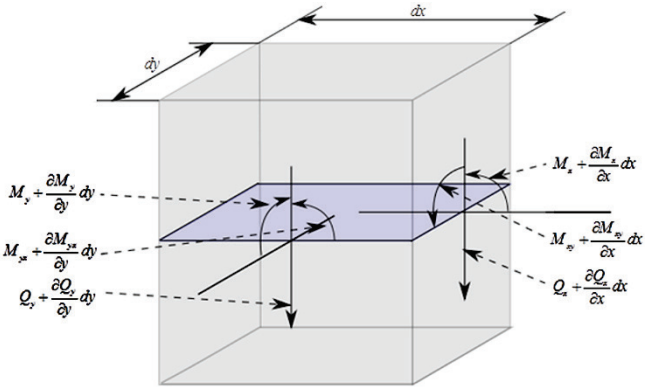

Figure 5 Bending of a differential element [1]

Shear forces shown in Fig. 5 are:

$$Q_x = \int_{-h/2}^{h/2} \tau_{xz} \mathrm{d}z \tag{18}$$

$$Q_y = \int_{-h/2}^{h/2} \tau_{yz} \mathrm{d}z \tag{19}$$

Taking into consideration all moments and forces the following equilibrium equation is:

$$\frac{\partial M_{yx}}{\partial y}\mathrm{d}x\mathrm{d}y + \frac{\partial M_x}{\partial x}\mathrm{d}y\mathrm{d}x - Q_x \mathrm{d}x\mathrm{d}y = 0 \tag{20}$$

Simplified:

$$\frac{\partial M_{yx}}{\partial y} + \frac{\partial M_x}{\partial x} - Q_x = 0 \tag{21}$$

Equation of differential element is:

$$\frac{\partial^2 M_x}{\partial x^2} + \frac{\partial^2 M_y}{\partial y^2} + 2\frac{\partial^2 M_{xy}}{\partial x \partial y} = -q \tag{22}$$

Moments are equal to:

$$M_x = -D\left(\frac{\partial^2 w}{\partial x^2} + \nu \frac{\partial^2 w}{\partial y^2}\right) \tag{23}$$

$$M_y = -D\left(\frac{\partial^2 w}{\partial y^2} + \nu \frac{\partial^2 w}{\partial x^2}\right) \tag{24}$$

and

$$M_{xy} = -M_{yx} = D(1-\nu)\frac{\partial^2 w}{\partial x \partial y} \tag{25}$$

Deflection equation is [1, 2, 3, 4]

$$\frac{\partial^4 w}{\partial x^4} + 2\frac{\partial^4 w}{\partial x^2 \partial y^2} + \frac{\partial^4 w}{\partial y^4} = \frac{q}{D} \tag{26}$$

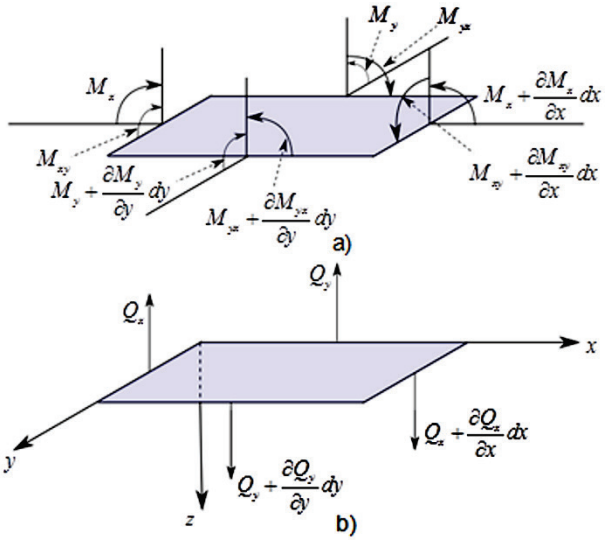

Figure 6 Middle plane of differential element [1]

5 BOUNDARY CONDITIONS

Assuming the plate is rectangular and the edges are parallel to coordinate axes, we set boundary conditions for the plate.

5.1 Wedged Edge

If the edge is wedged, deflection on the edge equals zero and tangential plane is corresponding to middle plane of unloaded plate. For edge $x = a$

$$(w)_{x=a} = 0\,, \tag{27}$$

$$\left(\frac{\partial w}{\partial x}\right)_{x=a} = 0 \tag{28}$$

5.2 Freely Supported Edge

If the edge $x = a$ is freely supported, deflection on the boundary must be zero and bending moment must be zero; the conditions are the following:

$$(w)_{x=a} = 0 \tag{29}$$

$$\left(\frac{\partial^2 w}{\partial x^2} + \nu \frac{\partial^2 w}{\partial y^2}\right)_{x=a} = 0 \tag{30}$$

6 FINITE DIFFERENCE METHOD

Finite difference method is a numerical method for solving differential equations. While solving problem of plate bending, derivations of functions of deflection, moment and shear force are approximated by finite differences of deflection in neighboring points. These points are called nodes and they represent finite difference mesh [4, 5]. When solving plate bending, we use two-dimensional mesh, shown in Fig. 7.

The definition of derivation is a starting point for finite difference method:

$$\left(\frac{\mathrm{d}\phi}{\mathrm{d}x}\right) = \lim_{\Delta x \to 0} \frac{\phi(x_i + \Delta x) - \phi(x_i)}{\Delta x} \tag{31}$$

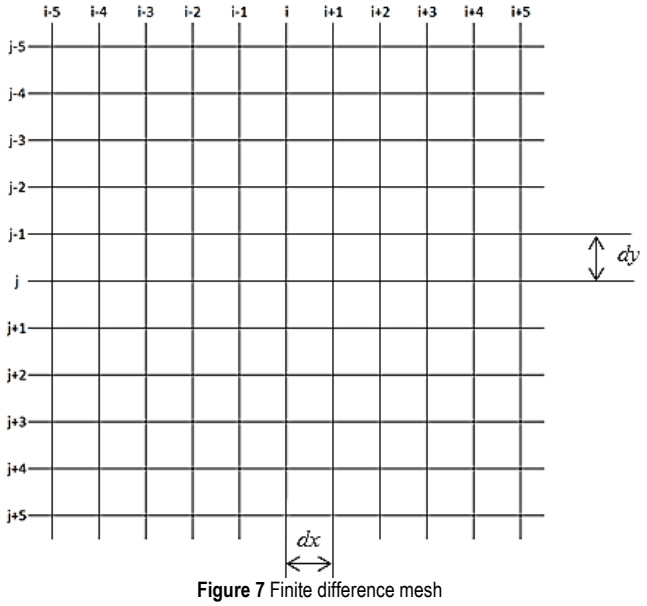

Figure 7 Finite difference mesh

Fig. 8 shows derivation as a tangent of a function $\phi(x)$. We can approximate the tangent of a function with the line which represents forward difference, backward difference or central difference [5]

Forward difference is given by:

$$\left(\frac{\mathrm{d}\phi}{\mathrm{d}x}\right)_i = \frac{\phi_{i+1} - \phi_i}{x_{i+1} - x_i} = \frac{\phi_{i+1} - \phi_i}{\Delta x} \tag{32}$$

Forward difference is calculated by:

$$\left(\frac{\mathrm{d}\phi}{\mathrm{d}x}\right)_i = \frac{\phi_{i+1} - \phi_i}{x_{i+1} - x_i} = \frac{\phi_{i+1} - \phi_i}{\Delta x} \tag{33}$$

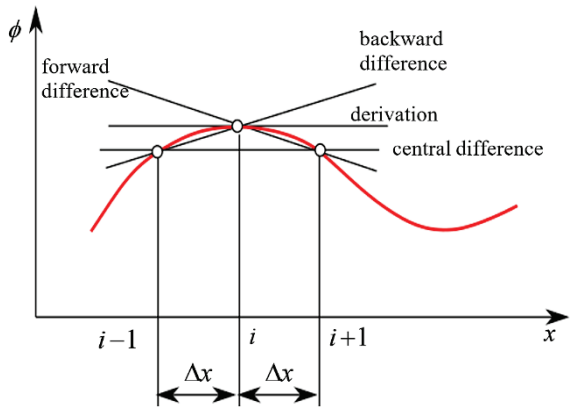

Figure 8 Finite difference schemes

Backward difference is calculated by:

$$\left(\frac{\mathrm{d}\phi}{\mathrm{d}x}\right)_i = \frac{\phi_i - \phi_{i-1}}{x_i - x_{i-1}} = \frac{\phi_i - \phi_{i-1}}{\Delta x} \tag{34}$$

Central difference:

$$\left(\frac{\mathrm{d}\phi}{\mathrm{d}x}\right)_i = \frac{\phi_{i+1} - \phi_{i-1}}{x_{i+1} - x_{i-1}} = \frac{\phi_{i+1} - \phi_{i-1}}{2\Delta x} \tag{35}$$

Using central difference derivatives have following forms:

$$\frac{\partial w}{\partial x} = \frac{w_{i+1,j} - w_{i-1,j}}{2\Delta x} \tag{36}$$

$$\frac{\partial w}{\partial y} = \frac{w_{i,j+1} - w_{i,j-1}}{2\Delta y} \tag{37}$$

$$\frac{\partial^2 w}{\partial x^2} = \frac{w_{i+1,j} - 2w_{i,j} + w_{i-1,j}}{\Delta x^2} \tag{38}$$

$$\frac{\partial^2 w}{\partial y^2} = \frac{w_{i,j+1} - 2w_{i,j} + w_{i,j-1}}{\Delta y^2} \tag{39}$$

$$\frac{\partial^4 w}{\partial x^4} = \frac{w_{i+2,j} - 4w_{i+1,j} + 6w_{i,j} - 4w_{i-1,j} + w_{i-2,j}}{\Delta x^4} \tag{40}$$

$$\frac{\partial^4 w}{\partial y^4} = \frac{w_{i,j+2} - 4w_{i,j+1} + 6w_{i,j} - 4w_{i,j-1} + w_{i,j-2}}{\Delta y^4} \tag{41}$$

$$\frac{\partial^4 w}{\partial x^2 \partial y^2} = \frac{w_{i+1,j+1} - 2w_{i+1,j} + w_{i+1,j-1} - 2w_{i,j+1} + 4w_{i,j} - 2w_{i,j-1} + w_{i-1,j+1} - 2w_{i-1,j} + w_{i-1,j-1}}{\Delta x^2 \Delta y^2} \tag{42}$$

7 PLATE BENDING SOLUTION

In this paper, the problem of bending a rectangular plate with a continuous load across the surface will be solved. Plate has edges freely supported on three sides, and the fourth edge is wedged, as shown in Fig. 9. The rectangular plate is 5 mm thick and the size of the final element is 50 mm. The plate is loaded with a pressure of 20 MPa.

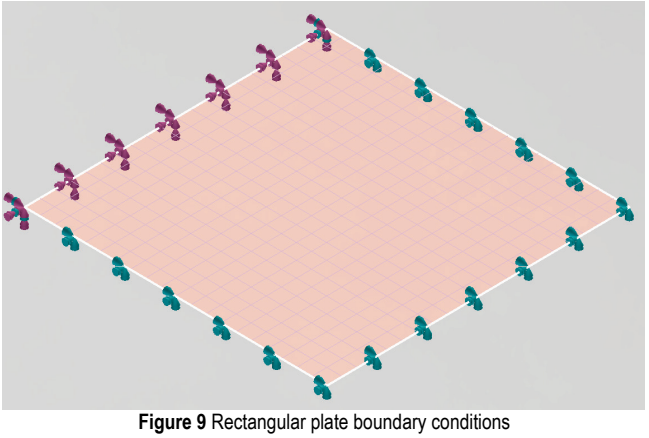

Figure 9 Rectangular plate boundary conditions

7.1 Wolfram Mathematica Code

The Wolfram Mathematica program was used to solve the system of algebraic equations. The matrix of the finite difference elements was created and by mapping function each element was mapped to corresponding expression of finite differences [7, 8]. Additional equations are set for edge elements, according to boundary conditions.

The code is given in segments:

1. We define constants.

```
v=0.3;
ee=210*10^9;
p=-20000;
h=5;
DD=(ee h^3)/(12 (1-v^2));
a=1000;
b=1a;
q0=p;
```

2. We define number of elements and boundary elements.

```
xmin=-(1/2)a;
xmax=1/2 a;
ymin=-(1/2)b;
ymax=1/2 b;
xdivisions=20;
ydivisions=20;
dx=(xmax-xmin)/xdivisions
dy=(ymax-ymin)/ydivisions
```

3. We define grid.

```
xmino=xmin-2dx;
ymino=ymin-2dy;
xmaxo=xmax+2dx;
ymaxo=ymax+2dy;
xgrid=Range[xmino,xmaxo,dx];
ygrid=Range[ymino,ymaxo,dy];
grid=Outer[{#1,#2}&,xgrid,ygrid];
```

4. We make an array of values for the solution. Each entry in the array corresponds to the value of the unknown function at a point in space.

```
W=Array[w,{xdivisions+5,ydivisions+5},{{xmino,xmax
o},{ymino,ymaxo}}];
WW=Array[w,{xdivisions+1,ydivisions+1},{{xmin,xma
x},{ymin,ymax}}];
```

5. We set find finite difference approximations for different derivatives of w.

```
dwdx=Table[(W[[i+1,j]]-W[[i-
1,j]])/(2*dx),{i,3,Length[xgrid]-2},{j,3,Length[ygrid]-2}];
dwdy=Table[(W[[i,j+1]]-W[[i,j-
1]])/(2*dy),{i,3,Length[xgrid]-2},{j,3,Length[ygrid]-2}];
dwdx2=Table[(W[[i+1,j]]-2W[[i,j]]+W[[i-
1,j]])/(dx^2),{i,3,Length[xgrid]-2},{j,3,Length[ygrid]-2}];
dwdy2=Table[(W[[i,j+1]]-2W[[i,j]]+W[[i,j-
1]])/(dy^2),{i,3,Length[xgrid]-2},{j,3,Length[ygrid]-2}];
dwdx4=Table[(W[[i+2,j]]-4W[[i+1,j]]+6W[[i,j]]-4W[[i-
1,j]]+W[[i-2,j]])/(dx^4),{i,3,Length[xgrid]-
2},{j,3,Length[ygrid]-2}];
```

```
dwdy4=Table[(W[[i,j+2]]-4W[[i,j+1]]+6W[[i,j]]-4W[[i,j-
1]]+W[[i,j-2]])/(dy^4),{i,3,Length[xgrid]-
2},{j,3,Length[ygrid]-2}];
dwdx2dy2=Table[(W[[i+1,j+1]]-2W[[i+1,j]]+W[[i+1,j-1]]-
2W[[i,j+1]]+4W[[i,j]]-2W[[i,j-1]]+W[[i-1,j+1]]-2W[[i-
1,j]]+W[[i-1,j-1]])/(dx^2*dy^2),{i,3,Length[xgrid]-
2},{j,3,Length[ygrid]-2}];
```

6. We specify boundary conditions.

```
(*Consider the left-side bc *)
    leftbc=Table[dwdx[[1,k+1]],{k,1,Length[ygrid]-6}];
    leftbcw=Table[W[[3,k+1]],{k,3,Length[ygrid]-3}];
(*Do the same for the right-side bc*)
    rightbc=Table[dwdx2[[-1,k+1]],{k,1,Length[ygrid]-6}];
    rightbcw=Table[W[[-3,k+1]],{k,2,Length[ygrid]-4}];
(*And for the bottom side boundary condition*)
    bottombc=Table[dwdy2[[k+1,1]],{k,1,Length[xgrid]-6}];
    bottombcw=Table[W[[k+1,3]],{k,2,Length[xgrid]-4}];
(*And for the top side bc*)
    topbc=Table[dwdy2[[k+1,-1]],{k,1,Length[xgrid]-6}];
    topbcw=Table[W[[k+1,-3]],{k,3,Length[xgrid]-3}];
```

7. We solve boundary equations.

```
(*takes the left boundary conditions, and solves them
to yield the values of w along the left side *)
        wleftw=NSolve[Map[#==0&,leftbcw],Table[W[[3,
        k]],{k,4,Length[ygrid]-2}]];
        wleft=NSolve[Map[#==0&,leftbc],Table[W[[2,k]],
        {k,4,Length[ygrid]-3}]];
(*takes the right boundary conditions, and solves
them to yield the values of w along the right side *)
        wrightw=NSolve[Map[#==0&,rightbcw],Table[W[
        [-3,k]],{k,3,Length[ygrid]-3}]];
        wrightt=NSolve[Map[#==0&,rightbc],Table[W[[-
        2,k]],{k,4,Length[ygrid]-3}]];
        wright=Flatten [wrightt/.wrightw,1];
(*takes the bottom boundary conditions, and solves
them to yield the values of w along the bottom side *)
        wbottomw=NSolve[Map[#==0&,bottombcw],Tab
        le[W[[k,3]],{k,3,Length[xgrid]-3}]];
        wbottomm=NSolve[Map[#==0&,bottombc],Tabl
        e[W[[k,2]],{k,4,Length[xgrid]-3}]];
        wbottom=Flatten [wbottomm/.wbottomw,1];
(*takes the top boundary conditions, and solves them
to yield the values of w along the top side *)
        wtopw=NSolve[Map[#==0&,topbcw],Table[W[[k,
        -3]],{k,4,Length[xgrid]-2}]];
        wtopp=NSolve[Map[#==0&,topbc],Table[W[[k,-
        2]],{k,4,Length[xgrid]-3}]];
        wtop=Flatten [wtopp/.wtopw,1];
(*This is a list of all the boundary values of w*)
        boundary1=Flatten[Join[wleft,wright,wtop,wbott
        om]];
    boundary2=Flatten[Join[wleftw,wrightw,wtopw,wb
    ottomw]];
```

8. We now create a set of equations. We make a table, with each entry corresponding to an interior grid point. Each entry in the table becomes an equation, from the discretized partial differential equation. We use our knowledge of the boundary conditions to eliminate the values of w on the boundary [7, 8].

```
equations=Map[(q0/DD==#)&,Flatten[Table[dwdx4[[i,
j]]+2*dwdx2dy2[[i,j]]+dwdy4[[i,j]],{i,2,xdivisions},{j,2,y
divisions}],1]/.boundary1/.boundary2];
```

9. We solve equations and substitute interior values of w into the equations.

```
intSol=NSolve[equations,Flatten[W[[4;;Length[xgrid]
-3,4;;Length[ygrid]-3]]][[1]];
boundarySol=boundary1/.intSol;
solution1=W/.intSol;
solutionArray1=solution1/.intSol/.boundary2;
solutionArray=solutionArray1[[3;;Length[xgrid]-
2,3;;Length[ygrid]-2]];
```

10. We make table of coordinates in three dimensional space and plot solution.

```
dataPoints=Table[{xmin+i*dx,ymin+j*dy,solutionArr
ay[[i+1,j+1]]},{i,0,Length[xgrid]-5},{j,0,Length[ygrid]-
5}];
Min[solutionArray]
ListPlot3D[Flatten[dataPoints,1],AxesLabel->
{Style[x,Medium,Blue],
Style[y,Medium,Blue],Style[u,Medium,Blue]},
PlotRange->All,ColorFunction-
>Function[{x,y,z},Hue[z]]]
```

7 SOLUTION

Using Wolfram Mathamatica program, the program code from the previous chapters, we obtained maximum deflection of 23.874 mm. A three dimensional graph of this solution is given in Fig. 10.

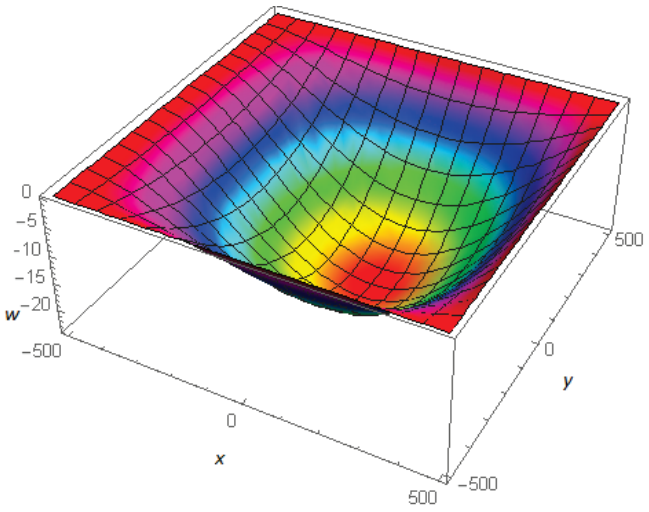

Figure 10 Finite difference solution

In order to prove that this solution is correct, the NastranInCad finite element analysis program was used. NastranInCad is used as a part of Autodesk Inventor. In the Inventor, the finite element method has the maximum error of 23.67 mm. This solution is shown in Fig. 11.

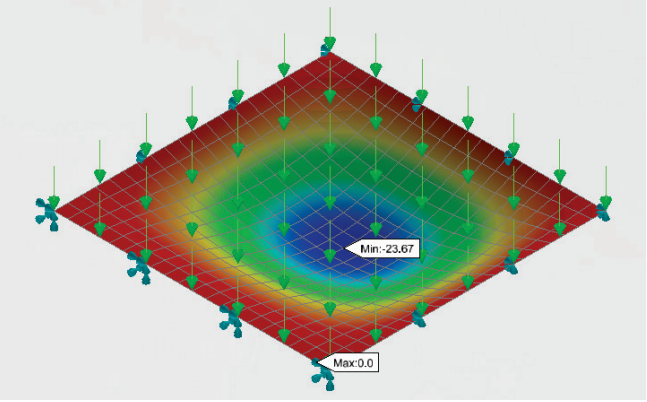

Figure 11 Finite element solution

8 CONCLUSION

To solve plate bending problem Wolfram Mathematica's mapping function was used to create a matrix of equations so that each element was provided with correct finite difference equation. Mathematica solver function NSolve was used for solving the system of equations.

It is also possible to program a custom method that is most appropriate for diagonal dominant matrices as used in [9]. Observing the terms, equations and elements, it is apparent that we deal with sparse matrices, and the built-in solver takes quite some time to compute the solution. Time is shortened by decreasing the number of elements, but then the solution has the larger error.

For this problem, when the element size is 50 mm, the deviation from finite element method is very small, the Mathematica solution is 23.87 mm, and Inventor solution is 23.67 mm for the maximum deflection. Unlike the manual calculation and the use of symbolic programming software, the use of finite element method (FEM) solver accelerates the computation process.

5 REFERENCES

[1] Timoshenko, S. & Woinowsky-Krieger, S. (1987). *Theory of plates and shells*, McGraw-Hill International Editions, Engineering Societies Monograph.

[2] Alfirević, I. (2011). *Linearna analiza konstrukcija*, Sveučilište u Zagrebu, Fakultet strojarstva i brodogradnje, Zagreb

[3] Grubišić, R. (1997). *Teorija konstrukcija I-dio, Primjeri statičke analize elemenata konstrukcije*, Sveučilište u Zagrebu, Fakultet strojarstva i brodogradnje, Zagreb.

[4] Radenković, D.(1953). *Bending of A Rectangular Plate Weakend By A Hole*, Beograd, Publication de l'Institut Mathématique, V(05),

[5] Sorić, J. (2009). *Uvod u numeričke metode u strojarstvu*, Fakultet strojarstva i brodogradnje, Zagreb 2009.

[6] Roknuzzaman, Md. Hossain, B., Haque, R., & Ahmed, T. U. (2015) Analysis of Rectangular Plate with Opening by Finite Difference Method, *American Journal of Civil Engineering and Architecture,* 3(5), 165-173.

[7] Nolting, B. *Numerically solving PDEs in Mathematica using finite difference methods,* http://datavoreconsulting.com/programming-tips/numerically-solving-pdes-mathematica-finite-differences/, available March 2019.

[8] Nolting, B. *Finite Difference Method (now with free code!),* http://datavoreconsulting.com/programming-tips/finite-difference-method-now-free-code/, available March 2019.

[9] Sertic, J., Kozak, D., & Scitovski, R. (2008) LU-decomposition for solving sparse band matrix systems and its application in thin plate bending. *Transactions of FAMENA*, 32(2), 41-48.

Authors' contacts:

Katarina PISAČIĆ, dipl. ing. mech., Senior Lecturer
(Corresponding author)
University North, University center Varaždin
104. brigade 3, 42000 Varaždin, Croatia
katarina.pisacic@unin.hr

Marko HORVAT, dipl. ing. mech., Lecturer
University North, University center Varaždin
104. brigade 3, 42000 Varaždin, Croatia
marko.horvat@unin.hr

Zlatko BOTAK, PhD, dipl. ing. mech., Senior Lecturer
University North, University center Varaždin
104. brigade 3, 42000 Varaždin, Croatia
zlatko.botak@unin.hr

ISSN 1846-6168 (Print), ISSN 1848-5588 (Online)
https://doi.org/10.31803/tg-20190215200430

Subject review

INTERNET OF THINGS AND SMART WAREHOUSES AS THE FUTURE OF LOGISTICS

Krešimir BUNTAK, Matija KOVAČIĆ, Maja MUTAVDŽIJA

Abstract: Innovations and market changes in warehouse and logistics systems force the adaptation and transformation of the existing business model into a business model based on modern technology. With the development of the Internet, RFID (radio-frequency identification) technology and sensors, new innovations are being created that allow the improvement of the existing mode of activity. Implementation of the new technology brings along a number of challenges that organizations must find an adequate response to. However, warehouse systems are not the only affected by the new technologies. The development of technology and technological innovations enable organizations to develop sustainability. Sustainable development is imperative due to increasing awareness of the need for environmental protection. The supply chain can also be managed much more efficiently if sensors that collect information of customer habits and process performance are implemented. Given the accelerating development of Industry 4.0 and the opportunities offered by newly developed technology, this paper provides an overview of current developments in the implementation of Industry 4.0 technological innovations in logistics.

Keywords: Internet of things; radio-frequency identification; smart technologies; supply chain; warehouses

1 INTRODUCTION

Along with the development of new technologies, new ways of managing warehouse systems and logistics operations are being developed. Internet technologies have made it possible to connect physical elements to the network, which is the basis for development of the IoT (Internet of Things).

The IoT is a network that interconnects physical elements capable of collecting performance information that evolves the process or its components such as machines and devices as well as enabling their management. [1]

Accordingly, this paper is based on the secondary research with the aim to present current trends in the development of technological innovations of industry 4.0 in logistics, which can determine the sustainable development of the organizational logistics system.

With the development of awareness of sustainable development, green logistics and the reduction of the impact of logistic and other operations on the environment, the applicability of IoT technology is increasing. IoT also allows control of individual components within logistic processes and systems and provides ongoing improvements based on the data collected by sensors placed inside and outside the installed warehouse infrastructure and superstructures.

The growth of the industry is the consequence of an increase in the emissions of harmful gases, especially carbon dioxide [2], which is an increasing problem for the environment.

Development of technology enables the reduction of the negative impact of economic growth. Newly developed technologies are often used in the environmental protection and securing the foundation for sustainable development.

The issue of environmental pollution is not the only problem that today's business organizations are facing. The demands of interested parties and the environment that is often susceptible to turbulence, places on the organization the imperative of developing new approaches that will meet the increasing demands in organizational environments.

Responding to the increasing demands for quality has influenced the development of continuous improvement systems. Permanent improvements are a particularly important factor for the logistics industry, which faces ecological challenges faced with competitiveness-related costs.

The supply chain consists of warehouses, transport organizations, manufacturers, etc. The importance of creating a sustainable development of the supply chain is increasing because warehouses, production systems, transport organizations and other stakeholders in the supply chain are large energy consumers, which means the release of large quantities of greenhouse gases. Optimization of the supply chain with the help of technological innovations of industry 4.0 enables reducing the amount of greenhouse gases emitted as well as increasing energy efficiency.

Furthermore, warehouses become automated under the pressure of the decline in human work efficiency, employee fluctuation dependency, natural migration, and the requirement to reduce the cost of logistical processes.

Costs of logistic processes directly correlate with the profitability and economic viability of the logistics system. By reducing them and implementing new technology that will enable efficiency and productivity increase, logistic systems become economically viable. The economic viability of the system is the basis for achieving ecological and social sustainability, which will, as a result, have a positive impact on the overall economy.

Existing systems used to monitor and manage performance, which as a result provide data that can be used to improve the system, should therefore be enhanced by technologies such as IoT. The effects of such technologies are long-term, and the return on invested resources is inevitable at later stages of business after their implementation.

2 REVIEW OF INDUSTRY 4.0 LITERATURE

IoT technology emerges in the 90th century of the last century. As the concept, it officially got its name in 1999 [3] but was officially introduced only in 2008. In 2010, the

Chinese economy recognized the importance of this technology and started investing in its development. [4]

Automation of production began in the 1950s, when robots were used for the first time in manufacturing for simple operations [5]. From 2000 to 2015, the use of industrial robots increased by 150% [6], whereby the trend of growth is evident. Automation of the manufacturing process has often been applied in the automotive industry where in the past 9 of 10 robots were sold to one of the car manufacturers. Furthermore, the importance of robotics and automation also comes from the fact that the number of robots that are implemented in the todays automotive industry is 50% of the total number of manufactured robots [7] which can imply a gradual return to human labor, or an increase in the number of industrial sectors that apply robots in their business.

Parallel to the development and implementation of robots in industrial production warehouses are implementing automated systems that allow faster and easier transportation of goods [7].

Traditionally, in warehouse, all products have been labeled with RFID technology developed during the 70s of the last century, enabling a revolutionary approach to improving warehouse operations and reducing storage costs. The development of RFID technology is based on IFF (Identification friend or foe) technology used during World War II. [8] Although the purpose of RFID was initially to be built into the automotive industry, the banking industry, security and healthcare, [9] later adaptation and refinement proved to be an ideal storage system. Robotization, automation and internet development transform traditional warehouses into warehouses that, through the IoT and modern computer support, improve their performance and, above all, productivity, efficiency and effectiveness.

Growth of globalization and the strengthening of capitalism increases the need for industrial development. Industry development results in increasing emissions of harmful gases. The first attempts to raise awareness of the issues and challenges related to ecological problems were first shown in 1962. In 1987, in the report published by WCED, the concept of sustainable development is mentioned for the first time in the history. Five years later, in 1992, the basic environmental goals were defined. In 2015, the UN defined the 17 sustainable development goals recommended by Member States [10], one of which is closely linked to IoT. [11]

Past trends have transformed traditional approaches to business and sustainability management into a modern approach based on technologies developed alongside the development of needs for a different approach and environmental protection relationship.

3 REVIEW OF RESEARCH

The topic of sustainable logistics and the IoT has often been explored and there is a considerable number of papers that closely deal with this topic, especially the impact of the IoT on warehouse and logistics systems. However, there are many of research papers that address the topic of the impact of Industry 4.0 on the logistics system. But there are few that provide an overview of all technologies affecting the logistics system. In accordance with this, this chapter provides an overview of all technologies affecting the logistics system.

3.1 Warehouse Systems and Industry 4.0

The warehouse system itself contains a large number of operations aimed at meeting the requirements of the interested parties. Lee, C.K.M., et al (2017) state that the development of industry 4.0 has affected a different way in which past activities within the warehouse are taking place. The fourth industrial revolution at the same time marked the use of the IoT technology in warehouses which reflected in the efficiency and performance of the storage systems. Traditional WMS (warehouse management system) is enhanced by the IoT, which exploits the full potential of RFID technology. With the IoT all activities as well as goods within the warehouse are controlled, which enables their manageability. However, the use of the IoT also entails the security issues of such systems as they may often become the target of online attacks. [12] Industry 4.0 does not only involve the use of the IoT, but also of other technologies that, through communication as one of the feedback components, have an impact on the improvement of logistic processes.

The IoT does not only affect warehouses and warehouse operations, but also the entire supply chain. Sensors as an integral part of this technology collect a large amount of data that affects the challenges associated with their storage and management. Machado and Shah emphasize that precisely because of this fact the existing warehouses have to be reorganized. In addition, by deploying intelligent systems to the warehouse, the logistic superstructure, which has so far been managed by employees, becomes autonomous, allowing it to move through the warehouse without or with a slight employee intervention. Furthermore, IoT provides immediate insight into inventory stock status. Particular importance is the ability to manage the entire supply chain as well as communication between its stakeholders. Real-time information enables logistical operators to gain insight into logistics operations, in particular the conditions under which freight transport is carried out by means of transport, which increases transparency and reduces the possibility of damage to goods [13].

3.2 Warehouses Based on Cyber-Physical System

Innovations that occur within industry 4.0 create new technologies that facilitate system management. The Cyber-Physical System (CPS) can track and create a virtual copy of the actual process that can be used to monitor process performance. In addition, the CPS is very similar to the IoT concept that allows all components within the system to communicate with one another i.e. that the physical components are virtually connected, allowing for cost savings in parallel with increasing efficiency. But, there is one big difference between the CPS and the IoT. The CPS is only focused on physical objects while it may be focused on creating network of things that are focused to service

providing. Warehouses based on this technology include RFID sensors, Bluetooth technology, Wi-Fi access points, cameras and robots that are coordinated in the system to perform a defined task. The role of a man in such a warehouse is primarily related to monitoring and reprogramming the system if necessary. However, the CPS technology also enables inter-machine co-operation between robotic systems, thus reducing the need for human work. Such designed robotic systems also enable human movement to recognize what enables employees to use robotic help in carrying out activities. [14] By replacing human labor with automated and robotized systems, or through the implementation of such systems as humanitarian aid, the efficiency of the warehouse system increases. Activities that are dangerous for a man can be robotized, thus reducing the risk of injury and unlucky cases.

3.3 IoT Conducted Inventory Management

The possibilities of using the IoT technology are growing in parallel with innovations. In the context of warehousing systems, the IoT allows the connection of previously unreliable physical components to the network, thus managing the storage facility and facilitating it. Particularly problematic components of each warehouse are inventories and operations associated with their management. Traditional systems in most cases include manual manipulations of inventory as well as inventory management based on human. However, by deploying sensors and linking them to the network, sensors can look at real-time inventory, which greatly facilitates their management. Therefore, the new warehouse system is based only on IT with human as an operator that only controls the process. This approach is based on RFID technology, which is the basis for deploying and using this approach. [15] The IoT and RFID technology not only simplify inventory deployment, but anticipate future orders, tracking product durability, temperature, humidity in the air, and other parameters that could affect product damage. RIFD technology is the foundation for the functioning and development of the IoT system. [16] The application of RFID technology in warehouse management has a number of advantages that primarily relate to increasing efficiency, accuracy and updating of information, as well as tracking stocks and inventory losses. [17] By implementing the IoT and RFID technology in organization's storage systems, they provide competitive advantage based on lower operating costs and greater efficiency of the process.

3.4 Impact of Warehousing on the Environment

Warehousing, just like logistics, is an activity that generates a certain amount of greenhouse gases. Poor energy efficiency of warehouses as well as environmentally unacceptable heating, air conditioning or lighting systems are just some of the factors that affect the amount of carbon dioxide discharged. In order to increase the ecological acceptance of storage processes, Đukić, Česnik and Opetuk (2010) propose the implementation of energy-efficient lighting, the production of electricity from renewable energy sources, energy-efficient building materials which, by their construction, are insulators, improvements in logistics supra-structure by improving the forklift, by installing automatic closing doors, etc. [18] On the other hand, Amith and Harrison (2013) emphasize that ecological acceptance of the storage system is ensured through awareness of the impact of such a system on the environment and suggest a warehouse design that will maximize the use of natural lighting, water supply and wastewater management systems, noise reduction to the surrounding community and improved temperature control. [19]

The transformation of the traditional logistics system into the environmentally sustainable results in the improvement of all elements of sustainable development. Reducing costs increases funding available to improve ecological acceptability, which also affects the social component of sustainability. Furthermore, through the optimization of the commissioning route through the WMS, it affects the performance that the logistics processes develop, that is, their efficiency, which ultimately results in greater sustainability. [18]

Many authors point out that logistics is one of the fundamental components that needs to be paid particular attention, especially in large cities where it is timely supplying the necessary resources, crucial to the development of all processes inherent in cities. [20] Robotics, automation, electrification, sensing as well as the application of the IoT technology, the storage system is managed more efficiently, which reduces the negative impact on the environment.

3.5 Future of Warehouse Systems

By implementing technologies of Industry 4.0, such as the IoT, warehouse systems become more efficient and their performance is improving. By automating warehouse operations, the warehouse system becomes less dependent and responsive to human work variability. By applying autonomous systems in transportation, transshipment-loading operations, and operations of palletized goods to warehouse regal, the flow of goods through warehouses becomes more fluent. However, autonomous systems must be tailored to the storage environment to minimize the risk of collisions. Existing autonomous systems in a large number of cases, by having a barrier remain standing in place, that is, they can only move through previously defined and narrowly restricted corridors. [21]

A potential solution to such and similar problems of implementation is the development of artificial intelligence that is capable of making decisions similar to man-made decisions. Robotic systems with artificial intelligence enable making simpler decisions and adaptation to new circumstances in the environment. [22] As such, artificial intelligence is already present in a number of daily-used technologies such as internet browsers as well as systems for predicting earthquakes and weather conditions. [23] The Deep Learning concept moves artificial intelligence and its application to a higher level through the ability of such systems to learn and improve their knowledge without the

need for human intervention. [24] The necessity of developing new warehouse management technology and automation of warehouse operations is growing with increasing storage space size. The potential for warehouse technology development is growing with the drop in the number of workforce available, which is one of the problems that EU countries face. [21] Increasing the demand of the interested parties and market growth is one of the conditions that are placed on storage systems, which is their flexibility and sensitivity to the requirements set. [25] Theresponse to such requests is often seen through the implementation of smart technologies that improve storage processes. One example of technology is glasses that signal an employee an item to take [26]. Further, the challenges facing storage systems in the future are the reason why an increasing number of organizations become virtual, allowing customers to create orders online and request that the purchased product be delivered to the required location [27].

The implementation of a large number of sensors generates a large amount of information and data stored on the foreseen servers. The Big Data Concept is a new paradigm for warehouse systems and organizations, enabling tracking and prediction of customer orders, resulting in easier stock management. [28] However, the implementation of smart systems as a result has some challenges and risks that need to be adequately managed.

One of the underlying challenges of warehouses based on industry 4.0 is their security. Security problems are related to risk of lack of data. Security problems are also related to the security on the Internet generally because all communications are based on an internet connection. This is explicitly related to the storage systems that have Big data databases implemented. The existing encryption methods are no longer sufficient to ensure a satisfactory level of security. Likewise, there is a lack of adequate software solutions for managing, analyzing, and printing such a large number of data. [29] Stealing or releasing information stored in databases as a result may have disruption of user privacy [30], i.e. logistic customer service. Because of the simplicity, convenience, speed and ease of logistic organization, they decide to use cloud computing technology that places data on servers that are often found in other countries. [31] The security of such systems does not only relate to encryption protection, but also to limit the availability of data. [32] But the challenges are not just about data protection, but also the need to reduce operating costs. It is very likely that part of the logistics and warehouse operations will be outsourced, i.e. that other companies which as a primary activity have no logistics will begin to outsource logistics operations. [33] Furthermore, one of the technologies that finds application in warehouse systems is augmented reality. Augmented reality lets you add real-time digital elements to reality. The use of such technology allows employees to be instructed and guided according to the place where the defined activities are to be performed. [34]

4 CONCLUSION

Almost all organizations operating in today's market are affected by the development of the Internet. [15] The development of the Internet is also developing technologies related to it, such as the IoT. Therefore, it is appropriate for the development and implementation of the IoT technologies to be in the focus of today's logistics industry and the improvement of warehouse systems. [35] The imperative to deploy industry-based 4.0 technologies stems from the requirement to maintain an organization's competitiveness.

Organizational completeness may be increased whit implementation and upgrading of the existing WMS to advanced IT solutions as well as through the implementation of solutions, technologies of industry 4.0 like it, Big Data, sensors, robots etc. [36]

By developing different organizational forms such as e-organization, the challenges and requirements encountered by storage systems are growing. One of the ways of adjusting is the automation and robotization of the warehouse system. Robotization does not mean completely replacing human work with machines, but increasing the efficiency of human work with robotic systems. [37] The use of robots in warehouses also means the possibility of increasing the rate of picking from warehouse shelf using the fastest or simpler route of movement, thus reducing total costs [38], and possibly by improving existing WMSs in warehouse systems that regulate and set up an order picker's route. Existence and level of warehousing system competitiveness depends on their ability to adapt to new technologies as the ability to meet customer requirements.

This secondary research found that industry 4.0 has a significant impact on warehousing operations, which are becoming more efficient by implementing technology such CPS, it and other industry-based 4.0 technologies. Future researchers are advised to conduct a primary survey aimed at identifying the number of warehouses that use Industry 4.0 technologies as well as identifying the type of technology they are using.

5 REFERENCES

[1] Wortmann, F. & Flüchter, K. (2015). Internet of things. *Business & Information Systems Engineering*, *57*(3), 221-224. https://doi.org/10.1007/s12599-015-0383-3

[2] Aye, G. C. & Edoja, P. E. (2017). Effect of economic growth on CO2 emission in developing countries: Evidence from a dynamic panel threshold model. *Cogent Economics & Finance*, *5*(1), 1379239. https://doi.org/10.1080/23322039.2017.1379239

[3] A Brief History of the Internet of Things. http://www.dataversity.net/brief-history-internet-things/ (11.08.2018)

[4] Internet of Things (IoT) History. https://www.postscapes.com/internet-of-things-history/ (12.08.2018)

[5] Grau, A., Indri, M., Bello, L. L., & Sauter, T. (2017, October). Industrial robotics in factory automation: From the early stage to the Internet of Things. In *IECON 2017 - 43rd Annual Conference of the IEEE Industrial Electronics Society* (pp. 6159-6164). IEEE. https://doi.org/10.1109/IECON.2017.8217070

[6] Grau, A., Indri, M., Bello, L. L., & Sauter, T. (2017, October). Industrial robotics in factory automation: From the early stage to the Internet of Things. In *IECON 2017 - 43rd Annual Conference of the IEEE Industrial Electronics Society* (pp. 6159-6164). IEEE. https://doi.org/10.1109/IECON.2017.8217070

[7] Robots in automobile industry. https://www.slideshare.net/NirajRajan/robots-in-automobile-industry-59415113 (10.08.2018)

[8] Ahuja, S. & Potti, P. (2010). An introduction to RFID technology. *Communications and Network*, *2*(3), 183-186. https://doi.org/10.4236/cn.2010.23026

[9] Cardullo, M. (2005). Genesis of the versatile RFID tag. *RFID Journal*, *2*(1), 13-15.

[10] Hedenus, F., Persson, M., & Sprei, F. (2016). *Sustainable Development. History, Definition & the Role of the Engineer*. Chalmers University of Technology.

[11] The effect of the Internet of Things on sustainability. https://www.weforum.org/agenda/2018/01/effect-technology-sustainability-sdgs-internet-things-iot/ (12.08.2018)

[12] Lee, C. K. M., Lv, Y., Ng, K. K. H., Ho, W., & Choy, K. L. (2018). Design and application of Internet of things-based warehouse management system for smart logistics. *International Journal of Production Research*, *56*(8), 2753-2768. https://doi.org/10.1080/00207543.2017.1394592

[13] Machado, H. & Shah, K. (2016). Internet of Things (IoT) impacts on Supply Chain. *Retrieved*, *19*, 2016.

[14] Ding, W. (2013). Study of smart warehouse management system based on the IOT. In *Intelligence computation and evolutionary computation* (pp. 203-207). Springer, Berlin, Heidelberg. https://doi.org/10.1007/978-3-642-31656-2_30

[15] Yerpude, S. & Singhal, T. K. (2018). SMART Warehouse with Internet of Things supported Inventory Management System.

[16] Jia, X., Feng, Q., Fan, T., & Lei, Q. (2012, April). RFID technology and its applications in Internet of Things (IoT). In *Consumer Electronics, Communications and Networks (CECNet), 2012 2nd International Conference on* (pp. 1282-1285). IEEE. https://doi.org/10.1109/CECNet.2012.6201508

[17] Krishna, A., Ravinchandra, L., Abdulla, R., & Thang, K. F. (2016). Smart Stock Management Control. *International Journal of Applied Engineering Research*, *11*(1), 492-500.

[18] Đukić, G., Česnik, V., & Opetuk, T. (2010). Order-picking methods and technologies for greener warehousing. *Strojarstvo, 52*(1), 23-31.

[19] Amjed, T. W. & Harrison, N. J. (2013). A Model for sustainable warehousing: from theory to best practices. In *Proceedings of the International Decision Sciences Institute and Asia Pacific DSI Conference*.

[20] Rakhmangulov, A., Sladkowski, A., Osintsev, N., & Muravev, D. (2017). Green logistics: element of the sustainable development concept. Part 1. *NAŠE MORE, 64*(3), 120-126. https://doi.org/10.17818/NM/2017/3.7

[21] Pechanová, Ľ., Stareček, A., Bachár, M., & Caganova, D. (2017). The suggestion for newspapers application improvement. 1-5. https://doi.org/10.1109/ICETA.2017.8102518

[22] Thamer, Hendrik & Börold, Axel & Yoga Benggolo, Ariandy & Freitag, Michael. (2018). Artificial intelligence in warehouse automation for flexible material handling.

[23] See https://ai.google/

[24] Kim, K. G. (2016). Book Review: Deep Learning. *Healthcare informatics research*, *22*(4), 351-354. https://doi.org/10.4258/hir.2016.22.4.351

[25] Brockmann, T. & Godin, P., 1997. Flexibility for the future in warehouse design. *IIE Solutions, 29*(7), pp.22-26.

[26] Diete, A., Weiland, L., Sztyler, T., & Stuckenschmidt, H. (2016, September). Exploring a multi-sensor picking process in the future warehouse. In *Proceedings of the 2016 ACM International Joint Conference on Pervasive and Ubiquitous Computing: Adjunct* (pp. 1755-1758). ACM. https://doi.org/10.1145/2968219.2968270

[27] Giannikas, E., Woodall, P., McFarlane, D., & Lu, W. (2017, July). The impact of B2C commerce on traditional B2B warehousing. In *ISL 2017: 22nd International Symposium on Logistics* (pp. 375-383). Nottingham University Business School.

[28] Rozados, I. V. & Tjahjono, B. (2014, December). Big data analytics in supply chain management: Trends and related research. In *6th International Conference on Operations and Supply Chain Management, Bali*.

[29] Toshniwal, R., Dastidar, K. G., & Nath, A. (2015). Big data security issues and challenges. *International Journal of Innovative Research in Advanced Engineering (IJIRAE)*, *2*(2).

[30] Terzi, D. S., Terzi, R., & Sagiroglu, S. (2015, December). A survey on security and privacy issues in big data. In *Internet Technology and Secured Transactions (ICITST), 2015 10th International Conference for* (pp. 202-207). IEEE. https://doi.org/10.1109/ICITST.2015.7412089

[31] Jadeja, Y. & Modi, K. (2012, March). Cloud computing-concepts, architecture and challenges. In *Computing, Electronics and Electrical Technologies (ICCEET), 2012 International Conference on* (pp. 877-880). IEEE. https://doi.org/10.1109/ICCEET.2012.6203873

[32] Inukollu, V. N., Arsi, S., & Ravuri, S. R. (2014). Security issues associated with big data in cloud computing. *International Journal of Network Security & Its Applications*, *6*(3), 45. https://doi.org/10.5121/ijnsa.2014.6304

[33] Roth, M., Klarmann, A., & Franczyk, B. (2013). Future logistics-challenges, requirements and solutions for logistics networks. *International Journal of Mechanical, Aerospace, Industrial, Mechatronic and Manufacturing Engineering*, *7*(10), 898-903.

[34] Stoltz, M. H., Giannikas, V., McFarlane, D., Strachan, J., Um, J., & Srinivasan, R. (2017). Augmented Reality in Warehouse Operations: Opportunities and Barriers. *IFAC-PapersOnLine*, *50*(1), 12979-12984. https://doi.org/10.1016/j.ifacol.2017.08.1807

[35] Yang, L. & Ye, M. (2014, May). The Design and Development of Intelligent Warehouse Management System based on. NET and Internet of Things. In *International Conference on Logistics Engineering, Management and Computer Science (LEMCS 2014)*. Atlantis Press. https://doi.org/10.2991/lemcs-14.2014.98

[36] Kim, J. Y. & Park, D. J. (2016). Internet-of-Things Based Approach for Warehouse Management System. *International journal of Multimedia and ubiquitous Engineering*, *11*(10), 159-166. https://doi.org/10.14257/ijmue.2016.11.10.15

[37] Liang, C., Chee, K. J., Zou, Y., Zhu, H., Causo, A., Vidas, S., ... & Cheah, C. C. (2015). *Automated robot picking system for e-commerce fulfillment warehouse application*. International federation for the promotion of mechanism and machine science.

[38] Mikušová, N., Čujan, Z., & Tomková, E. (2017). Robotization of Logistics Processes. In *MATEC Web of Conferences* (Vol. 134, p. 00038). EDP Sciences. https://doi.org/10.1051/matecconf/201713400038

Authors' contacts:

Krešimir BUNTAK, Ph.D. Assoc. Prof.
Corresponding author
University North,
Trg dr. Žarka Dolinara 1, 48000 Koprivnica, Croatia
krbuntak@unin.hr

Matija KOVAČIĆ, B.Ec.
University North,
Trg dr. Žarka Dolinara 1, 48000 Koprivnica, Croatia
matkovacic@unin.hr

Maja MUTAVDŽIJA, B.Ec.
University North,
Trg dr. Žarka Dolinara 1, 48000 Koprivnica, Croatia
mamutavdzija@unin.hr

ISSN 1846-6168 (Print), ISSN 1848-5588 (Online)
https://doi.org/10.31803/tg-20180810113043

Subject review

ASSESSMENT OF THE EFFECT OF INTEGRATION REALISATION IN CONSTRUCTION PROJECTS

Roman TRACH, Marzena LENDO-SIWICKA, Katarzyna PAWLUK, Nina BILOUS

Abstract: The aim of the article is to develop an assessment model for the effect received from the integration of enterprises during the realization of investment projects in the construction. Having analysed the existing methods of the economic effect evaluation, we came to the conclusion that it is impossible to use them completely to assess the economic effect of the integration of enterprises during the investment projects in the construction. In the case of an integrated realization of a project in the construction sector, it is the information and communication links that are combined, and not the enterprises themselves. In addition to that, not all models take into account the synergistic effect. To solve the above-mentioned problem, we analysed the advantages gained by participants during the realization of the integrated project in construction and the benefits that have the greatest impact on the synergy effect. The calculation of the effect of the information and communication system management and the innovative nature of the process of its implementation suggest that this process has a clear investment component. Consequently, the process of enterprise integration should be considered as an investment project implemented at the level of network association.

Keywords: construction project; information and communication system; integration; synergetic effect

1 INTRODUCTION

The questions of cooperation and integration during the delivery process were a great concern of scientists for a long period. For instance, it recalls how the separation of the design and construction phases of projects was identified as a problem by government industry reports in the UK as early as 1962 by Emerson, who identified how removed the responsibility for design is from the responsibility of production [1]. He suggests that the procurement models which omit the contractor can increase risk, reduce communication between team members, cause delays and create incorrect information which can lead to disputes and claims. The importance of the integration processes was emphasized by Chinowsky [2] who developed what is called an "Integration Matrix" (Fig. 1).

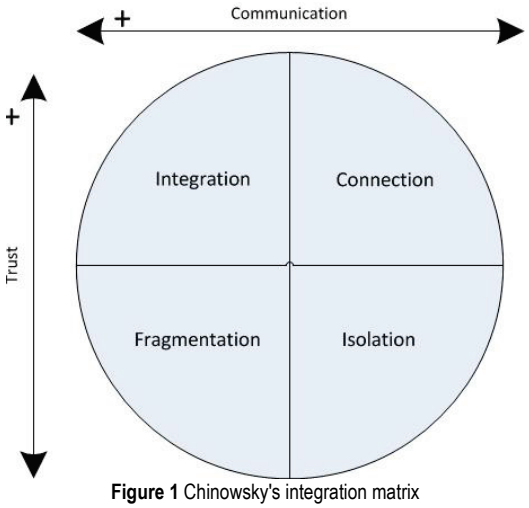

Figure 1 Chinowsky's integration matrix

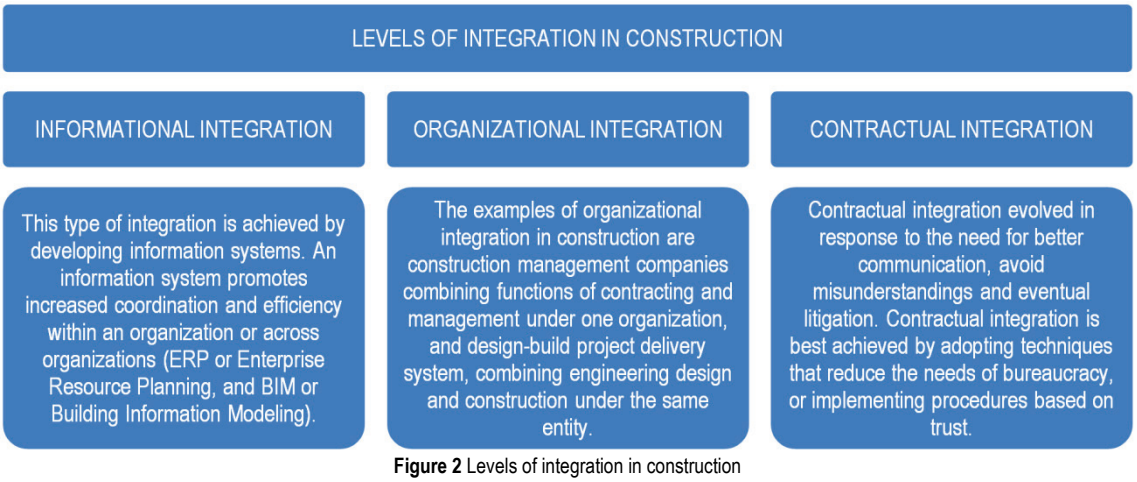

Figure 2 Levels of integration in construction

The four quadrants of the matrix refer to the varying levels of trust and communication. The final state is that of integration, where both trust and communication levels are high. They note that this is the preferred state for collaboration to occur. The concept of high performance is routinely implemented in diverse industries but has received

little attention in the construction industry, where success is typically measured using traditional indicators, such as time, cost and quality. Authors suggests that the problem can be addressed by viewing the construction team as an integrated group of participants within a network, rather than as a group of participants. The team needs to consist of a cohesive network where members focus on building long term relationships that are transferred from activity to activity.

The project delivery method is selected by the owner of the construction project. That method establishes the preconditions for the realization of the project, such as the roles and responsibilities of the participants, including the legal agreements between the parties by setting the project target and payment method. This tends to be a critical factor so if selected correctly, it enables the successful implementation of a construction project. Fig. 2 shows three levels of integration in construction.

The aim of the article is to develop the assessment model for the effect received from the integration of enterprises during project delivery in construction.

2 MATERIALS AND METHODS

Network structures have different configurations including heterogeneous elements that provide the highest level of collaboration. Such elements in each particular case have their own unique list that provides the energy of cooperation in each particular situation. The overall economic effect depends not only on the elements the network consists of, but also on the nature and quality of the links between them.

In modern economic conditions, the decision on the economic agents' integration considerably allows the change of the competitive position of the enterprise. The integration process leads to new subsystem formation and the interconnections between them. At the same time, the interaction and influence of the subsystems in an integrated structure is characterized by the emergence of a new synergetic component, which is considered to be the effect of enterprise integration, and is the basis of the goals and motives of integration. The synergistic effect presence means that the result of the integrated system of enterprises is higher than the sum of the results of individually operating enterprises united in the process of integration. Depending on synergy effect it can evaluate the effectiveness of the integration itself.

The efficiency of the integration process depends largely on how effectively the management of various forms of interaction between construction enterprises is carried out. The results of the integrated enterprise's production processes are not always clear and, in some cases, can lead to an efficiency decrease, because the enterprises do not fully use the potential of business units' interaction and the additional effects are the results of such potential. If the interaction of enterprises within the framework of integrated structures does not provide the desired effects, it is important to update the methodological approaches that help improve the mechanism of the integrated structures management. The presence or absence of economic connections with certain characteristics affords ground for affirming or denying the existence of a network structure. In our opinion, it is the interrelationships that can be distinguished from the general system of elements and can be used as the basis for identifying the network organizational structures. This is especially important for the network structures of the investment and construction complex, since they are characterized by the absence of legal consolidation of integration relationships, such as participation in capital, the transfer of property rights between economic entities.

The effect of network interaction between enterprises has its own specifics. It is not only the effect of consolidation because enterprises retain some independence (there is no saving in management costs, for instant, because the management apparatus of each of the enterprises remains the same). At the same time, a systemic dynamic should arise in the process of interaction and should become the consequence of it. It means that the coordinated work of independent companies provides an additional synergetic effect of the system interaction as a whole.

The investigation of the synergy phenomenon began to develop with the activation of integration processes in the economy, although the very point of the synergetic effect was described by Aristotle. In the IV century BC, he noted that "the whole is greater than the sum of its parts" [3]. I. Ansoff defined the synergy effect as the possibility of getting the better economic effect from the joint work of several business units in comparison with the results of their independent activity [4]. In his concept of synergy, he focuses on the role the economic base has, on the potential of material and non-material assets and their close connection with the potential of the enterprise.

X. Itami considered that the synergy effect received from integration is a result of resource utilization efficiency and it is growing in an integrated corporation in comparison to their use by companies before integration [5]. He identified two types of resources: physical resources (fixed assets, inventories, etc.) and intangible assets (brand, technology and know-how, corporate culture, etc.). In his opinion, two types of effects can be formed as a result of integration:

- complementary effect which refers to the improvement of physical resources usage (the corporation uses its resource potential in full),
- synergetic effect which is achieved only by using invisible assets.

In our opinion, using a network organizational structure during the delivery process in the construction industry has the most interesting and at the same time the most difficult issue to study. It is the issue of information synergy evaluation that is formed due to the optimization of information and communication management.

The analysis of theoretical and practical research in the field of economic entities integration [6, 7, 8] showed that the efficiency of integration is mainly assessed by minimizing the costs of the enterprises (they are transactions in most cases). In this article, only this approach is not sufficient, since it is planned to assess the efficiency of integration not only from the position of the interacting entities themselves,

but also from the position of the whole integrated system, within the framework of their interests and its coordination. It is expedient to assess the "cumulative effect" of acts of initiating integration chains of interaction between the socio-economic entities during project delivery in construction. Such effect can be evaluated only within the framework of a synergetic approach to integration evaluation.

Synergy can be classified according to the impact on the company's cash flows [9, 10] (Fig. 3).

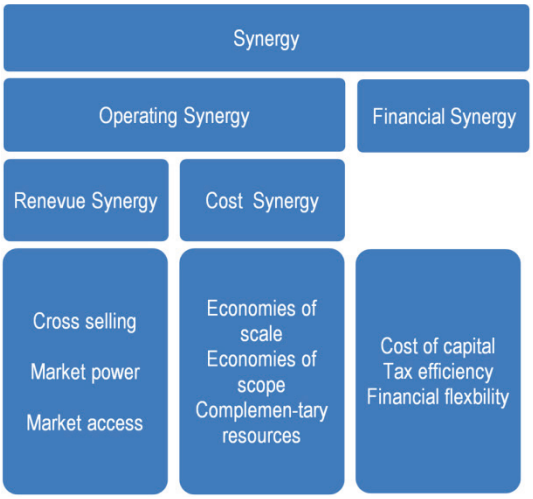

Figure 3 Classification of synergy

One of the main methods for synergistic effect evaluation is to compare the value of integrated enterprises, before and after their combination [11-13]. Net Assets Value Method, Market Method and Capital Assets Pricing Method can be used in this case. The Net Assets Value method is often used in takeovers and mergers and includes a set of methods to assess the value of enterprises, based on the costs that are necessary to restore the object of takeover. The main principle on which this method is based is the principle of substitution. It means that the buyer will never acquire an object at a price exceeding the cost of acquiring or reproducing an object similar in its consumer characteristics. This approach does not allow taking into account the changes in performance indicators in future periods. A typical example of the net assets' value method is the method proposed by A. Damodoran, who determines the synergetic effect as a result of exceeding the value of integrated companies over the sum of the companies' value before integration [14]. In particular, the Net Acquisition Value, NAV, is calculated according to the following formula:

$$NAV = \left[V_{ij} - (V_i + V_j) \right] - (P + E) \quad (1)$$

Using the following notations: V_{ij} - the value of the combined firms i and j; V_i - the value of the standalone firm I; V_j - the value of the standalone firm j; P - the premium paid for the acquisition; E - the amount of expenses engaged in the acquisition process.

The value in $V_{ij} - (V_i + V_j)$ is a synergistic effect. To recoup the integration, this effect should be greater than the sum $(P + E)$.

Methods that are used in the framework of the comparative approach make it possible to compare the assessed object with similar objects and on this basis, to establish its value. A comparative approach can be used for both market valuation and the valuation of investment value. However, since there are no two absolutely identical associations, some average market multipliers are expertly determined and used to calculate the cost using comparative approach methods and that reduces the accuracy of the results.

In practice, the Capital Assets Pricing Method is used more often and it gives the most objective assessment of the effect received from the integration. In this approach, the discounted cash flow method is used to estimate the value of the company. The very core of the method is to determine the current value of cash flows that will be received in the future. In the framework of the Capital Assets Pricing Method, there are a significant number of models suitable to calculate the economic effect.

In particular, S. A. Orekhov [15] calculates the effect received from integration into the holding structure as follows:

$$C_n = D(PN)_n + D(PA)_n + (EE)_n - DI_n + DT_n - I_o \quad (2)$$

Where: n - the calculated period of time; $D(PN)_n$ - the additional profit received from activity expansion; $D(PA)_n$ - the additional profit taken from risk reduction due to the diversification of the holding's activities; $(EE)_n$ - the saving current production costs; DI_n - the additional investments for reconstruction and expansion; DT_n - the increase (saving) of tax payments; I_o - the investments at the time of takeover.

A number of authors [16] propose to use the method of discounted cash flows in the framework of this approach. The synergistic effect is calculated in accordance with:

$$S = \sum_{t=1}^{T} \frac{\Delta CF_t}{(1+R)^t} \quad (3)$$

Where: ΔCF_t - the difference between the cash flows of the integrated company and the amount of cash flows of each company separately before the time t; R - the mathematical discount factor expectation that is calculated according to the planned rate of return to the net worth of the company that is taken over.

The increase in cash flows is as follows:

$$\Delta CF_t = \Delta R_t - \Delta C_t - \Delta T_t - \Delta I_t \quad (4)$$

Where: ΔR_t - the increase of the income received from the takeover; ΔC_t - the increase in costs; ΔT_t - the increase in tax payments; ΔI_t - the increase of additional working capital investments and fixed assets.

Having analysed the above methods and approaches, we can conclude that they cannot be fully used to evaluate the effect received from enterprise integration during project delivery in construction, since the vast majority of these methods are based on the analysis of enterprise amalgamation and their cash flows after the takeover. In the case of integrated project delivery in the construction industry, it is the information and communication links that are united, but not the enterprises themselves. Additionally, the synergistic (immaterial) effect is not taken into account in all models. Moreover, it is necessary to distinguish more clearly between the terms of economic effect evaluation and integration and the synergetic effect which is one of the main factors, but not the only one.

3 RESULTS AND DISCUSSIONS

This article proposes, in the framework of the synergetic approach, to take the ratio of the additional income received from the association of enterprises to the costs on this project delivery as a criterion for the economic efficiency of enterprise integration programs.

The calculation of the economic effect received from managing the information and communication system and the innovative character of the process of its implementation shows that this process has a clear investment component. Therefore, the process of enterprise integration should be considered as an investment project delivered at the level of a network association. Accordingly, regarding the innovative process of the information and communication system network model realization, the predictive efficiency of investments can be expressed by the following economic and mathematical dependence:

$$E_t = \frac{\sum_{i=1}^{m} \frac{I_t}{(1+n_t)^t}}{\sum_{i=1}^{m} \frac{CI_t}{(1+n_t)^t} + \sum_{i=1}^{m} \frac{CO_t}{(1+n_t)^t}} \quad (5)$$

Where: E_t - the efficiency of the information and communication system operation in the integrated project delivery over a period of time; I_t - the total revenue stream that the integrated enterprise receives from the information and communication system implementation over a period of time; CI_t - the investment costs that the enterprise spends to launch and implement the integrated information and communication system; CO_t - the operational costs to manage the information and communication system of the business entity; t - the analysed period of time; n_t - the rate of discounting accepted for calculations; m - the number of enterprises that integrate.

The synergy effect calculation is the most difficult part in the total revenue stream calculation. It is possible to use various factors to assess the synergy, and their sum-total is formed according to the direction and the logic of the research. Therefore, it is a situation similar to the economic efficiency integration evaluation, namely the isolation of the effects that are indicative for the integrated project delivery in construction. Taking into account the specifics of this research, namely, the evaluation of the effect formed after the information and communication system introduction in the integrated project delivery in construction, we can identify the following synergistic effects:

$$I_t = \sum \Delta S = S_1 + S_2 + S_3 + S_4 + S_5 + S_6 \quad (6)$$

Where: ΔS - the synergy effect, which is formed from the introduction of the information and communication system in the integrated project delivery; S_1 - the synergetic effect formed from reducing the number of errors and collisions in the construction project delivery; S_2 - the synergistic effect from the overall reduction of project duration due to a higher coordination of actions; S_3 - the synergistic effect of transaction costs reduction; S_4 - the synergetic effect from the cost reduction at the stage of facilities' management; S_5 - the synergistic effect of a new value creation; S_6 - the synergistic effect from the production scale increase.

The next stage is the analysis of the cost structure connected with the integrated project delivery. The expenses can be divided into two parts, the sustainable (investment) and variable (operational) costs.

The structure of investment expenses is determined by the task to introduce the integrated model into the network organizational structure of enterprises and is as follows:

$$CI_t = \left[\sum_{i=1}^{y} (C_e * T_{s\ bas} + C_{st}) + CI_{ce} + CI_s + CI_{db} \right] + \\ + \sum_{i=1}^{j} (C_{as} * T_{adapt}) \quad (7)$$

Where: C_e - the average wage rate of an employee who is having the training; $T_{s\ bas}$ - the time of training, one employee coordination and workplace integration; C_{st} - the average cost of training; CI_{ce} - the investment costs for computer equipment acquisition; CI_{ce} - the investment costs for software acquisition; CI_{db} - the investment costs for database acquisition; C_{as} - the average wage rate of the project manager assistant; T_{adapt} - the time the assistant needs to adapt in an integrated system; y - the number of employees and workplaces integrated into the system; j - the number of the project manager "assistant".

As it is seen from the expression (7), investment costs can be divided into the following three groups:

1) the costs of training for the employees to learn the new innovative model of network relationships (including both the costs of pay for those who conduct training and the loss of time during the training period when the employees of the enterprise are not engaged in the performance of their immediate duties);
2) the expenses for the computer equipment, software and database acquisition and adaptation;
3) the costs to adapt the project manager assistant to the integrated system.

The first two groups of expenses are reflected in the formula (7) in square brackets and include the training, computer equipment, software and database acquisition for all employees participating in the integrated process. The third term presents the expenses for the project manager "assistant".

Operating costs are given in the following expression:

$$CO_t = \sum_{i=1}^{y}(CO_{ce} + CO_s + CO_{db}) + \sum_{i=1}^{j}(C_{as} * T_w) + \\ + \sum_{i=1}^{x}(C_t * T_{s\ add}) \quad (8)$$

Where: CO_{ce} - the operating costs for computer services; CO_s - the operating costs for software maintenance; CO_{db} is the operating costs for database maintenance; T_w - the project manager assistant work duration; $T_{s\ add}$ - the time for additional training, consultation and formalization of knowledge for the employee; x - the number of employees who need additional training and consultations.

m - the duration of the project, years.

They also form three clear groups:

1) expenses for computer services, software and database maintenance;

2) expenses for the salary of the project manager assistant;

3) expenses for the additional training, consultations and formalization of knowledge for employees.

Taking into account the expressions (6)-(8), the formula (5) can be expressed by the following economic-mathematical dependence:

$$E_t = \frac{\sum_{i=1}^{m}\frac{S_1 + S_2 + S_3 + S_4 + S_5 + S_6}{(1+n_t)^t}}{\sum_{i=1}^{m}\frac{\left[\sum_{i=1}^{y}(C_e * T_{s\ bas} + C_{st}) + CI_{ce} + CI_s + CI_{db}\right] + \sum_{i=1}^{j}(C_{as} * T_{adapt})}{(1+n_t)^t} + \sum_{i=1}^{m}\frac{\sum_{i=1}^{y}(CO_{ce} + CO_s + CO_{db}) + \sum_{i=1}^{j}(C_{as} * T_w) + \sum_{i=1}^{x}(C_t * T_{s\ add})}{(1+n_t)^t}} \quad (9)$$

The predictive efficiency indicator E_t of the information and communication structure integration during project delivery in construction should not be less than one. At the same time, the value $E_t > 1$ indicates a positive effect of innovation.

4 CONCLUSIONS

A system of economic and mathematical dependencies has therefore been formed to assess the effect of enterprise integration during project delivery in construction. The criterion for the efficiency of enterprise integration programs is the ratio of the additional income received from the association of enterprises to the costs on this project delivery. The additional income is the total synergistic effect that the integrated enterprise receives from the information and communication system implementation. The costs is the sustainable (investment) and variable (operational) costs on this project delivery. The paper proposes how to solve the issue of separating the share, which is formed as a result of integration processes, from the general effects of the enterprise's economic activity. Finally, the advantages obtained by the participants of the integrated project in construction are analyzed and the advantages that have the greatest impact on the synergistic effect are highlighted. In our opinion, it is warranted to use projections to make a decision on integration, and retrospective evaluation should be used to determine how well the business combination operates. Further studies will be related to the practical application of the model proposed to evaluate the economic effect received from the integration of enterprises during project delivery in construction.

Abbreviations

NAV - Net Acquisition Value
ERP - Enterprise Resource Planning
BIM - Building Information Modelling

5 REFERENCES

[1] Mosey, D. (2009). *Early contractor involvement in building procurement: contracts, partnering and project management*, Chichester: John Wiley & Sons Ltd. https://doi.org/10.1002/9781444309867

[2] Chinowsky, P. & Songer, A. (2011). *Organizational management in construction*, New York: Spon Press. https://doi.org/10.4324/9780203856109

[3] Aristotel. (2006). *Metaphysika (Metaphysics)*. Moskva: Eksmo (in Russian).

[4] Ansoff, I. (2009). *Strategicheskiy menedzhment (Strategic management).* Sankt-Peterburg: Piter (in Russian).

[5] Asaul, A. N. & Ivanov, S. N. (2008). *Snizhenie transaktsionnyih zatrat v stroitelstve za schYot optimizatsii informatsionnogo prostranstva (Decrease in transaction costs in construction due to optimization of the information space).* Sankt-Peterburg: ANO IPEV (in Russian).

[6] Rowley, J. (2002). Synergy and strategy in e-business. *Marketing Intelligence and Planning*, 20(4), 215-222. https://doi.org/10.1108/02634500210431603

[7] Franzsen, D., Van der Merwe, R., Buys, S., Bischoff, A. Courtney, F., Varachia, A., Cox, E., & Miller, C. (2001). *Synergies in the distribution business of Barloworld*. Unpublished manuscript, Barloworld Leadership Development Programme, Gordon Institute of Business Science, Johannesburg.

[8] Naudé, A., Heyns, D., Bester, C., Puig, J. & Tucker, G. (2002). *Synergies within Barloworld*. Unpublished manuscript,

Barloworld Executive Development Programme, Gordon Institute of Business Science, Johannesburg. https://doi.org/10.1111/j.1745-6622.2009.00255.x
[9] Baldi, F., & Trigeorgis, L. (2009). Assessing the value of growth option synergies from business combinations and testing for goodwill impairment. *Journal of Applied Corporate Finance*, 21(4), 115-124.
[10] DePamphilis, D. (2010). *Mergers, acquisitions and other restructuring activities*. Burlington: Academic Press Advanced Finance Series.
[11] Sehleanu, M. (2015). Creating or destroying value through mergers and acquisitions? *Annals of the University of Oradea. Economic Science Series*, 24(1), 593-600.
[12] Hamza, T., Schaier, A., & Thraya, M. H. (2016). How do takeovers create synergies? Evidence from France. *Studies in Business and Economics, 11*(1), 54-72. https://doi.org/10.1515/sbe-2016-0005
[13] Shaver, M. (2006). A paradox of synergy: contagion and capacity effects in mergers and acquisitions. *Academy of management review, 31*(4), 962-976. https://doi.org/10.5465/amr.2006.22527468
[14] Damodaran, A. (2005). *The value of synergy (working paper)*, New York: Stern School of Business. https://doi.org/10.2139/ssrn.841486
[15] Orekhov, S. A. (2001). *Statisticheskie aspektyi issledovaniya diversifikatsii korporatsiy [Statistical aspects of research of diversification of corporations]*. Moskva: INION RAN (in Russian).
[16] Basmah, A. Q. & Rahatullah, M. K. (2013). Financial synergy in mergers and acquisitions in Saudi Arabia, *Finance - Challenges of the Future Yea*, XIII (15), 181-192.

Authors' contacts:

Roman TRACH, PhD
Warsaw University of Life Sciences,
Nowoursynowska 166, 02-787 Warsaw, Poland
roman_trach@sggw.pl

Marzena LENDO-SIWICKA, PhD
Warsaw University of Life Sciences,
Nowoursynowska 166, 02-787 Warsaw, Poland
marzena_lendo_siwicka@sggw.pl

Katarzyna PAWLUK, PhD
Warsaw University of Life Sciences,
Nowoursynowska 166, 02-787 Warsaw, Poland
katarzyna_pawluk@sggw.pl

Nina BILOUS, PhD
National University of Water and Environmental Engineering,
11 Soborna, 33028 Rivne, Ukraine
n.m.bilous@nuwm.edu.ua

TOPICS

DESIGN METHODS
- Requirements Engineering
- Design for X
- Ecodesign implementation
- Design for additive manufacturing
- Product service engineering
- Computational design synthesis
- Engineering design in mechatronics
- Change management

DESIGN PROCESSES
- Configuration and modularisation
- Modelling and management of engineering processes
- Product development models and strategies
- Conceptual design cognition
- Design for product life cycle
- Resilient processes

INFORMATION & KNOWLEDGE
- Design knowledge and collaboration
- Collaborative systems
- Representations of design information
- Decision making and decision support
- Knowledge intensive design
- Artificial intelligence in design
- Data driven design

THEORY AND RESEARCH METHODS
- Empirical studies of design and design support
- New approaches to the design theories
- Design science research methods
- Design theory

ENGINEERING DESIGN PRACTICE
- Geometrical modelling, simulation and tolerancing
- Simulation based design
- Optimisation
- Visualisation and virtualisation

DESIGN INNOVATION
- Creativity and ideation
- Innovation methods and tools
- Open innovation
- Social innovation

DESIGN2020

SYSTEMS ENGINEERING
- Defining a systems approach
- Managing structural complexity
- Simulation within complex systems
- Complex systems design
- Interdependencies in complex systems
- Model-based systems engineering (MBSE)
- Cyber-physical systems design

ORGANISATION & MANAGEMENT
- Organisational understanding of product development
- Multi-product development
- Life cycle management
- Market and business implications
- Global product development
- Globalisation, legislation, remanufacturing

DESIGN SUPPORT TOOLS
- Tools for DfX and product development
- IT in product development
- Usage and integration of supportive technologies
- Virtual product development
- PDM/PLM

SOCIOTECHNICAL ISSUES
- Approaches to socio-technical systems design
- Human factors in design
- Socially responsible design
- Technology and sustainable development
- Life science and design for healthcare

HUMAN BEHAVIOUR
- Cooperation and collaboration
- Designer's attitudes and skills
- Human thinking
- Emotional engineering

INDUSTRIAL DESIGN
- User-centred design
- Aesthetics and visual impressions
- User interaction design

DESIGN EDUCATION
- Design education strategy
- Tools and environments for design education
- Project-based education

INVITATION

By tradition, DESIGN Conference is a forum for discussion and further development of all aspects of design knowledge from cognition and philosophy to methods and tools, from research theory to practice.

The goal of DESIGN Conference is to bring together researchers and practitioners who have worked on or thought about engineering and industrial design from a variety of perspectives, disciplines, and fields: engineering, aesthetics, ergonomics, psychology, sociology and the like.

Programme Chairs welcome the high-quality submissions covering substantial, original and previously unpublished research.

Rigour academic research should provide designers with the next generation of method and tools that will be appropriate to the demands. The paper submitted should address the key questions of the DESIGN 2020 conference. What are the new advances in design theory and research? How to improve design methodologies and tools, projects and processes, development of products and services? Which competencies, information, and communication technologies are needed? What is the impact on everyday design work? What social and legal issues should be considered? How we can harmonize the research outcomes so they can be transferred to design practice?

Applied, theoretical and results-oriented papers from both academia and industry, based on thorough analysis or argumentation, will all be considered for the conference programme.

The submitted papers should fit into one of the proposed conference topics. It is expected that these specific topics are extensive and non-exhaustive.

A list of examples is added for illustrating the core topics. It is required explicitly from all contributors to show how they are contributing to the overall research within these areas.

A detailed description of topics and instructions for online submission are available at **www.designconference.org**

REVIEWING POLICY

The papers will be accepted on the double-blind review basis made by the members of the Scientific Advisory Board.

The review criteria will be the novelty and level of contribution, validity of conclusions, industrial or application perspective and formal qualities of the contribution.

DESIGN Conference papers are indexed in SCOPUS and WOS - CPCI and referenced in CrossRef with DOI identifier.

Selected papers will be recommended for publication in international journals.

PROGRAMME

The DESIGN Conference provides an interactive environment where participants proactively create opportunities to share design knowledge and new cross-disciplinary research that leads to innovation.

PLENARY SESSIONS
The new ideas and visions will be presented by the keynote speakers.

TOPIC-ORIENTED SESSIONS
Will host papers selected around common research questions in order to foster discussion.

WORKSHOPS
DESIGN 2020 workshops will promote the integration of different views, approaches, and methods. Workshop coordinators could invite selected presentations and demonstrations in order to stimulate the debate as well as to propose any format of delivery that inspires interaction. The workshops will be organised on the 18th of May.

PH.D. STUDENTS' FORUM
The forum will be a unique opportunity for younger researchers and Ph.D. students to discuss their research questions and ideas with experienced researchers, practitioners and R&D managers in order to facilitate their research efforts.

THE DESIGN DEBATE
The purpose of the design debate is to investigate in a forensic manner some key topics that affect the engineering design research community. Two opponents and the debate moderator will be distinguished key players in the community presenting evidence for or against a particular topic.

INDUSTRIAL FORUM
The industrial forum will be an opportunity to discuss industrial views, needs and expectations of design research, tracing the emerging trends in industrial innovation and the right strategies for a sustainable future. The forum will offer a platform for debate among decision-makers, practitioners and academics about the future of design research, needs and expectations.

1. Full paper submission deadline **November, 15 2019**
2. Final acceptance of papers **January, 27 2020**
3. Publish-ready papers **February, 21 2020**
4. Final Conference programme **April, 2020**
5. **DESIGN 2020 Conference May, 18-21 2020**

CONFERENCE VENUE
Hotel Croatia Cavtat
Frankopanska ul. 10, 20210 Cavtat, Croatia

PROGRAMME CHAIRS
John Clarkson
University of Cambridge, United Kingdom
Tim McAloone
Technical University of Denmark, Denmark
Julie Stal-Le Cardinal
CentraleSupélec, Paris, France
Mario Štorga
University of Zagreb, Croatia
Christian Weber
Technical University Ilmenau, Germany
Dorian Marjanović
University of Zagreb, Croatia

ORGANISING SECRETARIAT ADDRESS
DESIGN Conference Secretariat
Faculty of Mechanical Engineering and Naval Architecture
Ivana Lučića 5, 10 000 Zagreb, Croatia
Phone: +385 1 6168 432
design2020@fsb.hr
www.designconference.org

the Design Society – a worldwide community
cad lab
FSB 100

ISSN 1846-6168 (Print), ISSN 1848-5588 (Online)
https://doi.org/10.31803/tg-20.....

14pt
14pt

ARTICLE TITLE ONLY IN ENGLISH (Style: Arial Narrow, Bold, 14pt)

14pt

Ivan HORVAT, Thomas JOHNSON (Style: Arial Narrow, Bold, 11pt)

11pt
11pt

Abstract: Article abstract contains maximum of 150 words and is written in the language of the article. The abstract should reflect the content of the article as precisely as possible. TECHNICAL JOURNAL is a trade journal that publishes scientific and professional papers from the domain(s) of mechanical engineering, electrical engineering, civil engineering, multimedia, logistics, etc., and their boundary areas. This document must be used as the template for writing articles so that all the articles have the same layout. (Style: Arial Narraw, 8pt)

8pt

Keywords: keywords in alphabetical order (5-6 key words). Keywords are generally taken from the article title and/or from the abstract. (Style: Arial Narraw, 8pt)

10pt
10pt

1 ARTICLE DESIGN

(Style: Arial Narrow, Bold, 10pt)

10pt

(Tab 6 mm) The article is written in Latin script and Greek symbols can be used for labelling. The length of the article is limited to eight pages of international paper size of Letter (in accordance with the template with all the tables and figures included). When formatting the text the syllabification option is not to be used.

10pt

1.1 General Guidelines

(Style: Arial Narrow, 10pt, Bold, Align Left)

10pt

The document format is Letter with margins in accordance with the template. A two column layout is used with the column spacing of 10 mm. The running text is written in Times New Roman with single line spacing, font size 10 pt, alignment justified.

Article title must clearly reflect the issues covered by the article (it should not contain more than 15 words).

Body of the text is divided into chapters and the chapters are divided into subchapters, if needed. Chapters are numbered with Arabic numerals (followed by a period). Subchapters, as a part of a chapter, are marked with two Arabic numerals i.e. 1.1, 1.2, 1.3, etc. Subchapters can be divided into even smaller units that are marked with three Arabic numerals i.e. 1.1.1, 1.1.2, etc. Further divisions are not to be made.

Titles of chapters are written in capital letters (uppercase) and are aligned in the centre. The titles of subchapters (and smaller units) are written in small letters (lowercase) and are aligned left. If the text in the title of the subchapter is longer than one line, no hanging indents.

10pt

Typographical symbols (bullets), which are being used for marking an item in a list or for enumeration, are placed at a beginning of a line. There is a spacing of 10pt following the last item:

- Item 1
- Item 2
- Item 3

10pt

The same rule is valid when items are numbered in a list:

1. Item 1
2. Item 2
3. Item 3

10pt

1.2 Formatting of Pictures, Tables and Equations

(Style: Arial Narrow, 10pt, Bold, Align Left)

10pt

Figures (drawings, diagrams, photographs) that are part of the content are embedded into the article and aligned in the centre. In order for the figure to always be in the same position in relation to the text, the following settings should be defined when importing it: text wrapping / in line with text.

Pictures must be formatted for graphic reproduction with minimal resolution of 300 dpi. Pictures downloaded from the internet in ratio 1:1 are not suitable for print reproduction because of unsatisfying quality.

10pt

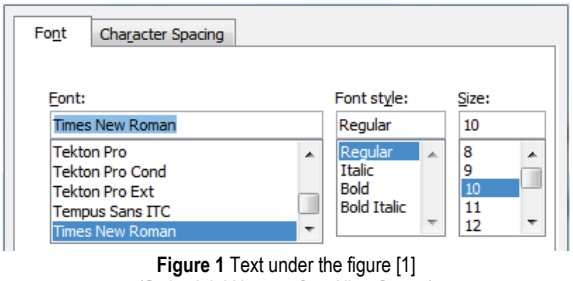

Figure 1 Text under the figure [1]
(Style: Arial Narraw, 8pt, Align Centre)

10pt

The journal is printed in black ink and the figures have to be prepared accordingly so that bright tones are printed in a satisfactory manner and are readable. Figures are to be in colour for the purpose of digital format publishing. Figures in the article are numbered with Arabic numerals (followed by a period).

Text and other data in tables are formatted - Times New Roman, 8pt, Normal, Align Center.

When describing figures and tables, physical units and their factors are written in italics with Latin or Greek letters,

while the measuring values and numbers are written upright.

10pt

Table 1 Table title aligned centre

(Style: Arial Narraw, 8pt, Align Centre)

	1	2	3	4	5	6
ABC	ab	ab	ab	ab	ab	ab
DEF	cd	cd	cd	cd	cd	cd
GHI	ef	ef	ef	ef	ef	ef

10 pt

Equations in the text are numbered with Arabic numerals inside the round brackets on the right side of the text. Inside the text they are referred to with equation number inside the round brackets i.e. ".... from Eq. (5) follows ...." (Create equations with MathType Equation Editor - some examples are given below).

10pt

$$F_{\text{avg}}(t,t_0)=\frac{1}{t}\int_{t_0}^{t_0+t}F\big(q(\tau),p(\tau)\big)\,\mathrm{d}\tau, \tag{1}$$

10pt

$$\cos\alpha+\cos\beta=2\cos\frac{\alpha+\beta}{2}\cdot\cos\frac{\alpha-\beta}{2}. \tag{2}$$

10pt

Variables that are used in equations and also in the text or tables of the article are formatted as *italics* in the same font size as the text.

10pt

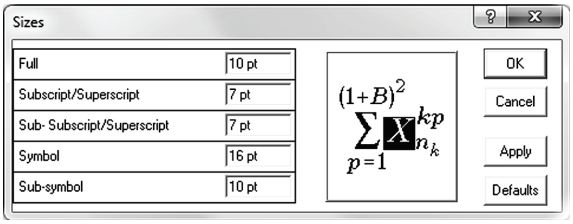

Figure 2 The texts under figures

(Style: Arial Narraw, 8pt, Align Centre)

10pt

Figures and tables that are a part of the article have to be mentioned inside the text and thus connected to the content i.e. „ … as shown in Fig. 1…" or „data from Tab. 1…" and similar.

10pt

2 PRELIMINARY ANNOTATION

10pt

Article that is offered for publication cannot be published beforehand, be it in the same or similar form, and it cannot be offered at the same time to a different journal. Author or authors are solely responsible for the content of the article and the authenticity of information and statements written in the article.

Articles that are accepted for publishing are classified into four categories: original scientific papers, preliminary communications, subject reviews and professional papers.

Original scientific papers are articles that according to the reviewer and the editorial board contain original theoretical or practical results of research. These articles need to be written in such a way that based on the information given, the experiment can be repeated and the results described can be achieved together with the author's observations, theoretical statements or measurements.

Preliminary communication contains one or more pieces of new scientific information, but without details that allow recollection as in original scientific papers. Preliminary communication can give results of an experimental research, results of a shorter research or research in progress that is deemed useful for publishing.

Subject review contains a complete depiction of conditions and tendencies of a specific domain of theory, technology or application. Articles in this category have an overview character with a critical review and evaluation. Cited literature must be complete enough to allow a good insight and comprehension of the depicted domain.

Professional paper can contain a description of an original solution to a device, assembly or instrument, depiction of important practical solutions, and similar. The article need not be related to the original research, but it should contains a contribution to an application of known scientific results and their adaptation to practical needs, so it presents a contribution to spreading knowledge, etc.

Outside the mentioned categorization, the Editorial board of the journal will publish articles of interesting content in a special column. These articles provide descriptions of practical implementation and solutions from the area of production, experiences from device application, and similar.

10pt

3 WRITING AN ARTICLE

10pt

Article is written in the English language and the terminology and the measurement system should be adjusted to legal regulations, standards (ISO 80 000 series) and the SI international system of units. The article should be written in third person.

Introduction contains the depiction of the problem and an account of important results that come from the articles that are listed in the cited literature.

Main section of the article can be divided into several parts or chapters. Mathematical statements that obstruct the reading of the article should be avoided. Mathematical statements that cannot be avoided can be written as one or more addendums, when needed. It is recommended to use an example when an experiment procedure, the use of the work in a concrete situation or an algorithm of the suggested method must be illustrated. In general, an analysis should be experimentally confirmed.

Conclusion is a part of the article where the results are being given and efficiency of the procedure used is emphasized. Possible procedure and domain constraints where the obtained results can be applied should be emphasized.

10pt

4 RECAPITULATION ANNOTATION

10pt

In order for the articles to be formatted in the same manner as in this template, this document is recommended for use when writing the article. Finished articles written in MS Word for Windows and formatted according to this

template must be submitted using our The Paper Submission Tool (PST) (https://tehnickiglasnik.unin.hr/authors.php) or eventually sent to the Editorial board of the Technical Journal to the following e-mail address: tehnickiglasnik@unin.hr

The editorial board reserves the right to minor redaction corrections of the article within the framework of prepress procedures. Articles that in any way do not follow these authors' instructions will be returned to the author by the editorial board. Should any questions arise, the editorial board contacts only the first author and accepts only the reflections given by the first author.

10pt

5 REFERENCES (According to APA)

10pt

The literature is cited in the order it is used in the article. Individual references from the listed literature inside the text are addressed with the corresponding number inside square brackets i.e. "… in [7] is shown …". If the literature references are web links, the hyperlink is to be removed as shown with the reference number 8. Also, the hyperlinks from the e-mail addresses of the authors are to be removed. In the literature list, each unit is marked with a number and listed according to the following examples (omit the subtitles over the references – they are here only to show possible types of references):

9pt

[1] See http://www.bibme.org/citation-guide/apa/

[2] See http://sites.umuc.edu/library/libhow/apa_examples.cfm

[3] (Style: Times New Roman, 9pt, according to APA)

[4] Amidzic, O., Riehle, H. J., & Elbert, T. (2006). Toward a psychophysiology of expertise: Focal magnetic gamma bursts as a signature of memory chunks and the aptitude of chess players. *Journal of Psychophysiology, 20*(4), 253-258. https://doi.org/10.1027/0269-8803.20.4.253

[5] Reitzes, D. C. & Mutran, E. J. (2004). The transition to retirement: Stages and factors that influence retirement adjustment. *International Journal of Aging and Human Development, 59*(1), 63-84. Retrieved from http://www.baywood.com/journals/PreviewJournals.asp?Id=0091-4150

[6] Jans, N. (1993). *The last light breaking: Life among Alaska's Inupiat Eskimos*. Anchorage, AK: Alaska Northwest Books.

[7] Miller, J., & Smith, T. (Eds.). (1996). *Cape Cod stories: Tales from Cape Cod, Nantucket, and Martha's Vineyard*. San Francisco, CA: Chronicle Books.

[8] Chaffe-Stengel, P. & Stengel, D. (2012). *Working with sample data: Exploration and inference*. https://doi.org/10.4128/9781606492147

[9] Freitas, N. (2015, January 6). People around the world are voluntarily submitting to China's Great Firewall. Why? Retrieved from http://www.slate.com/blogs/future_tense/2015/01/06/tencent_s_wechat_worldwide_internet_users_are_voluntarily_submitting_to.html (Style: Times New Roman, 9pt, according to APA)

10pt

10pt

Authors' contacts:

8pt

Full Name, title
Institution, company
Address
Tel./Fax, e-mail

8pt

Full Name, title
Institution, company
Address
Tel./Fax, e-mail

ichd-home.com

ICHD 2020

14th International Conference on Hydrodynamics

Hosting Institutes
CNR-INM
Roma Tre University

Rome
Aug 30 - Sept 4
2020

Chairmen
Prof. Massimo Gennaretti
(Roma Tre University)
Dr. Claudio Lugni
(CNR-INM)

To encourage the interdisciplinary research, each day of the Symposium, a plenary session will be dedicated to one of the following fundamental topic:

- Climate Change
- Ocean Pollution
- Marine Biotechnology
- Next Generation of Marine Renewable Energy

For each of them, a keynote lecture, followed by 2-3 extended presentations and an open discussion, will provide a multidisciplinary vision of the subject

Istituto di INgegneria del Mare
INM

ROMA TRE
UNIVERSITÀ DEGLI STUDI

The 14th ICHD represents a unique arena for the cooperation between traditionally different but scientifically similar engineering fields. This cross-fertilization of reaearch areas will encourage the cooperation among scientists from different nations and disciplines.

Objective of the Conference

The topics widely range over several areas of theoretical and applied hydrodynamics, but are not limited to them:

- Fluid-structure interactions and hydroelasticity
- Hydroacustics
- Hydraulic engineering

- Experimental fluid dynamics
- Aquaculture

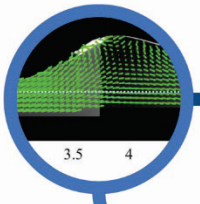

- Advanced experimental techniques
- Ocean and atmosphere dynamics

- Theoretical hydrodynamics
- Cavitation and liquid flows with air cavities

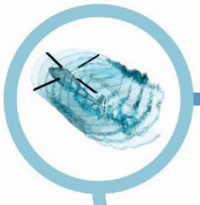

- Computational fluid dynamics
- Marine robotics

- Ocean engineering
- Coastal engineering
- Marine renewable energy

As a supporting journal for the ICHD'2020, Journal of Hydrodynamics (http://www.springer.com/journal/42241) will select some excellent papers to publish a special issue/column in the journal.

TEHNIČKI GLASNIK / TECHNICAL JOURNAL – GODIŠTE / VOLUME 13 – BROJ / NUMBER 3

RUJAN 2019 / SEPTEMBER 2019 – STRANICA / PAGES 165-259

Sveučilište Sjever

SVEUČILIŠTE SJEVER / UNIVERSITY NORTH – CROATIA – EUROPE

ISSN 1846-6168 (PRINT) / ISSN 1848-5588 (ONLINE)

TEHNICKIGLASNIK@UNIN.HR – HTTP://TEHNICKIGLASNIK.UNIN.HR